Detection of Weak Bonds in Bond ed CFRP Assemblies using Symmetrical LAser Shock Adhesion Test (S-LASAT)

Maxime Sagnard

▶ **To cite this version:**

HAL Id: tel-02896258
https://pastel.hal.science/tel-02896258

Submitted on 10 Jul 2020

École doctorale n° 432 : Science des Métiers de l'ingénieur

Doctorat ParisTech

T H È S E

pour obtenir le grade de docteur délivré par

l'École Nationale Supérieure d'Arts et Métiers

Spécialité " Génie Mécanique et Matériaux "

présentée et soutenue publiquement par

Maxime Sagnard

le 7 mai 2019

Detection of Weak Bonds in Bonded CFRP Assemblies using Symmetrical LAser Shock Adhesion Test (S-LASAT)

Directeur de thèse : **Laurent BERTHE**
Co-encadrement de la thèse : **Fabienne TOUCHARD, Romain ECAULT, Michel BOUSTIE**

Jury

Mme Nadia BAHLOULI	Professor	ICube	Univ. Strasbourg	Présidente
M. Konstantinos TSERPES	Professor	LTSM-UPAT	Univ. Patras	Rapporteur
M. Michel ARRIGONI	Professor	IRDL	ENSTA	Rapporteur
Mme Véronique FAVIER	Directrice de Recherche	PIMM	ENSAM	Examinatrice
M. Laurent VIDEAU	Ingénieur	CEA/DAM/DIF	CEA	Examinateur
M. Laurent BERTHE	Directeur de Recherche	PIMM	ENSAM	Examinateur
M. Romain ECAULT	Ingénieur	Airbus	Airbus	Examinateur
Mme Fabienne TOUCHARD	Directrice de Recherche	PPRIM	ENSMA	Invitée
M. Michel BOUSTIE	Directeur de Recherche	PPRIM	ENSAM	Invité

T
H
È
S
E

Arts et Métiers ParisTech - Campus de Paris
Laboratoire PIMM – Procédés et Ingénierie en Mécanique et Matériaux

REMERCIEMENTS

Je souhaite tout d'abord remercier **Laurent Berthe**, mon directeur de thèse. Ta confiance et ton soutien tout au long de ces années m'ont sans cesse poussé à me dépasser, et à donner le meilleur de moi-même. Au-delà d'un encadrant, tu as été pour moi un véritable mentor.

Mes remerciements vont ensuite à **Fabienne Touchard et Michel Boustie**, co-encadrants de la thèse. Fabienne, ta rigueur et ton recul vis-à-vis des résultats m'ont amené à chercher plus loin, et à rester curieux et critique face aux données acquises lors de la thèse. Quant à toi Michel, je ne peux que te remercier pour tous tes conseils, ces petites graines d'expérience que tu as partagées tout au long de notre collaboration.

Un grand merci à **Romain Ecault**, également co-encadrant de cette thèse. J'ai beaucoup apprécié ta capacité à « garder le cap », à toujours avoir en tête l'objectif de nos recherches. Couplé à ton recul et ta connaissance de la technologie LASAT, ces atouts nous ont permis d'avancer.

Je souhaite également remercier les membres du jury de cette thèse. **Nadia Bahlouli**, merci beaucoup de l'avoir présidé. Votre curiosité et votre bienveillance ont permis de créer un environnement propice à l'échange, rendant nos discussions particulièrement intéressantes.

A really big thank you to **Konstantinos Tserpes** and **Michel Arrigoni**, both reviewers of my work. Kostas, it has been a real pleasure to work with you and I was really honoured you accepted to be part of the jury. Michel, j'étais particulièrement content de te présenter mes travaux. Tu fais partie de cette lignée de chercheurs qui ont travaillé sur le sujet, et te montrer les avancés de la technologie m'a vraiment fait plaisir.

Laurent Videau, merci non seulement d'avoir fait partie de mon jury, mais aussi pour tous les échanges constructifs que nous avons pu avoir lors de ces 3 années.

Pour finir je voudrais remercier **Véronique Favier**, directrice du laboratoire PIMM. Merci beaucoup pour ton soutien lors de la soutenance, mais aussi pour tout ce que tu fais pour le labo. Ton énergie et ton implication ont été une réelle source d'inspiration pour moi.

En parlant du labo, je voudrais maintenant remercier cette communauté qui m'a permis de m'épanouir tant sur le plan professionnel que personnel. Mes pensées vont tout d'abord aux membres des « Shed laser », laseristes hors pair, que rien n'arrête, surtout pas des blocs d'acier (n'est-ce pas Habibi ?)

Un grand merci à tous les doctorants : **Damien Courapied**, **Abbas « Habibi » Hamie**, **Valérie Gunenthiram**, **Emna Abouda**, **Olivier Andreau**, **Thibaud De Terris**, **Elise Ferreira**, **Socona Traore**, **Yaasin Mayi**, **Marine Scius Bertrand**, **Khaled Ayfi** et **Alexandre Rondepierre**. Vous

avez eu à me supporter pendant de longues journées, moi, ma fixette sur vos plats préférés et ces musiques « de pub » que je sifflotais (c'était quand même du Simon & Garfunkel !). Vous avez été l'un des piliers de ma thèse et je ne vous remercierai jamais assez pour votre soutien. Je tiens tout particulièrement à remercier les Marines et leur fidèle compagnon à fourrure **Stormy**. Leur énergie et leur bonne humeur ont à coup sûr joué un grand rôle.

Simon Bardy, je ne t'oublie pas. Compagnons de choc comme tu le dis toi-même, nos pérégrinations et toutes ces conversations sont autant de souvenirs qui me sont chers. Merci à toi aussi **Sondes Metoui** pour ton implication et ta gentillesse.

Un grand merci également à l'homme qui murmurait à l'oreille de Comsol, **Morgan Dal**. Nos discussions sur des sujet divers et variés me manquent déjà. Merci beaucoup pour tous ces échanges, et ce, malgré le fait de t'avoir littéralement trainé dans la boue (c'était quand même sympa le mudday !). Je pense aussi à **Maxime Lacuve**, un autre compagnon d'infortune lors de cette course.

Je voudrais remercier **Remy Fabbro**, **Patrice Peyre**, **Mathieu Schneider**, **Thierry Malot**, **Frédéric Coste**, **Didier Zagouri** et **Corinne Dupuy** pour tout ce qu'ils m'ont apporté et appris durant ces 3 années. Un immense merci également à **Yann Rouchausse** et ses jeux de mots qui me laissaient par moment sans voix, et **Cyril Gorny**, la bible du cinéma. Merci pour votre aide inestimable sur la plateforme Héphaïstos.

Bien évidemment je souhaite vous remercier vous tous au PIMM. Merci aux doctorants, **Tanguy et Samira Choupin**, **Nicolas Gay**, **Clément Frémont**, **Sara Aid**, **Fatima Essabti**, **Zaid Boussatine**, et tous ceux qui se reconnaitront. Un grand merci à tous les chercheurs et pour les échanges (verbaux, ou de balles) que l'on a eu. Je pense notamment à **Bruno Fayolle**, **Emmanuel Richaud**, **Pierre Gilormini**, **Sebastien Roland**, **Amran « Lounes » Illoul**, **Eric Monteiro** et **Francisco Chinesta**. Un grand merci à toi **Christophe Canu**, je n'ai franchement pas été un cadeau avec mes paquets de 2 ans de note de frais....

Enfin, je voudrais remercier ceux sans qui rien de tout ça n'aurait pu avoir lieu. Je pense notamment à toi **Amanda**. Sans ton soutien sans faille, beaucoup de choses n'auraient pas été possibles. Ton nom n'est pas dans les auteurs de ce document, mais cette thèse est autant la tienne que la mienne.

Merci à toi **Pierre**, pour ces tartes flambées aux 4 chouettes, ces week-ends au prieuré et à Munich, et surtout merci d'avoir été à mes côtés.

Seb, je t'en dois une belle aussi. Bien qu'à l'autre bout de la France, tes colis surprises et ta joie de vivre ont été d'un soutien inestimable.

Pour finir, merci à mes parent, **Marie-Elisabeth** et **Alain**, et à ma sœur **Mylène**. Votre présence et votre soutien pendant ces 28 années sont sans commune mesure. Vous avez toujours su me conseiller et m'aider à donner le meilleur de moi-même. Il y a quand même peu de fou pour faire 500km avec un bäckehoffe pour 50 personnes dans le coffre de leur voiture, juste pour le plaisir !

TABLE OF CONTENTS

INTRODUCTION

Composite materials combine high stiffness with low weight, making them ideal for aeronautic or space industries. The proportion of these materials within current structure is constantly increasing. For example, in 2005, 23% of the A380 structure was made using composite materials. Eight years later, the structure of the A350 XWB was mostly composed of composite materials (∼53%). The same observation can be done for the Ariane project, where Ariane 6 will have much more composite parts than its predecessor Ariane 5.

However, the current assembly processes reduce the effectiveness of such materials. Indeed, the historical use of rivets or bolts to assemble different parts creates high local constraints and favours corrosion, especially for Carbon Fibre Reinforced Polymers (CFRPs). To avoid such critical problems, composite parts are oversized, thus reducing the weight advantage provided by the material.

Using glue to bond composite parts together would be an alternative solution. Such glues already exist however, one major problem prevent their use: there is no Non-Destructive Technique (NDT) currently capable of assessing the mechanical strength of a bonded structure. This lack of NDT makes it impossible to detect weak bonds.

The LAser Shock Adhesion Test (LASAT) has already shown a high potential as a means to detect weak bonds within bonded CFRP structures. This manuscript is based on an optimisation of this technique, the Symmetrical LASAT (S-LASAT). Results presented in this work were obtained within the framework of the European project ComBoNDT.

Chapter 1 presents the main challenges behind the bonding of CFRP structures as well as the industrial context. A description of the ComBoNDT project is given as well as a brief overview of the technologies that are part of it. The last part of this chapter is dedicated to the state of the art of the LASAT technique, before concluding on the main objectives of this work.

All experimental tools are described in **Chapter 2**. Starting with the specification of Hephaïstos platform used to produce all the experimental results performed during this study, as well as the optimisation that have been implemented. Sets of samples were given to assess the capabilities of the technique to detect weak bonds. The manufacturing of these samples as well as their characterisation is also detailed in this section.

Chapter 3 is a numerical study used to explain results initially obtained on Hephaïstos platform. A description of the initial experimental setup is given followed by the main results it

generated. They will be used as references for the numerical investigation. This chapter presents the current state of numerical simulations for LASAT related processes, as well as the new lead that was explored. It also describes the impact of poor spatial distribution of the laser beam and concludes on the need for Diffractive Optic Elements.

Chapter 4 gathers the main experimental results obtained with the platform after its optimisation. The new experimental protocol is presented as well as S-LASAT results on both the coupon and pilot samples. Assisted by the LTSM lab from Patras University, a study of the influence of S-LASAT over healthy bonds is realised, followed by a comparison with results obtained using the non-optimised LASAT. Tests realised on real aircraft parts are also presented, before concluding on the TRL level of S-LASAT at the end of the European project as well as its results compared with the other techniques.

The global **Conclusion** as well as the **Perspectives** are presented at the end of the manuscript.

Chapter 1. CONTEXT AND LITERATURE REVIEW

TABLE OF CONTENTS

1.1 Context

The reduction of carbon dioxide emissions is one of today's greatest challenge regardless of the sector. This is especially true in the field of transportations where regulations are becoming more demanding every year [1], [2]. Whether it is in the automotive or the aircraft industry, major improvements have been made over the last years to decrease CO2 emissions [3], [4]. However, the objectives set by the European commission, or international regulation have not been met yet [5].

The International Air Transportation Association (IATA) underlined that most of the upcoming improvement will be the results of "incremental technology changes" [6]. For instance, the LEAP engine, equipped on the A320 neo and the C919, reduced the fuel consumption by 15% using overall lighter structures and a better efficiency. New technologies are also under development such as open rotors or counter rotating fans [7], [8].

Great improvements have also been done regarding the aircraft structure. Parts have better aerodynamism [9] and new concepts such as the blended wing body are under investigation to further reduce the drag and improve the flow control [10]. The weight is also among the main factor that could reduce the CO2 emissions. The A320 neo is a great display of these changes: with a reduced weight, improved aerodynamism and the LEAP engine, its fuel consumption dropped by 20%.

The main ways to lighten current structures is either by optimising them or changing their material. A considerable focus has been done on the latter solution over the last decades. For example, for the A350 XWB or the 787 Dreamliner, more than 50% of the aircraft's part are made of composite, a material with high strength-to-weight ratio. Because it can be moulded into complicated shapes, composites also allow a higher design flexibility than standard material, diminishing at the same time the number of parts required in a structure.

Moreover, the weight reduction for aircrafts (planes, rockets, ….) not only reduces the CO2 emission, it also has a great economic impact. The price of 1kg of matter on an airplane ranges from 500€ to 2000€ [11]. Costs are even higher for space rockets where it can reach 20000€/kg [11].

However, if materials have evolved, the assembly process did not evolve alongside with them. Composite materials are currently assembled using rivets or bolts, which implies drilling holes in the panel. This creates high local constrains and favours corrosion [12]. To overcome these problems, parts are usually oversized, neutralizing the impact of composite on the structure's weight.

These materials require new assembly techniques and bonding them has been seen as the best solution for decades (see next section), but several problems still remain, one of the most critical being weak bonding which prevents from structural bonding certification.

1.2 A Brief Introduction to Adhesion

1.2.1 Bonding in the Aeronautic Industry

The use of glue goes back to the very beginning of aircraft development. In 1903, for their first flying iteration, the Wright brothers glued their spruce propellers together [13]. Later, in 1920, aircraft were mainly built using plywood. The successive wood layers were held together using casein glue, an animal sourced glue [14]. The use of casein glue was specially intensive during WWI, when the engine's power saw little to no improvement, and one of the only remaining leverage remaining to improve aircraft's speed and performances was the weight [15].

 After WWII, wood-based structures slowly started to be replaced by metallic structures. New bonding agent such as the Redux [16] were used to create metal-to-wood and metal-to-metal bonds. In 1958, Fokker released the F-27 friendship. This plane was partially assembled using bonding processes (see Figure 1-1). The use of bonding was then extended to aerospace applications [17].

Currently the aeronautic field is undergoing another big material shift, as it did at the end of WWII. Metallic parts are slowly replaced by composite structures. These new materials do not perform well when drilled. Thereby, there development heavily relies on bonding processes and as specified earlier, on their post bonding certification. Moreover, it seems that engines' efficiency cannot be much more improved. Again, weight saving is considered as one of the most effective way to achieve aeronautic current goals… Who said History is not a cyclic process?

1.2.2 Adhesion mechanisms

Adhesion is a complicated process and scientist even disagree on its definition [18], [19]. There are also different approaches to the problem. Some of them are more chemistry oriented [20], while other have a more mechanical approach. A bond is not only defined by the bonding material, but also by the *adherends* (or *substrate*), i.e. the materials that are bonded together. Parameters such as their bulk properties or their surface state play an important role in the final bonding quality [21]. Combined with the wide variety of bonding process currently available, it is very difficult to give a clear definition regrouping all the different bonding mechanisms.
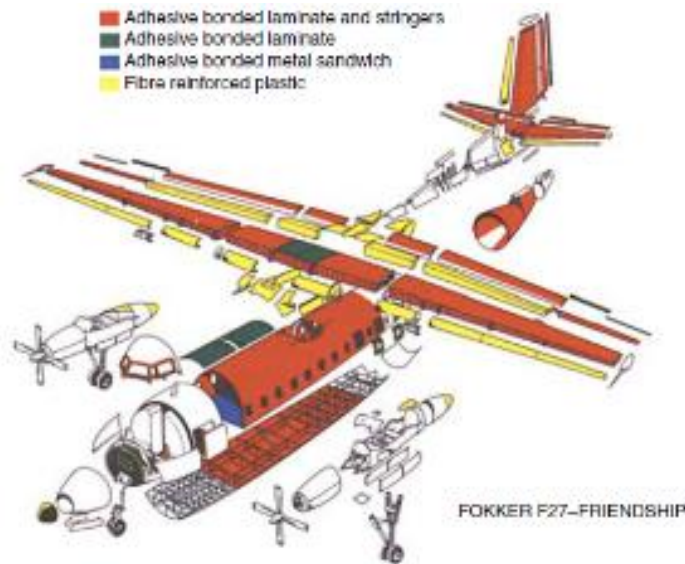
Figure 1-1 Schema of the Fokker F-27 and display of its bonded parts [15]

Scientists however are trying to regroup them by family, but improvements in the comprehension of the phenomenon [22] tend to extend the list [18], [23]. It is also important to note that these families are not to be taken separately. Usually, a bond relies not only on one, but on several bonding mechanism. Among the main theories one can find:

- Mechanical interlocking: this assembly technique may be among the oldest and more natural way to assemble parts together [24]. There are two main groups of mechanical interlocking: friction base interlocking and dovetailing (Figure 1-2) [23]. If they both heavily rely on material properties such as: crystal structure, hardness, surface energy, … [25], the first one is directly linked to the material friction properties.

Figure 1-2 Mechanical interlocking: a) friction-based b) dovetailing

- Diffusion theory: this mechanism is based on the solubility of the bonded materials. Using this process, if part A is bonded to part B, an interface between A and B will be created, and will be made of the material coming from both parts. It allows for a smooth transition between parts, without the addition of another material. Having two materials that are soluble in one another is however pretty rare, and usually, it is only very partially that this mechanism occurs.
- Adsorption theory: considered as one of the most applicable theory [18], this adhesion occurs when the two bonded materials are brought so close from one another

that an interaction between the molecules or even between atoms is created. This type of close relation between the adhesive and the adherend is often found in the biological field [26].

These are among the most common adhesion theories, but many more exist: electrostatic bonding, covalent bonding, ..., etc [23].

There is however one important theory formulated in 1967 by Bikerman [27]and that takes into account "Weak Boundary Layers" or WBLs. A WBL finds its origin in mechanical or chemical contaminations (Figure 1-3).
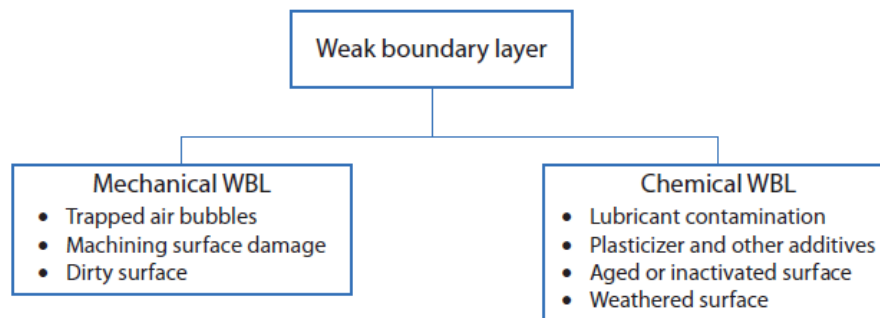
Figure 1-3 Examples of Weak Boundary Layer origin [23]

When other theories are created to quantify an adherence, the WBL theory rather explains a loss of mechanical properties [28]. The WBLs theory states that a layer, that could be infinitely thin, made of contaminant can lower the expected mechanical properties of the bond. This is in most cases due to poor surface preparation: dirty surface, machining surface damage, lubricant contamination, ... etc.

1.2.3 Advantages of adhesive bonding

Bonding parts together is not a new process [29].In the case of composite structure, this assembly technique offers unique structural advantages such as a better stress distribution [30], [31]. Since no holes are required, this technique avoid local constraints, improving not only the structural health, but its fatigue resistance at the same time. Bonded joints also have good damping properties, making them less sensitive to vibrations. All combined, these advantages help optimising structures: there is no more need for extra material or specific designs to compensate process induced stresses.

The bond assembly process also allows for an overall better durability of the structure [32]. Indeed, these bonds are usually great sealant, making the structure leak free, and tend to better behave when damaged, limiting the parts contamination during their lifespan. Combined with their good mechanical properties, bonded composites tend to have a much longer life cycle compared to more standard assembly processes.

Moreover, all extra materials such as bolts or rivets are no more required which further participates to the global weight reduction of structures. It is said that after structures optimisation, one can save up to 15% of the total mass of plane by using bonds instead of the standard mechanical techniques.

This process is also much easier to automate and can handle much larger surfaces. It not only reduces process variability and thereby its reliability, but also increases the production rate. This makes for faster and most cost-effective production lines.

More and more structures are built using composite. Thereby, the maintenance, repair and overhaul (MRO) market for composite is growing at a very fast rate [21], [33]–[35], and manufacturers or third party contractor are heavily investing to develop repair techniques that could better handle composites. Currently, when a structure is locally damaged, major replacements are not possible. Patching the damages would be the most appropriate solution since it is both time and cost-efficient.

1.2.4 Limitation of adhesive bonding

Currently, adhesive bonding cannot be 100% tested using Non-Destructive Techniques (NDTs). Because of it, just as for the welding process, bonding procedures are defined as "special" by the ISO 9001. There are today a lot of different ways to assess the integrity of a composite structure, but none of them can certify the mechanical properties of the bond.

There was initially no need for mechanical test on interfaces, since the assembly processes such as riveting or bolting do not require it. Indeed, each component would be separately certified, and if no apparent default was spotted on the rivetted structure, the assembly would be considered as sound.

This supposition cannot be done when dealing with bonded structures. It has been noticed that the bond strength may vary depending on surface cleanliness. If contaminations such as humidity due to a high ambient humidity level, remains of release agent from the composite moulding process, or even finger print left after manipulating the plate, are present on the bonded surface, the overall strength of the bond can drop drastically. The influence of surface contamination on a bond's mechanical strength was already addressed in 1.2.2, when introducing the WBL theory. These faulty bonds are often referred to as "weak bonds", a.k.a. bonds which adhesive strength is weaker than its supposed nominal strength.

Current NDTs are efficient at detecting default that include openings. The most common defects being voids, cracks, disbondings or porosity [36]. Many studies have shown and compared the effectiveness of NDT to reveal these defaults [37]–[39]. Ehrhart has compared them using 10 different criteria [39] (cf Figure 1-4). The table shows that even if basic tests

such as direct visual inspection (VT) seem to lack precision and repeatability, available technologies like Ultrasonic Tests (UT) are very efficient at spotting them. However, this table also underlines the fact that none of these techniques can be used to certify the adhesive strength of a bond.

	NDT Method legend: - not satisfying, + acceptable, ++ good, +++ optimal, + 3D information				
	VT	UT	IRT	RT	CT
Detection Capability Indicative Range (size)	- Eye resolution at surface only	+++ mm	+++ mm	+ mm	+++ + µm
Cost-efficiency	+++	+	+++	-	-
Time-efficiency	+++	++	+++	++	-
Mobility/Measurement size	+++	++	+++	++	-
Reproducibility	-	+++	+++	+++	+++
Ease of use / Training required	++	++	-	-	-
Maximal resolution	+	+	++	++	+++
Adhesive Strength	-	-	-	-	-

Figure 1-4 Comparison between 5 common NDT techniques: Visual Testing (VT), Ultrasound Testing (UT), InfraRed Thermography (IRT), Resonance Testing(RT) and Computed Tomography (CT) [39]

Indeed, to spot an adherence loss, an interface as to be mechanically stimulated. There are currently ways of assessing a bond strength such as the Double Cantilever Beam (DCB) test that can give the mode I mechanical resistance of a given assembly. However, all available mechanical tests are destructive and thereby cannot be used on production or repair line to assess the quality of produced and ready to use parts.

In 2016 a new standard for bonding quality assurance was created: the DIN 2304 [40]. If this regulation now gives proper quality management system (QMS), bonds still cannot be certified defect-less with a 100% certainty, and qualified operators are required.

1.3 European Projects for Weak Bonds Detection

From 2010 to 2014, the European project ENCOMB (Extend Non-destructive testing for COMposite Bonds) performed researches to find a new way of detecting weak bond within carbon epoxy laminate used in structures like the A350. The project screened 31 different Extended NDTs (ENDTs), regardless of their Technology Readiness Level (TRL), and tested

their effectiveness for pre and post-bonding contamination detection. During the project, 5 different contamination scenarios were tested: release agent (RA), moisture (MO), hydraulic fluid/water (HF), thermal degradation (TD), and poor curing (PC). For each contaminant, 3 to 4 different levels of contamination were produced, and each time a mode-I fracture test was realised to assess the adherent loss associated with [41].

	METHOD	PARTNER	Step 1 Scenarios				Step 2 Potential for detection of				VALIDATION
			RA	MO	HF	TD	RA	MO	HF	TD	
Adherend surface quality	X-ray fluorescence spectroscopy	IFAM	-	-	✓	-	used as reference methods				
	Infrared spectroscopy	IFAM	-	✓	✓	✓					
	Reflectometry / Ellipsometry	IFAM	-	-	-	-					
	Laser scanning vibrometry*	IMP PAN	✓	✓	✓	✓	○	•	○	○	Fail
	Optically stimulated electron emission	IFAM	✓	-	✓	✓	••	•	••	•	Pass
	Infrared spectroscopy	RECENDT	✓	✓	✓	✓	•	••	••	••	Pass
	Aerosol wetting test	IFAM	✓	-	✓	✓	••	○	•	•	Fail
	Portable Handheld FTIR spectroscopy	AGILENT	✓	✓	✓	✓	••	••	••	••	Pass
	Laser induced breakdown spectroscopy	IFAM	✓	-	✓	-	••	○	••	○	Pass
	THz/GHz reflectometry	IRE NASU	✓	✓	✓	-	•	•	•	○	Pass
	Optical fibre sensors*	EPFL	-	✓	✓	-	N/T	••	••	N/T	N/T
	Electrochemical impedance spectroscopy*	IFAM	-	✓	✓	-	N/T	•	N/T	N/T	N/T
	Electronic nose technology	ENEA	-	-	✓	-	•	•	••	N/T	Fail
	Dual-band active thermography	IZFP	-	-	-	-	○	•	•	•	Fail
	Laser induced fluorescence	IMP PAN	-	-	-	✓	○	○	••	••	Fail
	THz technology	RECENDT	-	-	-	-					
	Optical coherence tomography	RECENDT	-	-	-	-					

	TECHNIQUE	PARTNER	Step 1 Scenarios			Step 2 Potential to detect weak bonds caused by			VALIDATION
			RA	MO	PC	RA	MO	PC	
Adhesive bond quality	Active thermography using ultrasonic excitation	EADS -D	-	-	-				
	Terahertz technology	IRE NASU	-	-	-	○	○	○	N/T
	Linear Ultrasound	UnivBris	✓	-	-	••	N/T	○	Uncertain
	Nonlinear ultrasound	UnivBris	✓	-	-	•	N/T	○	Pass
	LASAT technique	CNRS	✓	-	-	••	•	•	Pass
	Laser ultrasound	RECENDT	-	-	-	○	○	○	Fail
	Active thermography using optical excitation	IZFP	✓	✓	-	•	•	N/T	Uncertain
	Laser scanning vibrometry*	IMP PAN	-	✓	-	○	•	••	Fail
	Electromechanical impedance*	IMP PAN	✓	✓	✓	••	•	••	Fail
	Ultrasonic frequency analysis	EADS-D	-	✓	-	•	••	○	Pass
	Laser ultrasound	EADS IW F	-	-	-	○	•	•	Fail
	Active thermography (for T_g analysis)	IFAM	-	-	-				

Figure 1-5 Overview of ENCOMB results; ✓: Clear detection of contaminant, differentiable from reference surface state, -: No differentiation from reference state, ••: High, •: Low, ○: No, N/T: Not Tested,*: With structure integrated sensor [41].

To detect weak bonds, two different solutions were proposed: scan each surface prior to the bonding and assure no contamination is present or test the fully bonded part and assess the bond mechanical properties. 19 out of the 31 technologies were presented as ENDTs for pre-bond surface quality assurance. The remaining 12 were tested for the weak-bond detection, after composite laminates were assembled.

A total of 8 promising technologies were highlighted after ENCOMB project: 5 for the adherence surface quality and 3 for the adhesive bond quality (Figure 1-5).

Based on these results, a second European project, ComBoNDT, was launched in 2015 as part of the H2020 framework. Its goal was not to screen anymore technology, but to rise the TRL of the ones selected during Encomb. Moreover, the weak bond threshold has been increased. For the Encomb project, weak bonds were described as bond with an adherence level equivalent to 20% or less of a reference bond. For ComBoNDT, bonds with an adherence level of 80% of a reference one are now considered as weak bonds, further increasing the detection pre-requisites of the technologies.
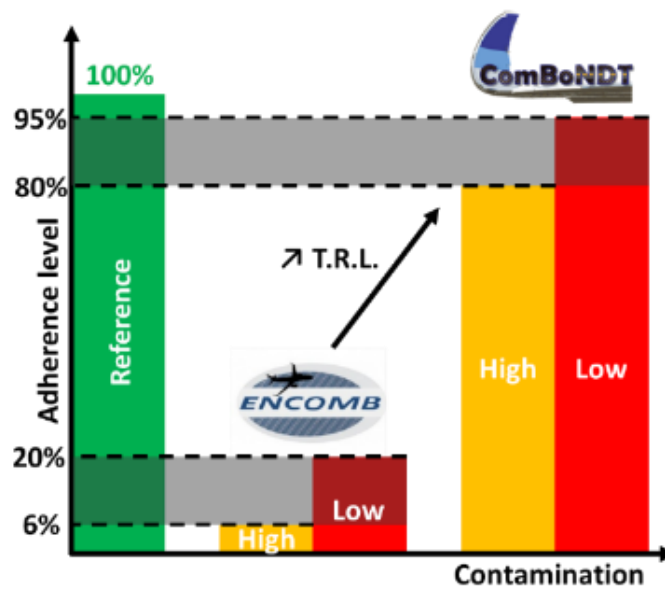
Figure 1-6 Comparison between the adherence level of Encomb project and ComBoNDT goals

Figure 1-6 shows the difference of adherence properties between the two projects. ComBoNDT adherence's values are the one defined at the beginning of the project, not to be mistaken with the real adherence value later given in this manuscript.

Figure 1-7 Graph describing ComBoNDT partners and the technologies they are developing

Figure 1-7 describes the technologies and partners involved in the project. They are divided in two technological solutions: surface characterisation (blue) and the post-bonding inspection (orange).

1.3.1 Pre-Bonding Surface Quality Testing

Because no reliable NDT is currently available to test bonded structure strength, assessing the surface quality before bonding to avoid weak bond can help better control the bonded parts quality throughout the whole process, whether it is in production or repair lines. The developed technologies must be robust and efficient at spotting contaminated surfaces. Eight different technologies have been selected and will be described in this section.

The Optically Stimulated Electron Emission (OSEE) [42]–[46]: this technique consists in recording charged particle emitted by a surface after it has absorbed radiant energy. A UV light is used to illuminated a given surface. While illuminated, a certain amount of electron will "escape" from the surface, and this electron flux will be estimated by a collector (Figure 1-8). This collector provides a photocurrent value that varies depending on the surface. If a contaminant is present on the scanned surface, a variation of the photocurrent will be measured by the collector.

This technique has the advantage of being contactless, fast and robust. It however requires keeping a constant sensor-to-surface distance to assure the good quality of the signal.
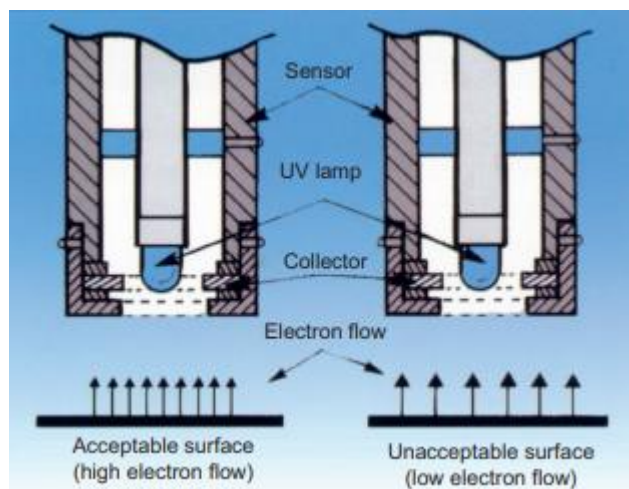
Figure 1-8 Cross section of an OSEE sensor [45]

The Laser Induced Breakdown Spectroscopy (LIBS) [46]–[50]: LIBS is used in a wide variety of domain, and is used to determine the elemental composition of solids, liquids or gases. A plasma is generated by a high-power laser, ablating a very thin amount of the sample (a couple of micrometres). The emitted light is then collected and analysed by spectroscopy (Figure 1-9). This technique allows for a very fast scan of the sample and is available in

portable format. Because of the power of the laser (class 4 laser [51]), a special environment is required to protect the user from laser emissions.
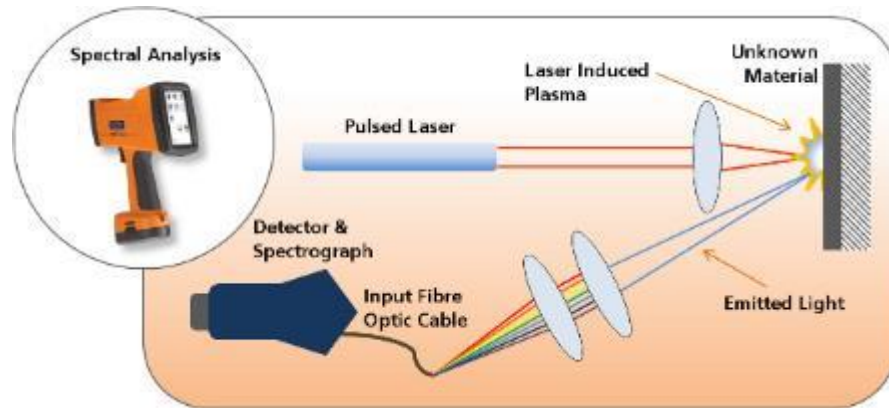
Figure 1-9 Representation of a surface study using LIBS [50]

Electronic nose (E-Nose) [52]–[57]: As for the LIBS, electronic noses also has a wide range of applications. From the agricultural field to aerospace mission, the capabilities of these setup to analyse environmental substances are well-known. The setups developed within ComBoNDT rely on an array of sensors located in a sealed environment (Figure 1-10). Each sensor is sensible to a given compound. The surface substances are caught by the sensors and the output data is analysed by a program. To avoid any contamination from outside "smells", a vacuum system as well as filters are used to isolate the tested area. To optimise the scanning time, an infrared (IR) lighting is used to slightly heat the surface and allow for more particles to go through the sensor. The system can easily be transported and can generate high accuracy results. However, results highly depend on the air quality around the tested area: the cleaner the air, the better the results.
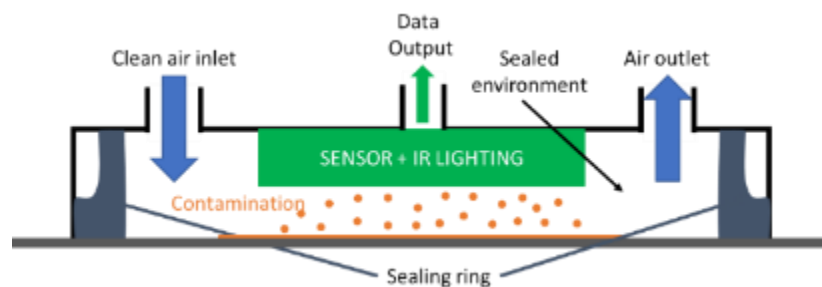
Figure 1-10 Example of an E-NOSE probe head

Fourier-transform Infrared Spectroscopy (FTIR) [58]: When scanning a sample using FTIR spectroscopy, a large range of IR radiation are emitted toward the tested area. Each compound absorbs a specific wavelength, depending on its composition. The reflected spectrum is then numerically analysed by a software, and the missing radiations are inferred. This information eventually helps finding the composition of the surface. This technique can give

fast results but may lack of precision compared with the dispersive spectroscopy that only study the interaction of a single wavelength.

Aerosol Wetting Test (AWT) [59]–[63]: The AWT relies on the surface energy and its impact on water droplets. An ultrasonic atomiser produces calibrated droplets and a high-resolution camera captures the water pattern (Figure 1-11). The surface's physical or chemical state directly influences its energy and by extension the shape of the droplets. The technique allows for a high degree of automation for both the droplets dispersion or the pattern analysis by software and can handle large parts. However, the scan of intricate parts may prove really challenging.
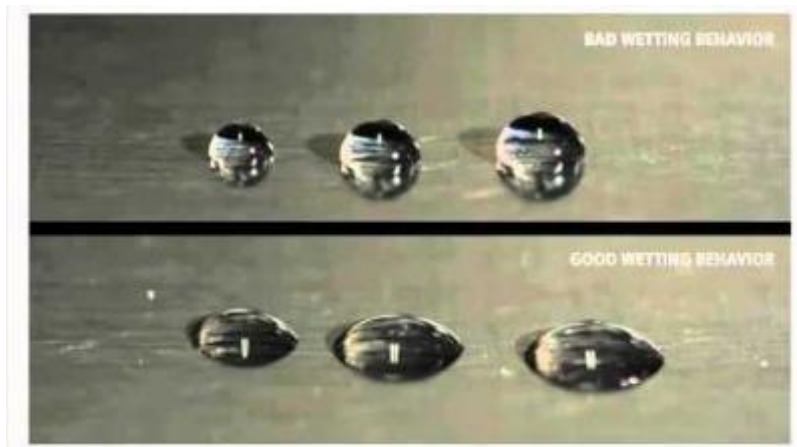
Figure 1-11 Different droplet shapes depending on the surface energy [60]

Full Field Vibrometry (FFV) [64]–[66]: also known as Laser Doppler Velocimetry (LDV), it relies on the vibration measurement of a surface using a laser. This technique is often used for the characterisation physical defaults such as delamination of bonding defect within composite structure. To assess the quality of a surface using this technique, one relies on the fact that the vibration signature of each material is different. Hence, if a contamination is present on the surface, some properties may locally be modified, modifying the vibratory pattern of the plate. Piezoelectric transducers were used to generate the vibration along the tested samples. This technique has shown good results in the detection of default within structure, but its setup can be really complicated, and is not currently easily transportable.

Laser Induced Fluorescence (LIF) [67]: using a Nd:YAG laser, energy is brought to the surface of the tested sample. This energy stimulates the molecules which, after a characteristic time of a few nanoseconds, release this energy in the form of wavelength. A study of these radiations can give indications of the type of molecules present on the sample surface.

1.3.2 Post-Bond Quality Assessment

Directly assessing the bond quality, without going through a step by step procedure validation can help saving both time and money. The technique must be efficient at detecting any type of alteration generating a loss of 20% of adherence (compared to theoretical adhesion level of the bond). It also needs to be robust, and as little invasive as possible to easy up the process. In this section, 4 different techniques are presented. The LAser Shock Adhesion Test will be presented in the next section.

Computed Tomography (CT-scan) [68]–[70]: an X-ray source emits a beam onto the sample, placed on a rotating table. X-rays are then captured by a camera, and the signal is reconstructed into 2D images (Figure 1-12). The amount of signal is directly linked to both, the material thickness – the thicker the material, the less radiation goes through – and the material X-ray attenuation coefficient. Moreover, as depicted in Figure 1-12, X-rays are emitted in a cone beam. To optimize the amount of radiations seen by the sample the sample has to be as close from the source as possible. Hence, a compromise has to be done between the size of the sample and the resolution of the scan. After the image is taken, the sample is rotated, and the process restarts until the whole sample has been scanned. Eventually a 3D reconstruction is generated based on the 2D images.
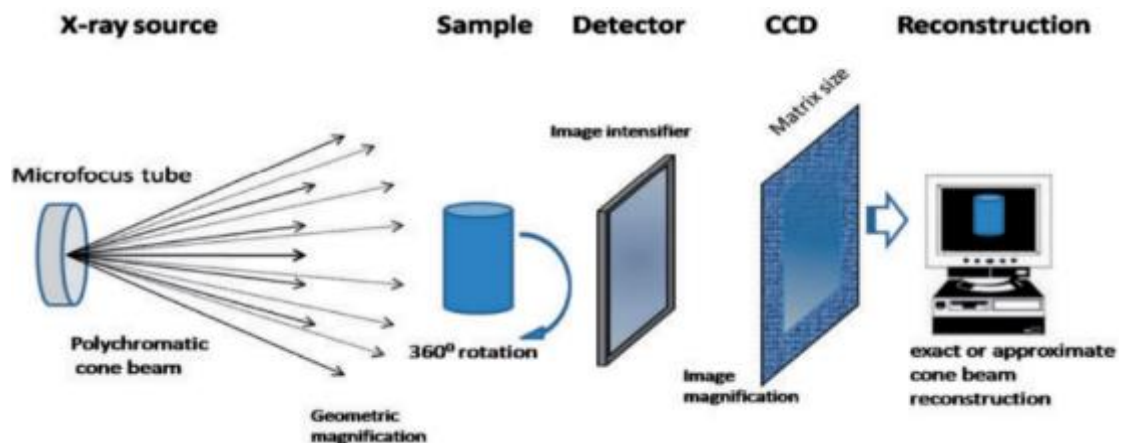
Figure 1-12 Scheme of the µ-tomography principle [70]

Non-Linear Ultrasonic Scanning (NLUS) [71]–[74]: The binding force between two surfaces grows as the distance between these surfaces increases. The increase is first linear, then becomes non-linear if the distance is sufficient. In the case of weak bonds, the non-linear effect arises sooner than with a sound bond. NLUS relies on the generation of high intensity ultrasonic waves to generate a local mechanical deformation on the bond. A probe registers the output response of the structure, and based on the non-linear behaviour of the interface, it is possible to assess the integrity of the joint. This technique has already shown good results, but contrary to the other techniques, this is not contact free.

Magnetostrictive Strain Sensing (MGSS) [75]–[78]: the Villari effect, or inverse magnetostrictive effect, characterises the changes in the magnetic permeability of a material due to a mechanical loading. This property is often used in Structural Health Monitoring (SHM) to detect the presence of default. For bond assessment, the technique relies on a magnetostrictive ribbon placed on the tested structure. A magnetic field is generated using a transducer generating a magnetic circuit between the ribbon and the transducer. This field is measured using a Hall sensor. Upon applying a load, the magnetic properties of the ribbon will be modified (Villari effect), altering the magnetic field (Figure 1-13). This technique supposes a contaminated bond will change the response of structure under a four-point bending load. If this is the case, the comparison between the signal of a bended sound plate and the one of a contaminated one should be different. This technique is considered contact-less but requires however to bond the magnetostrictive ribbon on the sample.
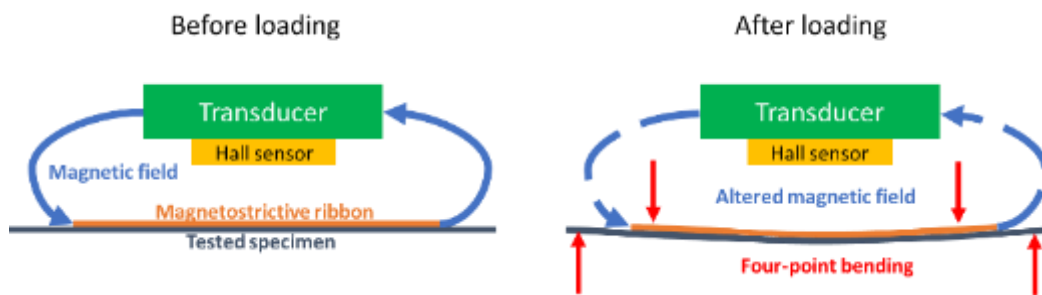
Figure 1-13 Shema of the MSS procedure to test bonded interfaces

Electromechanical Impedance (EMI) [79]–[82]: for this technique, in order to mechanically stimulate the bond, piezoelectric transducers are used. They can both act as actuators or sensors. The actuators generate a deformation of the sample, the signal is then recorded by the sensors before the data is analysed in the frequency domain. The mechanical properties of the tested sample directly influence the wave propagation, thereby the signal recorded by the sensors. If the bond behaves differently, for example because of a loss of adherence, the record signal should be different from the one generated by a sound structure. This technique is often used in SHM to localise and characterise defects within the structure. It however requires bonding transducers on the surface.

1.4 The LAser Shock Adhesion Test (LASAT)

The last method, and main topic of this manuscript, is the LAser Shock Adhesion Test (LASAT). The technique relies on laser generated shockwaves to generate high tensile stresses at the interface. If the interface can withstand the load, the part is validated. Else the bond is damaged, meaning it was not strong enough, thereby part did not meet the specification and must be rebuilt. This section will further go in the detail of the LASAT principle and sum up the major advances that were implemented during the last decades.

1.4.1 Shockwave creation and generated pressure

A shockwave is generated by transferring part of the laser's energy to the tested sample. This transfer occurs when the sample is locally ablated by a high-power density laser (GW/cm²) in a hot pressure plasma (GPa). In reaction a shockwave is transferred into the material (Figure 1-14 a)).
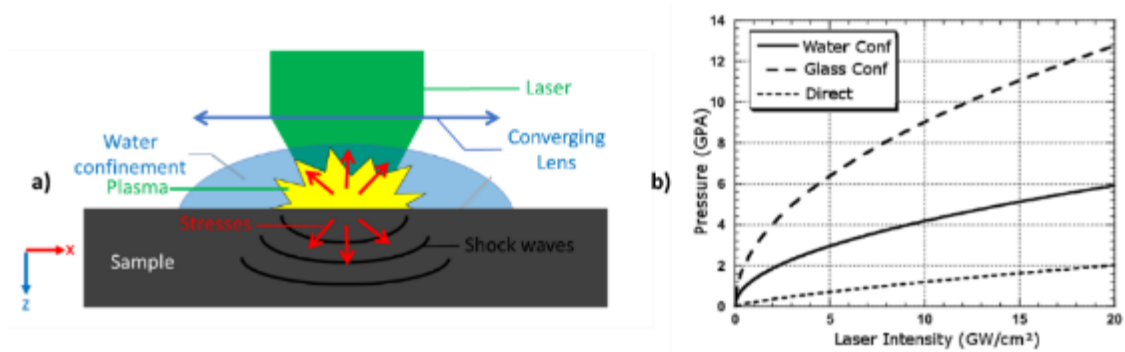
Figure 1-14 a) Schema of a laser generated shockwaves b) generated pressure as a function of the laser intensity for a direct ablation, water confined abalation and glass confined ablation

In 1990, Fabbro [83] correlated the pressure generated by a laser impulsion and later, in 1997, Berthe [84] validated it experimentally. Berthe also showed that the amount of energy used to generate shockwaves could be improve up to a factor 4 [85], by constraining the plasma using a medium transparent to the laser's wavelength, typically water. The maximum pressure at the surface of the material could be obtained using the following equation:

$$P(GPa) = 0.01\sqrt{\frac{\alpha}{2\alpha + 3}}\sqrt{I}\sqrt{Z_{rel}} \qquad (1.1)$$

where:

- P = pressure (GPa)
- α = part of the energy being used for the gas ionization
- I = laser intensity $(GW \cdot cm^{-2})$
- Z_{rel} = the relative impedance $(kg \cdot m^{-2} \cdot s^{-1})$

The laser intensity can be calculated using the laser's properties:

$$I = \frac{E}{\tau \cdot S} \qquad (1.2)$$

With E the energy (J), τ the laser's pulse length (ns) and S the laser spot size (cm²). The relative impedance is a ratio between the material acoustic impedance of the sample (z_{sample}) and the confinement acoustic impedance (Z_{conf}):

$$Z_{rel} = 2 \cdot \frac{Z_{conf} \cdot Z_{sample}}{Z_{conf} + Z_{sample}} \tag{1.3}$$

The formulation suggested by Fabbro (1.1) highlights the intricate relation between the generated pressure on one side and both the intensity and the material properties (respectively α and Z) on the other side. Figure 1-14 b) compares the pressure generated during a direct ablation (calculated using the Phipps law [86]), with no constraining medium, and the ones generated when using a water or glass confinement – calculated using (1.1), with $\alpha = 0.2$, $Z_{water} = 1.65 \cdot 10^6 \ Pa \cdot s^{-1}$ and $Z_{glass} = 13 \cdot 10^6 \ Pa \cdot s^{-1}$). Using a confinement clearly increases the generated pressure for a given laser intensity.

1.4.2 Shockwave propagation

The shock wave propagation within a medium mainly relies on the acoustic impedance (Z, expressed in $Pa \cdot s \cdot m^{-1}$) of the material:

$$Z = \rho_0 \cdot D \tag{1.4}$$

With ρ_0 the material density and $D \ (m \cdot s^{-1})$ the shockwave velocity within the material:

$$D = C_0 + S \cdot u \tag{1.5}$$

u being the material velocity, C_0 the sound velocity within the material and S a dimensionless material constant.
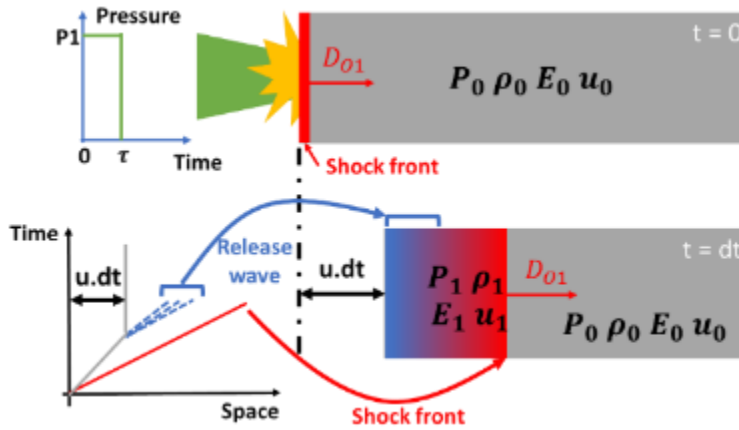
Figure 1-15 Representation of a shock wave propagating inside a solid after a laser shock

When placed, the sample is at a rested state (P_0, ρ_0, E_0, u_0). Generating a shock on surface of the sample will create a local discontinuity that will modify the state of the material (P_1, ρ_1, E_1, u_1) (Figure 1-15). The delimitation between state 0 (rested) and state 1 (shocked) is called the shock front and propagates at the velocity D_{01} (cf. equation (1.5)). It is followed by a fan of release waves which progressively unload the material until the pressure is back to P_0. To describe the material state, one can use Cauchy stress tensor:

$$\bar{\bar{T}} = \frac{s}{3}.\bar{I} + \bar{\bar{T_d}} \tag{1.6}$$

where $\bar{\bar{T_d}}$ is the deviatoric part and $\frac{s}{3}.\bar{I}$ the spherical part with $s = \sigma_I + \sigma_{II} + \sigma_{III}$. The deviatoric part is defined by the material's constitutive laws. In "standard" cases, the spherical part of the equation is very small when studying solids. However, the pressure generated by a shock wave is so great, that the spherical part of the tensor must be considered. One can imagine the solid being under such heavy load that it behaves almost like a liquid. The equations of conservation give the following relations:

Conservation of energy
$$E_1 - E_0 = \frac{1}{2}(P_1 + P_0)(V_0 - V_1) \tag{1.7}$$

Conservation of momentum $\qquad \boldsymbol{P_1 - P_0 = \rho_0(D - u_0)(u_1 - u_0)}$ **(1.8)**

Conservation of mass $\qquad \boldsymbol{\rho_0(D - u_0) = \rho_1(D - u_1)}$ **(1.9)**

To link the generated pressure with the local volume variation, Mie-Grüneisen's equation (1.10) [87] of state can be used to link E, P and V:

$$P - P_{ref} = \frac{\gamma}{V}(E - E_{ref}) \tag{1.10}$$

Hence the relation linking P and V:

$$P - P_0 = \frac{C_0^2\left(1 - \frac{V}{V_0}\right)}{V_0\left[1 - S\left(1 - \frac{V}{V_0}\right)\right]^2} \tag{1.11}$$

(1.11) is known as the Hugoniot equation. It is also possible to link the pressure to the material velocity:

$$P - P_0 = \rho_0(C_0 + Su)u \tag{1.12}$$

Equation (1.12) is referred to as the "Hugoniot".

1.4.3 Analytical study of the shockwave propagation

Equations (1.11) and (1.12) are represented in Figure 1-16. Each curve can be separated in two main phases: for low pressure, the material has an elastic behaviour. In this case, the spherical part of equation (1.6) is not very important compared to the deviatoric part, the material response is mainly described by its constitutive law. When going above this limit (also referred to as Hugoniot Elastic Limit – not to be mixed with the standard elastic limit [88]), the material experiences plastic deformation, and due to the high pressures involved, the spherical (1.6) will prevail more and more. In his research work, Balard [89] studied the

pressure's role on the mechanical behaviour of a material. He especially studied pressure ranges and their associated dominant mechanical behaviour.
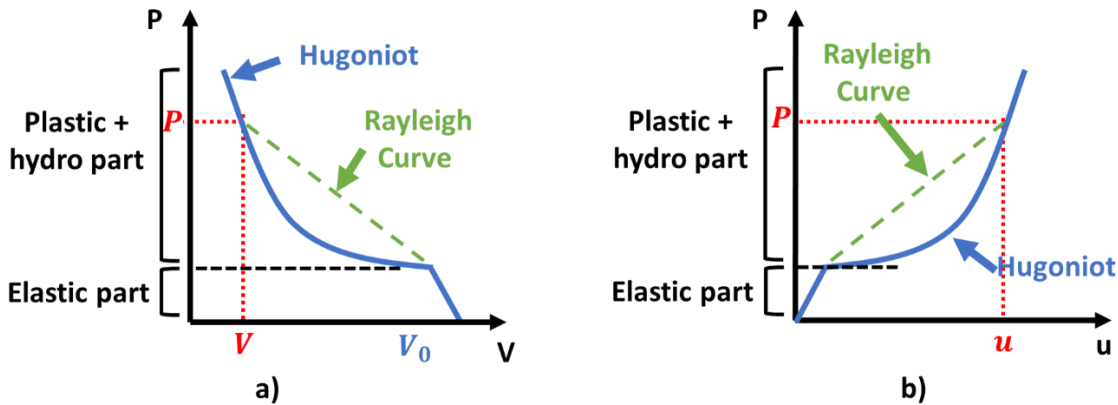
Figure 1-16 Plotting of: a) the Hugoniot curve - P(V) b) the shock polar P(u)

In all the cases covered by this manuscript, pressures will be under 10 GPa. The acoustic approximation can be used to represent the Hugoniot. This hypothesis implies that the shock waves propagate at the speed of sound within the material. So, for here on out, the shock polar can be represented using a straight line. The slope of the curve is equal to Z, the acoustic impedance :

$$u = \frac{P}{Z} \tag{1.13}$$

with:

$$Z = \rho_0 \cdot C_0 \tag{1.14}$$

where ρ_0 the material density, and C_0 the sound velocity in the material. For a shockwave which material velocity is positive (propagating from left to right), the slope of the Hugoniot is positive. For shockwaves propagating in the other direction, the slope is negative.

1.4.4 Shockwave propagation in single block isotropic material

Let us start with the simple example of single block of aluminium, loaded at a pressure P_1 during a time τ (Figure 1-15). The acoustic impedance of air is negligible compared to the one from aluminium, $Z_{alu} \gg Z_{air}$. Figure 1-17 a) is the time/space diagram of the shock propagation within the aluminium sample. Shock fronts are represented with straight red lines. The fans of release waves are here simplified and represented by single waves (stripped blue lines). Figure 1-17 b) represents the pressure state of 4 different areas of the space time diagram.
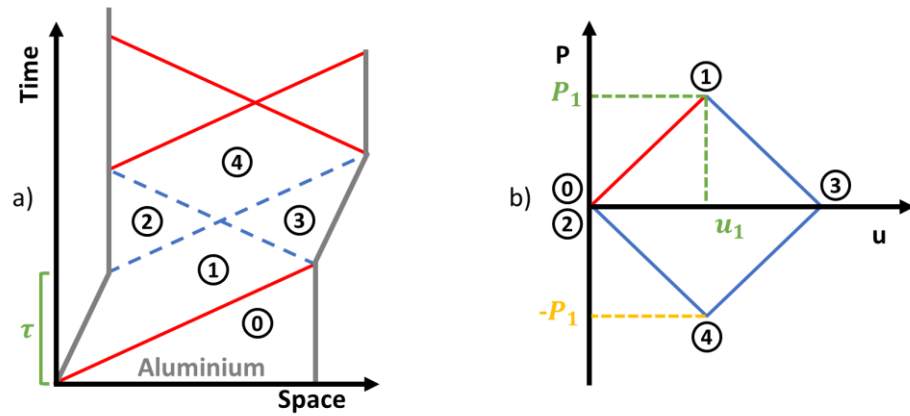
Figure 1-17 a) space-time diagram of a shockwave propagating inside an aluminium block b) its associated Hugoniot diagram

State 0 is the state of the material at rest. P_0 is equal to the environmental pressure, here P_{air}. The laser shock increases the pressure within the material to P_1, and sets the medium in state 1. The material velocity u_1 can be deduced using (1.13). At a time τ, the laser's loading ends, and the release wave unloads the material to its original state, state 2 = state 0.

Upon reaching the back face of the sample, the shockwave turns into a release wave. The material went from state 1 to state 3. To obtain state 3, one must draw a line of slope $-Z_{alu}$ that passes by state 1. For continuity reason, the pressure at the back face must be equal to P_0, so the state 3 is obtained when the curve reaches P_0.

State 4 is obtained by plotting the intersection between the shock polar of the incident release wave passing by 2, and the one coming from the shockwave reflection on the back face of the sample, passing by 3. One obtains a negative pressure, so by extension a tensile stress, of amplitude $-P_1$.

1.4.5 Shock wave behaviour at interface

The difference between the two materials acoustic impedance plays an important role in the shockwave's propagation. A stack of aluminium and copper is considered as example. Their impedance properties are summarised in Table 1-1. For simplicity purpose, no attenuation will be considered in the following cases.

	$\rho \ (kg \cdot m^3)$	$C_0 \ (m \cdot s^{-1})$	Z
Al	2700	5386	1.45+E06
Cu	8930	3933	3.51E+06

Table 1-1 Acoustic properties of aluminium (Al) and copper (Cu)

<u>Case 1</u>: Shock propagation from copper to aluminium

In this configuration, the copper faces the laser shot and transmits the energy to the aluminium plate. In this configuration the shockwave goes from a higher acoustic impedance material, to a lower one ($Z_{copper} > Z_{aluminium}$). Hence, upon arriving at the interface, the shockwave will be reflected into a release wave and transmitted as a shockwave.

Figure 1-18 a) is a space time diagram obtained with pyHugo. It is a python script that was developed based on acoustic approximation [90] (cf. appendix B). In addition to display the shockwaves path within the sample, pyHugo also gives the estimated pressure, using (**1.13**). This result was obtained for a loading of 1 GPa during 10ns. The aluminium plate (on the left) is 500µm thick, and the copper plate (on the right) is 250µm thick.
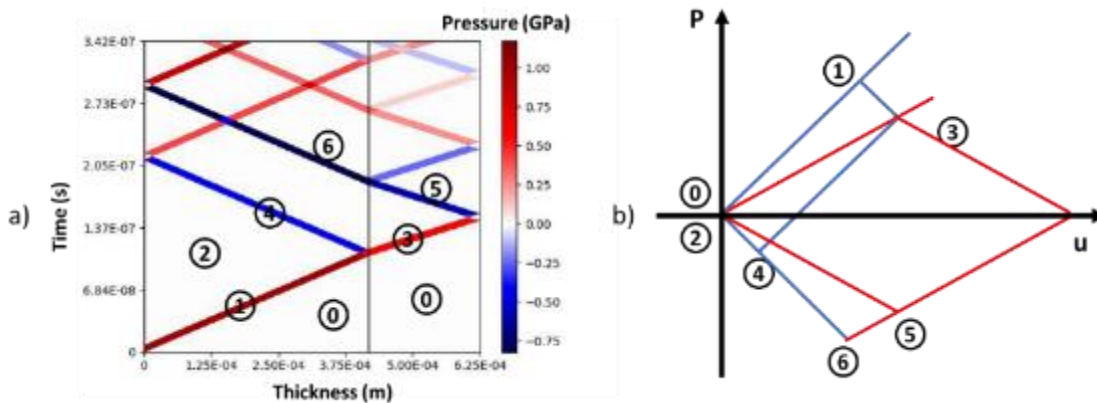
Figure 1-18 a) Space/time diagram of a copper/ aluminium stack b) Shock diagram associated to a)

Figure 1-18 b) is the (P,u) diagram associated to the stack simulated in Figure 1-18 a). Aluminium shock polars are represented in red, and the copper's one in blue. A tensile stress is generated when the shockwave reaches the first interface, but the main one is obtained later, for state 6, and occurs at the interface between the aluminium and the copper. This is without considering the attenuation. This case can be achieved when the back plate is thin making the material damping negligible. The thicker the back plate, the more the material damping plays an important role, lowering the actual generated tensile strength.

Case 2: Shock propagation from aluminium to copper

The same study as for case 1 is done, except this time, the aluminium plate faces the laser shot and transmits the energy to the copper plate. This time the shockwave goes from a lower acoustic impedance material, to a higher one ($Z_{aluminium} < Z_{copper}$).

The space/time diagram as well as the (P,u) diagram are represented in Figure 1-19. Compared to the previous case, one can note that no tensile stress is created when the shockwave reaches the interface for the first time. Moreover, the highest tensile stress is now localised on the back face of the sample (state 5), when the shockwave transmitted by the

aluminium reaches the free surface. The stress intensity is almost more important in this case.
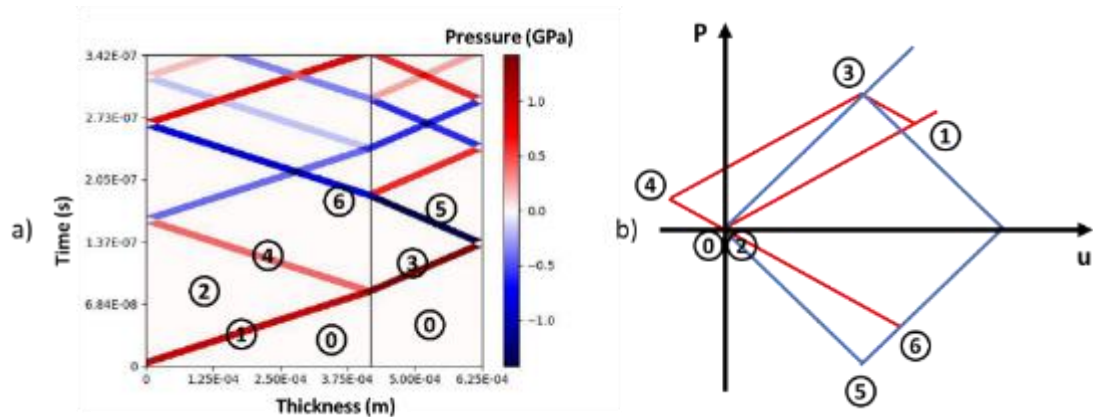
Figure 1-19 a) Space/time diagram of an aluminium / copper stack b) Shock diagram associated to a)

1.4.6 Application to interface testing

As shown in the previous section, it is possible to generate a high tensile stress within the material. If this stress is properly localised on the interface, its strength can be evaluated.

In 1978, Vossen [91] experimented with laser induced shock to test the adherence of thin film layers. Later, in 1993, Gupta and al. used the same principle to measure interfacial strength. This study was published on a three parts article [92]–[94], that not only studied the phenomenon, but also tried to optimise it. More recently, Boustie [95] and Bolis [96], extend laser shock technique to thicker metallic coatings.

Gilath was among the first to test bonds' adhesion using laser shock generated tensile stresses [97]. Later composite material [98], [99] and bonded composite material [100] were also studied using the LAser Shock Adhesion Test.

The company LSP Technologies is developing a similar technique on the other side of the pond. Called "Laser Bond Inspection" or LBI, it also relies on laser shock driven adherence tests [98], [101]–[104]. The process has been patented in the U.S. for both the LBI [101] and structure debonding [102]. Their technique relies on dynamic measurements realised using ElectroMagnetic Acoustic Transducer (EMAC) on the shot surface [104], [105].

The LBI is currently commercialised and uses a portable laser with an adjustable pulse energy (10 to 50J) as well as an adjustable pulse duration (100-300 ns). Moreover, the size of it makes it easily transportable using a trailer [106].

The idea behind the LASAT is straightforward. Let us take a part that has defined specifications concerning the load its bond should be able to withstand. Using laser shots, a stress equal to the one from the specifications is applied on the interface. If the interface properly

does not fail to the applied load, it passes the test. Else, an opening is created on the interface, the part is not validated, and the bond has to be re-done.

However, the latter study, which was part of the Encomb project, also showed the limitations of the process. Indeed, in this "single shot" setup (laser hitting only one of the free surfaces), Ecault demonstrated that this technique was not precise enough to test bonds which adherence level is above 20% of their nominal strength, without damaging the substrates [107]. The major problem was the localisation of the tensile stress. Indeed, the single shot setup generates a tensile stress close from the back-face of the sample. Hence, if the bond is far from the back-face, the stress level perceived by the bond will only be a fraction of the one generated at the intersection of the release waves (Figure 1-20 a)-b), the reflection of the bond's interfaces have been deliberately remove for clarity purpose, and the material properties of A and B are considered alike.).

One possibility to generate the tensile stress around the right location would be to change the pulse duration τ, in order to postpone the intersection of the two release waves (Figure 1-20 c)). However, interaction in water confinement regime with long pulses is not well known.
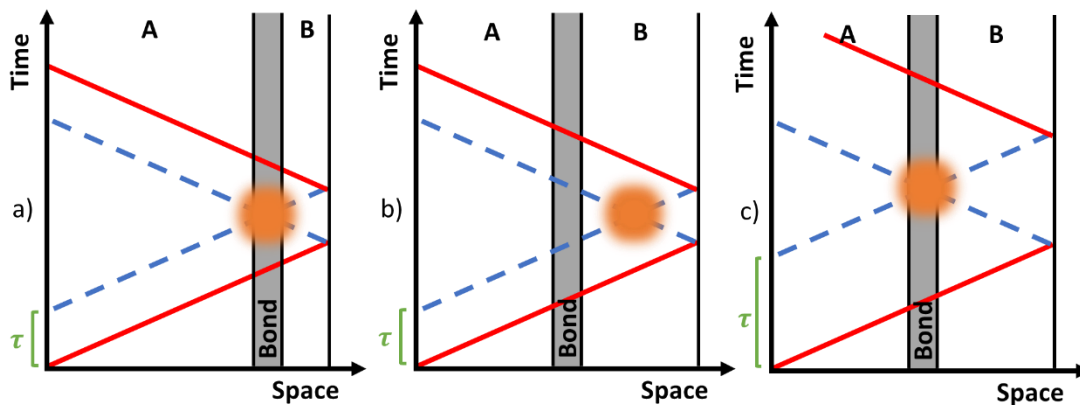
Figure 1-20 Position of the high tensile stress (orange circle) during a single laser shot adhesion test: a) optimum configuration b) non-optimum configuration c) with adapted pulse duration.

To overcome this problem, Ecault proposed two optimisations: the double shock and the symmetrical shot [107].

1.4.7 The optimised LASAT

1.4.7.1 The Double Shock Setup

As shown earlier, when two release waves cross, a high tensile stress is generated. The double shock setup uses a second laser generated shock to intersect the release wave created by the reflection of the initial shock wave on the back-face (Figure 1-21).
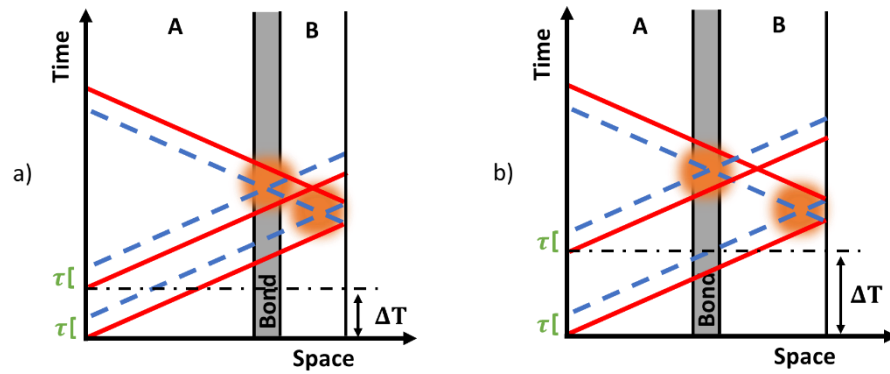
Figure 1-21 Space time diagrams of the double shock optimisation demonstrating its capability to localise the stress around a specific location

This technique offers the advantage of moving the maximum tensile stress area without changing the laser inherent parameters. As shown in Figure 1-21, the stress location relies on the timing of the two release waves intersect. By modifying the delay between each shock, one can generate another high tensile stress area [108]–[110].

There are however two major drawbacks: the level of stress generated, and the energy required for the second shock.

The second generated stress area has the same level of intensity as the first one. This means that if the bond has better mechanical properties than the substrate, it will be impossible to assess its adherence level passes a certain point. Moreover, this is a theoretical view of the problem. Because of material damping, there are also great chances that the second shock creates a lower tensile stress (energy loss when the initial shock wave propagates though the sample).

Concerning the second problem: when the second laser shot reaches the sample, the setup has already been altered by the first shot. Indeed, left-overs plasma from the initial shot are still present on the surface of the sample. The interaction generating the high-pressure shock shifts from a laser/matter interaction, to a laser/plasma interaction. The latter being less effective, one needs higher laser energies to achieve the same pressure as with the first shot [108]–[110].

1.4.7.2 The Symmetrical LASAT (S-LASAT)

This technique was investigated in 2001, on iron samples, by Resseguier [111]. As for the double shock setup, this optimisation relies on the delay between two consecutive laser shots. This time however, the sample is shot from both sides.
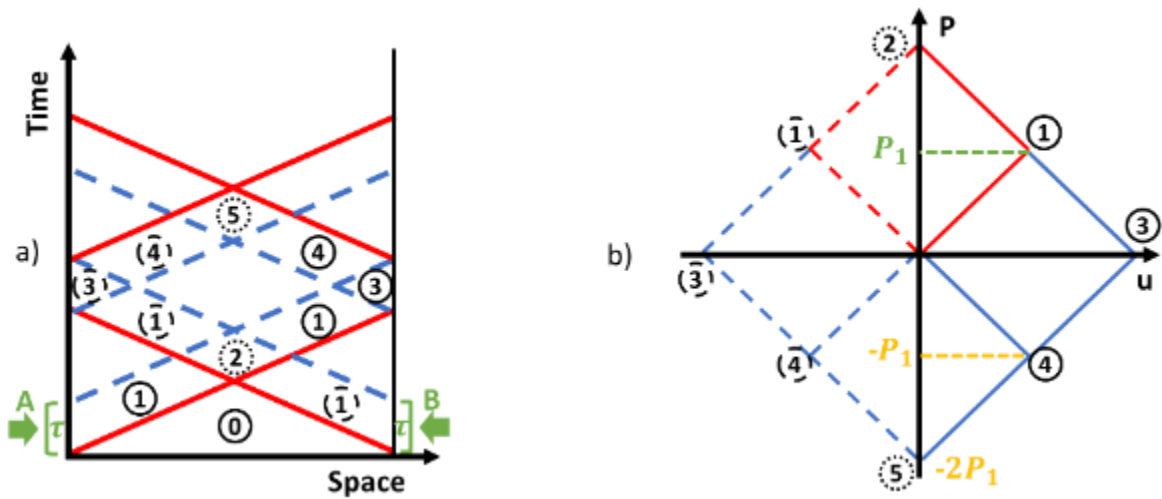
Figure 1-22 a) Space/time diagram of a symmetrical shot and b) its associated (P,u) diagram

Figure 1-22 depicts the shockwaves behaviour (Figure 1-22 a)) and the pressure they generate (Figure 1-22 b) on a mono material. As in 1.4.4, the shock front is represented in red lines, and the release wave in dashed blue lines. The pulse duration, τ, is the same for both lasers. On the (P,u) diagram, the polars created by laser A are in full lines, and the one from laser B in dashed lines. Same for the state: full circle for A and dashed ones for B. When a state is common to both shot, it is represented using a doted circle.

The common parts taken away, one can see two separated single shots, one coming from the right face, and the other one from the left face. Hence, as for the single shot setup, two tensile stress areas are generated (state 3).

When both waves first meet (state 2), the sample is locally put under a high compressive stress theoretically equal to -2P_1 when the attenuation is ignored. More importantly, during their second intersection (state 5), a tensile stress equal to twice the one generated in state 4 is created. Hence, with this technique, one can generate a stress theoretically twice higher than the one in a single shot setup therefore focussing the main tensile load on the bond and not the laminates.

Figure 1-23 shows the effect of a time delay between the two laser shots on the localisation of the tensile stress areas. The principal tensile stress area is represented with a orange circle, and the secondary ones with green circles.
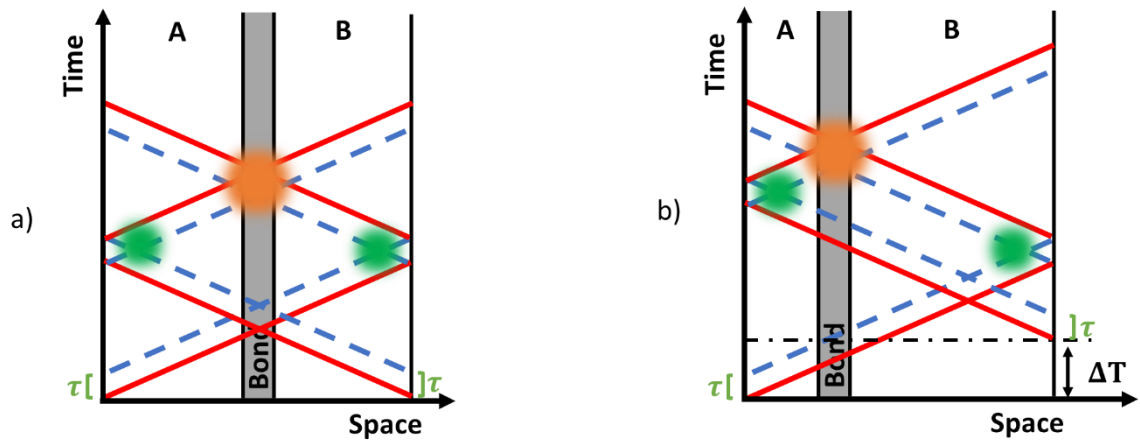
Figure 1-23 Symmetrical laser shock: a) without time delay b) with time delay

By delaying the laser shot on one of the free surfaces, one can note that the maximum tensile stress area is offset toward the opposite free surface, allowing a better stress location within the material. The required delay can be obtained using the following formula:

$$\Delta T = \sum_i t_{l_i} \times \frac{\rho_{l_i}}{Z_{l_i}} - \sum_j t_{r_j} \times \frac{\rho_{r_j}}{Z_{r_j}} \tag{1.15}$$

where t_{l_i} is the thickness of a layer i situated on the left of the zone that need to be tested (the bond in this case), ρ_{l_i} its density and Z_{l_i} its impedance. The same way, each variable with the index letter "r" refers to the right part of the area under test.

The technique does not have the drawbacks the double shock has: the stress generated at the intersection of the two reflected shockwaves is higher than the one created by a single shot setup, and the shot are made on two different locations, so no problem concerning a second interaction with the sample. This again is without accounting for the material damping. Initial studies were realised on a 3mm CFRP composed of two 1.5mm bonded laminates [107]. They showed that, when considering material damping, the pressure in state 5 is equal to -1,3xP_1.

The main limitation of this technique is its requirement to have access to both faces of the sample.

This optimisation will be the main focus of this manuscript. Recent studies made by Ghrib [112] already showed the capability of the technique to generate controlled damage within laminate structures, both in their size and location. Indeed, in her paper she used the symmetrical laser shot to generate a delamination inside of a CFRP laminate at a specific location by modifying the time delay between each laser impulse.

1.4.8 S-LASAT Comparison Using Acoustic Approximation

In order to theoretically compare the symmetrical shot optimisation, a study based on acoustic approximation is proposed. This technique will be compared with the single shot setup based on the estimated size of the tensile stress area, both temporally and spatially. The study is realised on a sample with three isotropic layers.

As for the single shot setup, the question of the stacking sequence is studied. The same two materials are used (cf. Table 1-1). Two sequences are studied Al/Cu/Al and Cu/Al/Cu. The outer layers will be 600µm thick, and the one in the middle 150µm. The load applied is 1GPa for each impact.

<u>Case 1: Al/Cu/ Al</u>
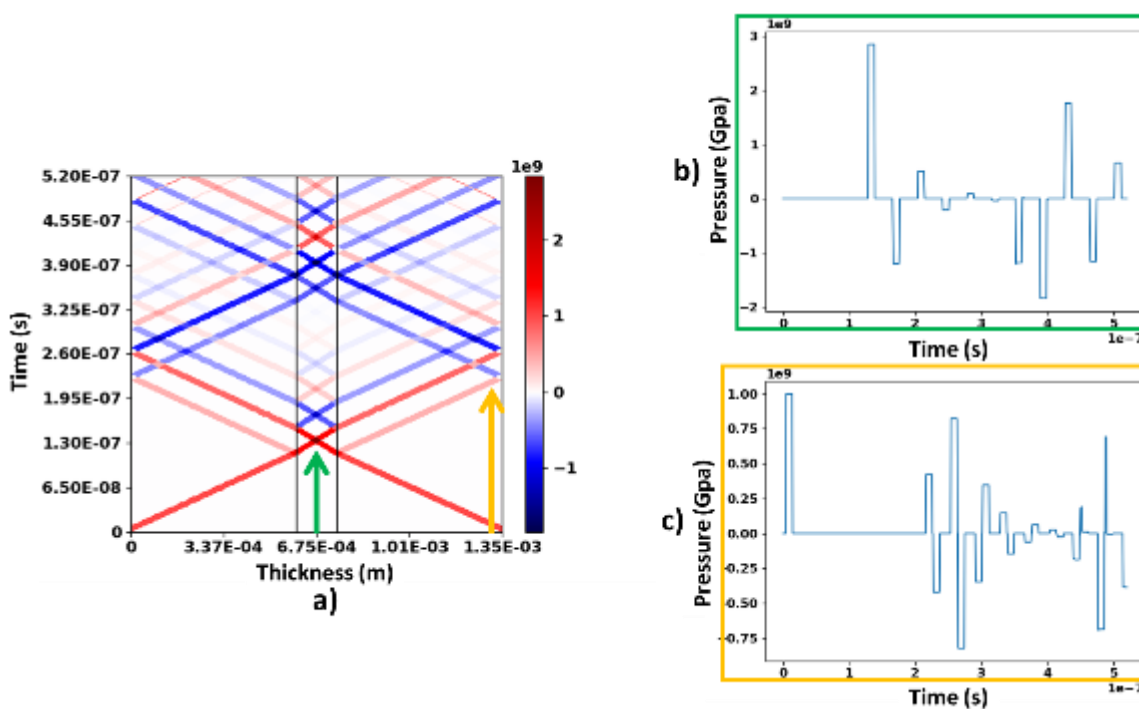
Figure 1-24 a) XT diagram of symmetrical choc on the sequence Al/Cu/Al. b) Load profile in the middle of the sample. c) Load profile on the edges of the sample

Figure 1-24 a) shows the XT diagram of a symmetrical laser shot applied on a three layers samples. The lowest acoustic impedance material is on both side. This leads to the creation of an early tensile stress area in the middle of the sample 18ns after the initial shock (intersection of the blue lines). The pressure profile around the central axis of the sample (green arrow) is plotted in Figure 1-24 b). It confirms the presence of a tensile stress area following high local compressive stresses. The highest tensile stress, however, is generated at the 40ns mark. Its value is -1.8Gpa. The theoretical -2GPa (2x-P_0) is not reached. Indeed, because of the difference of impedance between each material, part of the pressure was lost when the shockwave crossed the interface Al/Cu.

Figure 1-24 c) shows the pressure profile a single shot would generate (orange arrow on the XT diagram). There is indeed 1GPa of pressure applied on one of the surfaces, and the resulting pressure in the secondary tensile area (Figure 1-23) is -0.80Gpa.

Hence, in this configuration, a higher tensile stress is generated at the primary tensile area than around the secondary tensile area, as expected.

<u>Case 2: Cu/Al/Cu</u>
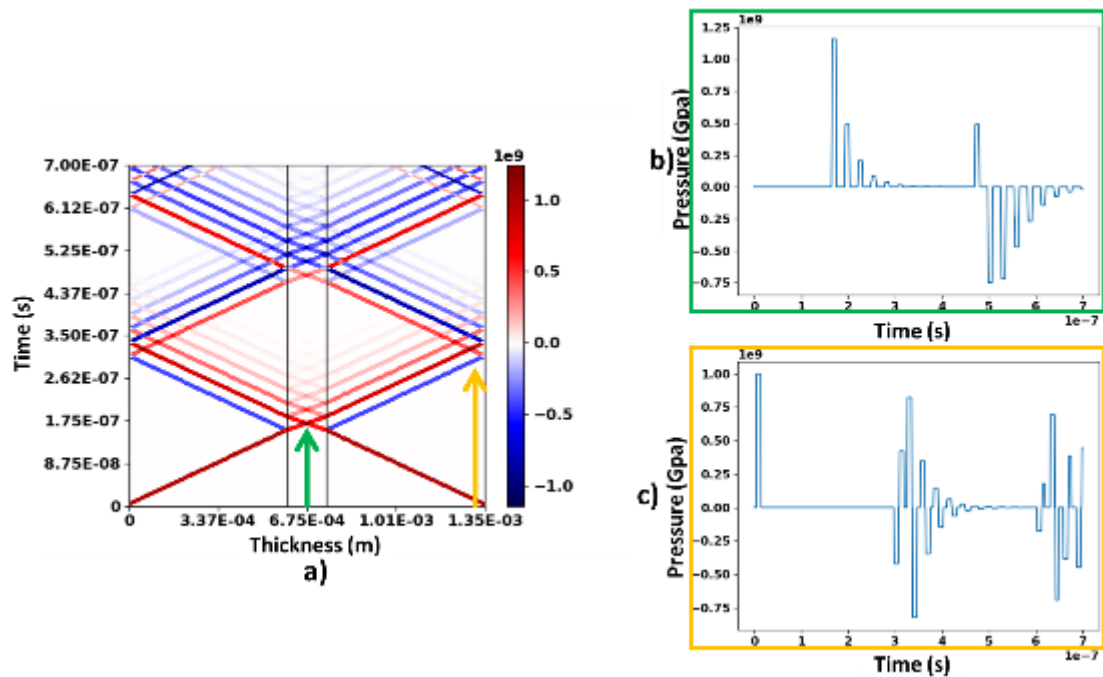
Figure 1-25 a) XT diagram of symmetrical choc on the sequence Cu/Al/Cu. b) Load profile in the middle of the sample. c) Load profile on the edges of the sample

Figure 1-25 a) shows the shockwave pattern within a sample where the highest acoustic impedance material in on both sides. Compared to the previous one, no initial tensile load is recorded. The main reason is the behaviour of shockwaves at the interface Al/Cu. They go from a low acoustic impedance material to a higher one.

However, a closer look at the load profile along the centre of the material (Figure 1-25 b) shows that the generated tensile stress within the principal area has significantly dropped. It is now at -0.75GPa vs the -1.8GPa obtained previously.

Moreover, the generated tensile stress around the secondary areas has not changed. So, given this configuration the highest levels of tensile stresses are achieved in the same location as standard LASAT, removing the main perk of S-LASAT.

The problem is that composite samples fit this material sequence. CFRP laminates with a higher acoustic impedance than epoxy (cf. Table 1-2) are placed on both sides, the epoxy bond being in the middle.

	$\rho\ (kg \cdot m^3)$	$C_0\ (m \cdot s^{-1})$	Z
CFRP	1630	3000	4.89+E06
Epoxy	1260	2600	3.28E+06

Table 1-2 Acoustic impedance of CFRP and Epoxy

Case 3: CFRP/Epoxy/CFRP
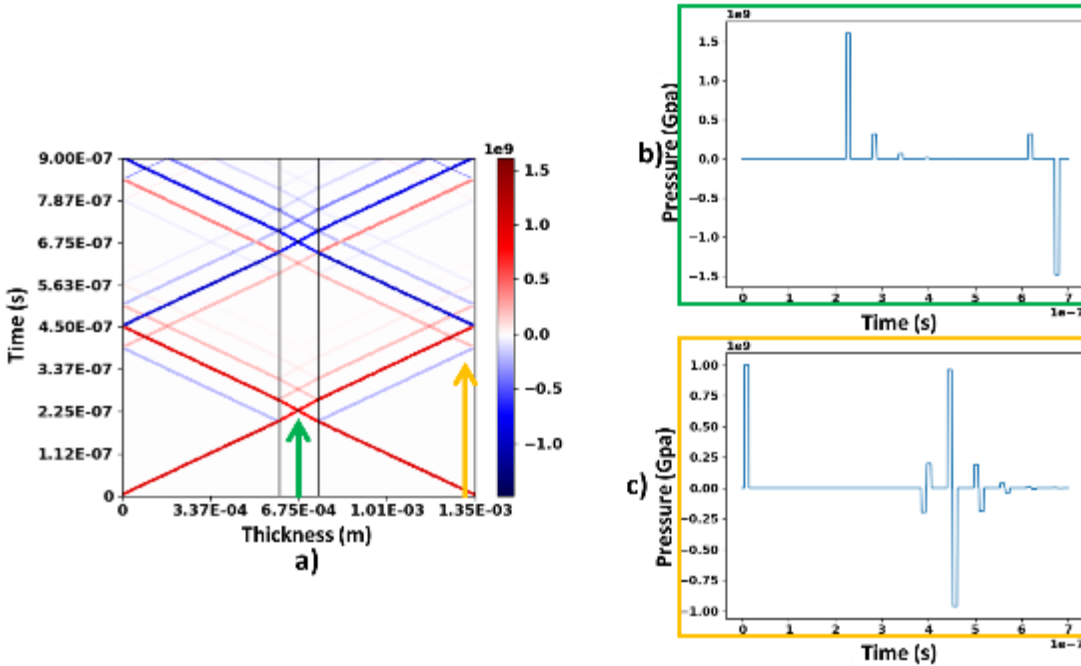
Figure 1-26 a) XT diagram of symmetrical choc on the sequence Co/Al/Co. b) Load profile in the middle of the sample. c) Load profile on the edges of the sample

The shockwaves pattern from Figure 1-26 a) is really similar to the one found in Figure 1-25 a). However, there are less reflections on the interface Epoxy/CFRP than Al/Cu. This is due to the small difference in acoustic impedance between CFRP and epoxy. The principal effect this has on the load pattern, is the diminishing of the pressure loss once a shockwave crosses an interface.

Thereby, when focusing of the load pattern around the centre of the material (Figure 1-26 b) one can note an increase in the generate tensile stress in the principal stress area –1.5GPa vs -0.75GPa) compared with the Cu/Al/Cu sequence.

Moreover, the tensile stress generated in the secondary tensile stress area (orange arrow on Figure 1-26 a) is now smaller.

In conclusion this configuration can be tested using S-LASAT with however a maximum tensile stress that is smaller that what it could be in if the highest acoustic impedance material was placed in the centre.

Using acoustic approximation, one can also retrieve the theoretical size of the maximum tensile stress area. In this case, for a 10ns pulse, its width is 90μm. As described in chap 2, the thickness of one CFRP plies is around 150μm. So, if the tensile stress is properly set on the interface using **eq. (1.15)**, no load should be directly applied to the interlaminar area of the CFRP laminate.

Moreover, timewise, the load is in this case applied during 15ns. Hence this technique allows for a much more local load (location and timewise) and should be able to generate the load only in the area of interest.

1.4.9 Additional effects

1.4.9.1 Edge effects

The presented theory so far only described the shock propagation given a 1D propagation. This kind of approximation can be used when the laser spot is rather large compared to the sample's thickness. However, it is known that for thicker parts, edge and transversal effects can arise [100], [113], [114]. Because of the important local pressure variation on the edge of the focal spot, part of the release wave is deflected (a and b in Figure 1-27).
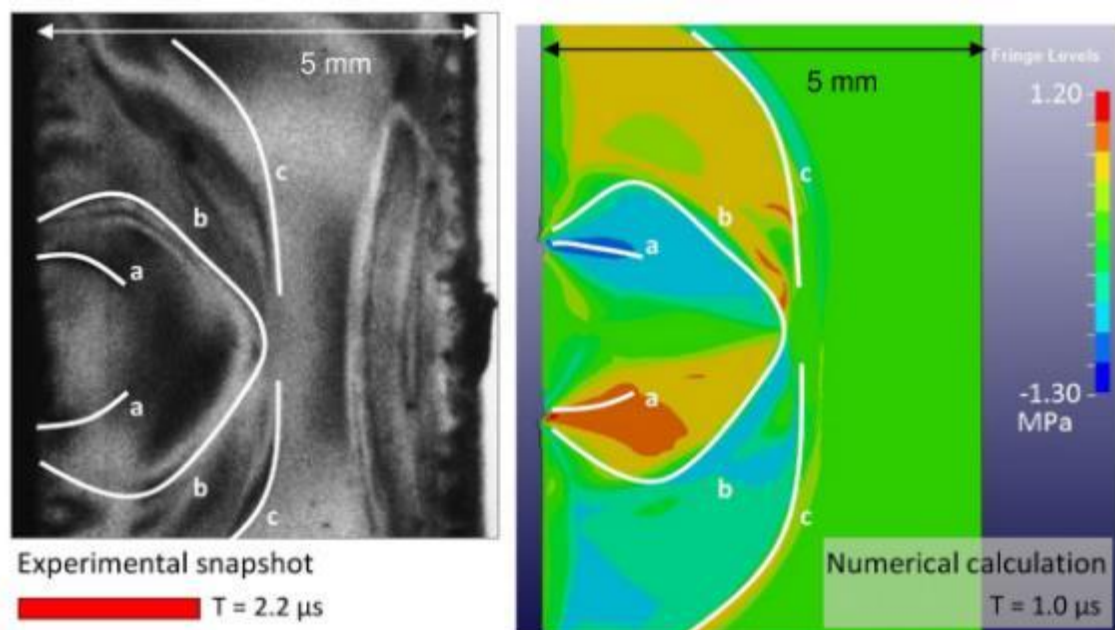
Figure 1-27 Taken from [100] , the left image is a shadowgraphy realised on a 5mm thick epoxy sample, the right image being a LS-Dyna simulation of the process, both experimental and numerical work were done by Romain Ecault.

Once the release waves generated by this phenomenon cross each other, a zone of high tensile stress is created. This could create damages in unwanted areas, or on the contrary, allow for the test of otherwise unreachable zones of the sample.

1.4.9.2 Attenuations

The shockwave velocity, D, was introduced in equation (1.5). As explained, the shock front creates a discontinuity that makes the pressure shift from a pressure P_0 to P_1. Hence the following release wave travels in a medium under shock which has a material velocity u_1, making the velocity of release wave ($C_1 + u_1$) higher than the shockwave one (D). Thereby, the release wave eventually catches up the shock wave and starts trimming the generated pressure within the material (Figure 1-28).

Moreover, the tip of the release wave travels in a medium which pressure and velocity are almost back to their original state P_0 and u_0. Hence the release waves directly following the shock front have a higher velocity than the one at the end of the shock. It results in a widening of the release wave.
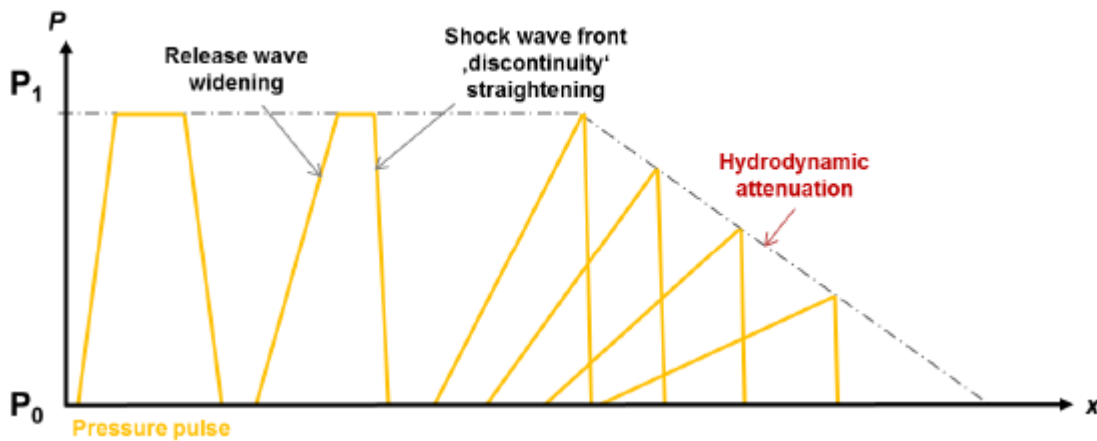
Figure 1-28 Diagram showing the modification of the shock wave over the time due to elasto-plastic and hydrodynamic effects [39]

The same phenomenon can be observed with the shock front, this time however, the medium goes from the state (P_0, u_0) to (P_1, u_1) with $u_1 > u_0$ resulting in the stiffering of the shock front.

1.4.10 Damage and Ultrasonic Scanning

Although laser driven shockwaves can generate an opening within a sample, it is (most of the time) impossible to spot with bare eyes, which is especially true for weak bond testing, or bond threshold definition. Moreover, in the specific case of composite in symmetrical attack, both faces are occulted by a plasma during the shock, rendering velocity diagnostics (such as the Visar or the Photonic Doppler Velocimetry) unusable. Thereby, S-LASAT requires an additional technique to properly spot the default generation inside of the sample.

In the years 2010s, before the Encomb project, a joint French/Canadian research program named Shock Adhesion Test for Adhesively Bonded Composites (SATAC), studied bond

strength within composite bonded structures. During this project, Perton [115] used, with great success, ultrasonic scans (US) to assess whether or not a disbonding was generated within the material. As it was specified in 1.2.4, this NDT suits this kind of analysis.

US are easy to use, fast, have a decent resolution and are considered as a standard NDT for composite structure [116], [117]. This technique analyses the way a group of wave travels through a sample. Like for a shock, their travelling time highly depends on the sample's Young modulus and geometry.

A lot of different scanning technique are available, such as the non-linear imaging described earlier in this chapter, and they have their own preferred applications (medical, mechanical, …) as well as their preferred geometry (thick/thin samples, multiple/single defects, …).

In this study, a standard longitudinal incidence US technique was chosen. It is one of the easiest technique to implement and is adapted to the composite defect spotting [29], [38]. A group of ultrasonic waves is emitted by a probe, at a selected frequency. The signal propagates through the sample, and each time the acoustic impedance is lowered, part of the signal is reflected (Figure 1-29). The behaviour is comparable to the shockwaves reflection described in 1.4.5. The "amount" of reflected waves is proportional to the impedance mismatch between two areas. The bigger the difference, the more signal is reflected. The probe acts as both, a transmitter, and a receiver.

This technique also allows for different types of scan, depending on the probe used:

- A-scan: displays the material response right below the probe. It can be seen as a 1D scan.
- B/D-scans: these are 2 different scanning planes, that create a 2D slice of the sample. These scans are only available for multi-elements prob, a.k.a. probe with multiple transmitter/receiver elements.
- C-scan: this is a 3D scan that combines the measurements from the B and D-scans
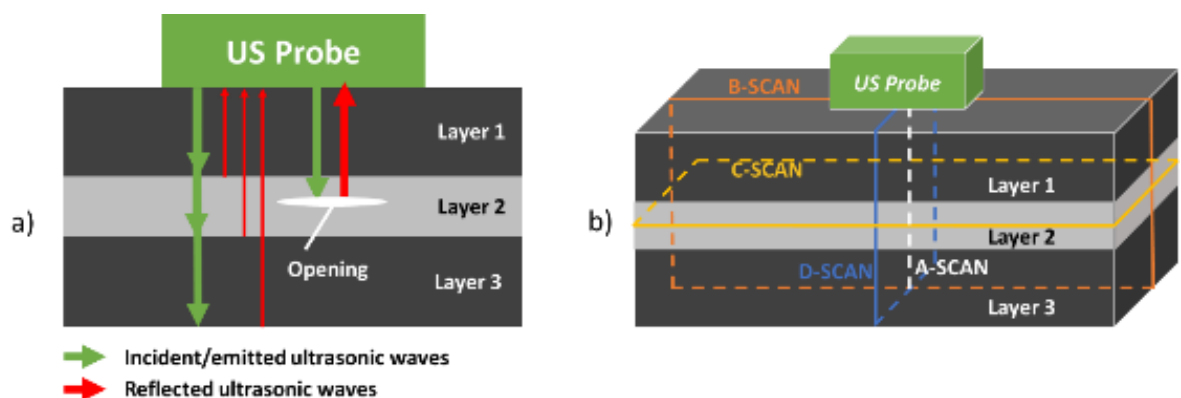
Figure 1-29 a) Diagram of the US normal incidence technique b) The different scanning plane associated with the technique, inspired by [107]

1.5 PhD objectives

Ecault thoroughly studied the laser shock as a means of adhesion test with both, experimental and numerical data. He showed the capabilities of the technique to spot weak bond, as well as its limitation. This study is focused on the adhesion test of bonded Carbon Fibre Reinforced Polymers (CFRP) laminates using symmetrical laser shots, one of the solution he suggested [107].

The objectives of this study are numerous, but can however be divided in two groups, the increase of the technology maturity though European project, and the comprehension of the S-LASAT.

1.5.1 European Project: ComBoNDT

The ComBoNDT project is a unique opportunity to study weak bond and to further develop technique to spot them. The project is divided in three main phases of study. First, coupon samples, altered by a wide range of contaminant, are studied using the technique. This first part aims at assessing the weak bond detection capability of the technology depending on the contaminant. The second phase still includes contaminated bond, but the tested samples have now a more complicated geometry. Eventually, during the third and last part, real parts are tested. The goal of the project is to increase the Technology Readiness Level of the technique.

1.5.2 Comprehension of S-LASAT

The project offers a fertile environment for the study of the mechanism behind the S-LASAT. Initial studies have been realised on this technique, but there are a lot of questions still unanswered, especially concerning the requirements of the technology. Indeed, the goal is to test weak bonds with very little contaminations. Hence, both the tensile load intensity and its location need to be controlled.

One of the main problem concerning the technique is the wide range of parameters involved in the process:

- Laser driven parameters such as the pulse time delay, the laser energy, the pulse duration, ….
- Process driven parameters such as the confinement material or the good symmetry of the shock
- Material driven parameters such as the uncertainties concerning the sample (thickness, layup, …), or the behaviour of the composite under such heavy loads

Overall, a dozen of parameters need to be fully understood in order to properly master the process. The amount of sample being limited, and for time reason, an initial study is realised using numerical tools. The goal is to grasp the influence of each parameters and assimilate them when performing a real test. This leads to the second part. Using the data gathered from the simulations, ComBoNDT samples are tested.

The main questions to be answered concerning the process are the level of control required to properly use the S-LASAT to assess lightly contaminated bond, as well as the impact of the different parameters on the final result.

Chapter 2. EXPERIMENTAL TOOLS

TABLE OF CONTENTS

2.1 Tools

2.1.1 Laser

All laser shocks were produced within Hephaïtos facilities in Paris. It is a multi-purpose platform designed for both LASAT application and shock peening (surface treatment using laser) applications. The laser and its infrastructures were installed in 2015, so this work is the first of its kind realised in this facility and as it will later be described, several parameters had to be modified and/or optimised in order to perform S-LASAT.

The laser source of the facility was chosen to best fit its applications. As mentioned in chapter 1, the shock generated highly depends on the laser matter interaction. One of the most critical part is the laser's length wave. A material will absorb a certain quantity of energy coming from a specific length wave depending on its molar absorption (Figure 2-1).

Whether this is for shock peening or LASAT application, the vast majority of shots are realised on full aluminium samples or sacrificial layers made out of aluminium. Moreover, a water confinement is used to increase the generated pressure. Hence, ideally, the laser's wave length should be well absorbed by aluminium, and the confinement should be completely transparent to it.

Nd:YAG lasers emit an infrared light with a wavelength at 1064nm. Their frequency can be doubled using crystals ($L_iB_3O_5$ in that case) to generate a 532nm light (green). At that wavelength, water barely absorbs anything [118], making it very interesting for LASAT applications. Having this crystal in the beam path also act as a protection, since it avoids unwanted laser reflection from coming back within the laser and damaging it.
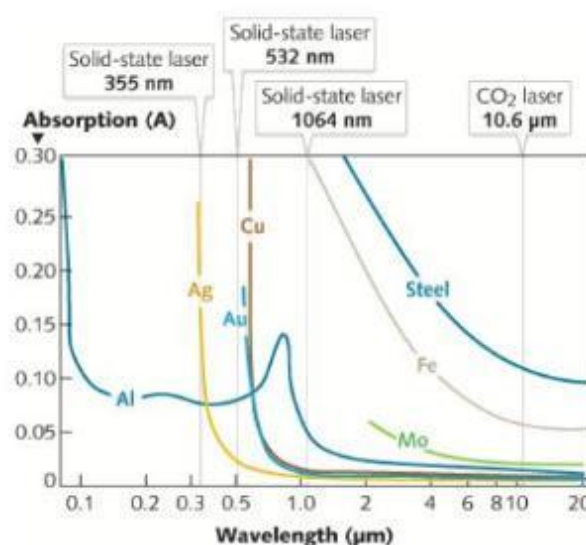
Figure 2-1 Absorption as a functino of wavelength for aluminium (Al), silver (Ag), gold (Au), copper (Cu), molybdenum (Mo), iron (Fe), steel (Steel) [119]

Moreover, the laser should cover all three LASAT configurations: single shot, symmetrical shot and double shock (cf. chap. 1). The single shot setup does not represent any additional challenge however, two beams are required to shock a sample symmetrically, and short laser bursts are needed for the double shock.

Ecault showed in his study that to open a healthy bond, the laser should generate at least an intensity of 1GW/cm^2 [107]. To avoid any edge effect when testing samples from the ComBoNDT project, a rather large spot size of 8mm was chosen. The choice was made based on ComBoNDT samples later describe.

Figure 2-2 a) Gaïa-HP laser b) Hephaïstos control room c) example of a symmetrical setup

The Gaïa HP from Thales used on the Hephaïstos platform (Figure 2-2 a) & b) meets these requirements. It is made out of 2 Nd:YAG lasers. They can both reach an energy of 7J per shot, with a pulse duration of 7ns. Using an 8 mm focal spot, each beam can create an intensity up to 1,4GW/cm^2. Both beams are polarised, making it easy to separate them using a polariser. Figure 2-2 c) shows an example of symmetrical setup. On the bottom left of the picture, both beams arrived combined on the setup (green line), and are then separated in two beams, beam A (blue) and beam B (red). Each beam can be fired independently in short consecutive bursts. The shot rate for each laser is 2Hz.

2.1.2 Test and Optimisation of the Setup

2.1.2.1 Energy Variations

A series of 15 shots per level of energy were realised to grasp the energy variation/error that may occur during a standard shot campaign. To measure the laser energy, two different calorimeters were used. One is already inside the laser with a deviation of 4% of the laser energy into a calorimeter. The real energy value is then extrapolated. Another set of calorimeters were put right after the polariser splitting beam B from beam A.
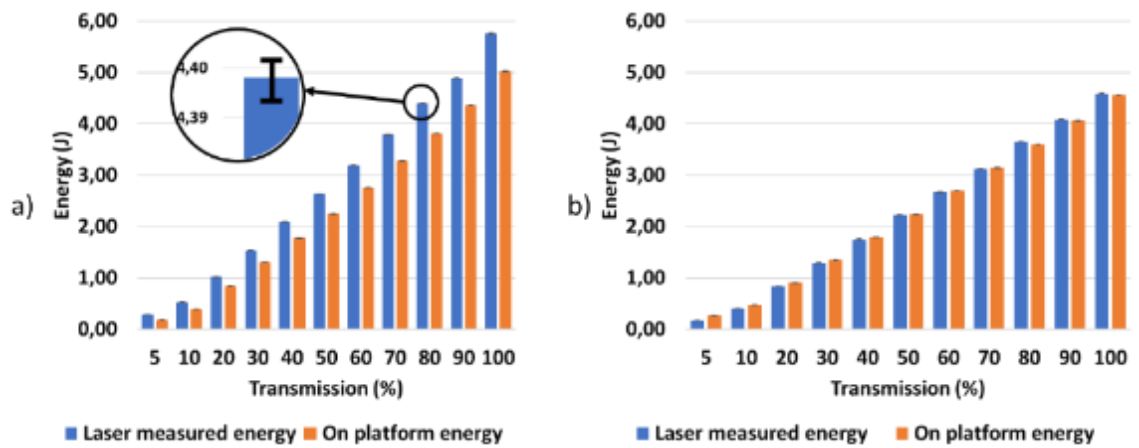
Figure 2-3 Energy variations at given laser transmission for a) Beam A b) Beam B

Figure 2-3 represents the energy level reached for each beam (Figure 2-3 a) for beam A and b) for beam B). Each time measurements realised within the laser are compared with the energy effectively obtained by the experimental setup. The laser's intensity is driven by the transmission. At the end of the laser stands a half-wave plate. It is positioned between a polariser and an analyser. By rotating the half-wave plate, one can change the amount of energy "transiting" through the device. Hence a 5% transmission means only 5% of the laser energy goes out of the laser.

The energy value given directly by the laser is compared with the one from the calorimeters placed on the experiment table. One can see the laser value is always a little bit higher. This can be due to losses in the laser transportation. The laser and the platform are 10m away. Moreover, the discrepancy seems higher for beam A, than for beam B. When reaching the polariser, beam B is reflected while beam A passes through the optic which can result in extra losses.

The uncertainty bars have also been placed onto the graphs. They were given by the value spread obtained for each series of 15 shots. However, the laser showed little to no energy variations.

2.1.2.2 Beams' Energy Balancing and Loss Quantification

As shown by Figure 2-3, a given transmission level will not generate the same amount of energy on both beams. During a shot campaign, the laser intensity is measured on the experiment table every other day. The energy of the weakest beam is taken as a reference (here beam B), and the associated transmission level for the other beam is extrapolated, insuring a good energy symmetry throughout the whole campaign.

Part of the energy is also dissipated every time a beam crosses an optic. Two sets of measurements were realised before the first optic, and after the last one, to estimate the energy

loss. The measurement was done for 10 different transmission values ranging from 10% to 100% (step 10%). The difference between the energy measured when both lasers arrive on the first optic of the experimental setup, and the one obtained after both beams have been through all optics and reached the sample was around 9%. This difference was consistent, regardless of the energy level. Data given in this manuscript will always refer to the energy value after the last optic, which is closer from the one perceived by the sample itself.

2.1.2.3 Optics

The laser's energy is too high to be transported using conventional method such as optic fibres. Therefore, a series of mirror are used to bring the laser from the source to the testing area. To limit energy loss per optics, each one of them was treated to properly reflect 532nm light wavelength.
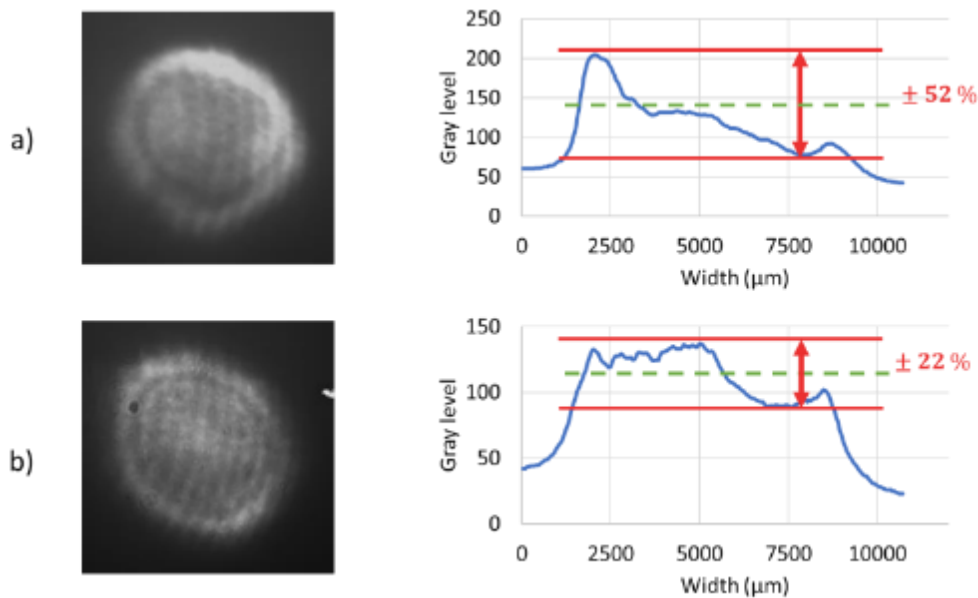
Figure 2-4 Spatial repartition of the laser intensity for a 8mm spot for a) beam A and b) beam B

The focal spots upon arriving on the S-LASAT platform are presented in Figure 2-4. They were measured using a high-speed camera with optical densities placed in front of it to limit the energy perceived by the camera sensor.

Both focal spots had an over intensity ring and a poor spatial repartition of the laser intensity over the spot. None of them were completely round. The shape, as well as the spatial repartition may be due to the transportation, and the distance the platform is from the actual laser (beam path ~3m). The generated pressure is closely linked to the laser intensity thereby, a poor spatial repartition of the laser light implies an equivalently poor repartition of pressure. For beam spot A, variations go above 100% between the lowest intensity area and the highest one. Moreover, these variations are spread over the whole surface of the spot.

To overcome this problem, Diffractive Optic Elements (DOE) were added on the beam path, just before the lenses focalise the laser on the sample. These optics break the incoming beam and diffract it in the shape of the desired geometry. For LASAT application, a standard round top hat was chosen. The spot diameter is linked to the focal length of the lens. Figure 2-5 shows the same study as the one done in Figure 2-4, but with DOEs placed on the beam path.
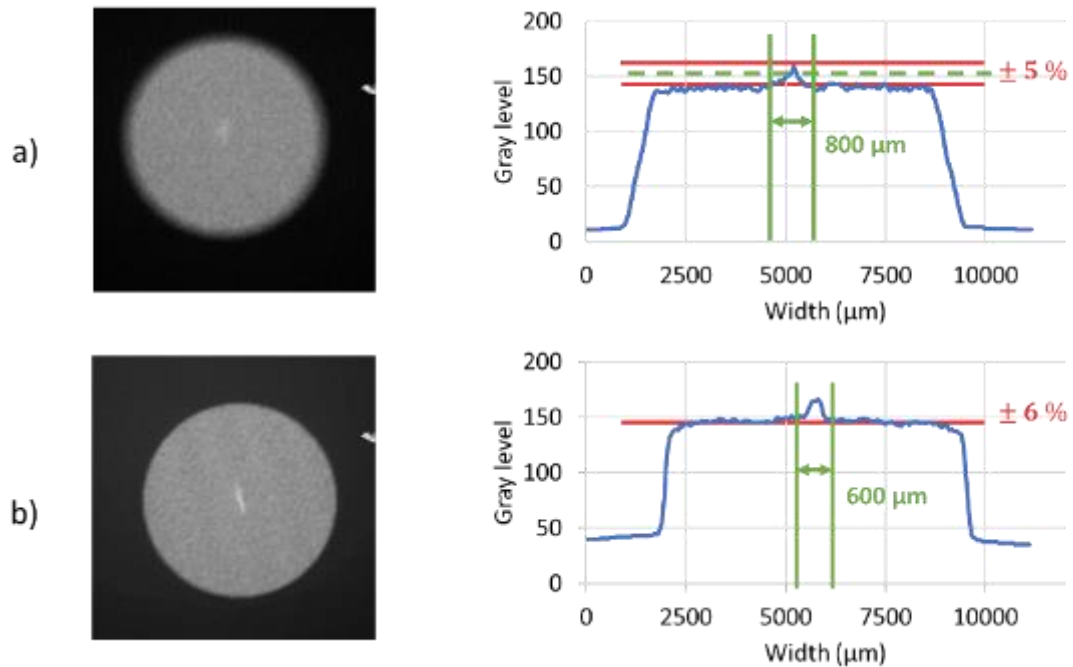
Figure 2-5 Spatial repartition, using DOEs, of the laser intensity for an 8mm spot for a) beam A and b) beam B

A better repartition of laser intensity can be observed in a well-defined round shape. For example, intensity's variations of beam sport A are now down at 10% and are space over 800µm. The small over intensity in the middle of the spot is due to a low-order optical aberration. This can be corrected by offsetting the target from the focal spot. In this case, beam spot A has been moved by 2mm from the focal point of the lens to obtain the same spatial repartition as for B. This is reason why beam spot B is sharper than beam spot A and shows stiffer intensity variation around the edges.

2.1.2.4 Confinement

The generated pressure can be enhanced by using confinement materials (cf. chap. 1). Indeed, when using a confinement material, not only is the pressure spike higher, it also lasts longer. However, pass a certain threshold, the plasma can be generated not on the material, but a little before. The phenomenon is called "plasma breakdown" and greatly reduces (if not annul) the generated pressure on top of the sample [83], [84], [120], [121]. Each confinement material has its own laser intensity breakdown threshold. Hence, when selecting the confinement, one must make sure the breakdown threshold is above the intensity range used for the application.

The "historical" material is water. It is cheap, easy to apply and remove from the sample, available in large quantity and has great constraining capabilities. However, this medium can be hard to manage in industrial environments such as repair lines. Courapied [109] further investigated nine other constraining medium. To compare them, three main criteria were used: the generated pressure, the laser breakdown threshold, and the pulse duration.

Results are summarised in Table 2-3. The parameter β is directly linked to the shock confinement properties of the material. The higher the number, the more pressure is generated for a given laser intensity. The "breakdown threshold" gives the maximum intensity usable with this confinement. If for certain applications such as shock peening this data can be of importance, in the case of LASAT test, the maximum intensity required is around 1.5GW/cm². All medium can withstand it.

Constraining medium		Breakdown threshold (GW/cm²)	Pulse duration (ns)	Max pressure (GPa)	Ease of use
Tape n°17	0.61	9	38.61	1.8	++
Varnish n°1	0.8	6	21.34	2	++
Vacuum grease	0.85	12.5	30.17	3	-
Liquid glass	0.98	14	34.59	3.7	--
Epoxy	1	6.5	34.64	2.5	--
Varnish n°2	1.27	10	21.2	4	++
Tape n°16	1.73	11.5	37.63	5.9	++
9010 SPT Coroplast tape	1.98	13	31.9	7.1	++
Cooking oil	2.02	>25	31.25	Unkown	-
Water	2.06	6	30.51	Unkown	+

Table 2-3 Performances over 5 criteria of 10 different constraining mediums [109]

The "pulse duration" in Table 2-3 gives information on the localisation of the tensile strength and its width. Indeed, the longer the pulse duration is, the larger the generated tensile stress area. These measurements were realised using a laser with a pulse duration of 7ns. The pulse duration with a constraining medium was increased by at least a factor 3.

For most of these mediums, the generated pressure grows with the laser intensity up to a certain point. After that the generated pressure reaches a plateau and increasing the laser intensity will not change the generated pressure. Again, this will not be a discriminating criterion since all confinement can generated the required pressure.

The last column in Table 2-3 gives an idea on the efforts required to use to confinement. For example, the epoxy glue used here needed 24h to dry, and was not easy to remove whereas the tapes were much more convenient.

Hence, the only separating parameters will be β and the ease of use of the material. The best candidates (apart from water, the most widely used) would be either the Coroplast tape, a double double-sided tape, or the tape n°16 which is a basic office tape. Both of them are easy

to use and have high constraining capabilities, but the first one has the advantage of being thicker (1mm vs 51μm), which could be interesting when facing testing rough surfaces. Other parameters such as the stiffness and elasticity properties of the confinement also play a role in its constraining capacities, however, these were not tested during this study.

2.1.2.5 Sacrificial Layer

The sacrificial layer serves three main purposes:

- Thermal insulation of the sample from the plasma (~20000 °K [121])
- Avoid ablating the actual sample to generate the plasma
- Insure the same laser/matter interaction, regardless of the sample's material

Two main types of sacrificial have been used for LASAT: sprayed aluminium and aluminium tapes. The first type of confinement was quick to apply, but it was hard to have a consistent thickness of sprayed aluminium over the whole sample. Method such as the Physical Vapor Deposition (PVD) is available and was used [122], but it is more time consuming and requires specific installations. Moreover, because of the aluminium coating, it was impossible to perform ultrasonic testing (US), because all the signals were reflected [107].

Tape on the other hand allows a better consistency of both thickness and aluminium surface (critical for the laser matter interaction [122]). El-Karnighi-Tanguy and Courapied studied the influence of aluminium tape's parameters on the generated shock wave [109].

Their study revealed the influence of the thickness of the glue layer of the tape on the shock propagation. As shown in the chapter one, the impedance difference between two materials can lead to different physical phenomena. In the case "aluminium to copper", where the shocked material had a lower impedance than the back face one, a higher pressure was generated after the interface. The same thing happens when the shock wave goes from the glue of the tape (small material impedance), to the tested material. And the greater the difference is, the stronger is the resulting pressure (cf. chap 1). This could allow for the use of less powerful lasers.

Hence, they showed that the pressure at the interface glue/sample raises until the glue layer is thick enough (Figure 2-6 case 1) to fully contain the pressure raise creating by the shock (Figure 2-6 case 2). Pass that thickness threshold, the glue will start to attenuate the shock, limiting this phenomenon (Figure 2-6 case 3).
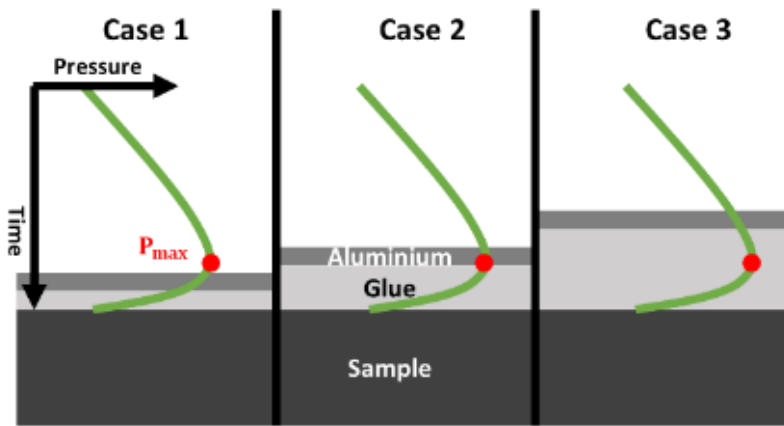
Figure 2-6 Glue thickness and shock enhancement [109]

The best candidate, and the one that will be use in every experiment in this study is an aluminium tape with 40µm of glue and 30µm of aluminium from Advance Tapes.

2.1.3 Ultrasound Scanning

The non-detectability of the adherence loss by common NDT methods is one of the key elements of weak bonds definition. Thereby, after a sample has been contaminated and assembled, US were performed by Airbus following their standard procedure. If no default is found, the contaminated sample validates the first step toward the validation of the presence of weak bond.

Ultrasounds (US) were performed using M2M's Gekko™. Samples were arranged in the bottom of a water tank and scanned using a 64 elements linear probes with a frequency of 5MHz and a cylindrical focus.

Ultrasonic waves are reflected upon reaching a discontinuity of acoustic impedance. When scanning a bonded CFRP assembly, it happens 3 times: when the waves first reach the CFRP laminates, when it reaches the epoxy bond, and when it leaves the sample. Figure 2-7 a) is a typical A-scan for bonded structures, with three distinct peaks corresponding to each interface.

There should be two peaks for the bond, one upon entering and one when leaving it. However, the ultrasound resolution is around 100/150µm, and the bond itself is 150µm. It is thus impossible to differentiate the two signals.

Moreover, the US signal gets weaker whenever it reflects on an interface. To compensate that behaviour, a Time Corrected Gain (TCG) method is used. This method will locally enhance the signal by several dB to make up for the losses at interfaces.
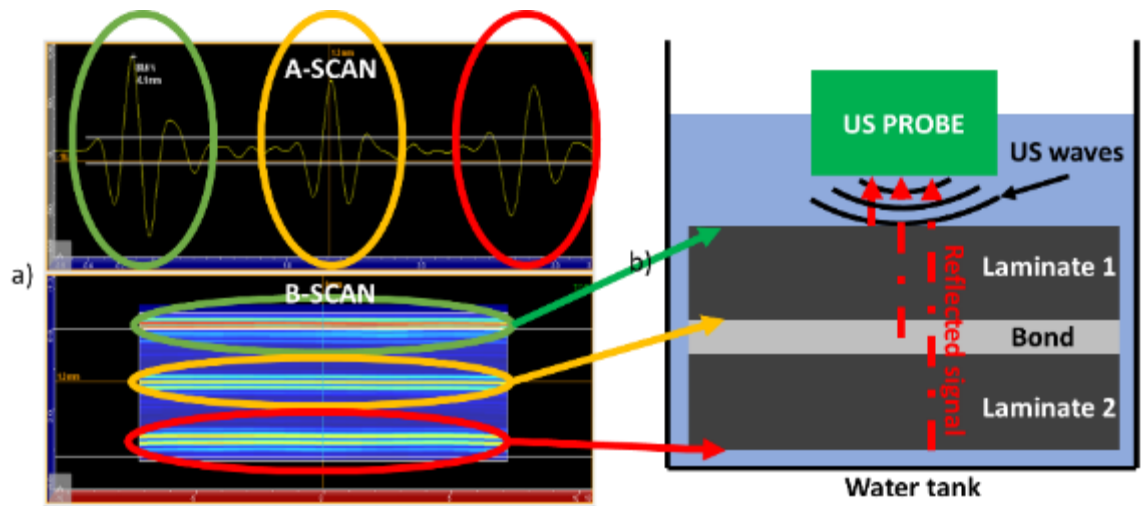
Figure 2-7 a) A-Scan and B-Scan of a bonded composite structure using 32 elements linear probe b) Diagram describing ultrasonic setup at Airbus and its behaviour

To assess the integrity of a structure, C-Scan is the most widely used representation of ultrasonic propagation. C-scans allow for a scan at a define sample depth. For example, Figure 2-8 displays a C-Scan of the samples contaminated with release agent (RA) and the production reference sample (P-RE).
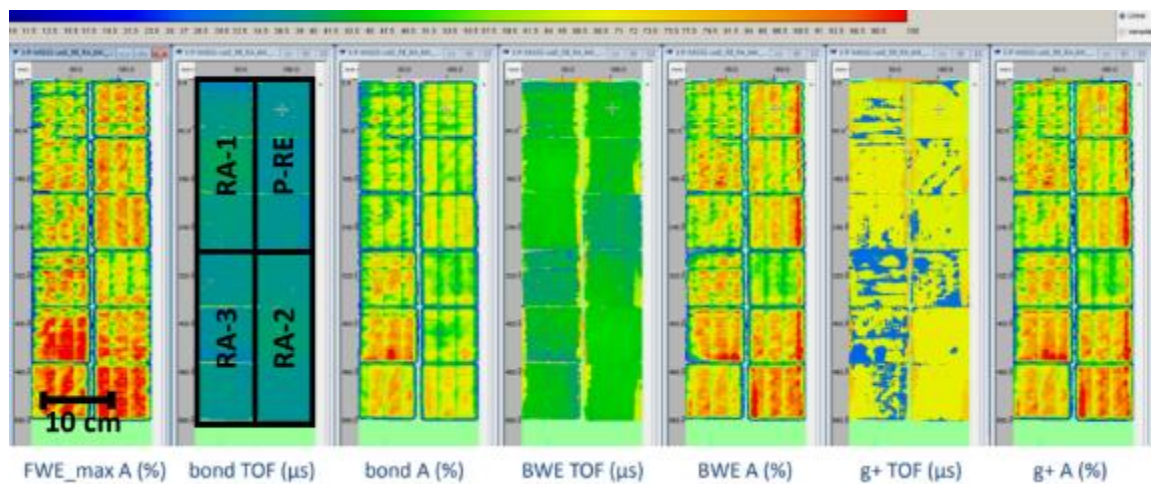
Figure 2-8 C-Scans performed at Airbus facilities on P-RE and RA samples.

A total of nine coupon samples were scanned at the same time: 3 reference samples (P-RE – top right), low level contamination (RA-1 – top left), medium contamination (RA-2 – bottom right) and high contamination (RA-3 – bottom left).

Four different C-scans were realised. The first one labelled "FWE" for Front Wall Echo is a scan of the front face (green arrow in Figure 2-7). The second one was done at the bond depth (orange arrow in Figure 2-7). This one, and the next ones were realised twice. Once using ToF or Time of Flight parameters, and the second time using Amplitude measures. The first one compares the travel duration between the emitted ultrasonic wave and its

echo. It is directly proportional to the distance but can be tricked if a default is at the same level as an interface. The amplitude on the other hand is a representation of the quantity of reflected waves. This is directly linked to the impedance mismatch, meaning it could spot a default regardless of its position. However, heterogeneities could show up as defects. Hence combining both visualisations greatly reduces misinterpretations of US.

The last two depths of scanning are the BWE or Back Wall Echo (red arrow in Figure 2-7) and the g+ is a summary over the whole sample thickness.

On this set of samples, C-scans did not reveal any major defect, the contamination was a success, and if a mechanical loss is observed on these samples, the weak bond creation process will be validated.

2.1.4 Mechanical Testing

The determination of the mechanical adherence loss was realised through GIC and GIIC tests done by the Laboratory of Technology and Strength of Material of Patras University (LTSM-UPAT) [123]–[125]. GIC tests are standard for Airbus, thus fully representing a real situation.
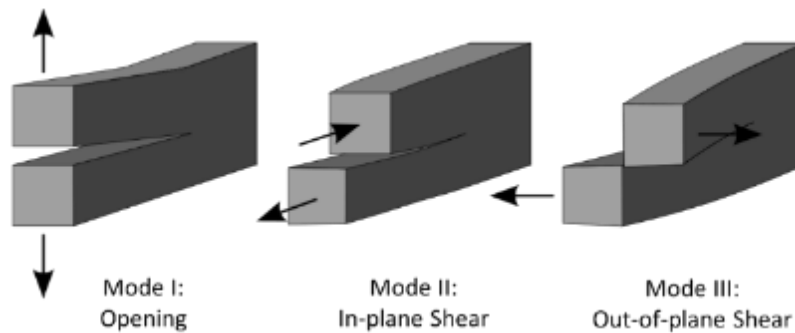
Figure 2-9 Fracture modes

GIC TEST

GIC tests assess the required energy to initiate a crack in mode (I) fracture mode (Figure 2-9). This test was performed using a Double Cantilever Beam (DCB) setup, following Airbus specification AITM 1-0053. The DCB samples were design using the same process as the coupon samples. Metallic piano hinges were bond to one end of the sample and a 10-15mm pre-crack was induced (Figure 2-10 a).

During a GIC test, both the load and the crosshead displacement of the machine are recorded. One can then deduce GI energy using (2.16):

$$G_I = \frac{12P^2a^2}{b^2E_xh^3} \tag{2.16}$$

Where *P* is the applied load, *a* the relative crack length, *b* the specimen width, E_x is the longitudinal modulus and *h* the half thickness.
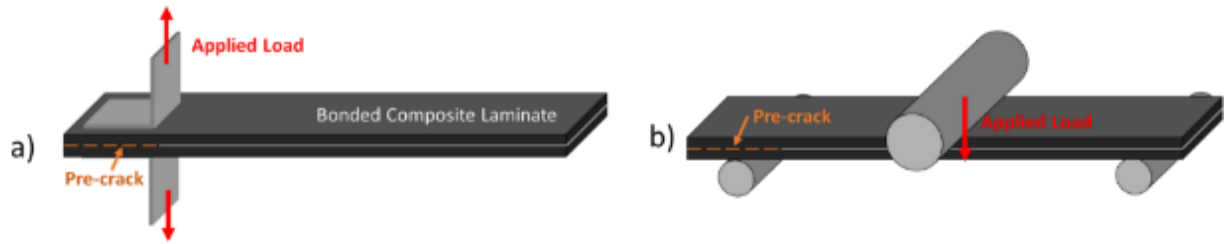
Figure 2-10 a) Scheme of a DCB test b) Scheme of an ENF test

GIIC TEST

GIIC tests evaluated in-plane shear resistance of samples. Numerous tests are currently available [126], [127], but the End Notch Flexure (ENF) test was chosen during the project (also found under 3ENF test) [128]. It is basically a 3-node bending point test with a pre-crack already present at one end of the sample, as for the DCB test.

As for the GIC test, a pre-crack is induced within the bond, and the load and the crosshead displacement are correlated to deduce the energy required to initiate a mode II (Figure 2-9) fracture:

$$G_{II} = \frac{9P^2 a^2}{4b^2 E_x h^3}$$
(2.17)

2.2 Samples

In order to test the capabilities of the technology to detect weak bonds, contaminated parts have been produced within ComBoNDT project. These samples are divided in three groups: coupon samples, pilot samples and real part.

The assessment of S-LASAT performances for weak bond detection is made following these three categories. First, its capabilities to detect specific contaminant are tested. Samples do not have any specificity but their contamination (coupon samples). Then more complicated geometries and contamination scenarios are studied (pilot samples) to eventually test the technology on real parts.

Coupon samples: standard 90mm X 90mm x 3.2mm rectangular samples (Figure 2-11 b). The bond is in the middle of the sample, and only one type of contaminant at the time is present on the surface. The layup is symmetrical, cf. 2.2.1.
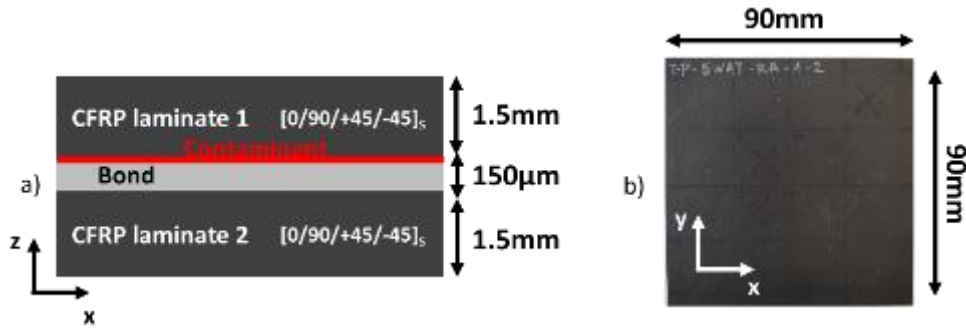
Figure 2-11 a) scheme of the stacking of a production coupon sample b) picture of a coupon sample

Pilot samples: their geometry is trickier. Half of them have a scarf bond, i.e. two bevelled composite laminate are bonded together (Figure 2-12 a) and b). The rest were moulded using based on a 2m radius cylinder to give a slight curvature to the sample (Figure 2-13 a) b). Both samples have a 3.2mm thickness. The surface of these samples is contaminated using two different agents at the same time.
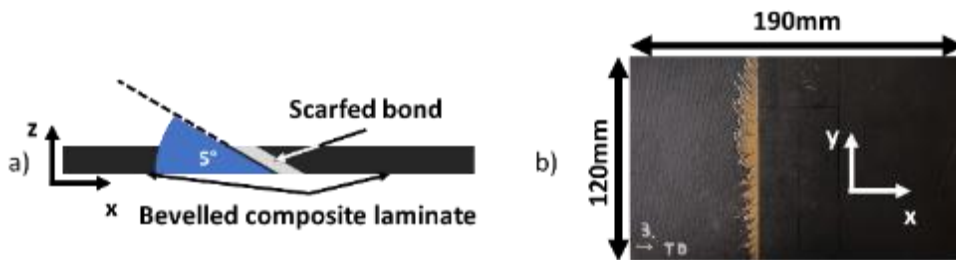
Figure 2-12 a) Scheme of the profile of a scarfed bond b) picture of a scarfed sample
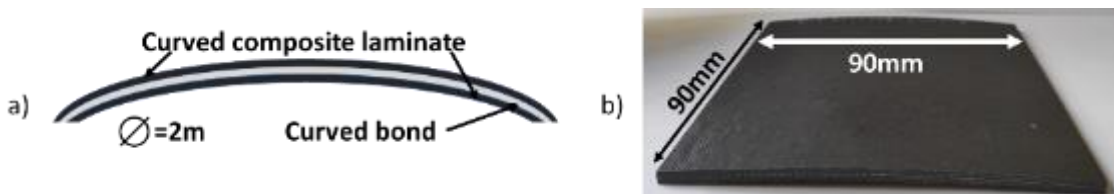
Figure 2-13 a) Scheme of the profile of a curved bond b) picture of a curved sample

Real parts are described in depth in 2.3

2.2.1 CFRP

All samples were made out of Carbon Fibre Reinforced Polymer (CFRP) produced by Hexcel. The HexPly M21E/IMA was chosen because it is already widely used by Airbus for composite applications.

The reinforcement of this CFRP is made with unidirectional HexTow IMA intermediate modulus fibre. These fibres were specifically designed for Airbus applications and show high tensile strength and high tensile modulus [129].

The matrix of the pre-impregnated (prepreg) is made of epoxy M21E. It also contains thermoplastic particles (polyamide) to enhance its shock absorption properties and limit the cracks' propagation (Figure 2-14 b)) [130], [131].
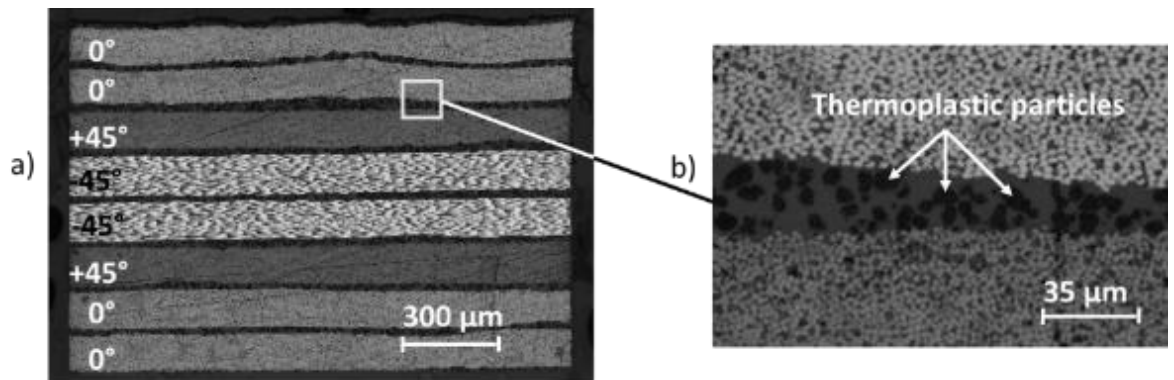
Figure 2-14 a) Typical composite laminate for the studied samples b) close up on the thermoplastic within the prepreg epoxy

The laminate was realised following Airbus CFRP manufacturing procedure AIPS 03-02-019. They were initially produced in the form of large panels (115cm x 75cm) and cut into smaller samples (90mm x 90mm). Plies have been laid-up according to the following stacking sequence: $[0/0/+45/-45]_S$ (Figure 2-14 a)).

2.2.2 Adhesives

Two types of assemblies were created for this study: production type samples (P) bonded with 150μm of FM300-K cured at 444°K and repair type samples (R) bonded with 200μm of FM300-2M cured at 394°K. The FM300-K has an integrated knit carrier to facilitate its manipulation in the production facilities (Figure 2-15 a)). This net is not present inside the FM300-2M bonds. Moreover, the samples have been prepared according to Airbus process: for repair sample, the side of the composite laminate where the bond is applied is grinded all the way to the fibres. This step is not required when creating production type parts.

Hence, for repair sample, the carbon fibres are directly in contact with the epoxy bond because all the excess epoxy from the prepreg has been grinded away (Figure 2-15 b)). However, for production samples, the M21E epoxy is still present. The adherence properties now depend on an epoxy/epoxy interface (Figure 2-15 a)).
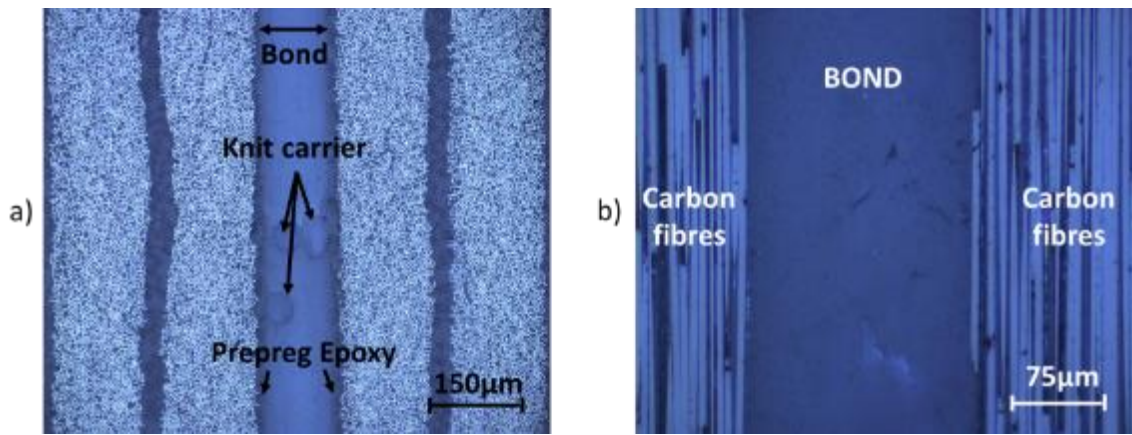
Figure 2-15 Photomicrographs of: a) The bond of a production sample b) The bond of a repair sample

2.2.3 Contaminations

Airbus defined two sets of contaminants, the one mainly found on production lines and the one typical from repair lines. A total of six contaminants have been selected, three per scenario. As for the Encomb project [107] different levels of contamination were set.

Figure 2-16 represents the different contamination scenarios. On top of the contaminated samples, reference ones were also manufactured. They will serve as standards to compare the results obtained with altered samples.

These contaminations are the most likely to appear on each the production and repair lines. Hence for the production scenario:

- Release agent: to ease up the de-moulding process of composite panel, a solution, release agent, is sprayed onto the mould before the part is cured. After the whole process, and the part removed from the mould, some traces of this solution can be found on the surface of the sample if not cleaned properly.
- Finger print: it can happen that finger print residues are left on the part during its manipulation. This contamination is local and is describe in DIN ISO 9022-12.
- Moisture: depending on the location of the manufacturer and/or the weather conditions or even the storage conditions, high humidity levels may be reached in the production line leading to water take-up. This water is later released during the curing process, weakening the bond strength.
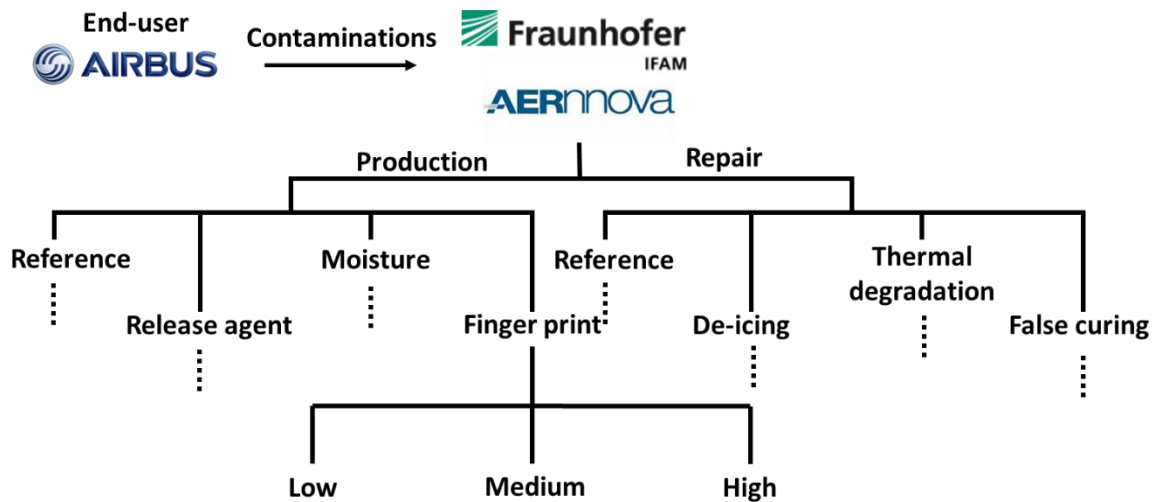
Figure 2-16 Diagram of the different ComBoNDT scenarios and their contaminations

For the repair scenario, three contaminants were also selected:

- De-icing fluid: during its life span, an aircraft may have to endure very cold temperatures. To prevent the wings from freezing, a de-icing fluid is applied on their surfaces. This fluid can penetrate through voids and leave residues deep inside of the structure. Hence, when grinding this area to apply a patch to fix the damage, one may have de-icer (DI) residues still on the surface.

- Thermal degradation: parts of the fuselage can be exposed to high temperature. Whether is it by mistake (heat sources placed too close), or due to an incident (lightning, fire, …), these high temperatures have a negative impact on the mechanical properties of the structure.

- Faulty curing: epoxy bonds need to be cured in order to be fully cross-linked. However, this curing may not always be homogeneous. Indeed, a misplacement of the heat blanket, or a bad insulation of the patched area during the curing cycle may generate a non-homogenous heat pattern, leading to various adherence levels on a same surface.

The three different contamination levels were defined based on adherence loss. A sample marked "low" has an adherence worth 95% of the adherence level of a reference sample, for a "medium" it is 90% and a "high", 80%. However, these values are purely theoretical at that point, a more exhaustive study on the adherence level is presented later in the manuscript.

The level of adherence loss that would qualify a bond as "weak" has been sets at around 20% by Airbus. This fits the description of a highly contaminated sample.

Results will be compared with Encomb data.

2.2.4 Sample Preparation

All ComBoNDT CFRP laminates were produced by Aernnova [132] and sent to the Fraunhofer Institute of Bremen (IFAM) for the contamination and eventually the bonding process.

To ensure the surface has been thoroughly cleaned, X-ray photoelectron spectroscopies (XPS) of the surfaces is done on three different locations. This technique is also later used to quantify the contamination level. XPS systems focalise an X-ray beam (~1,5kV) on the surface of sample at a given angle. The reflected electrons are then collected and analysed using an Electron Energy Analyser. A vacuum sealed environment is required for this technique to work. Subsequent data gives the atomic ration (at%) of a given element on the surface. To avoid heterogeneity problem, the IFAM took measurements on three different spots.

A five steps systematic treatment of the laminates was done by the IFAM to ensure no contaminant was left on the panels before the bonding.

1) First isopropanol wash of the surface to remove release agent (RA) traces as well as other soluble contaminants
2) Slight grind to make sure no contaminants are still trapped inside porosities
3) Water + isopropanol cleaning to remove grind dust and traces of contaminant
4) Another slight grid + water and isopropanol wash
5) Wiping the sample dry using methyl-ethyl-ketol (MEK)

XPS data showed that upon arriving from Aernnova, samples had between 3.8at% and 6.2at% of Si. Silicon is widely used in release agent solution. Hence, the at% of Si will be used as a contamination level reference [133]. The lower the value is, the cleaner the surface. The only exceptions are the MO contaminated samples. Instead of XPS measurement, water intake was measured to define the contamination level of the sample.

After the procedure described above, the atomic ratio was below 0.2at%. This amount being satisfactory, CFRP panels were cut to their final size: 90x90mm laminates.

2.2.5 Release Agent Scenario

A full description of the contamination process is presented here. Since the sample creation and assessment is comparable, regardless of the contaminant, other contamination will not be as thoroughly described as this one.

2.2.5.1 Contamination Process

The release agent solution, Frekote 700-NC, was diluted in heptane to obtain three different concentrations: 1%, 2% and 4%. Frekote was applied on the surface by deep-coating. To

ensure good homogeneity of contamination throughout the whole surface, IFAM set in place a special deep-coating process. The contaminated surface was then left to dry for 30 min at room temperature, before being heat treated at 80°C for one hour.

Three different XPS measurements were taken for each sample: at the top, at the centre and at the bottom of the plate. Indeed, usually during deep-coating, the substance applied on the surface tends to fall towards the bottom of the sample because of gravity. A specific process used by IFAM helps to avoid this effect.

From now on, and throughout the rest of this manuscript, contamination levels will be referred using number from 1 to 3, 1 being the lowest level of contamination and 3, the highest.

Silicium is highly present in Frekote 700-NC, hence Si XPS measurement are realised to assess the contamination level:

- RA-1: 3.2 (+/- 1.0) at% of Si
- RA-2: 5.1 (+/- 0.7) at% of Si
- RA-3: 6.2 (+/- 0.3) at% of Si

The bonding of the contaminated laminated and the reference one (i.e. not contaminated) was realised using the FM300K epoxy resin, cured in an autoclave at 171°C. It will be the same for all production samples

2.2.5.2 Weak Bond Status

The US obtained on the RA contaminated sample was already discussed and explained in 2.1.3. No apparent defect was spotted, validating the process used to create these samples. However, to assess the presence of weak bond, GIC and GIIC tests are also performed on samples coming from the same batch.

The mechanical test analysis was performed using 8 samples per contamination and contamination level. For each series, the maximum and minimum values were removed, resulting in Figure 2-17.

All values have been normalised by its reference sample. In this case, the release agent was a production line contaminant, it is thus compared with the production reference sample (P-RE).

The first observation that can be made concerns the level obtained using the GIC test. When considering the error bars, one can notice that the reference level, and the first two levels of contamination (low and medium) overlap. This test may not be, on its own, precise enough to properly asses the samples loss of adherence. Moreover, the highest degree of contamination level overlaps with the two other ones. Hence, if the general behaviour of the

contaminated samples tends to show a decrease in the adherence level with the increase of the contamination, it is not possible to clearly assess it.
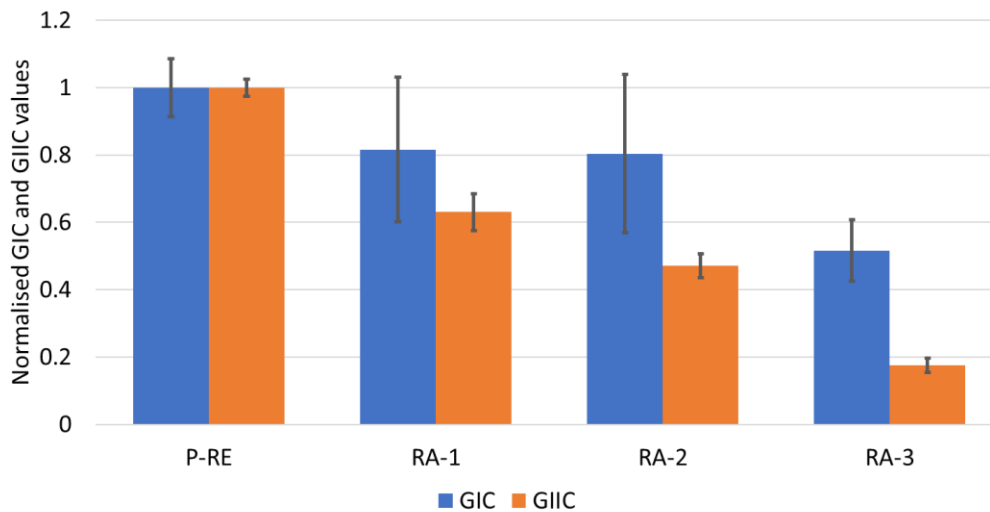
Figure 2-17 Normalised GIC and GIIC values for the production reference samples and the three different RA contamination levels - LTSM-UPAT

On the other hand, GIIC tests are much more replicable. On top of showing a clear decrease in the adherence level of the contaminated sample, errors bars do not overlap. These tests are much more conclusive than the GIC.

The GIC and GIIC behaviours displayed in the example of the release agent contamination can be generalised to the entirety of samples and contaminations, and these differences will not be further discussed.

The levels of adherence for the contaminated scenarios oscillated between 50 and 80% of the nominal adherence for the GIC test, and between 19 and 62% for GIIC test. For comparison purposes with the LASAT technique, the values from the GIC will be taken into account. Indeed, the load generated by the S-LASAT is comparable to the GIC (pure traction).

To summarize, no apparent defect was spotted using ultrasound and a mechanical loss was observed during mechanical testing. These samples have all the required characteristics of a weak bond and can be used as representative samples for the following experiments. All obtained results during the certification of RA contaminated samples are summarised in Table 2-4.

	Contamination level at% Si	US	GIC	GIIC	Weak bond representative
RA-1	3.2(+/-1.0)	Ok	81.6(+/-29) %	63.0(+/-8)%	Ok
RA-2	5.1(+/-0.7)	Ok	80.3(+/-33)%	47.2(+/-5)%	Ok
RA-3	6.2(+/-0.3)	Ok	51.6(+/-9)%	17.6(+/-3)%	Ok

Table 2-4 Summary of the release agent contamination procedure

2.2.6 Overall Results on Contaminated Samples Manufacturing

2.2.6.1 Moisture Contamination

To mimic different levels of moisture contamination, 3 different water-based solutions were placed inside of boxes heated at 80°C. Samples were dried, weighted and set in these boxes until their masses would not evolve anymore, i.e. until the sample were fully contaminated. They were then withdrawn and placed in 70°C with predefined humidity levels for at least two weeks. To avoid any external contamination, the samples were bonded to an untreated CFRP laminate as soon as they were taken out of the chamber.

Results of the procedure are displayed in Table 2-5.

	Contamination level mass% intake	US	GIC	GIIC	Weak bond representative
MO-1	0.4(+/-0.2)	Ok	106.8(+/-23) %	54.8(+/-6)%	Ok
MO-2	0.8(+/-0.1)	Ok	76.1(+/-25)%	27.0(+/-3)%	Ok
MO-3	1.4(+/-0.2)	Ok	91.6(+/-10)%	7.5(+/-0.4)%	Ok

Table 2-5 Summary of the moisture contamination procedure

This contamination showed to be very peculiar. Indeed, GIC tests did not show any decrease. This phenomenon has already been observed: the bond failure load would decrease up to a certain point and given a certain amount of water intake, it would rise back up to a plateau [134], [135]. It is however difficult to say whether this is the phenomenon observed here and further tests would be required.

Nevertheless, these samples are in agreement with the definition of weak bond in CFRP assemblies.

2.2.6.2 Finger Print Contamination

A standardised finger print solution (DIN ISO 9022-12) was used to mirror a FP contamination. It contains sodium chloride, urea, ammonium chloride, lactic acid, acetic acid, pyruvic acid, and butyric acid. The solution was diluted to obtain the desired adherence loss: low contamination was achieved by mixing 1 volume of solution with 9 volumes of demineralised water, the medium contamination was a 50/50 ratio, and the highest contamination was pure finger print solution (Table 2-6).

	Contamination level	US	GIC	GIIC	Weak bond representative
FP-1	0.2(+/-0.1) at% Na & 0.5(+/-0.1) at% Cl	Ok	99.8(+/-7) %	54.3(+/-6)%	Ok
FP-2	0.5(+/-0.1) at% Na & 0.9(+/-0.1) at% Cl	Ok	91.6(+/-17)%	32.4(+/-1)%	Ok
FP-3	0.7(+/-0.2) at% Na & 1.1(+/-0.1) at% Cl	Ok	60.7(+/-16)%	25.4(+/-8)%	Ok

Table 2-6 Summary of the finger print contamination procedure

To be as close from a real case of finger print contamination, the samples were only contaminated locally on an area roughly the size of a finger print. Thereby this contamination is not homogeneous throughout the whole sample

2.2.6.3 De-icing Fluid

The de-icer used was the Safeway KF developed by Clariant. The solution was diluted in demineralised water and applied, using a deep-coating method, with the following concentration (%vol): 2%, 7% and 10%. After pollution, the laminate was dried in a 40°C oven for 2 hours and let dry an addition 24h at room temperature (Table 2-7). The contaminated and healthy laminates are then bonded together using the FM300-2 epoxy bond, cured at 121°C in an autoclave. This step will be common to all repair scenario samples.

All samples are weak bond representative. This time however, the adherence values are rather far from the 80-95% range defined for the project

	Contamination level at% K	US	GIC	GIIC	Weak bond representative
DI-1	6.4(+/-1.8)	Ok	69.2(+/-13) %	43.9(+/-5)%	Ok
DI-2	10.9(+/-2.3)	Ok	63.0(+/-15)%	38.1(+/-2)%	Ok
DI-3	12.0(+/-1.4)	Ok	43.9(+/-12)%	17.2(+/-1)%	Ok

Table 2-7 Summary of the de-icing fluid contamination process

2.2.6.4 Thermal Degradation

The CFRP laminate was placed in an oven at a fixed temperature for 2h. It was then ground to the fibres before being bonded (Table 2-8).

	Temperature °C	US	GIC	GIIC	Weak bond representative
TD-1	220	Ok	67.6(+/-12) %	19.3(+/-1)%	Ok
TD-2	260	Ok	51.9(+/-13)%	12.5(+/-3)%	Ok
TD-3	280	Ok	58.7(+/-17)%	14.5(+/-1)%	Ok

Table 2-8 Summary of thermal degradation process for LASAT samples

It is important to underline that all samples were not equal. Indeed, the damage done by these heat exposures was not comparable from one sample to another, even when coming from the same batch. The samples created for the LASAT were the only set that pass the ultrasound test.
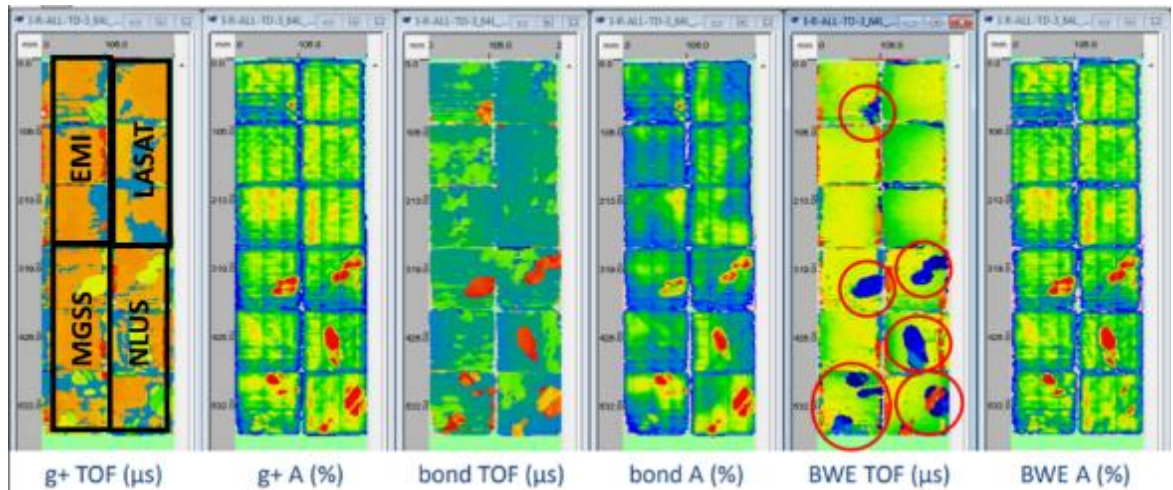
Figure 2-18 US scans of the TD samples produced for 4 techniques: EMI, MGSS, NLUS and LASAT – C-Scan realised in Airbus facilities

Figure 2-18 shows the US realised on bonded samples meant to be tested by EMI, MGSS, NLUSS and LASAT techniques. Each time, a sample for each contamination level was tested.

Samples for the LASAT technique are on the top right of the stack. As displayed by the results given by the back-wall echo signal, important disbondings where already present on the samples of all the techniques but LASAT. This sample passed the test in this case, but a direct comparison with the mechanical tests may not be relevant due to the huge discrepancies between the samples.

2.2.6.5 Faulty Curing

For this contamination, certain areas of the samples were pre-cured. This contamination is expected to drastically reduce the bond strength and has a high chance of creating kissing bonds i.e., weak bonds with no mechanical adherence at all.

	US	GIC	GIIC	Weak bond representative
FC-1	Fail	85.1(+/-11) %	53.6(+/-6)%	No
FC-2	Fail	84.4(+/-17)%	13.2(+/-4)%	No
FC-3	Fail	83.9(+/-10)%	17.8(+/-1)%	No

Table 2-9 Summary of the faulty curing contamination process

These are the only samples that did not pass the test (Table 2-9). If a decrease in the adherence level was indeed spotted by the mechanical tests, the samples were initially debonded (Figure 2-19). These would have been spotted by the standard Airbus verification procedure, making these samples not representative of a weak bond induced by a faulty curing.
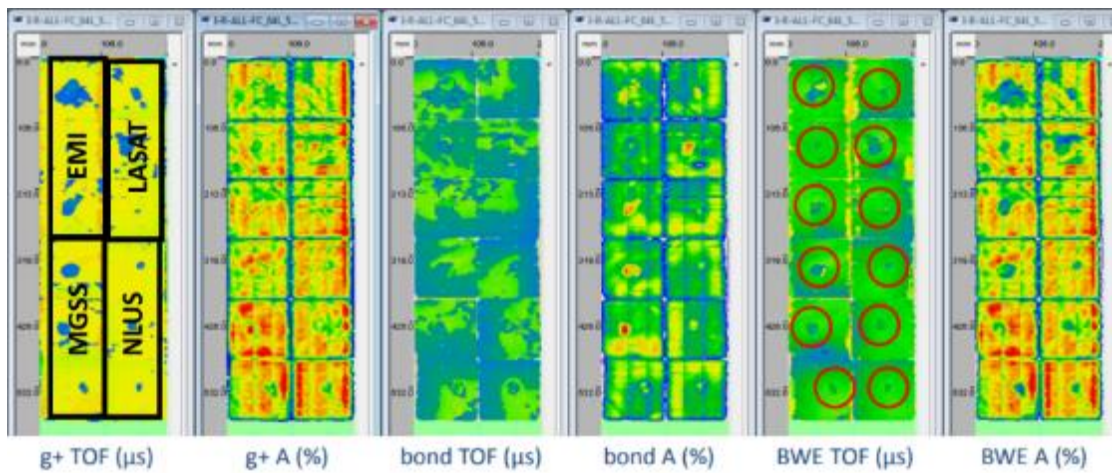
Figure 2-19 US scan of the FC samples produced for 4 techniques: EMI, MGSS, NLUS and LASAT – C-Scan realised in Airbus facilities

2.2.6.6 TD + DI for Scarfed Samples

The pilot samples were all done using mix contamination. As explained, two bond geometries are tested: a curved one and a scarfed one (Figure 2-12). The curved samples will be associated with the production scenario while the scarfed samples will face contaminant found on repair lines. Two levels of contamination were produced for each scenario.

The two selected combinations were: TD1+DI1 (first contamination level for both TD and DI), and TD1+DI2 (first level of thermal contamination and second level for the DI).

Samples were first heat treated at 220°C for 2h. Then the samples were ground with a 1:17 ratio (for every 17mm, the mill would go down 1mm). The scarfed surfaces were then manually grinded and cleaned using MEK. The laminate was then dip-coating in a de-icer/water mixture and bonded to its reference pair. A summary is represented Table 2-10

	Contamination level	US	GIC	Weak bond representative
TD-1 + DI-1	220°C + 6.4(+/-1.8) at% K	Ok	70.1(+/-22) %	Ok
TD-1 + DI-2	220°C + 10.9(+/-2.3)	Ok	47.5(+/-8)%	Ok

Table 2-10 Summary of the TD+DI contamination process

2.2.6.7 FP + RA for Curved Samples

As for the coupon samples, the release agent was applied through the dip-coating of the laminate into a Frekote solution at a given concentration. The laminate was then left to dry for 30 minutes at room temperature before putting it in a 80°C oven for 1h. The finger print solution was then applied on the surface, before bonding the contaminated laminate and its reference counterpart (Table 2-11).

	Contamination level	US	GIC	Weak bond representative
RA-1 + FP-3	0.7(+/-0.1) at% Na & 1.1(+/-0.2) at% Cl + 3.2(+/-1.0) at% Si	Fail	52.3(+/-13) %	Ok
RA-2 + FP-3	0.7(+/-0.1) at% Na & 1.1(+/-0.2) at% Cl + 5.1(+/-0.07 at% Si	Fail	62.6(+/-14)%	Ok

Table 2-11Summary of the RA+FP contamination process

The most contaminated case seems to have higher adherence properties. With no other comparison tool than the GIC tests it is however difficult to conclude.
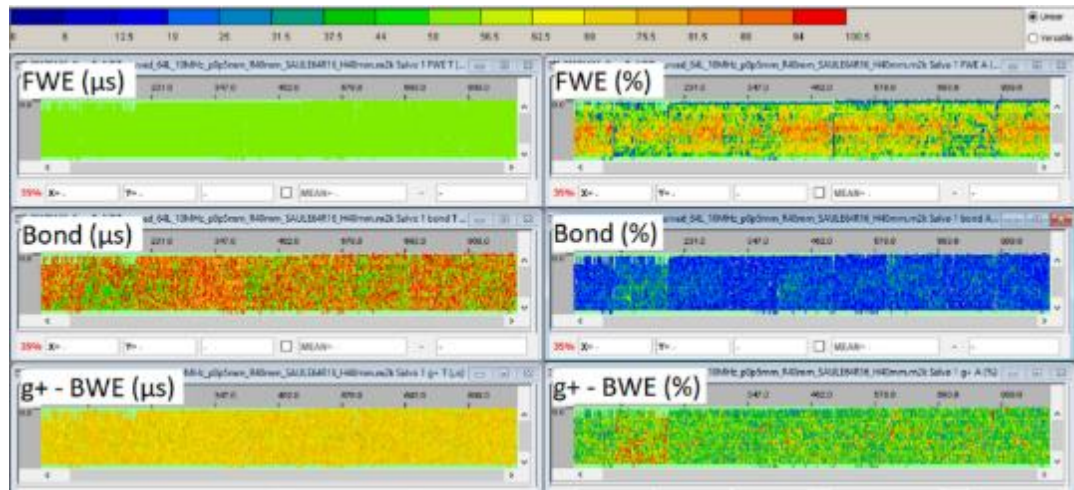
Figure 2-20 US obtained for the curved samples - C-Scan realised in Airbus facilities

More critically, none of the samples passed the US test. Delamination was observed across the whole bonding surface. As shown by the disparity of signal in the Figure 2-20, all samples showed important debonding. These samples are not valid and will not be tested using S-LASAT.

2.2.7 Comparison with ENCOMB

Two scenarios are common between ComBoNDT and ENCOMB: the release agent (labelled RE) and the moisture contamination (MO). Table 2-12 and Table 2-13 sum up both these contaminations and their outcomes.

	Contamination level at% Si	US	GIC	Weak bond representative
Enc RA-1	2.2(+/-0.3)	Ok	99.0(+/-11) %	Ok
Enc RA-2	6.1(+/-0.2)	Ok	40.9(+/-7) %	Ok
Enc RA-3	8.2(+/-0.8)	Ok	5.7(+/-2) %	Ok
Enc RA-4	10.5(+/-0.3)	Ok	3.8(+/-3)%	Ok

Table 2-12 Summary of ENCOMB release agent contamination

	Contamination level mass% intake	US	GIC	Weak bond representative
Enc MO-1	0.46(+/-0.01)	Ok	105.3(+/-17) %	Ok
Enc MO-2	0.84(+/-0.05)	Ok	85.2(+/-10) %	Ok
Enc MO-3	1.19(+/-0.01)	Ok	74.1(+/-9) %	Ok
Enc MO-4	1.29(+/-0.01)	Ok	82.5(+/-4)%	Ok

Table 2-13 Summary of ENCOMB moisture contamination scenario

Sample used for GIC tests were symmetrical with a stacking sequence comparable to ComBoNDT: [0°/90°/0°/90°]$_S$. It is important to mention that, in ENCOMB project, samples used to assess the capability of each technology had slightly different configuration. Indeed, the bonded samples were not symmetrical. Their layup was [0°, 90°, 0°] on one side of the bond, and [0°, 90°, 0°, 90°, 0°] on the other side and the CFRP used was the T700/M21. The adhesive was the same for the two projects.

Figure 2-21 shows the amount of contaminant used and the GIC results match from one project to another (given the error bars).

Figure 2-21 compares the normalised adherence levels of the RA contamination throughout the two projects. If the first contamination of ENCOMB was higher than the one from ComBoNDT, all the other adherence levels are between the RE-1 and RE-2.

The adherence levels of the sample series associated with the moisture contamination are comparable between ENCOMB and ComBoNDT (Figure 2-22). Moreover, in both cases the adherence decreases before increasing pass a certain amount of contamination.
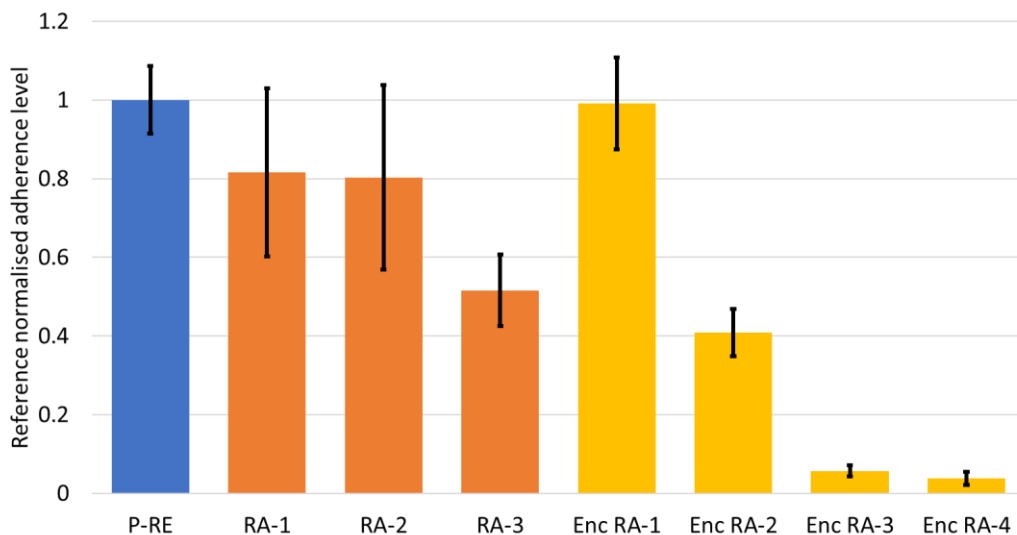
Figure 2-21 Comparison between a reference sample (blue bar), ComBoNDT RA contamination levels (orange bars) and ENCOMB levels (yellow bars). LTSM_UPAT
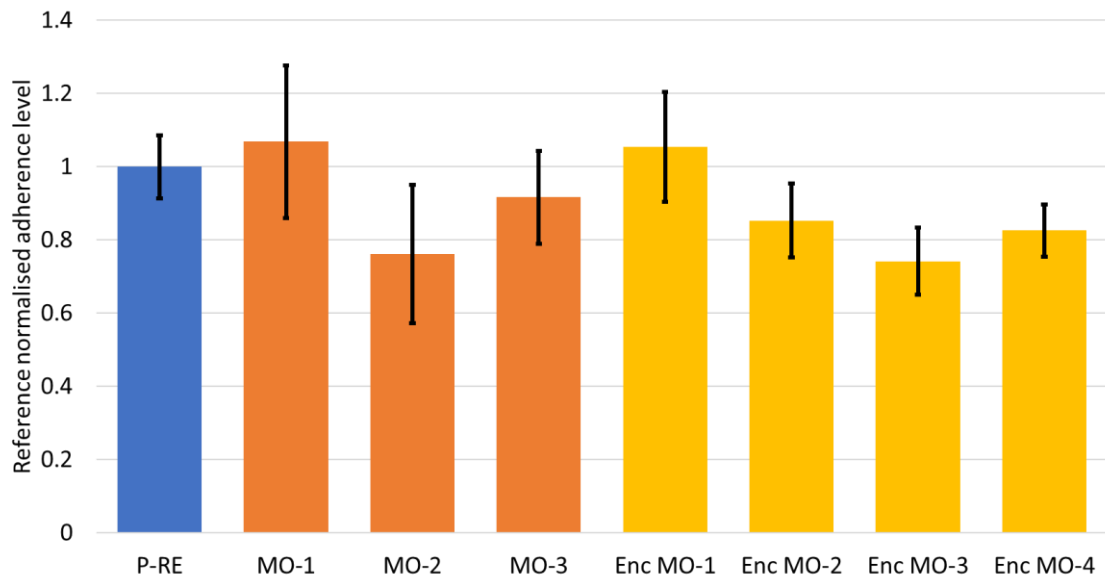
Figure 2-22 Comparison between a reference sample (blue bar), ComBoNDT MO contamination levels (orange bars) and ENCOMB levels (yellow bars). LTSM_UPAT

2.3 Real Parts

2.3.1 Production

A350 panels have been produced / recovered to test the technique using real parts. The production sample is an 800x800x1.5 mm CFRP plate on which two 700x50x1.7 CFRP stiffeners were bonded (Figure 2-23). The plate is made of 14 prepreg layers with the following lay-up: $[+45/90/0/90/+45/0/90]_S$. On one half, the stiffeners have been bonded without contamination, and on the other half of the plate both the de-icing fluid and the finger print solution have been applied on the stiffeners' surface before the bond. This is the type of assembly that can be found on the wings of an airplane.
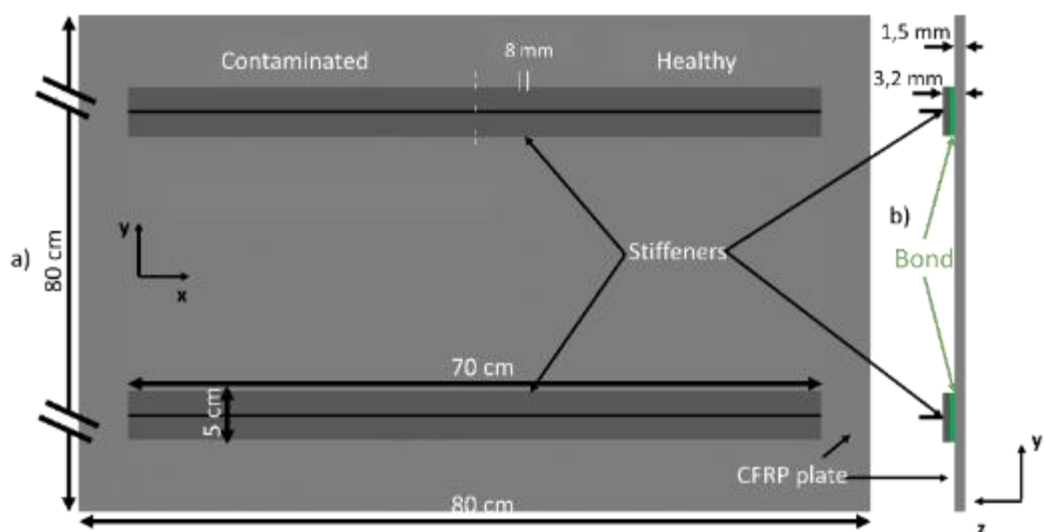
Figure 2-23 Diagram of the production panel

2.3.2 Repair

The repair panel has been cut out of a A350 structure. The middle part of the sample has been grinded all the way to the fibres in a conic shape. Half of the surface was contaminated with both finger print and de-icing fluid solutions (Figure 2-24b)). The hole created in the panel was then patched, starting from the centre to the edge, with the missing CFRP ring (cf. Figure 2-24 a)) while keeping the original lay-up of the part (ring diameter and orientation in Figure 2-24 a)). The composite was then cured by GMI's tool ANITA EZ0901 hot bonder.
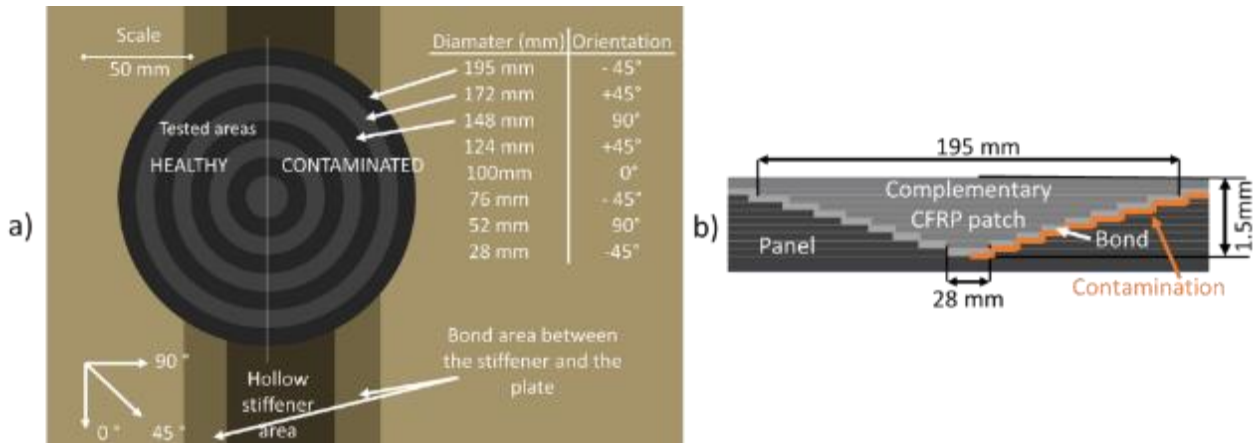
Figure 2-24 Diagram of the repair panel

Chapter 3. SYMMETRICAL LASAT OPTIMISATION

TABLE OF CONTENTS

3.1 Introduction

This chapter focuses on the first S-LASAT experiments realised before adding the DOEs. As shown in the previous chapter, several aspects of the LASAT have already been investigated and can be used for symmetrical testing.

Hence, in this section a first set of coupon samples are tested to assess the capability of the technology. There are two main goals for these experiments. First, define the sensibility of the process:

- Can it detect every type of contaminations?
- Can it distinguish different levels of contamination?
- How precise should a S-LASAT setup be?

Second, analyse the effect of the technique on the material:

- Is the process Non-destructive ?
- How did the mechanical properties of the material evolve?
- What kind of damage are generated inside of a sample that did no pass the test?

To help in the overall apprehension of the physics behind S-LASAT, numerical simulations are performed using Abaqus.

3.2 First Test on Coupon Samples

The initial setup is being describe in this section as well as the results obtained using both US and photomicrograph as post mortem inspection tools. The goal is to find the optimal parameters to test the coupon samples as well as defining the current limitations of Hephaïstos platform.

3.2.1 Experimental Setup

Each sample is 90mm by 90mm long. Heterogeneity problems on the border of the sample can arise because of the cutting process (creation of delamination, destruction of fibres, …) or the contamination. To avoid them, a margin of 5mm is left untouched around the sample.

The 80mm by 80mm square left to test is divided in sixteen 2cm by 2cm squares (Figure 3-1 a)). A predefined shot pattern was defined, ranging from 5% of the laser's maximum energy, up to 95%., with a step of 6% (Figure 3-1 b)).
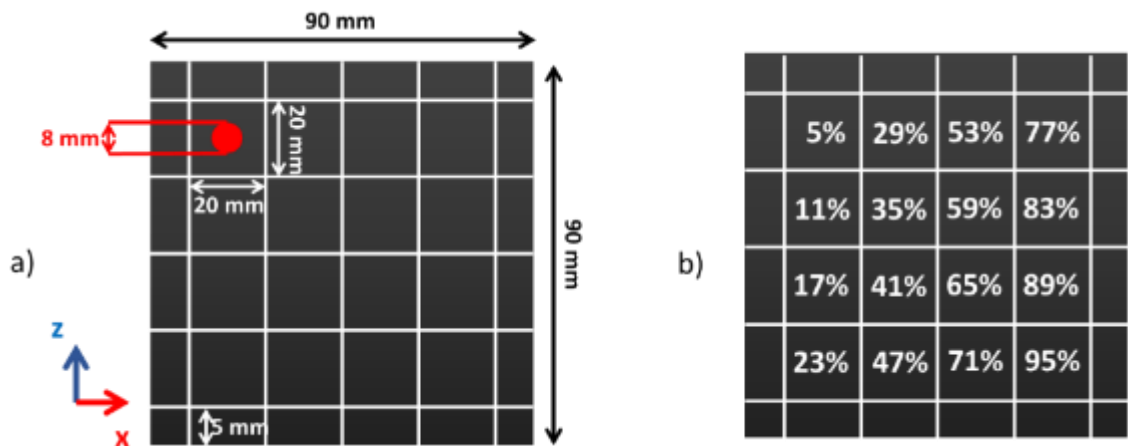
Figure 3-1 Diagram of the division of a sample in 16 equal areas b) Shot energy distribution

A diagram of the experimental setup is presented in Figure 3-2 a). Each sample was covered with aluminium tape (cf. chap 2). To ensure a proper confinement, two water trickles were set on both sides (Figure 3-2 b). No time delay has been set since the bond is in the middle of the sample.
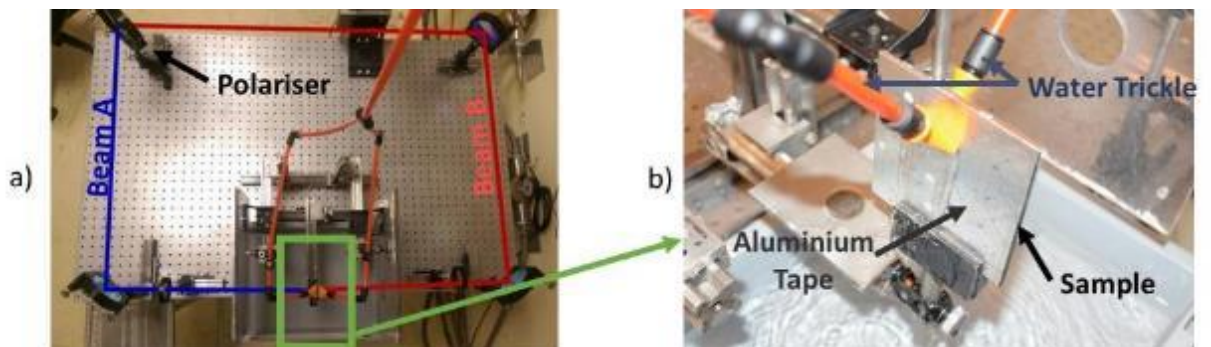
Figure 3-2 a) Experimental setup b) Close up on the sample after preparation

Once all samples were shot, initial results were obtained using the Gekko US device. They were then sent to Airbus to be confirmed and refined at their facilities.

3.2.2 Results

Results obtained using US scans can be classified in three main groups:

- No damage is spotted. This area of the coupon was not affected by S-LASAT.
- A debonding is spotted around the bond line. Its first appearance defines the bond threshold.
- Delaminations are spotted in the composite laminates. As for the bond threshold, the energy they are first created at will be referred to as the laminate threshold.

Two main points must be validated to confirm S-LASAT detection capability for a contamination:

1) the bond threshold needs to be lower than the laminate threshold. In the opposite scenario, it would be impossible to open the bond without damaging the composite structure, rendering the test destructive.

2) the bond threshold of a contaminated sample needs to be lower than the one from a healthy sample. Indeed, weak bonds are defined by a loss of mechanical properties. Hence, poorly bonded laminates should require less energy to be opened.

3.2.2.1 Reference Samples

Figure 3-3 a) is a C-Scan of a production reference sample after it was completely tested and Figure 3-3 b-c-d are the associated B scans. The first damage was spotted at shot 5, which was $0,34GW/cm^2$ per beam. Figure 3-3 b) shows a B-Scan done with face B (facing beam B) on top, right below the US probe, and face A at the bottom. The damage is characterised by a loss of signal around the bond line (see red circle labelled 5 in Figure 3-3 b), as well as a "shadow" on face A (blue circle) due to ultrasound occultation. No damage is spotted before the bond line. US spatial accuracy (around 150µm) is not good enough to allow a proper positioning of the damage on the bond. It is impossible to state currently whether the damage was inside of the bond, or at the interface between the bond and a CFRP laminate.
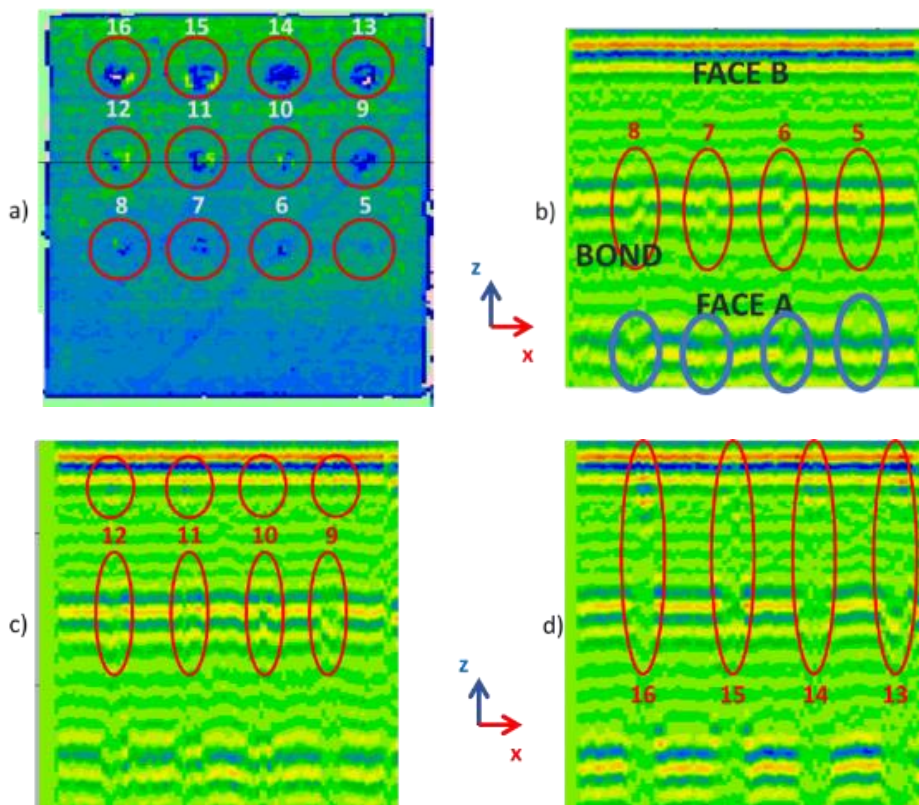
Figure 3-3 a) C-Scan of the production reference's sample b) B-Scan of shots 5 to 8 c) B-Scan of shots 9 to 12 d) B-Scan of shots 13 to 16

Starting from shot n°9 (0,73 GW/cm² per beam), a damage seems to appear on the front face. This damage is done by beam A which travelled up to face B. The laser beam was too energetic, and the tensile strength created on what was referred to as "secondary tensile stress location" in chapter 2 was high enough to generate a delamination in the CFRP laminate.

Once US detect a delamination, every default that may appear in the wake of that damage is hidden. Hence, after shot n°5, it is not possible to assess whether there is a delamination on face A or not. Thereby, US were also realised with face A on the top. Results of both studies are represented in Figure 3-4.
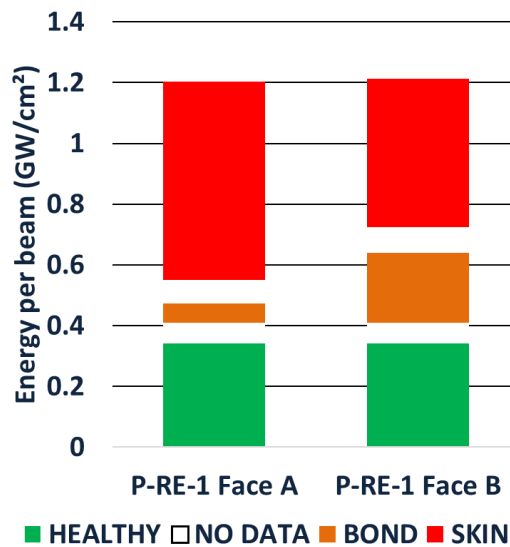
Figure 3-4 Summary of US results done from both faces for the production reference sample

The green bar represents the energy that, according to US, did not altered the coupon. The orange area shows the energy range where only the bond was damaged, and the red one represents energy levels that must not be reached because delaminations start to appear in the laminate. The blank areas in between labelled "no data" are due to the step based system used during this study. For example, in this case, a default on the bond line was spotted for shot n°5 while nothing was seen for shot n°4. It is however impossible to deduce the coupon state with an energy in between these two points.

These results show it is possible to only open a healthy bond, without damaging the CFRP laminates. This could not be achieved previously when using a single shot setup.

Both laminates are supposed to be the same, however, a big discrepancy between the laminate threshold was found. Face B was opened for intensity of 0,73 GW/cm² per beam and face A only at 0,53 GW/cm² per beam. There are two possibilities to explain this result: heterogeneities within the laminate structures, or a problem with the load generation. Indeed it has been noticed that the energy repartition differs from beam A to beam B (see chap.2).

Figure 3-5 shows the results obtained for the repair reference sample.
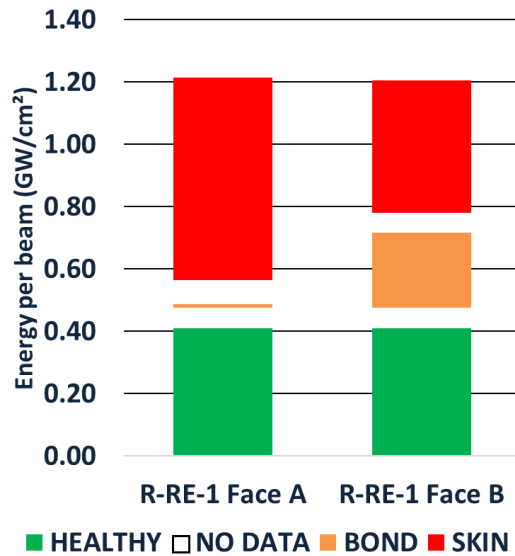
Figure 3-5 Summary of US results done from both faces for the repair reference sample

The same observations as for the production coupon can be made: there is a clear bond threshold (0,50 GW/cm²) however the laminate threshold varies, 0,57 GW/cm² per beam for face A, and 0,79 for face B.

3.2.2.2 Production Samples

Figure 3-6 displays results obtained for all the production contaminations: release agent (RA), moisture (MO) and finger print (FP). The red line shows the bond threshold for the reference sample. These results were obtained by scanning with face A on top.

Figure 3-6 shows all but one sample have a bond threshold equal to or lower than the reference sample's one. It is thus impossible to differentiate a healthy sample from these contaminated ones.
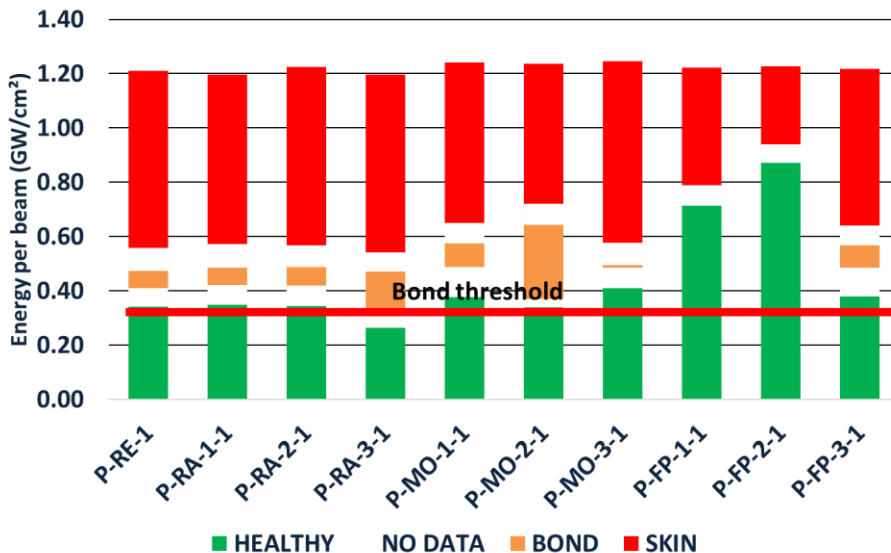
Figure 3-6 Results for production coupons, scanned from face A

Moreover, the laminate threshold is very different from one sample to another, raising again the question of the material homogeneity or the mechanical loading applied to the samples.

In some cases, the technique was not able to open the bond without damaging the skin. This is the case for example for the first and second level of finger print contamination (FP-1 and FP-2), where no orange bar is present in the graph.

No significant results were found during this experiment, regardless of the contaminant, or the contamination level.

3.2.2.3 Repair Samples

Figure 3-7 summarises results for the repair samples: de-icing fluid (DI), thermal degradation (TD) and faulty curing (FC).

In most cases, the bond threshold of contaminated samples is below the reference. The only exceptions are the lowest level of di-icing contamination, and the faulty cured samples. However, as seen in chapter 2, FC samples showed inherent delaminations after their creation, so results coming from these coupons need to be analysed with care.

Moreover, for the DI coupons, a decrease of the bond threshold with the increase of the contamination level can be observed. Same with the thermal degradation samples.

However, the same observations cannot be done when scanning the samples from face B (Figure 3-8 b). The second level of DI contamination displayed a higher bond threshold than when the scan was performed from face A. Moreover, where FC-1 and FC-2 did not seem to have a bond threshold, a clear bond opening level can be identified in Figure 3-8 b.
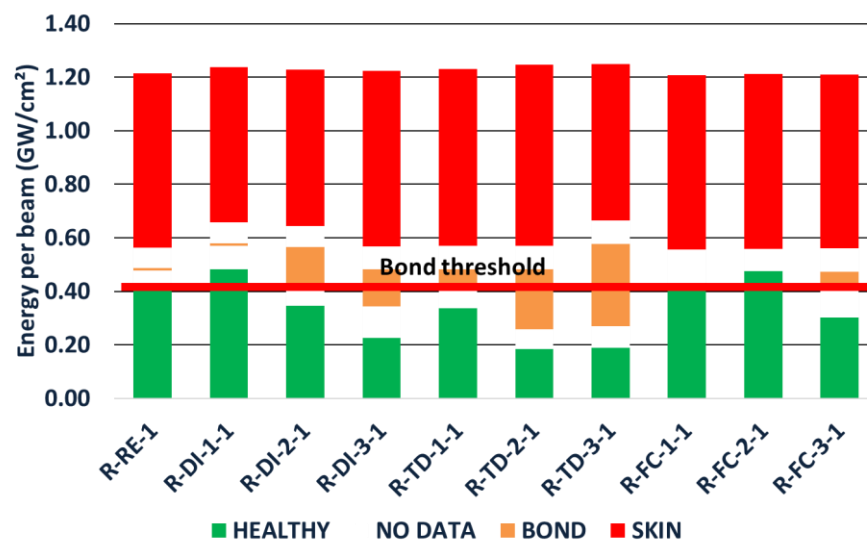
Figure 3-7 Results for repair coupons, scanned from face A
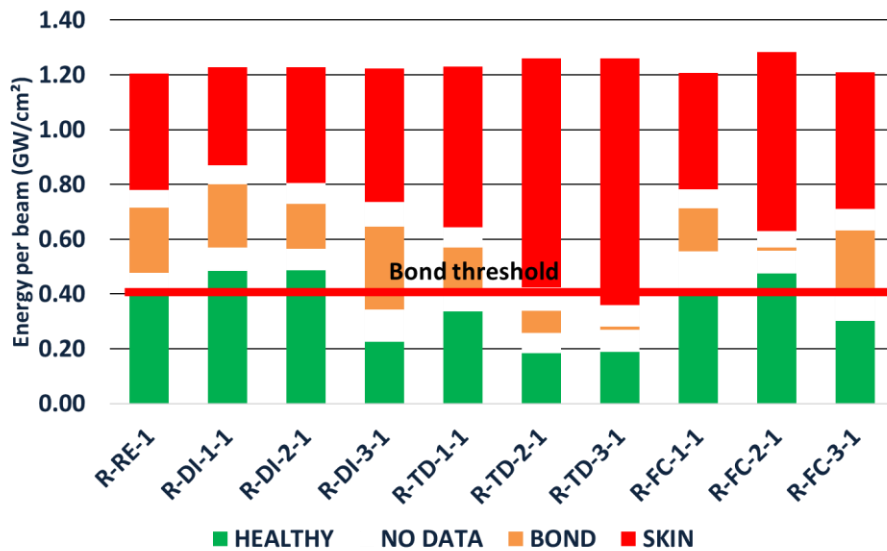
Figure 3-8 Results for repair coupons, scanned from face B

The laminate threshold is once again erratic, and no clear trend can be found. Those significant differences may underline a problem with US as a post shot analysis. The technique may not be robust enough for LASAT applications, failing at spotting small defects.

3.2.3 Photomicrographs

3.2.3.1 Observations

To validate ultrasounds scanning as a mean to assess the structure integrity post laser shock, 4 areas per samples were selected to be analysed through a microscope: the area right before the bond threshold, the one at the bond threshold. Same for the laminate threshold, one shot before, and the one at the limit.

The goal is to verify if US are sensitive enough to detect defaults at their first appearance, or if what is here defined as the threshold is not the initial default.

Each selected area was cut in half, cold mounted and polished. Because composite fibres are harder than the epoxy resin, a specific polishing technique was used to avoid smearing [136].

Figure 3-9 is a summary of the results obtained for the RA-1 sample. On the left, the results obtained using ultrasound are plotted. Photomicrograph observations are displayed in the middle column and observations are positioned, and scaled, on the diagram on the right.

The shot right below the bond threshold did not show any delamination. However, at the threshold, a very light defect was spotted. Its pattern resembles a closed delamination. This could be due to the high stiffness of CFRP materials. Indeed, if the energy is barely above the

threshold, the delamination may close again after the passing of the shockwave, becoming hardly visible.

Moreover, the delamination is very small and off-centered, which does not fit the observations made by Ecault when using the single shots setting. It is also important to note the debonding occurred on the contaminated surface.

When reaching face A threshold, delaminations start to appear inside the CFRP laminate itself, while no default is visible on the bond line. This default was generated by the shock coming from beam B, which bounced out of face A to create a secondary tensile stress area (see chap. 2). Since part of the shock energy was used to generate this delamination, when the reflection of beam A and beam B later criss-crosses to generate another high tensile stress area, the energy is not high enough to induce a delamination within the bond, hence the disappearance of the delamination around the bond.

However later, for an intensity of 0,88GW/cm^2, delaminations were spotted both in face A laminate and along the bond line. Despite the energy loss due to the face A delamination, enough tensile stress was created during both beam recombination at the bond line.

Equivalent observations can be done for the delamination on face B.
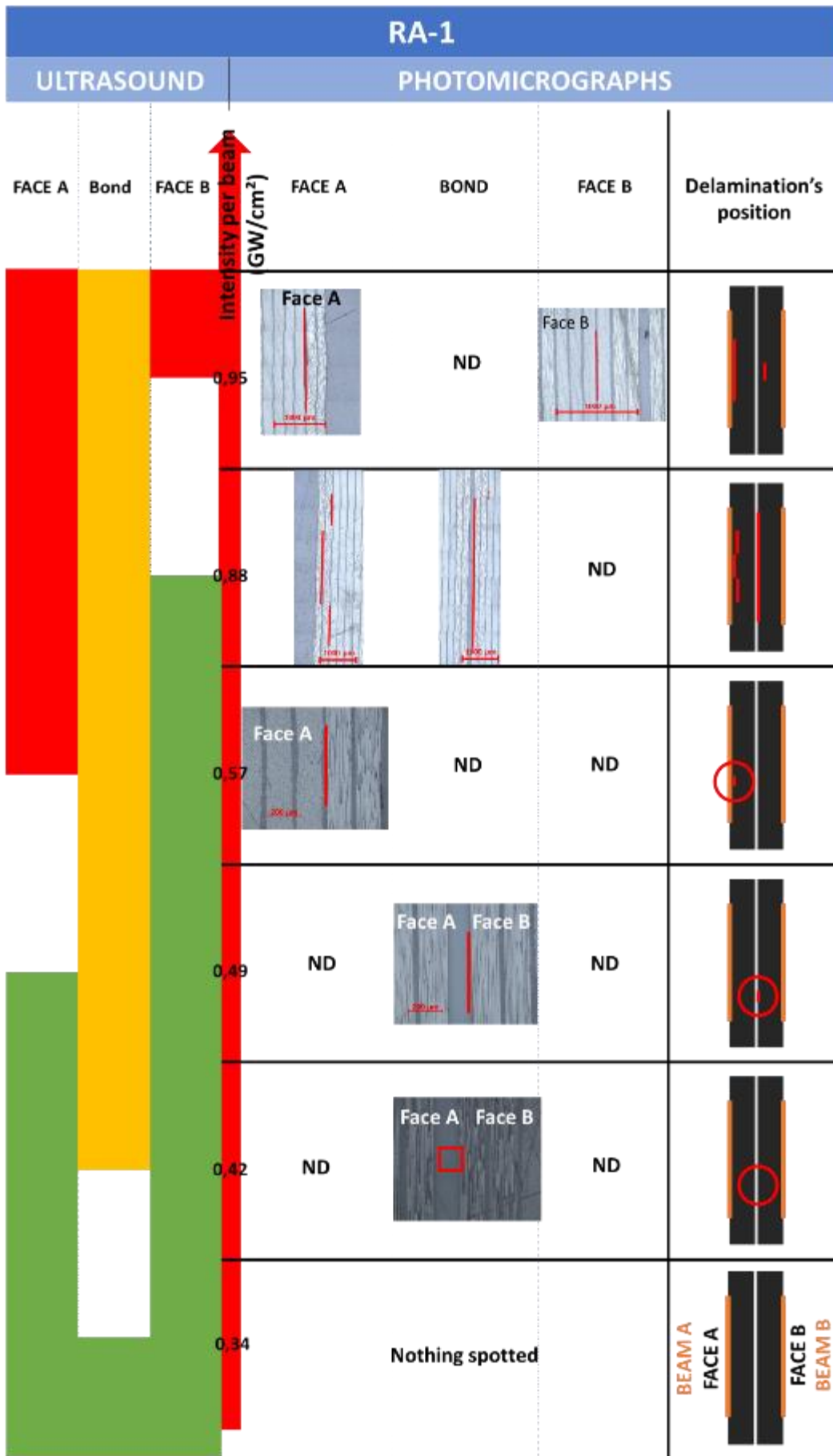
Figure 3-9 Summary of the micrographs obtained for the lowest level of release agent pollution

3.2.3.2 Discussion

For most of the samples, data gathered using photomicrographs were incomplete. As shown with the RA-1 sample, defect can become very small and hard to detect. Moreover, even when using a specific technique, smearing can quickly appear if the sample is polished for a long time.

To better analyse these defaults, some samples were scanned using a micro-CT scan. However, as shown by the micrographs, the delaminations are very small, and the size of the sample limited the CT resolution at around 12μm/voxel. Hence, apart from large defaults also seen using photomicrographs, the μCT-scan did not help to spot delaminations.

However, all defects spotted using photomicrographs were also spotted with US. Only the smaller ones, around thresholds, would not most of the time be seen using a photomicrograph. Thereby, even if only partial, this study showed that US were at least as effective as more direct method yet requiring far less preparation. US are validated as a mean of assessing the state of the sample post laser shock.

This study however revealed a core problem: the size and location of delaminations are not as expected. They are off-centered and smaller. As shown in chapter 2, without DOE, the initial energy distribution over the beam surface is erratic. This also implies the pressure applied on the sample is not uniform. The observations made using photomicrographs could be explained by significant local disparities between the applied load.

Indeed, it is highly probable that debondings or delaminations are first created by these high local intensity areas. Moreover, if for example, the top 20% intensity area from beam A only partially matches the one from beam B, the tensile stress area created by the symmetrical shot after the shock waves recombination could become very small, leading to damages that could barely be seen.

This initial experiment combined with US and photomicrograph assessments showed two main problems for S-LASAT in its current state:

- The damage threshold for the skin or the bond is unclear
- It is currently impossible to differentiate a healthy bond from a contaminated one

In order to better understand these current limitations, the parameters with the biggest influence on the tensile load generation (both the load intensity and location) need to be isolated, and their effects understood.

3.3 Numerical Study of the Process Parameters Influence

To better understand the way shockwaves are propagating through the sample, a Finite Element Analysis (FEA) of the phenomenon is realised. Its goal is to study whether the threshold detection problem is due to shockwave generation with the current laser setup or not. The main challenge with this numerical study is the high strain rates created by the laser shock used of S-LASAT. Indeed, these impacts are classified as High Velocity Impacts (HVI) and materials require specific constitutive law to model this phenomenon.

3.3.1 State of the Art of High Velocity Impact on CFRP

3.3.1.1 Generalities

The simulation of CFRP material under HVI is being investigated for almost two decades [137]. Many approaches exist, yet none of them seem to be fully able to completely describe the material behaviour, especially under the loadings it faces under laser shock. The lack of data is further enhanced by the high strain rate ($10^7 \ s^{-1}$) generated by laser shocks, which are 2 orders of magnitude higher than more conventional studies such as ballistic impacts.

For isotropic material it is common to use Equations of State (EOS) as explained in chapter I. Several studies have tried to use them for composite materials [138], [139]. However, because for orthotropic and anisotropic material the strain is not uniform for all three principal directions, specific formulations are required. Experimental as well as numerical studies are required to get all the needed parameters, and none of them can be neglected when simulating a HVI. Moreover, even the procedure to determine these values is not fully set as the difference between the two papers from Ryan and Wicklein shows ([138], [139]).

Moreover, numerous studies have shown the importance of the strain rate effect [140]–[142], however as described by Jacob and al. [143], results seem to depend on the layup and the type of FRP used. However, in the case of CFRP, studies seem to agree on the high dependence of both the stiffness and the strength of the material.

There are constitutive laws, used for epoxy material, that take into account the strain rate such as the Cowper-Symonds law [144]:

$$\sigma_D = \sigma_S \left(1 + \left(\frac{\dot{\epsilon}}{D} \right)^{\frac{1}{q}} \right) \tag{3.18}$$

Where σ_D is the dynamic yield stress, σ_S the static yield stress, $\dot{\epsilon}$ the strain rate and D and q two constants. This law simply adds a term to the standard equation to consider viscoplastic deformation[145].

To completely go through composite numerical modelling, the topic of damage initiation and propagation should be dealt with. However, in this study no damage will be taken into account (mechanical stresses below damage threshold).

3.3.1.2 Ecault's Model [107]

Ecault based his work on LS-DYNA software. This numerical code, well known for its capacities to manage crashes and shock propagation has predefined constitutive laws [146]. He used the MAT_022_COMPOSITE_DAMAGE which is an orthotropic elastic constitutive law [107]. The intralaminar damage model associated is the Chang-Chang criterion [147], [148]. The interface between each layer is defined by the AUTOMATIC_SURFACE_TO_SURFACE_TIEBREAK law (Figure 3-10 a)). This law has two main components:

- a surface to surface penalty contact law: when a layer is pushed inside another layer, numerical springs are created to limit the penetration. The spring stiffness is defined by a pressure-overclosure law linking the pullback force to the penetration depth [149]
- a tiebreak law: when equation (3.19) is fulfilled, the interface strength linearly decreases up to the point it is null.

$$\left(\frac{|\sigma_n|}{\sigma_N}\right)^2 + \left(\frac{|\sigma_s|}{\sigma_S}\right)^2 \geq 1 \tag{3.19}$$

To represent a full stack of composite, he used 3D quadratic solid element, with a mesh size around 5µm. The stack was only 1 element thick with symmetry properties on both sides.

The spatial loading is top-hat like, but with the pressure decreasing following stiff slope to avoid singular points with high shear stress variation (Figure 3-10 b).
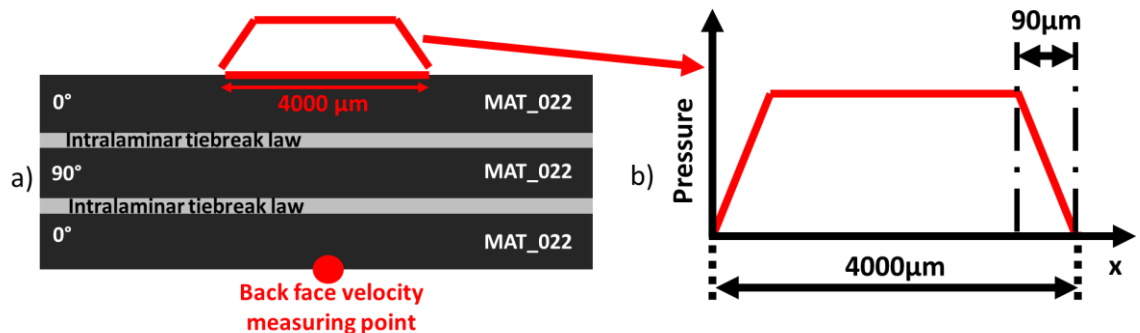
Figure 3-10 Representation of a 3 plies laminate with the laws associated to each part b) Spatial distribution of the laser intensity

Because the material law used is not strain rate dependant, Ecault developed a procedure to find the proper load and material parameters[150]. A factor of 0.7 was applied on Fab-

bro's formula to determine the generated pressure (see chap. I) to account for several experimental variations from the ideal case. Each important material parameter (especially Young's moduli) were then tuned to properly depict the state of the material under shock.

All calibrations were done on a 2 plies composite material by comparing the numerical and experimental data for the back-face velocity (Figure 3-10 a). After the correct parameters were set, the model was successfully compared with other experiments, this time done on a 7 layers CFRP laminate and a bonded CFRP structure, validating the numerical model. It also showed good results regardless of the input pressure and was able to properly describe the damage initiation within the structures

However, this model has one drawback. As specified by Ecault, it depends on the laser source parameters, especially its pulse. Nevertheless, this point needs to be nuanced in the case of the LASAT. Indeed, for LASAT application, the pulse duration is in most cases constant.

3.3.1.3 Metoui's Model

Metoui created a model in Abaqus, based on VUMAT to better describe the material under a laser shock.

In his work, Rozycki [145] showed that by adding a natural logarithmic law (ln) to the material constants, a good agreement was obtained. The Young's moduli were described using equation (3.20) :

$$E(\dot{\epsilon}, \eta) = E_0(1 + F) \tag{3.20}$$

With F a viscosity function described by:

$$F = 1 + C \cdot ln\left(\frac{\dot{\epsilon}}{\dot{\epsilon}_{ref}}\right) + ln(\eta) \tag{3.21}$$

Where C is a strain rate constant, $\dot{\epsilon}$ the strain rate, $\dot{\epsilon}_{ref}$ a reference strain rate and η the viscosity coefficient.

Given the very high strain rates generated under a laser shock all the terms but the strain rate based one could be simplified in equation (3.21), giving equation (3.22):

$$\{E(\dot{\epsilon})\} = \{E_0\}\left(1 + \{C\}\ln\left(\frac{\{\dot{\epsilon}\}}{\{\dot{\epsilon}_{Ref}\}}\right)\right) \tag{3.22}$$

With

$$\{E(\dot{\epsilon})\} = \begin{Bmatrix} E_1 \\ E_2 \\ E_3 \\ G_{12} \\ G_{23} \\ G_{13} \end{Bmatrix}, \quad \{C\} = \begin{Bmatrix} C_2 \\ C_3 \\ C_3 \\ C_4 \\ C_4 \\ C_4 \end{Bmatrix}, \text{and} \quad \{\dot{\epsilon}\} = \begin{Bmatrix} \dot{\epsilon}_1 \\ \dot{\epsilon}_2 \\ \dot{\epsilon}_3 \\ \dot{\epsilon}_{12} \\ \dot{\epsilon}_{23} \\ \dot{\epsilon}_{13} \end{Bmatrix}$$

Where E_1 is the Young's modulus in the fibre's direction, E_2 and E_3 in the transverse direction, and G_{12}, G_{23} and G_{13} the shear modulus in each plane. The same is for $\dot{\epsilon}$, which stands for the strain rate in the given directions and plane. Last, the C_X parameters are strain rate constants, specific to each material.

This is for example the formulation used for LS-Dyna's MAT_162 law. It is interesting to point out that the same associations were made by Ecault in his model: E_1 has its own constant and E_2 and E_3 also have their own constant they share.

The same way, the material strength is also defined as strain rate dependant using the following equation:

$$\{S(\dot{\epsilon})\} = \{S_0\}\left(1 + \{C_1\}\ln\left(\frac{\{\dot{\epsilon}\}}{\{\dot{\epsilon}_{Ref}\}}\right)\right) \tag{3.23}$$

With

$$\{S(\dot{\epsilon})\} = \begin{Bmatrix} X_T \\ X_C \\ Y_T \\ Y_C \\ Z_T \\ Z_C \\ S_L \\ S_H \end{Bmatrix} \quad \text{and} \quad \{\dot{\epsilon}\} = \begin{Bmatrix} \dot{\epsilon}_1 \\ \dot{\epsilon}_1 \\ \dot{\epsilon}_2 \\ \dot{\epsilon}_2 \\ \dot{\epsilon}_3 \\ \dot{\epsilon}_3 \\ \dot{\epsilon}_{12} \\ \sqrt{\dot{\epsilon}_{13}^2 + \dot{\epsilon}_{23}^2} \end{Bmatrix}$$

Where X_T and X_C are the tensile and compressive yield stresses along the fibre, and Y and Z along the transverse directions. S_L and S_H are respectively the yield shear stresses in and out of the plane.

Factors C_1 through C_4 where computed using an inverse method, using a least square approach to compare the back-face velocity obtained numerically and experimentally.

A convergence study gave the same results as Ecault found, showing elements need to be at most 1µm large. However, with this element size, the computer time was over 80h for a single simulation. As explained, the simulation must run several times inside of a script integrating an inverse method optimisation process to get all C parameters properly. The total required time was not affordable (estimation ~10,000h). In its current state, this solution is currently not feasible.

3.3.2 Modelling Choices for the Study

Several choices were made in order to perform numerical simulations within an acceptable calculation time while keeping a good accuracy physicswise. The simplifications as well as the model's details are presented below.

3.3.2.1 Isotropic model

To study the effects of irregularities on the tensile stress generation in the middle of the sample, a single block of FM300 will be used to model the sample. This is a simplified model which does not take into account the difference of shockwave velocity between the longitudinal and transversal directions.

However, FM300 mechanical properties are comparable to the one from FM300-K or FM300-2M and its behaviour under shock load is similar to the one from CFRP materials when only considering transverse propagation (neglecting the propagation along the fibres' direction) and could easily be modelized using elastic hydrodynamics isotropic model (fast computational time).

Simulation are realised using Abaqus Finite Elements (FE) software.

3.3.2.2 Geometry and Loadings

As for Ecault's model, only a slice of the sample will be represented. The dimensions of the numerical model are 10mm by 3.2mm by $5 \cdot 10^{-3}$mm. The thickness of the sample is 1 element wide.

A convergence study showed the optimal mesh size is obtain for 5μm. Smaller element sizes would not generate important variations of the back-face velocity computed values (Figure 3-11 a).
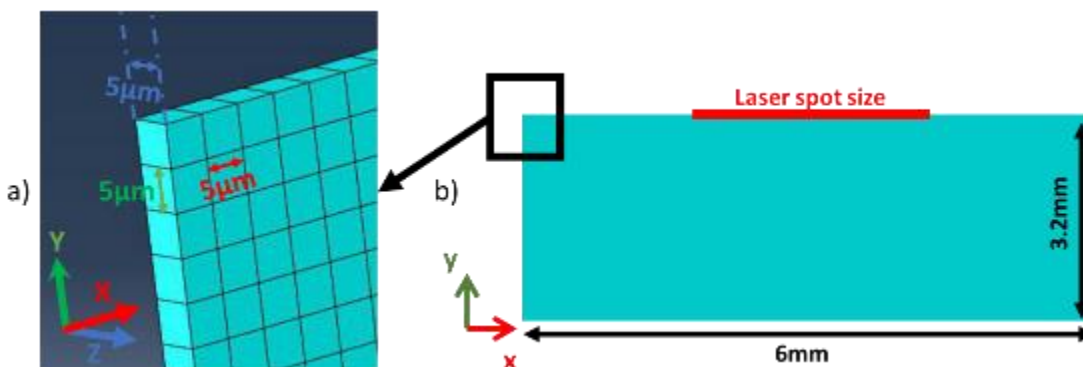
Figure 3-11 a) close-up of the mesh used for the epoxy simulation b) geometry of the simulated sample

The default spatial distribution is defined by a gaussian function (equation (3.24)):

$$g(R) = e^{-\left(\frac{R-A}{R_{foc}}\right)^n} \tag{3.24}$$

With R the radius, R_{foc} the focal spot size, n the coefficient defining the stiffness of the slope of the curve and A the position of the middle of the gaussian. The higher n is, the closer the spatial profile is from a perfect top-hat. Using a gaussian curve instead of a true top-hat better depicts reality and it avoids a big shear stress discontinuity on the borders of the spot (Figure 3-12 a)).
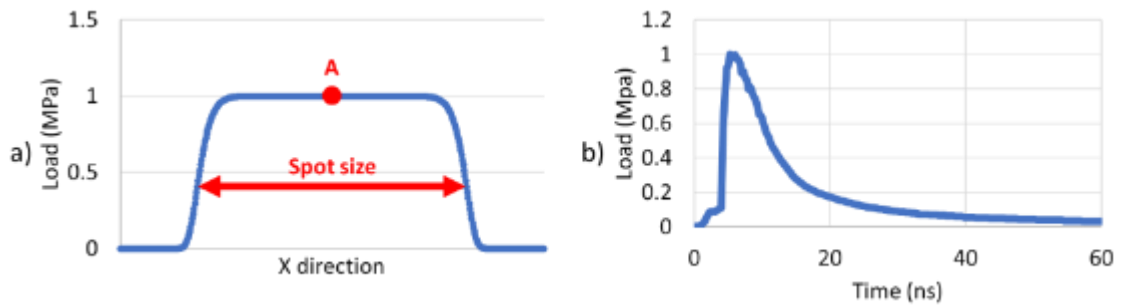
Figure 3-12 a) ideal spatial spread of the laser intensity b) time definition of the load

The temporal profile is represented Figure 3-12 b) and is also an ideal representation of a laser loading. The pulse is considered to be 10ns long (measured experimentally).

Both spatial and temporal loads are normalised when defined within the software. The spatial profile is then multiplied by a factor to achieve the proper pressure.

3.3.2.3 Constitutive Law and Validation

An elastic hydrodynamic isotropic constitutive law is considered for this study. As showed by Ecault in his research work, the behaviour of FM300 is close from the epoxy which could be properly simulated using this kind of constitutive law. The goal is the study of the propagation of a shock wave given a spatial irregularity of the laser intensity. Damage modelling is neglected in these simulations.

Elastic properties are the same as the one taken by Ecault [107] and the hydrodynamic law is taken from Laporte's work [151].

Mechanical properties			Equation of State		
E(Gpa)	ν	ρ (g/cm^3)	C_0 (cm/μs)	s	Γ_0
3.09	0.35	1.14	0.223	1.493	1.13

Table 3-14 FM300 material properties [107], [151]

To avoid unwanted edge effect as well as to reduce the size of the model, infinite solid elements are placed on both sides of the FM300 block. These elements are particularly useful when the experiment that needs to be modelized is very large, and the region of interest very localised, which is exactly the case here.

Two 6mm wide models were created: one with infinite elements on the edges, the other one without. A 4mm laser spot size was used, and the same time loading as in Figure 3-12 b) is used, and a pressure of 800MPa is applied. The computed back-face velocity of both simulations is compared with results obtain by Ecault with LS-Dyna.

No differences were detected between the two 6mm simulations, the back-face velocity profile is plotted in Figure 3-13. This first comparison showed these elements have no impact on the wave propagation behaviour. Moreover, the signal is comparable to the one obtained by Ecault: the back-face velocity has the same order of magnitude (around 150m/s), and the synchronisation of the shocks break out is comparable.

The only difference lies in the height of the second break-out spike (135m/s), which is much higher than the one obtained with LS-Dyna (~100m/s). A certain bulk viscosity is associated with explicit simulation in order to improve the convergence of a model. This default parameter can differ in both its value and its implementation within the finite element code, leading to such variations. However, the timing of the phenomenon matches, which, combined with the previous observation, validates the model.
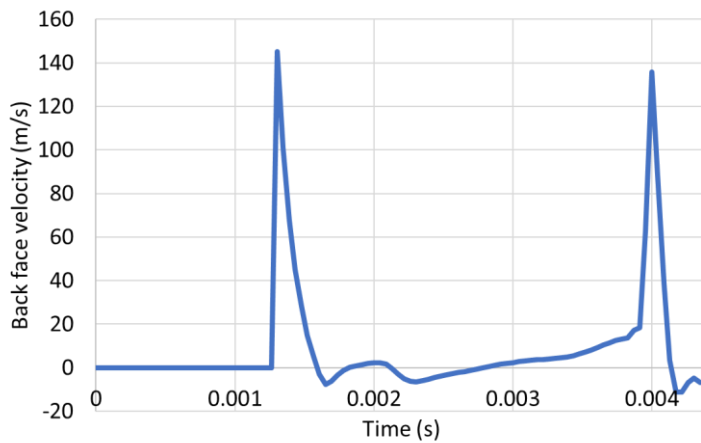
Figure 3-13 Back face velocity obtained with the 6mm wide model

3.3.3 Finite Element Analysis Results

3.3.3.1 Results with a Perfect Profile

To correctly comprehend the way shockwaves propagate within the sample, an 8mm focal spot is used for this study on a 3.2mm FM300 representation. This is comparable to the experimental setup. Simulations are realised at 1GPa, with symmetrical shocks. This is the

required load to open a reference sample with a top-hat like spatial repartition (see next chapter).

Figure 3-14 maps the stresses along the y direction, depicting the main phenomenon happening during S-LASAT. The grey areas around the sample are the infinite solid element where no stresses are displayed.

At t=51ns, the shockwaves barely start propagating, compressive stresses reach -972 MPa which is almost the initial load of 1000 MPa.

At t=712ns, the two shockwaves intersect, generating a high compressive load in the centre of the sample. At t=1140ns, both shockwaves have been reflected, and a high tensile stress is generated (~229 MPa). This is what was referred to as the "secondary" tensile area in chapter 1. 2D effects can also be seen on both side of the pressure "drag" of the shockwave.

Last, at t=2148ns, both reflected shockwaves cross, generating the principal tensile stress at 362 MPa. This is 1.58 times the secondary tensile max. This value is relatively close from the 1.3 ratio Ecault had in his studies.

The area in grey shows the top 20% tensile stress area. This area is used during the whole study as reference to analyse the way shockwaves interact around the principal stress area (see chapter I). For an 8mm focal spot, a 6.675mm wide area was achieved.
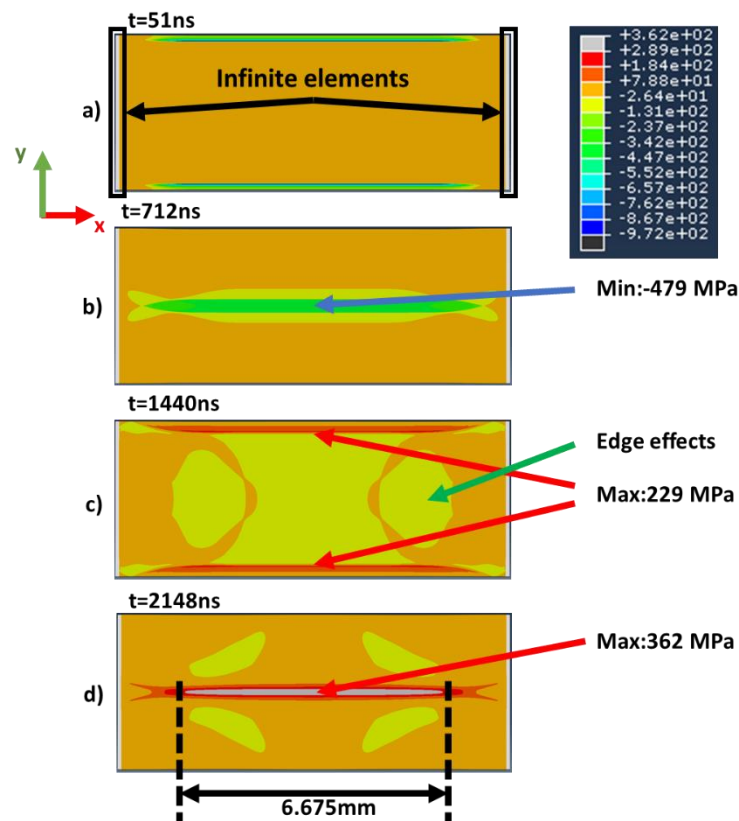
Figure 3-14 Stresses along the y direction during a shockwave propagation within a 3.2mm epoxy resin sample at a) t=51ns b) t=712ns c) t=1440ns d) t=2148ns

3.3.3.2 Symmetrical Shock with Real Profile

The same model as for the previous paragraph is used, however, instead of a perfect spatial distribution, the real profiles from beam A and B are used (cf. chapter 2).

As shown in Figure 3-15 a), the loading profile is not as smooth as for the perfect scenario, resulting in a local increase of the pressure, especially the one generated by beam A. This inhomogeneity has direct repercussions on the maximum tensile load width which dropped from 6.675mm to 1.215mm.

A poorly spread energy on the focal spot immediately resulted in a significantly smaller tensile stress area. This would explain the problems found earlier either to properly define a threshold and to find the opening area when using a more direct technique such as the photomicrograph.
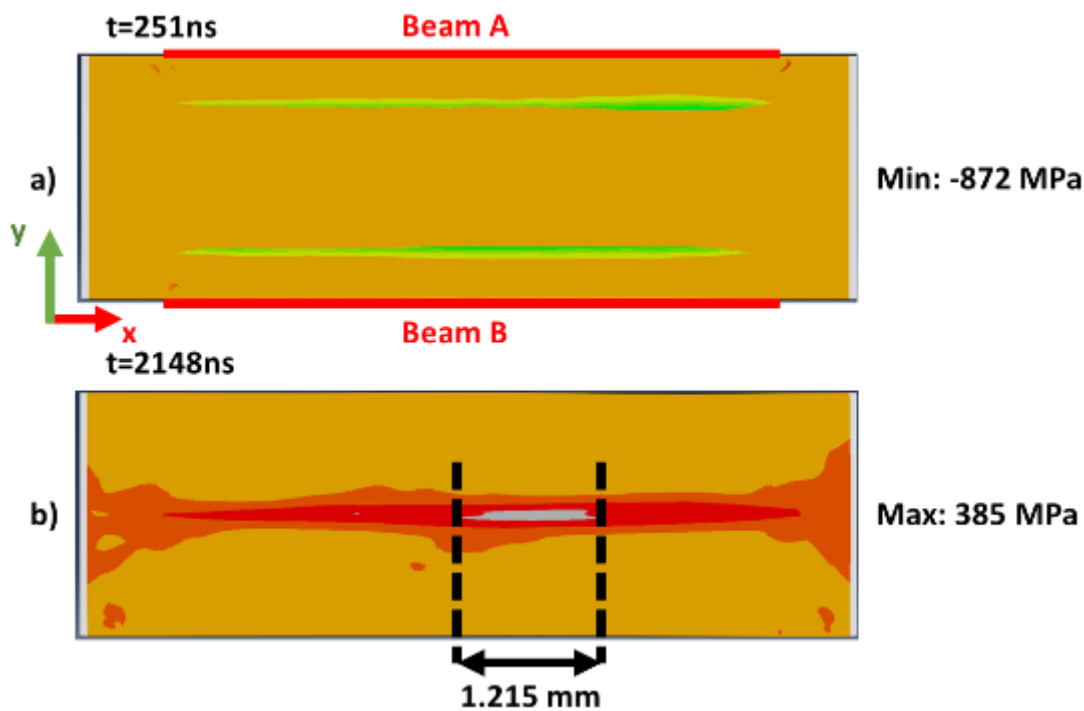
Figure 3-15 Shockwaves propagation using the real spatial experimental loading a) at t=251ns b) at t=2148ns

3.3.3.3 Definition of the Spatial Load

To analyse the effects of spatial irregularities of the laser beam, four different parameters are studied. The first two ones are experiment dependant:

- Sample thickness: the shorter the shockwave propagation distance is, the less likely load irregularities will be smoothened. Indeed, because of the material damping, load irregularities tend to disappear after a given distance. It is expected that the bigger the irregularities, the longer the distance should be to nullify their influence

- Laser spot size: larger spot size also implies large irregularities width. This parameter could also influence the way shockwaves cross each other within the sample

Two more parameters were defined to describe a spatial irregularity of the laser generated load: the width and the height of the defect. Figure 3-16 shows the parameters and the way they are fitted. The orange curve is the ideal loading case scenario for an 8mm focal spot. It is a gaussian, with a stiff slope on both sides (n=16). The blue curve is the real experimental loading from beam A.
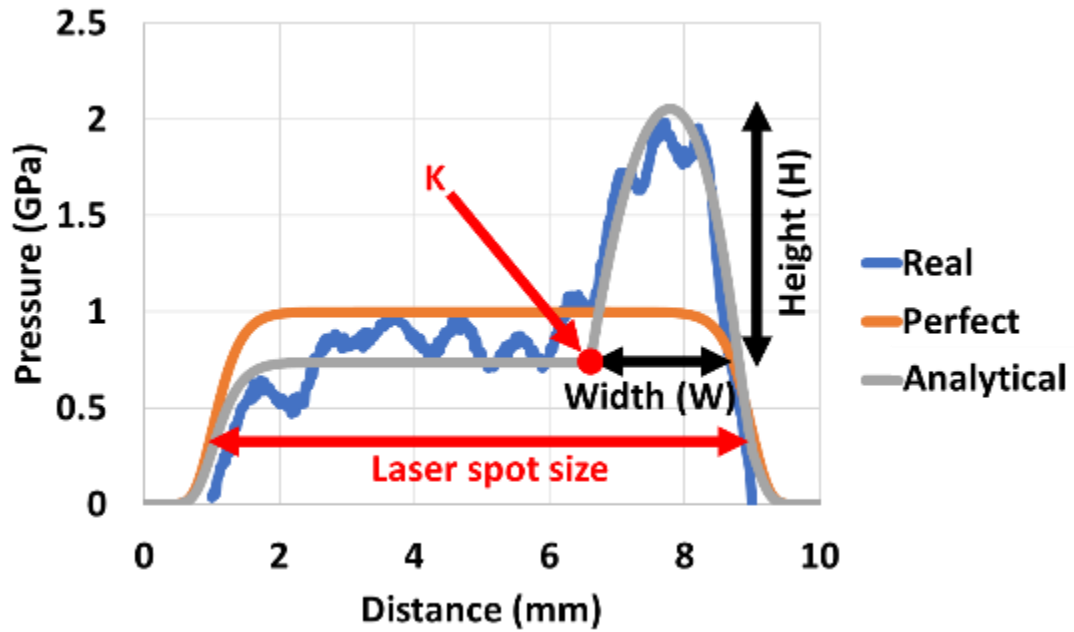
Figure 3-16 Definition of spatial irregularities parameters

To study each parameter's impact, an analytical formulation of a load including a defect was realised. It is the standard gaussian curve to which a parabola was added.

$$e^{-\left(\frac{x-A}{R_{foc}}\right)^n} \times g(x) \tag{3.25}$$

Where x is the position along the sample and g is the parabola defined by:

$$g(x) = \begin{cases} \left(-\frac{4}{W^2}\left(x-\left(K+\frac{W}{2}\right)\right)^2 + 1\right) \cdot H + 1 & \text{if } g(x) > 1 \\ 1 & \text{otherwise} \end{cases} \tag{3.26}$$

Where W is the defect width, H the defect's height and K the position of the defect (Figure 3-16). These three values are dimensionless. They can be assimilated to multiplying factors. The curve obtained using this load distribution formula is plotted in grey in Figure 3-16, with W=2.4 and H=1.8.

To insure a correct comparison, the energy density should stay the same, regardless of the spatial default. Hence, the area under the grey curve and the one under the perfect profile should stay the same, explaining the difference between the orange and the grey curve where no defects are added.

In conclusion there are three different numerical profiles for the intensity repartition:

- Real: the experimentally measured profile
- Perfect: the ideal gaussian shape
- Analytical: an analytical curve that adds a local irregularity to a gaussian function in order to best mimic the real profile.

3.3.3.4 Validation of the Spatial Irregularity Analytical Representation

To validate the spatial irregularity representation, two symmetrical shot models are compared. The first one has a perfect profile on one side, and the real beam A repartition on the other side. The second simulation again uses a perfect profile on one side, and the analytical one on the other side.
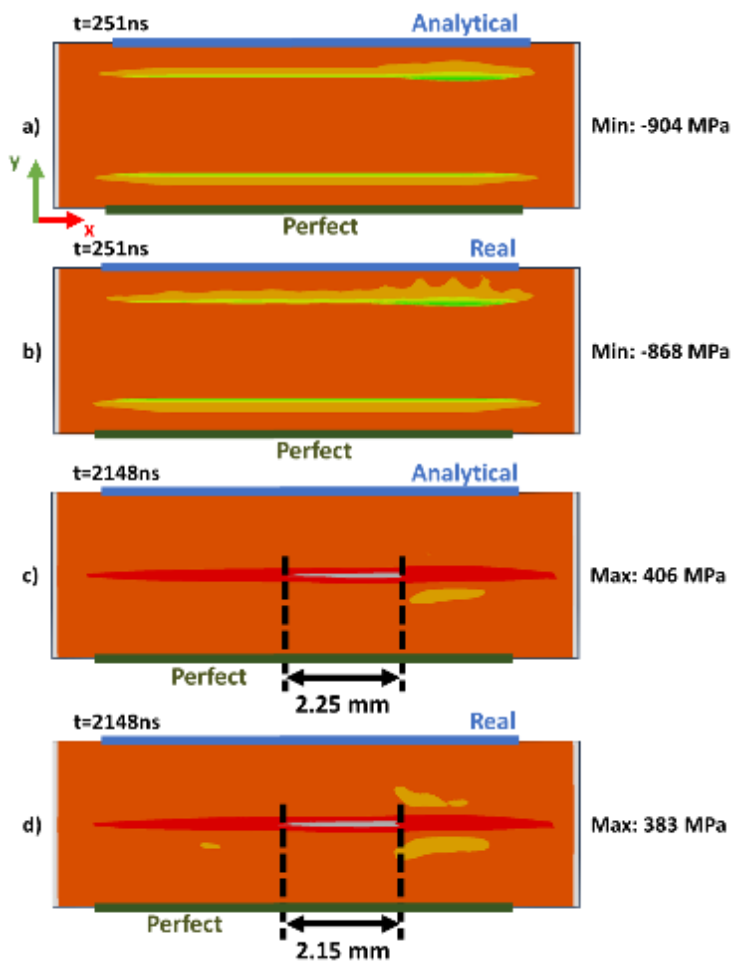
Figure 3-17 wave propagation at t=251ns for a) the analytical profile b) the real profile and at t=2148ns for c) the analytical profile d) the real profile

The comparison data is the width of the area under the principal tensile load. Indeed, the goal of this numerical study being to understand why damages are so small, making them difficult to be spotted using US.

As expected, the timing between the two simulations is the same. The presence of an irregularity modified the shape of the shock wave however, the analytical solution (Figure 3-17 a) and the real profile (Figure 3-17 b) are comparable. The real signal being noisier, the release wave pattern is not as smooth as for the analytical profile.

At t=2148 the width of the 80% maximum tensile stress area is slightly higher for analytical profile (Figure 3-17 c) than for the real one (Figure 3-17 d). Indeed, inhomogeneities present around the main irregularity spike tend to get smothered quicker than its equivalent analytical profile, leading to higher energy loss thus smaller tensile stress area.

However, both tensile areas for the analytical and the real profile are close enough, and the way spatial irregularities are analytically formulated can be validated.

3.3.4 Design of Experiment

3.3.4.1 Generalities

Because of the number of parameters, a Design of Experiment (DOX) is used to define the simulations required to properly assess the impact of spatial irregularities on the maximum tensile load area's width.

This method is an efficient way to evaluate the influence of each input parameters – sample's height, focal spot diameter, irregularity's height and width – on a solution, here the tensile load.

There are several methods based on DOX, such as the Taguchi method [152] however, in this case a Central Composite Circumcised Design (CCC) was chosen. It has the advantage of building a quadratic model and is very useful to study response surface like a standard Central Composite Design (CCD) [153], and also shows better prediction capabilities than other CCD like the Face Centered (CCF) or the inscribed one (CCI) [154], [155].

If the parameters, or factor, and their values, or levels, were correctly chosen, DOX can generate an analytical formula of the response. For example, for CCF the formulation is:

$$y = c_0 + \sum_{i=1}^{k} c_i x_i + \sum_{i=1}^{k} c_{ii} x_{ii}^2 + \sum_{j=i+1}^{k} \sum_{i=1}^{k-1} c_{ij} x_i x_j + \epsilon_{ij} \tag{3.27}$$

Where y is the response, c_i the parameter coefficients, x_i the input variable and ϵ the error.

3.3.4.2 Definition of the CCC

The CCC method requires 5 levels per parameter: $-\alpha$, -1, 0, 1 and α. In the case of a CCC method, $\alpha = \sqrt{k}$, with k the number of parameters. Four parameters (sample thickness, spot size, irregularity height and irregularity width) were isolated in this study case, setting $\alpha = 2$. The difference between the level 0 and 1 should then be the same than between 1 and 2. For example, level 0 of the focal spot is set at 7 (cf. Table 3-15) and level 1 at 8.5. The difference between level 1 and α should be equal to $(\alpha - 1) \times (8.5 - 7)$, so 1.5, setting level α value at 10.

The focal spot during the experiments is 8mm. Having a spot diameter below 4mm could imply strong 2D effects, and anything above 10mm would require a more powerful laser than the one from Hephaïstos facility.

The sample's thickness is 3.2mm. The thickness range has been set between 2mm and 4mm, to ensure enough variation to properly grasp the effect of this parameter on the solution.

The range used to define both the irregularity width and height is subjected to two constraints: it should include the parameters found to best fit the real spatial distribution and should not be equal to zero. Indeed, having either an irregularity height or width null would imply no default at all, and could alter the obtained results. Values are summarised in Table 3-15.

	Thickness (mm)	Focal Spot (mm)	Irregularity Height	Irregularity width
-α	2	4	0.2	0.2
-1	2.5	5.5	0.65	0.9
0	3	7	1.1	1.6
1	3.5	8.5	1.55	2.3
α	4	10	2	3

Table 3-15 Summary of the parameters' level

This work uses the software Minitab 18.1 (Minitab Inc.), to handle the DOX analysis. The results' matrix is available in Appendix A.

3.3.4.3 DOX Validation

To assess the precision of the model, several points need to be verified. The first one concerns the residual histogram. Figure 3-18a) shows the residuals' frequencies are following a normal distribution (gaussian line in Figure 3-18 a) and are reasonably spread. This is further validated by the normal probability plot (Figure 3-18 b) with the residual values closely following a straight line as well a p-value above 0.05 [156]–[158].
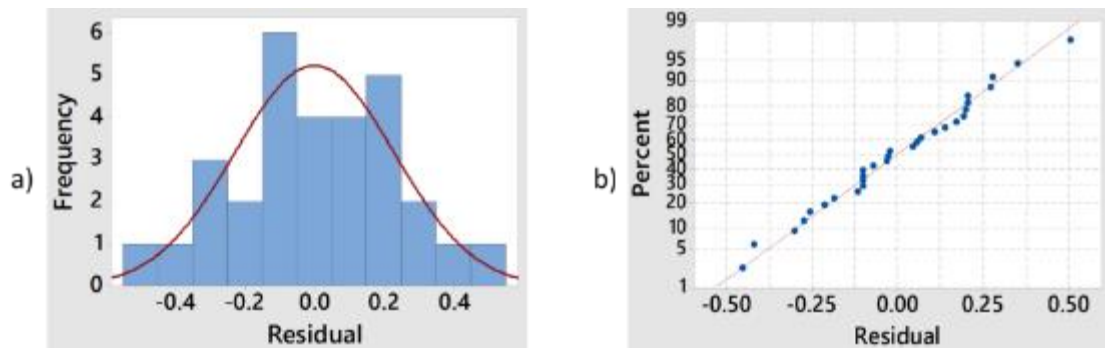
Figure 3-18 a) Histogram displaying residuals and their frequencies b) normal probability plot

Moreover, key values for this model are summarised in Table 3-16.

S	R-sq	R-sq(adj)	R-sq(pred)
0.329251	97.71%	95.26%	84.92%

Table 3-16 Model summary

The standard deviation, S, between the measured values of the 20% top tensile stress area width and the model is rather small, 0.32mm, showing a good agreement between the analytical model and the actual simulation. The R-sq (R^2) is the percentage of the variation in the response that is explained by the model [159]. It is comprised between 0% and 100% and the higher the value, the better closer the model is from the actual data. Last, the R^2(pred) evaluated the prediction capabilities of the model. Again, a high value indicates good forecast capabilities.

With a high R^2 both for the model fitting and its forecast capabilities as well as a decently small standard deviation, the model seems robust enough to be used for prediction. Minitab computed the following formula for the width of the tensile stress area, taking into account the four parameters:

$$y = 19.31 - 0.369F - 8.55T - 3.55H - 2.06W + 0.1227F^2 \qquad (3.28)$$
$$+ 1.366T^2 + 1.971H^2 + 0.931W^2 + 0.012(F \times T)$$
$$- 0.534(F \times H) - 0.0848(F \times W) + 0.642(T \times H)$$
$$- 0.249(T \times W) - 0.486(H \times W)$$

Where F is the focal spot size, T is the sample's thickness, H the irregularity's height and I its width. This formula is only valid on the domain defined by the parameters level (see Table 3-16).

Using equation 3.28 with the parameters found to best describe beam A spatial repartition (H=1.8, W=2.4), the experimental focal spot diameter (F=8) and the sample thickness (T=3.2), leads to the approximation in Table 3-17.

Fit (mm)	SE Fit (mm)	90% CI (mm)	90% PI (mm)
1.94	0.27	(1.46; 2.42)	(1.19; 2.69)

Table 3-17 Prediction for H=1.8, W=2.4, F=8, T=3.2

"Fit" is the mean value obtain for these parameters. "90% PI" is the 90% Prediction Interval, meaning that there is 90% of chances that the maximum tensile stress area width will fall within the range [1.19mm – 2.69mm] and "90% CI" represents the 90% Confidence Interval showing the range the value is likely to fall within [160].

The average value (1.94mm) is very close from the computed one (2.25 mm) which also falls in the CI. The model is validated.

3.3.4.4 Result: Laser Spot Parameters Influence

Since the model has been validated, a deeper study of the parameters influence on the solution can be realised. The pareto chart (Figure 3-19) summarises their effect.
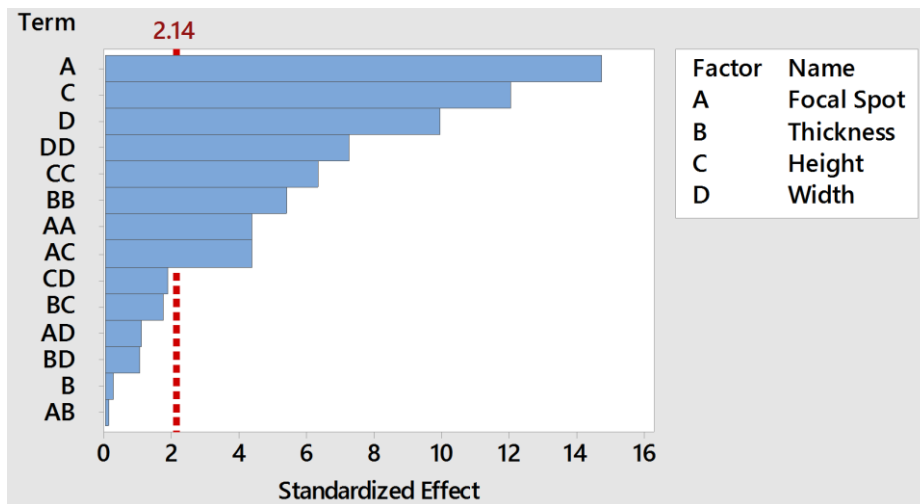
Figure 3-19 Model's Pareto chart (P = 0.05)

Any effect worth considering should be above the 2.14 dashed line. It represents the limit at which the parameters are statistically significant.

The coupled parameters DD, AC, … are not considered. They are required to generate a quadratic response, but do not have a physical signification. Figure 3-19 shows that the focal spot is the prevailing parameter followed by the irregularity height and width. The thickness standardized effect is below the 2.14 bar, meaning it is not relevant, at least for thickness variation range defined at the beginning of the study.

However, the main advantage of such analysis is the study of the response surface. Hence, for a set focal spot (8mm) and thickness (3.2mm), Figure 3-20 shows the top 20% tensile stress area width for irregularity height and width ranging respectively from [0-2.0] and [0-

3.0). For this study, the minimum acceptable width for given parameters is set at 3mm. Anything below displayed in red on the figure.
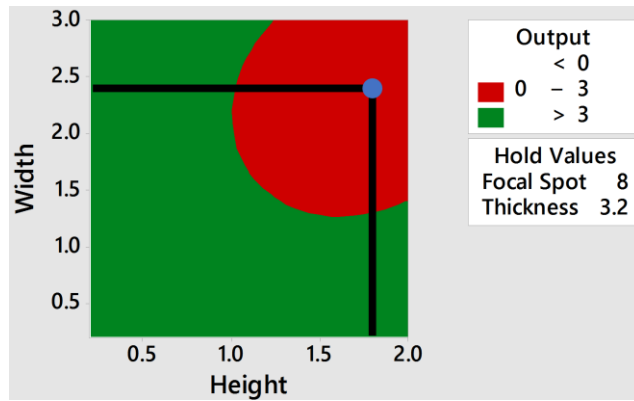
Figure 3-20 Surface response for an 8mm focal spot at a 3.2mm thick sample

Using equation 3.28 response surface allows for an instant estimation of the feasibility of the test. In this case, when taking the $H(1.8)$ and $W(2.4)$ values for beam A analytical model, one directly hits the red area (see Figure 3-20).
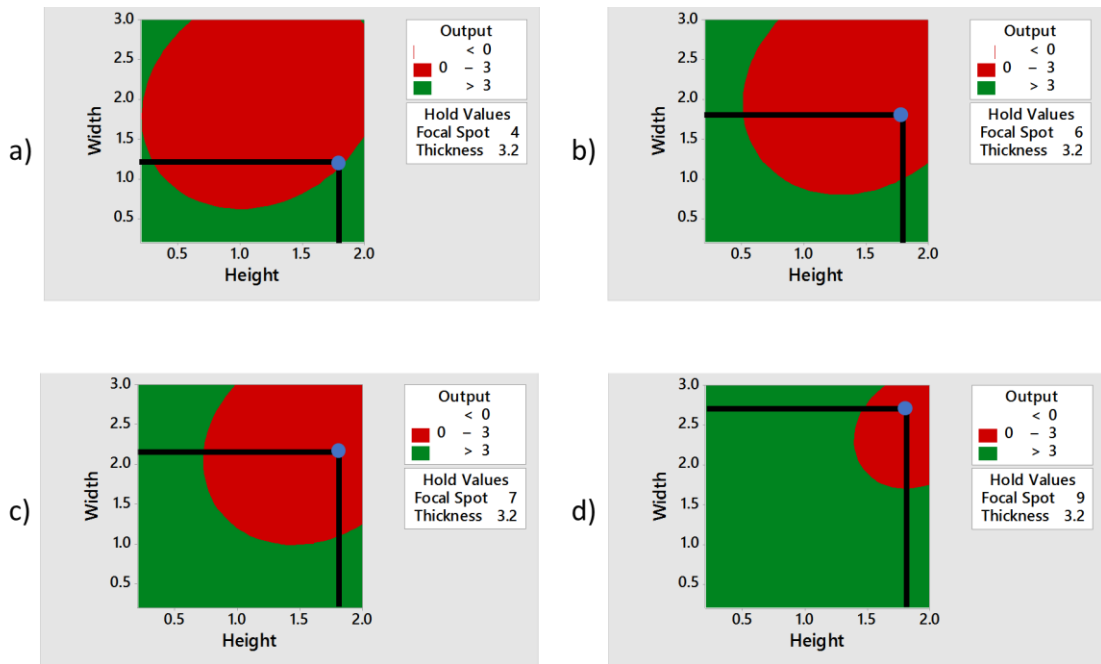
Figure 3-21 Surface response given 4 different spot sizes: a) 4mm b) 6mm c) 7mm d) 9mm

Figure 3-21 shows the evolution of the 3mm width limit for four different spot sizes: 4mm, 6mm, 7mm and 9mm. The first expected observation is that the larger the spot size, the bigger the default could be before being problematic (reduction of the red area).

For each case, the width and the height of the irregularity for the analytical loading were recalculated giving the spot size, so the analytical curve fits at best the real spatial repartition a given spot size (see Figure 3-16). Values are summarised in Table 3-18.

Focal spot (mm)	4	6	7	9
Irr. height	1.8	1.8	1.8	1.8
Irr. width	1.2	1.8	2.1	2.7

Table 3-18 Values of the irregularity parameters giving four different spot sizes

As expected, the width followed a linear function based on the spot size. However, the height of the irregularity did not change.

These values were reported in Figure 3-22, and represented by the blue dot. One can see that in most cases, the dot was inside the red area, meaning that with this set of parameters, the width would be smaller than 3mm. However, when the spot size is close to 4mm, given beam A irregularities, the 3mm threshold is almost obtained. When closely observing Figure 3-21 a), it seems that by increasing the irregularity height, with a constant width, one could reach the green area.

This result is counter intuitive, so to further explain this phenomenon, the analytical loading was plotted for a 4mm spot diameter, and a default irregularity width of W=1.2 (see Figure 3-22).
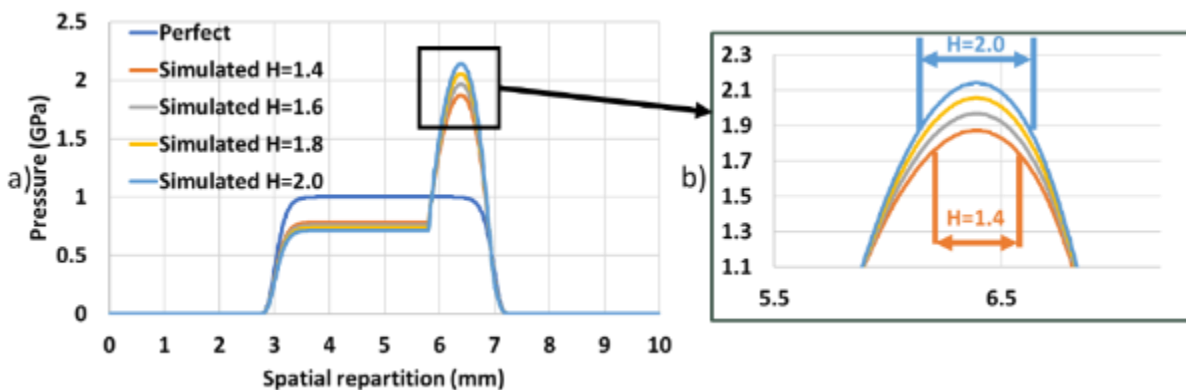
Figure 3-22 Evolution of the analytical profile with the irregularity height

Because the energy density between each spatial model was supposed constant, increasing the irregularity height had a second impact: the slope of the irregularity was generally stiffer as the height would increase, providing wider spike. Hence, for a H=2.0 the width corresponding at the top 20% of the loading ended up being larger than for a smaller default.

This also explains why a smaller spot size could lead to better results with high spatial irregularities.

This study allowed for a classification of spatial irregularities and their influence on the width of the maximum tensile stress area. Figure 3-21 showed that the larger the spot size is, the bigger the default could be before this area becomes too small to generate a decent size opening. However, if the irregularity is too important as it was the case for the Gaïa-HP

laser used in the Hephaïstos facility, a better solution would be to reduce the size of the spot to achieve a decent width for the max tensile area.

This numerical analysis stressed the load distribution is of the utmost importance S-LASAT applications. In order to increase the robustness of the technique, it is crucial to mastered it.

3.3.5 Diffractive Optical Elements (DOE)

The previous study only left a single solution in order to overcome the initial problem of localised bond opening: the energy repartition over the spot size needs to be smoother. Indeed, if reducing the spot size seemed to produce interesting results, it does not fit with the LASAT application where, to limit the testing time of a sample, the spot size should be as big as possible.

As explained in the previous chapter, DOEs are able to remove these kinds of irregularities by diffracting the beam over a circle spot with a predefined diameter.

As shown in Figure 3-23, the width of the maximum tensile strength area is now almost identical to the one obtained with the ideal spot size (see orange curve in Figure 3-16), providing a much wider opening area.
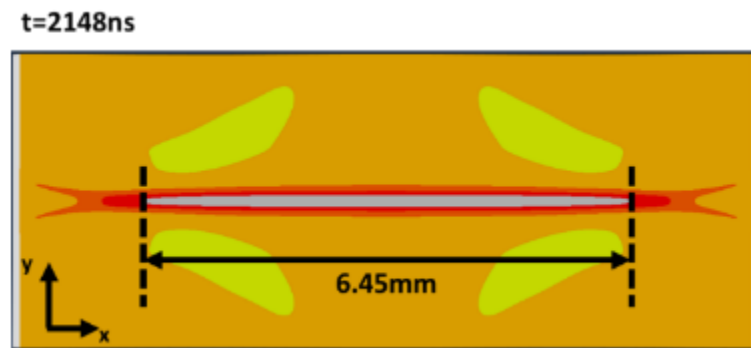
Figure 3-23 Width of the principal tensile stress area with a post DOE spatial loading

3.4 Conclusion

An initial experimental process was realised using S-LASAT without DOE, showing the capability of the technique to open a bond without damaging the CFRP laminated.

However, thresholds for both the laminate and the bond itself showed erratic results. Because of this lack of consistency, it was impossible to state whether a sample was contaminated or not.

To better comprehend the reason behind these results, photomicrographs were realised on key areas where thresholds were first noticed. This study confirmed the ultrasound scanning was precise enough to spot even the smallest defects. However, the size of the delamination that could have been observed did not match the theory: their diameters were too small, and they were off-centered.

The energy repartition over the laser spot size was not optimal and showed important irregularities. To study their effect, FE simulations were set in place. Initially, simulations of CFRP bonded laminated, based on Ecault's work [100] , where realised using Abaqus software. However, because of the computational time required for a simulation to run, this complex simulation was abandoned.

Other numerical simulations based on an isotropic model were realised, showing that the poor spatial repartition had a direct impact on the principal tensile stress area width.

To better understand the impact of these spatial irregularities, an analytical model of the laser spatial loading was defined. Four parameters were supposed to have an influence: the laser spot size, the sample's thickness and the irregularity height and width. To optimise the study, a statistical tool known as DOX was used.

This last study showed that the sample thickness (within the study range) had little to no effect on the maximum tensile stress area. It also allowed the study of response surface for given irregularities and laser spot dimension. The response surface study showed that these irregularities were too big to be absorbed by the parameters we could easily modify: the focal spot diameter.

The only remaining solution being the reduction of these irregularities, DOEs were installed on the experimental setup. Initial simulations showed that with these optics, the tensile stress should be much wider.

The next chapter goes through the experiments realised with this new experimental setup.

Chapter 4. RESULTS WITH OPTIMISED S-LASAT TECHNIQUE

TABLE OF CONTENTS

3.5 Introduction

Initial tests performed with S-LASAT technique on coupon samples highlighted the high level of process proficiency required to generate the expected phenomenon.

In the light of the previous study several parts of the experimental process as well as the experimental setup itself were modified to deliver more consistent results.

This chapter presents a new experimental process applied on both coupon and pilot samples. After concluding on these experiments, two real case scenarios are tested. These final tests will allow to assert the Technology Readiness Level (TRL).

3.6 Experimental process

Two main concerns were highlighted in the last chapter. The first one had to do with the S-LASAT parameters' control, especially the spatial repartition of the laser intensity. The problem has been overcame using DOE, allowing for a better propagation of the shockwave within the sample. The second remaining question is about the heterogeneity of the contamination over the sample. For example, in the case of the finger print contamination, the solution is applied very locally to mimic a thumb print. Hence, to insure no variations occurs from one shot to another, the sample was shot on the same area, and the intensity was gradually increased as before (Figure 4-1). The tested area was chosen to be in the centre of the sample to further limit heterogeneity problems. This technique should help producing more consistent results.
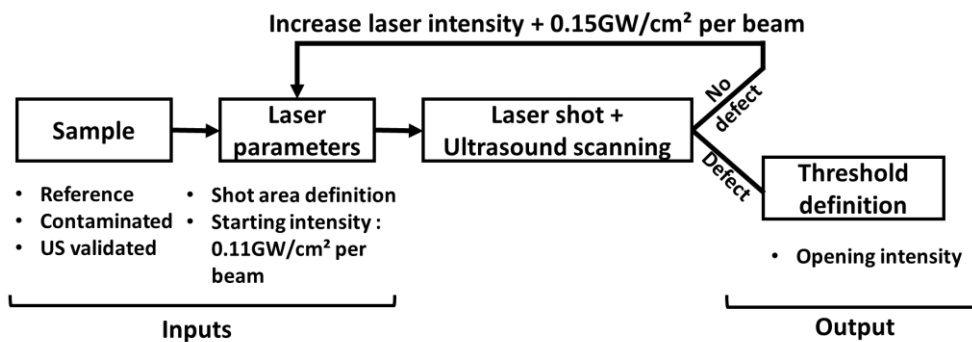
Figure 4-1 Diagram of the experimental procedure

Again, initial US are done before any test to verify no inherent defects are present in the tested area. These verifications are then done after each shot until a defect is spotted.

Shot intensity will start at $0.11GW/cm^2$ and are increased by $0.15GW/cm^2$ if the area is proven to be healthy.
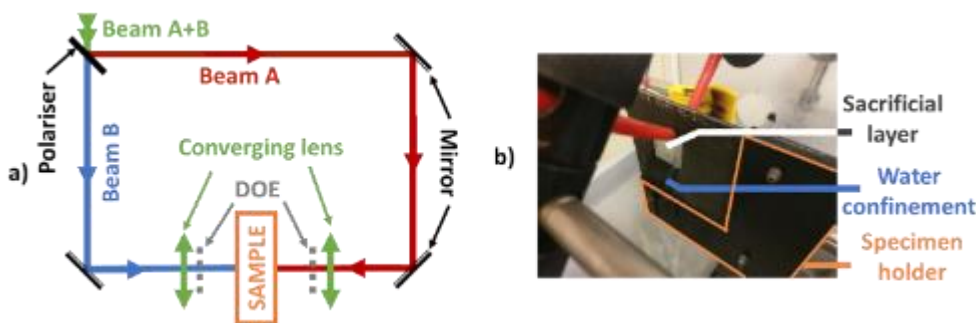
Figure 4-2a) Diagram of the experimental setup b) sample setup

Figure 4-2a) shows the new experimental setup including the DOEs, placed right after each converging lenses on both beams.

Because the sample needs to be taken off, and replaced on the S-LASAT setup, a specific specimen holder was designed, to ensure the sample faces the laser the same way from one shot to another (Figure 4-2b). Water is still used as a confinement material, and the surface of the sample is protected using the same aluminium tape as before. The laser spot diameter is still 8mm.

This experiment can only show the first created damage. Indeed, once damaged, the area is not representative anymore of a sound sample and should be discarded.

3.7 Results on Coupon Samples

3.7.1 Reference sample

Comparison between the bond threshold values obtained with the previous setting is summarised in Figure 4-3 a).
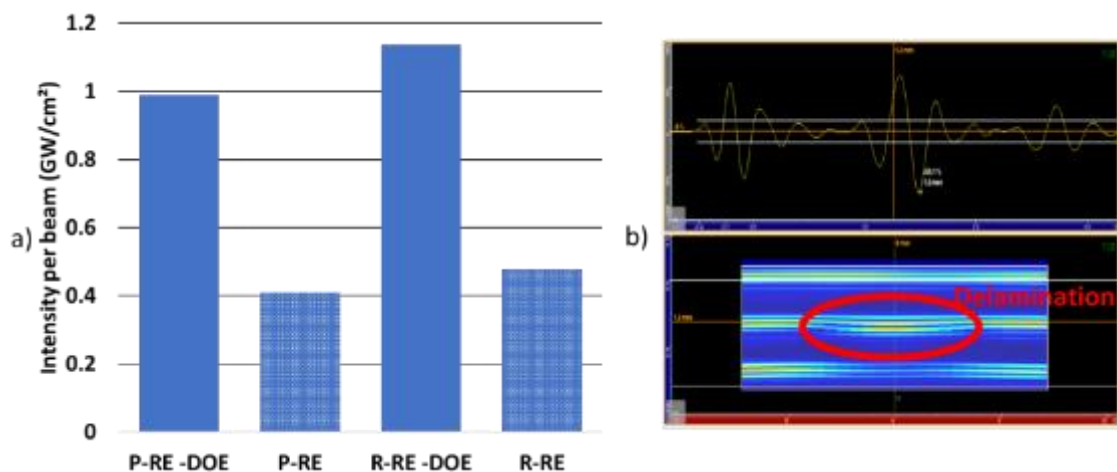
Figure 4-3 a) Comparison between bond thresholds obtained with the previous setup b) B-Scan of the production reference sample after the bond threshold was reached

For both the production and the repair reference samples, the bond threshold is higher with DOE than without. The production reference sample threshold went from 0.4GW/cm^2 per beam to 0.99GW/cm^2, and the repair one from 0.53GW/cm^2 to 1.14GW/cm^2. By smoothening the overall intensity profile over the laser spot, one avoids these very local high tensile stresses. Stresses are now more uniformly spread over the focal spot size, hence requiring a higher laser intensity, but also providing a much wider, and clearer apprehension of the damage using ultrasounds (Figure 4-3 b).

A threshold difference was spotted between the repair and the production sample in the same order of magnitude as previously, roughly 0.15GW/cm^2.

3.7.2 Production Coupon Samples

Figure 4-4 summarises the bond thresholds obtained for the production coupon samples using the current setup. The reference level is given by the blue bar, the orange colour is for release agent (RA), the green one for moisture contamination (MO) and the yellow one for the finger prints (FP).

In all cases, only debonding were spotted. Hence, all bars from this figure represent the bond threshold. Moreover, given the previous results, it is important to note that these values were obtained regardless of the scanned surface (face A or face B).

All contaminated sample but MO-3 showed signs of structural weakness around the bond line. The sample contaminated using release agent or finger print like solution could be correctly differentiated from a healthy sample.
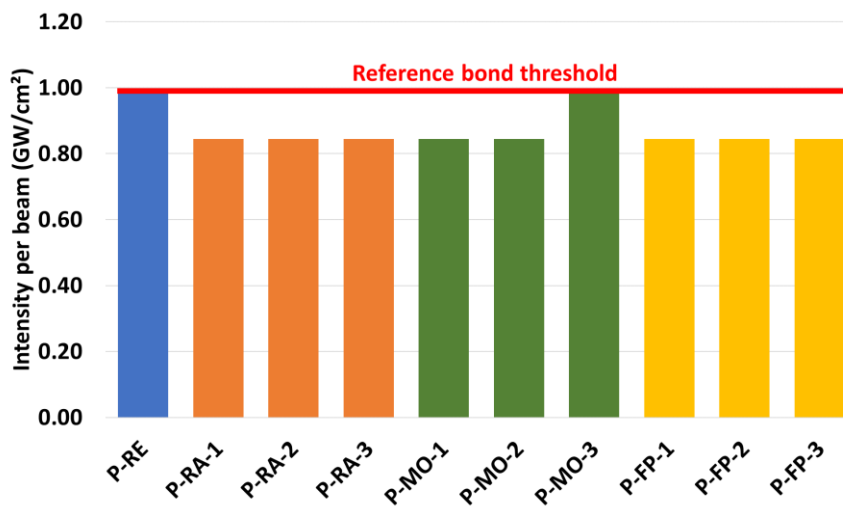
Figure 4-4 Results on production coupon samples

For moisture contaminated samples, a regain of adherence was observed for the highest level of contamination. Similar results have already been observed by Schoberleitner using a standard tensile testing machine [161], and was linked to a plasticisation effect after adding a certain amount of water to an epoxy resin. This effect is however limited, after a certain level of contamination, the adherence level would drop again.

S-LASAT successfully separated healthy samples from contaminated one. However, no difference of adherence level was recorded between each contamination level.

3.7.3 Repair Coupon Samples

The same study was realised on the repair coupon samples. Results are summarised in Figure 4-5. The reference repair sample bond threshold is represented in blue, the de-icing

fluid (DI) contamination in orange, the thermal degradation (TD) one in green and the falsely cured (FC) samples threshold in yellow.

The DI and TD cases showed different bond strength levels. In the case of DI, a differentiation between the lowest and the other contamination levels was also possible. Results are even more conclusive concerning thermal degradation where the bond threshold decreases with the degree of contamination.

A lower threshold was also found for FC-1 and FC-3. However, results could be biased because of the debonding that were initially spotted using US. The contamination process is not robust enough to lead to a conclusion in this case.
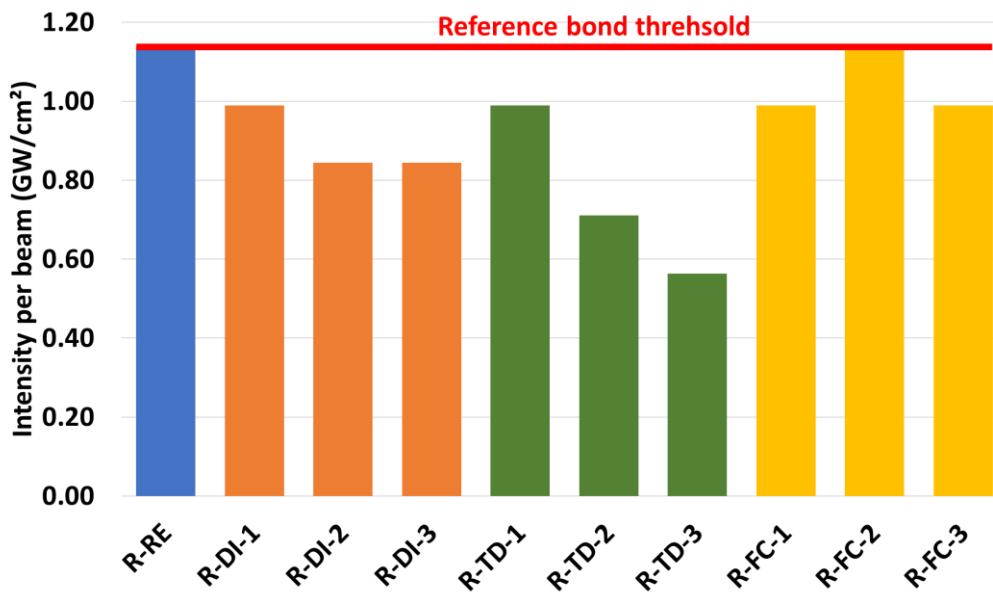
Figure 4-5 Results on repair coupon samples

Once again, results showed S-LASAT is able to only damage the bond given a certain laser intensity, and a healthy sample requires a higher laser intensity level than a contaminated one for its bond to be damaged.

3.7.4 Fracture Pattern

Photomicrographs of post mortem areas were taken to further analyse the way cracks would propagate within a sample. Figure 4-6 a) is a close up on a production reference sample. As described in the specification, there is a thin layer of pre-preg resin in-between the bond and the composite laminate. A closer study of the debonding shows that it only propagated at the interface between the pre-preg resin and the epoxy bond. More generally, when a debonding was spotted within a production type sample, regardless of the contaminant, it would appear at this interface, and only where the contamination occurred. Hence, for production samples, the failure mode was most likely adhesive.

Figure 4-6 b) shows the crack pattern obtained within the repair reference sample. This time the opening would mainly propagate in the centre of the bond, describing a cohesive failure mode.

Large particles were also spotted, but only in the case of a de-icing fluid contamination. It looks like they were migrating from the contaminated surface towards the centre of the bond. A physico-chemical study would be required to better understand where these come from and their impact on the adherence properties of the bond.
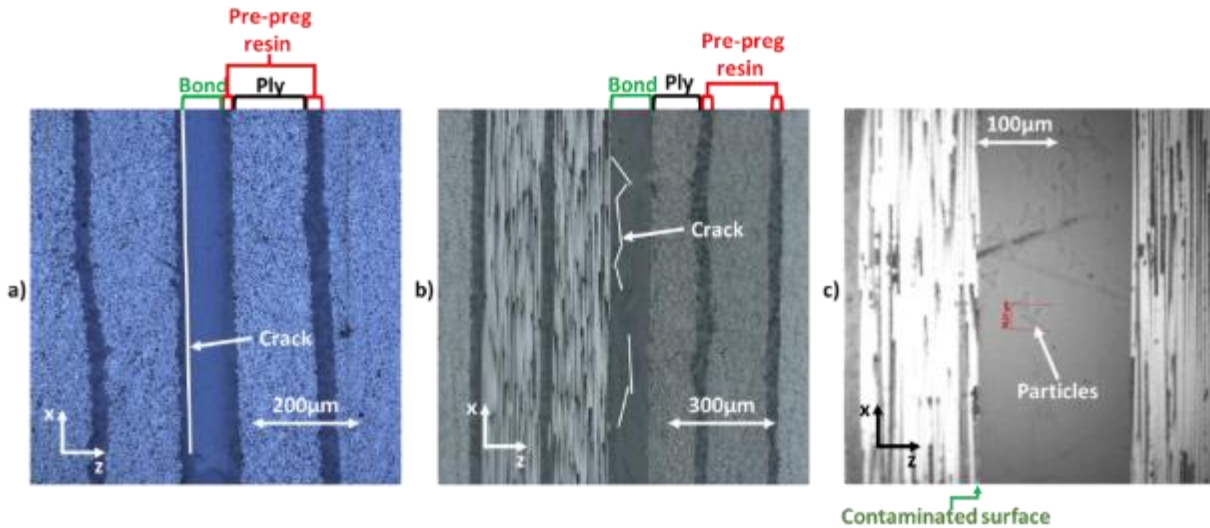
Figure 4-6 Photomicrographs of the bond after damage created by S-LASAT: a) production reference sample. b) repair reference sample. c) highest degree of de-icing fluid contamination

3.7.5 Threshold and Process Validation

These experiments on coupon samples showed promising results. However, two main questions arose: did the shock repetition over the same area influence the results? Are these shots reproducible?

To test repetition effects over an area, 3 random samples were selected: P-RE, P-RA-3, R-DI-1. The laser intensity was set one level below the bond threshold found for each sample (see Table 4-19), and one area of the sample was shot five consecutive times. US were performed between each shot, and the aluminium sacrificial layer was changed.

	Bond threshold (GW/cm²)	Tested intensity (GW/cm²)
P-RE	0.99	0.84
P-RA-3	0.84	0.71
R-DI-1	0.99	0.84

Table 4-19 Intensities used to assess the effect of repetitive shocks on the same area

Regardless of the sample, no delamination or debonding were spotted after 5 consecutive shocks.

Moreover, on a different area of these samples, a shot was performed at the threshold previously found. For each shot, the US showed signs of debonding. If this proof is only partial because of the uncertainties related to the heterogeneity of the contamination, it still shows promising results.

3.7.6 GIIC Tests

In his work, Ehrhart [39] mechanically tested samples that were shot using a single shot setup. These experiments were performed with an intensity below the debonding level and did not show signs of damage when scanned using US. However, the DCB test revealed a loss of 50% of the mechanical properties of these samples.

The Laboratory of Technology and Strength of Material of Patras University (LTSM-UPAT) provided 2 sets of 3 $G_{II}C$ sample. One set of reference repair samples and another one for production reference samples.
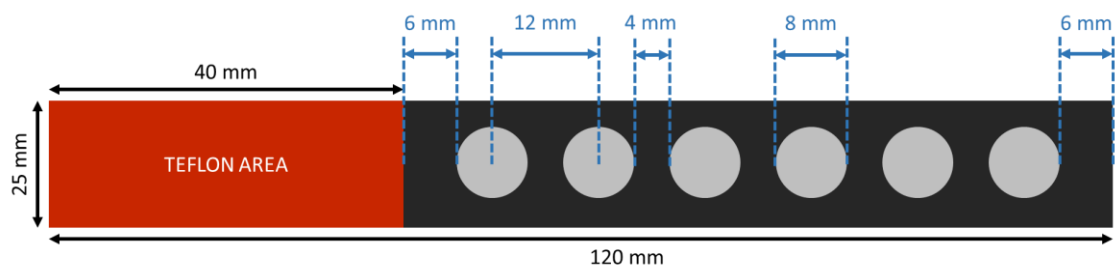
Figure 4-7 Shot repartition over a $G_{II}C$ sample

The first 40 mm of the sample have a teflon patch inserted to help the initiation of the crack. Six different shot areas were defined on the remaining 80mm. The distance between each shot was taken large enough so a shot would not influence the results from another area.

Two different intensity levels were selected for each scenario and all samples were tested using S-LASAT. For the production sample, two out of the three samples were shot at 0.84GW/cm² per beam. Experiments have shown that at this intensity level, reference samples do not open, while any of the contaminated sample should be debonded in the area of the laser shot. The last $G_{II}C$ sample for production was shot at 0.57GW/cm² which is 57% of the bond threshold. This value is far enough from the opening point, no damage should be visible. This sample will serve two purposes: in case the first two specimens have a decrease of their mechanical properties, one could compare both results and verify if the same be-

haviour happens at a much lower pressure. In the case where no mechanical loss is experienced by any of these samples, a comparison of the crack propagation within the sample as well as the behaviour of the sample under an ENF load can be realised.

Two different loadings were also chosen for the repair samples. Two were shot at 0.84GW/cm² or 0.73% of the bond threshold. The goal is to see whether S-LASAT has an unseen influence over the samples or not. The last one was shot at 0.99GW/cm² which is the energy prior to the debonding of the sample. Intensities are summarised in Table 4-20.

Intensity (GW/cm²)	P-RE	R-RE	Nb
0.84	X	X	2
0.99		X	1
0.57	X		1

Table 4-20 Intensities used to shoot the different ENF coupons

Figure 4-8 shows the results obtained by the LTSM-UPAT. The bending point on the load-displacement diagram gives the $G_{II}C$ value characterising the energy required to open the bond.
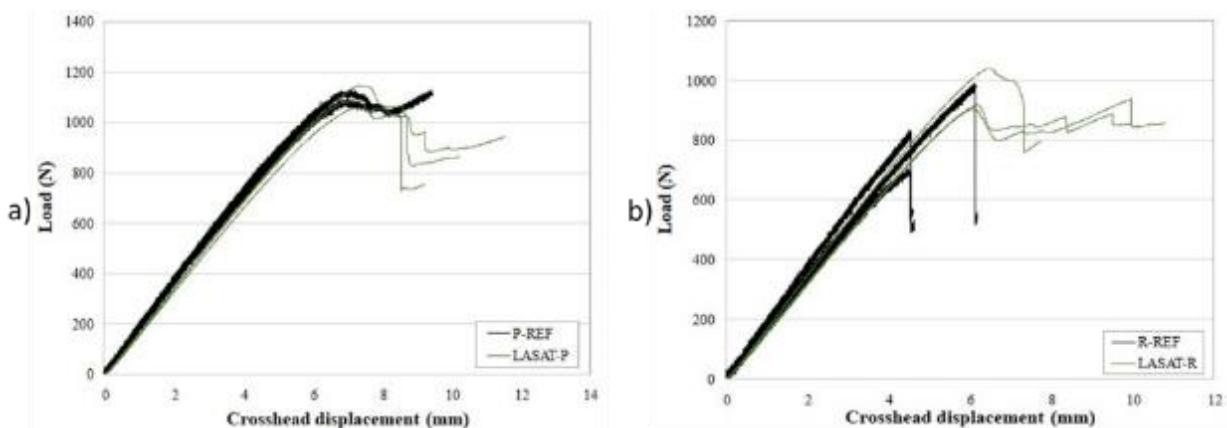
Figure 4-8 Load-displacement diagram obtained by the LTSM-UPAT for: a) production samples b) repair samples

Results for the reference samples that did not undergo S-LASAT are plotted in black. They will serve as a base reference for the S-LASAT samples, plotted in green. The measured $G_{II}C$ values are plotted in Figure 4-9. The average value obtained for the production sample has decreased by 2%. However, this is still within the error range. The repair sample has a decrease of 0.3% of its average value. This is also within the error range, however in this case, an increase of the error bars range was noted.

The study of the crack initiation did not reveal an influence of the S-LASAT over the mechanical properties of the sample. Ehrhart associated the loss of mechanical performances

with the apparition of local microcracks, invisible using US. The time duration of the maximum tensile stress was 4 to 5 times longer than the one of the Hephaïstos facility. Moreover, intensities used by Ehrhart were at about 70% of the threshold, comparable to the one used in this study. The main differences left between the two studies are the spatial repartition of the laser intensity and the load duration. Further comparison would be required to determine the relative importance of these two parameters over the creation of microcracks.
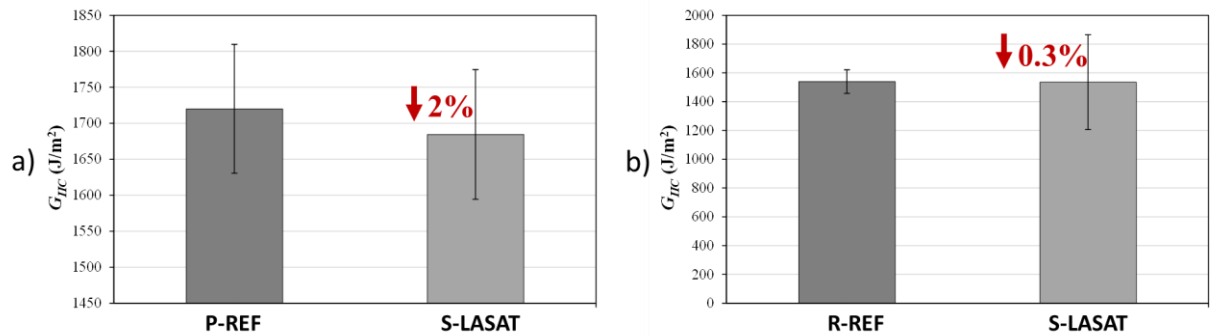
Figure 4-9 GIIC results obtained by the LTSM-UPAT for: a) production samples b) repair samples

3.7.7 Single Shot LASAT

The same experiment as the one described in 3.6 is realised using a single shot setup. Face A is facing the laser beam, so the contaminated surface is closer to the maximum tensile stress location.

Figure 4-10 summarises the results obtained on the production coupon samples. The colour code is the same as before however, using this non-optimised setup, it was most of the time impossible to open the bond before damaging the CFRP laminate. Bond threshold are represented using full bars, but when the laminate would fail before the bond, the laminate threshold is represented using striped bars. The reference threshold is in this case defined as the intensity level that generated the first default, may that be within the CFRP laminate or within the bond. These results are independent of the scanned surface (face A or face B).
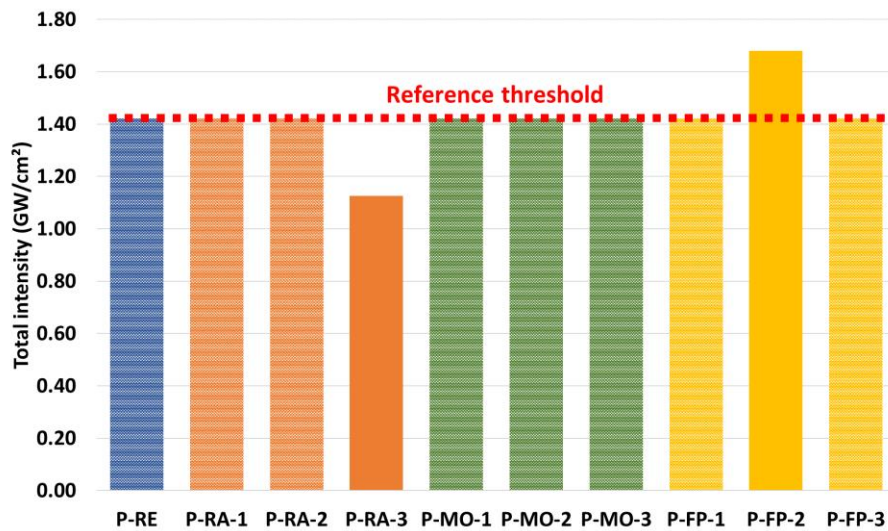
Figure 4-10 Threshold obtained on production samples using single shot LASAT

The value plotted on the graph is the total cumulated energy used for a shot. Apart from RA-3 and FP-2 samples, it was impossible to generate a debonding before damaging the CFRP laminate. Moreover, the FP-2 sample's threshold was above the CFRP threshold found for the reference sample, hence this result will not be considered.

The threshold found were consistent regardless of the tested sample, which was not the case in the experiments not using DOEs. Moreover, the reference level is at $1.40 GW/cm^2$. This value is 40% higher than the bond threshold found for the same sample using S-LASAT, giving a significant error range before damaging the structure.

Figure 4-11 summarised the results for the repair samples. Results for FC samples will be ignored due to the poor initial condition they were in. Once again, the reference sample's bond could not be open before damaging the CFRP laminate. Same for DI-1, DI-2 and TD-1.

Figure 4-12 shows a clear delamination of DI-2 sample towards the back face (face B) of the sample. The US signature (red circle) is rather light when scanned from face A however, the defect can clearly be identified in Figure 4-12 b).
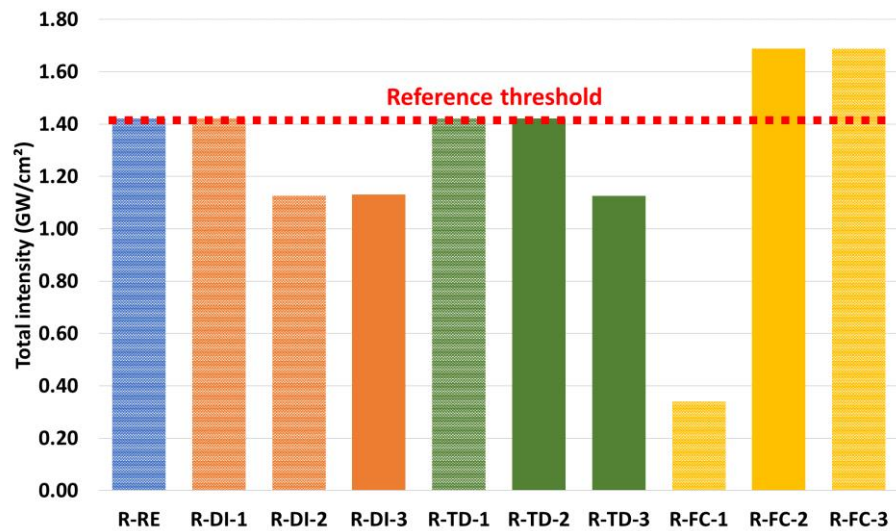
Figure 4-11 Threshold obtained on repair samples using single shot LASAT

Figure 4-13 shows the same US realised for the DI-3 samples. In this case, no delamination seemed to have occurred, and the signal is typical from a debonding. A material problem could explain this loss, but nothing was spotted using ultrasound. A second hypothesis could be that this intensity is right at the threshold, so even if the laser's variation is below the 1% mark, combined with small local material variation due to the fabrication process, it could lead to a jump of threshold value. A finer intensity scan would be required to better understand what happened.
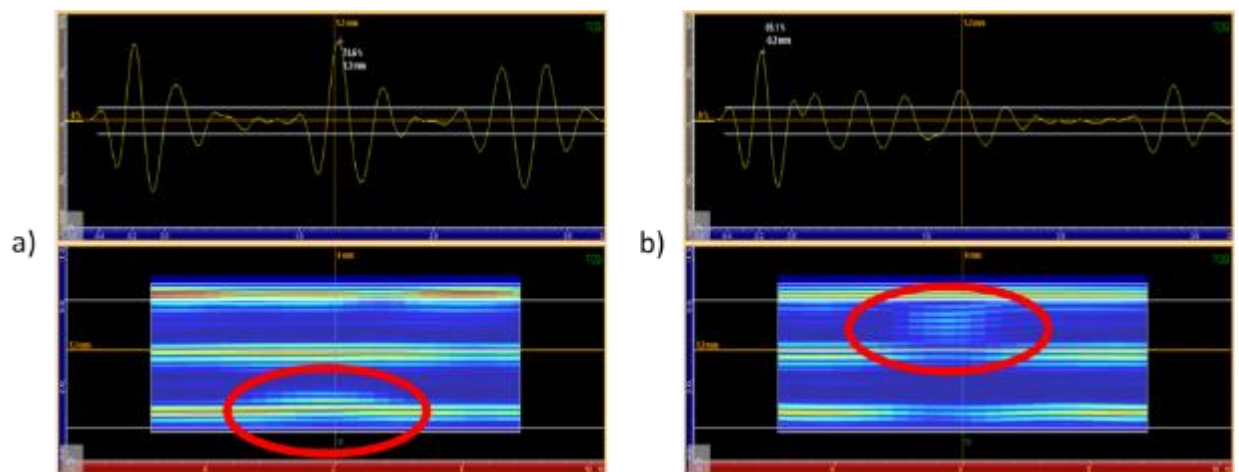
Figure 4-12 US of DI-2 after a shot at 1.14GW/cm² from a) face A b) face B

The same observations were made for TD-1 and TD-2 samples. However in this case, the threshold found for TD-1 was equivalent to the one from the reference sample. The contamination level may have been high enough for a debonding to occur even with a non-optimised technique.
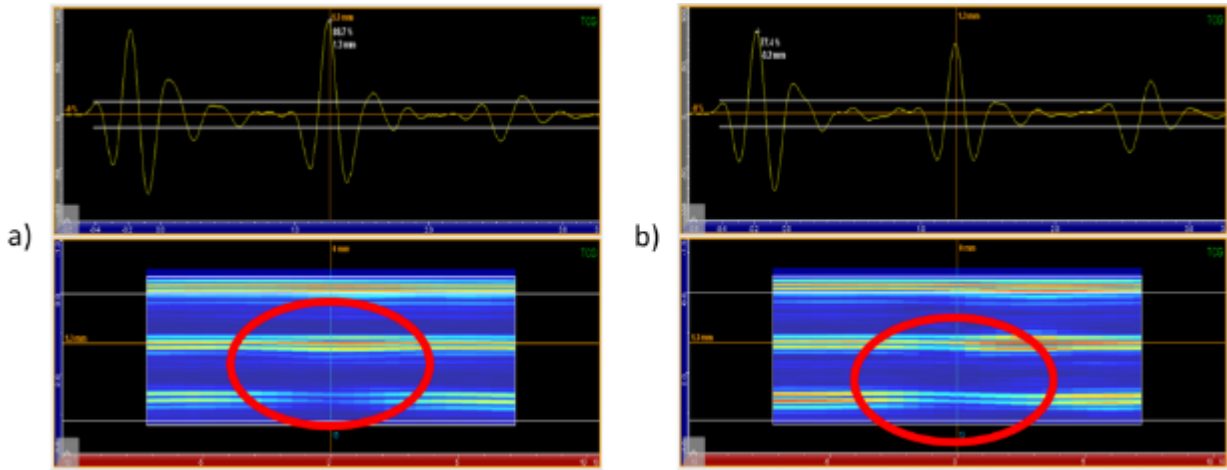
Figure 4-13 US of DI-3 after a shot at 1.13GW/cm² from a) face A b) face B

Laminate thresholds were consistent regardless of the scenario or the contamination. This result could not be achieved previously when no DOE were used, further underlining the necessity of a good control over the spatial repartition of the laser energy.

3.8 Pilot Samples

This section describes results obtained for the scarfed and coupon samples with multiple contaminants. As specified in chapter 2, the curved samples were initially too damaged and have been taken out of the experimental campaign.

3.8.1 Multiple Contaminations Coupons

Results are mixed for coupon samples with multiple contaminations (Figure 4-14). The S-LASAT did not differentiate production samples with multiple contaminations from the reference sample, and the intensity required to open the faulty joints was the same as for the standard. The results are also hard to explain in the repair scenario. The technology detected the least contaminated sample but was unable to clearly detect the most contaminated sample.
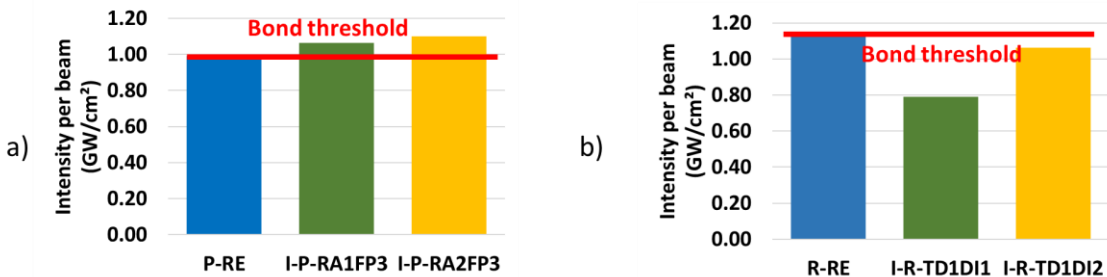
Figure 4-14 Summary of the S-LASAT results of multiple contaminations on coupon samples for a) production samples and b) repair samples.

3.8.2 Scarfed Samples

Scarfed samples have the particularity of having a bond at various distances from the edges of the sample. Three test areas were defined: one with the bond in the middle of the sample and two other zones with the bonds located more towards one face (Figure 4-15).
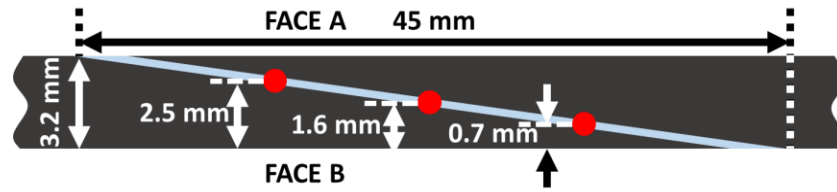
Figure 4-15 Diagram of the bond area of a scarfed sample and S-LASAT tensile stress location (red circles)

The laser only allows to delay beam B from beam A with a positive time value. Hence it is only possible to shift the maximum tensile stress location towards face A. To perform the shot 0.7mm away from face B, the sample needs to be turned around.

The same contaminations on the scarfed samples showed much better results (Figure 4-16). In this case, the LASAT technology was effective at differentiating a sound bond from a weak one. The difference between the results for the multiple contamination on coupon samples and the scarfed samples is not yet fully understood; the bond geometry may have played a role in the crack detection/propagation within the contaminated samples.
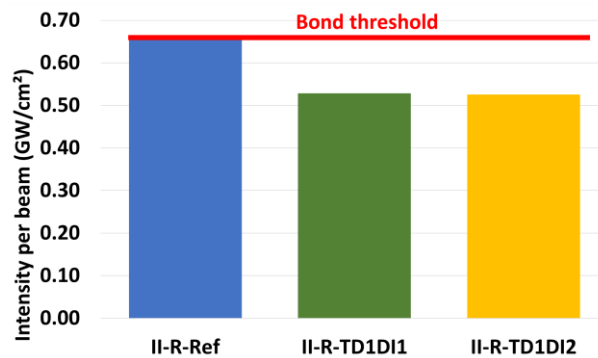
Figure 4-16. Summary the S-LASAT results for multiple contaminations on scarfed samples.

3.9 Real Aircraft Panels

The final validation of the technology is based on the results obtained for the two real panels described in chapter II. Due to the size of these panels, the whole experimental setup had to be modified, as well as the procedure.

3.9.1 Experimental Setup

Both panels are too large and heavy to fit in the specimen holder. There is also the problem of moving the target in order to scan the entirety of the bonded area.

To overcome these limitations, an articulated robot arm (Figure 4-17 b) was installed in Hephaistos facilities. To have enough room for the displacement of these panels, the experimental table was removed, and all the optics were placed on a separated mount (Figure 4-17 a).
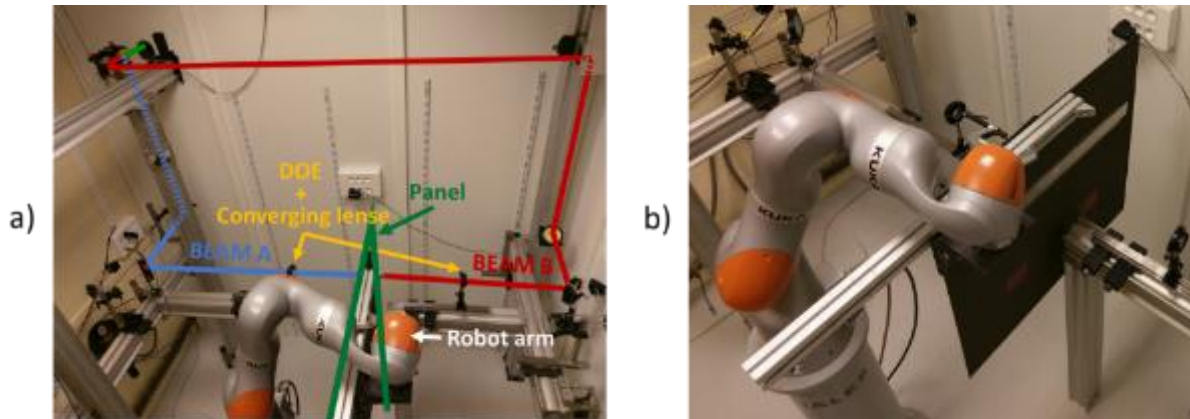
Figure 4-17 a) Experimental setup to test real aircraft panels b) Close-up on the articulated robot arm

Using water confinement was not feasible either, because no water collecting tank were available, instead a solid confinement material in the form of the 9010 SPT Coroplast tape was used (see Chapter II).

Last, US were so far realised using water to ensure a good contact between the probe and the composite structure. This would require unmounting the panel after each shot to lay it flat before performing the US. In order to improve the efficiency of the experimental process, water was replaced by a gelatinous coupling medium that would stay on the panel regardless of the position of the panel. This viscous liquid is however harder to clean, and to ensure a good adhesion between the aluminium tape and the sample, a thorough cleaning of the surface after each scan was required.

3.9.2 Repair Panel

Figure 4-18 a) shows the repair panel after being setup on the articulated robot arm. The pre-defined shot pattern is represented in Figure 4-18 b). 45 different shot areas were defined with a minimum distance between each of them of 1.3mm. Hence, if a shot creates a delamination or a debonding, given the previous observation, it should not affect the surrounding areas.

Two different types of shots were realised. Eleven shots were performed to find and confirm the bond threshold for different areas, and thus depth, of the panel. Single shot areas are marked in blue and the symmetrical ones in red. The remaining 34 shots were realised at 80% of the intensity found to open the bound of a non-contaminated area (green spot for symmetrical and yellow for single shots).
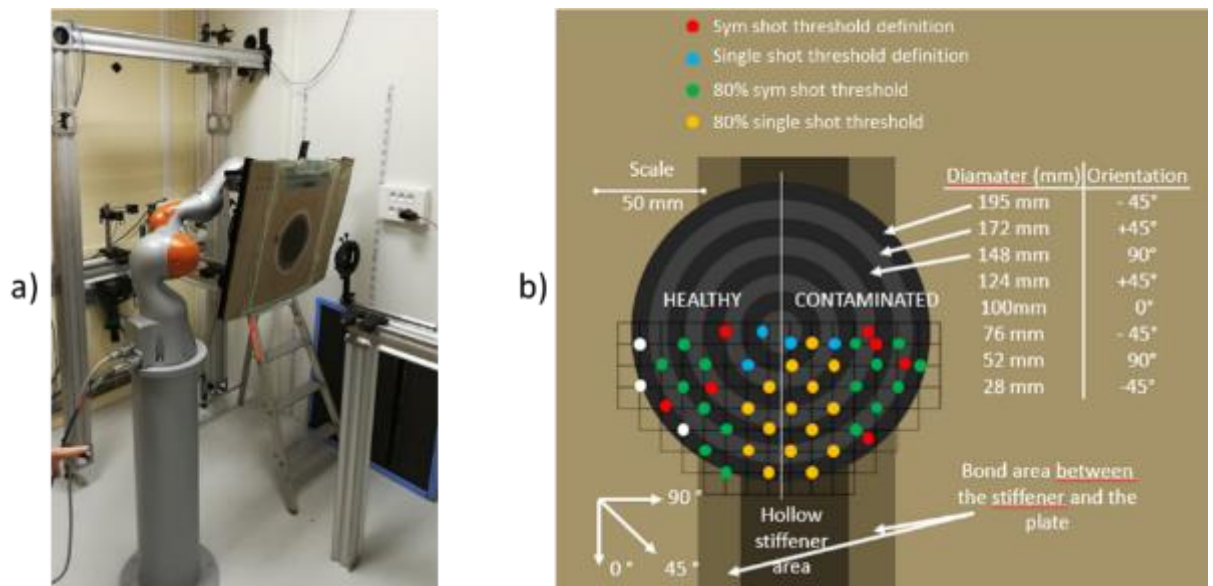
Figure 4-18 a) Setup with the repair panel on the robot b) Geometry of the panel and its complementary patch c) Shots repartition over the panel

Shot results are summarised in Table 4-21. Because the initial bonding quality of the repair panel was not up to the standard, US scanning using the multi-element probe was difficult and the signal was hard to analyse. Hence small variations of the threshold were recorded, especially for the single shot setup. Moreover, because of the variation of depth, and the lack of modularity of the single shot setup, the single shot bond threshold was hard to defined. It was decided to take the smallest value as a reference value.

Due to the lack of space on the repair patch, only one threshold definition was realised on the contaminated side. However, it proved to have a threshold equivalent to the healthy area. The remaining 5 shots on the sound part, and 10 shots on the contaminated one were done at 80% of the defined threshold to mimic the procedure that would be applied on a real repair line.

Panel	Area	SYMMETRICAL SHOT SETUP			SINGLE SHOT SETUP		
		S-LASAT threshold I_t (intensity per beam)	Total number of shots at 80% of I_t	Number of opened bonds	LASAT threshold I_t (total intensity)	Total number of single shots at 80% of I_t	Number of opened bonds
Repair	Healthy	0.72GW/cm²	8	0	0.84GW/cm²	5	0
	Contaminated		8	8		10	2
		Success rate: 100%			Success rate: 20%		

Table 4-21 Shot summary of repair panel LASAT tests

None of the sound area showed signs of damage, however only 20% of the contaminated areas were spotted using single shot setup. With a success rate that low, the non-optimised LASAT could not be used as is.

Results were more consistent using S-LASAT, and no variation of the bond threshold was recorded for a given area (healthy or contaminated). The threshold found was of 0.72GW/cm² per beam, which is lower than the minimal intensity required for the single shot setup. This follows the previous observations made on the coupon samples.
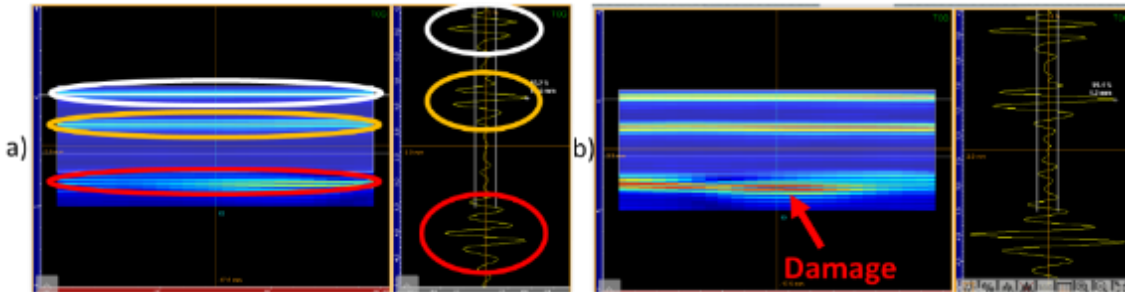
Figure 4-19 US of a S-LASAT area situated on a stiffener a) before the threshold b) after the threshold

The main challenge with the symmetrical areas were their location and the proximity of the bond from the actual side of the repair panel. For example, Figure 4-19 a) shows the US obtained from an area with no debonding. This area is located on the outer complementary ring patch (195mm), meaning there are only two plies left on one side of the maximum tensile stress location. The white circles in Figure 4-19 a) is the entrance echo in the stiffener. The yellow circles represent the interface between the stiffener and the panel. The last red circles show the combined signature of the entrance in the complementary patch and the back-face echo. These two interfaces are comprised within 300µm, making it difficult to separate with the current precision of the US device.

However, as shown in Figure 4-19 b), this was not a problem to assess the presence or not of the damage. Moreover, such off centered position was not an issue for S-LASAT since the time delay between the two beams allowed to properly load the bond, and not the composite laminates.

Number of complementary layers	1	2	3	4	5
Delay (ns)	1290	1085	950	814	685

Table 4-22 Time delay associated with the number of complementary layers over a stiffener

Table 4-22 summarised the time delay associated with each additional complementary layer added on an area with a stiffener. This delay calculation was based on a 190µm thick CFRP ply, a bond of 200µm, and a total thickness, stiffener included, of 4mm. The sound velocity within the composite was estimated at 2800m/s based on data given by US.

As shown in Table 4-21, the success rate using S-LASAT, regardless of the presence or not of stiffeners, was at 100%. None of the sound areas showed delamination or debonding after being shot at 80% of the threshold while this intensity opened all eight contaminated areas.

3.9.3 Production Panel

The same setup as for the repair panel was used for the production panel. Figure 4-20 a) shows the shot pattern used on the sample.
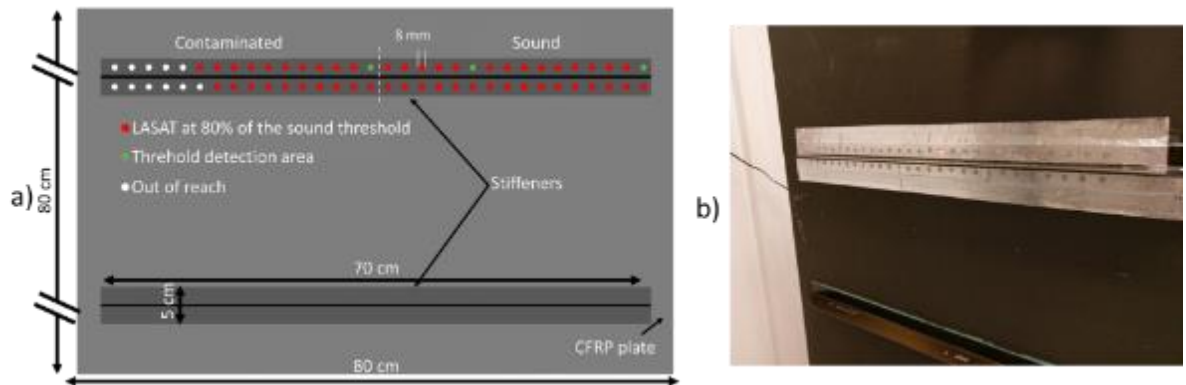
Figure 4-20 a) Diagram of the shots realised on the production panel b) picture of the production panel during the S-LASAT testing procedure

Only one of the two stiffeners were tested. As for the repair panel, a couple of points were used to assess both the sound and the contaminated thresholds. A threshold of 0.63GW/cm^2 was found for the contaminated side on two different spots and a one of 1.05GW/cm^2 for the sound area. The white areas represent the spots that were out of reach using the actual robot setup.

Figure 4-12 b) shows the production panel with both the aluminium sacrificial tape and on top, the solid confinement. The laser energy was set at 3.43J on both beams to generate 0.85GW/cm^2. Results are summarised in Table 4-23.

Panel	Area	SYMMETRICAL SHOT SETUP		
		S-LASAT threshold I_t (intensity per beam)	Total number of shots at 80% of I_t	Number of opened bonds
Production	Healthy	0.85GW/cm^2	32	0
	Contaminated		21	21
		Success rate: 100%		

Table 4-23 Summary of S-LASAT test on the production panel

Overall results are much more consistent than with the repair panel. None of the healthy areas were open at this intensity while all shots realised on a contaminated have been damaged. S-LASAT optimisation was 100% accurate on this test panel.

3.10 TRL Assessment

During his study, Ecault [107] demonstrated the technology reached a Technology Readiness Level of 3: the proof of concept was demonstrated both theoretically and experimentally.

The current study aims at pushing the TRL all the way up to the level 6, demonstrating the capabilities of the technology within a real environment. Table 4-24 summarises the prerequisites to achieve TRL5.

Criterion Code	Criterion Description
TRL5-1	Cross technology effects (if any) identified and established through analysis
TRL5-2	System interface requirements known
TRL5-3	System requirements flow down through work breakdown structure
TRL5-4	System software architecture established
TRL5-5	External interfaces described as to source, format, structure, content, and method of support
TRL5-6	Analysis of internal interface requirements completed
TRL5-7	Interfaces between components/subsystems are realistic (Breadboard with realistic interfaces)
TRL5-8	Significant engineering and design changes
TRL5-9	Coding of individual functions/modules completed
TRL5-10	Prototypes have been created
TRL5-11	Tooling and machines demonstrated in lab
TRL5-12	High fidelity lab integration of system completed, ready for test in realistic/simulated environments

TRL5-13	Form, fit, and function for application addressed in conjunction with end user
TRL5-14	Fidelity of system mock-up improves from breadboard to brassboard
TRL5-15	Quality and reliability considered, but target levels not yet established
TRL5-16	Some special purpose components combined with available laboratory components
TRL5-17	Three view drawings and wiring diagrams existing
TRL5-18	Laboratory environment modified to approximate operational environment
TRL5-19	Initial assesment of assembly needs performed
TRL5-20	Functions integrated into modules
TRL5-21	Individual functions tested to verify that they work
TRL5-22	Individual modules and functions tested for bugs
TRL5-23	Integration of modules/functions demonstrated in a laboratory environment
TRL5-24	Draft Test & Evaluation Master Plan (TEMP)
TRL5-25	Algorithms run on processor with characteristics representative of target environment
TRL5-26	TRL-4 results from testing a laboratory breadboard system are integrated with other supporting elements in a simulated operational environment
TRL5-27	Safety, maintenability, reliability and supportability issues mainly verified
	Overall assessment for completion of TRL-5

Table 4-24 TRL assessment [Airbus]

All of the pre-requisites for TRL5 were checked, validating this level for S-LASAT technology. Moreover, 16 out of the 23 requirements for TRL6 are either fully or partially completed. Further improvements are now required, especially in the full definition of the requirements for an industrial facility to run S-LASAT procedure.

3.11 Comparison with other Post-Bonding Techniques

3.11.1 Comparison on the Provided Samples and Panels

As described in the first chapter, LASAT was not the only technique selected to detect weak bond within a bonded composite structure. Table 4-25 summarises the results obtained for all technologies for coupon samples as well as for the pilot samples and the full-scale demonstration. The blue section shows the results obtained for prebonding techniques while the green one is for the post-bonding ones.

The E-nose seems to be the technology that was the most successful across the different scenarios. It was able to detect each contamination properly and was even able to differentiate the levels of contamination in the case of the pilot samples. The Aerosol Wetting Test (AWT) and LIBS also gave overall good results, except for one type of contamination. Their results on full scale panels are really promising.

For post-bonding techniques, two of them have to be treated separately. The mechanical tests performed by LTSM-UPAT showed really good results, however this is a destructive test. It was important to characterise the contamination sample but it cannot be used as an NDT. The µCT also has limitation especially when the size of the sample becomes too large. Indeed, the larger the sample is, the lower the resolution is. Panels such as the real one tested were too large to be analysed using this technique.

As demonstrated, S-LASAT passed all the detection scenarios, but was only able to differentiate the level of contamination in the TD case. Non-Linear Ultrasounds (NLUS) also produced good results and were in most cases able to go as far as differentiating the contamination levels. However, due to a lack of data on the real panels, no conclusions were drawn at the end of the project. It is however still really promising.

3.11.2 Technologies Comparison on Current and Foreseen Capabilities

Technologies have been compared on ten different technology criterions. There are regrouped in three main categories:

- The technology: its cost, its ease of integration within a industrial environment and its automation
- The process and everything related to the use of the technique: whether the technology is contactless or not, the calibration time, the inspection time of a 200x200mm sample, and the time required to gather all the data.
- Operation related pre-requisites: accessibility of the technology to new operators, the required warm up time and the consumables cost.

Indeed, if the detection capabilities of the technology is the key factor, all these parameters could influence on the final decision concerning the use or not of a technology within Airbus facilities.

ENDT	COUPONS						PILOT & FULL SCALE	
	PRODUCTION			REPAIR			PRODUCTION	REPAIR
	MO	RA	FP	DI	FP / FC	TD	RA+FP	R – DI+FP
OSEE	V	V	V	V	V	X		
LIBS	X	V+	V	V+	V+	X	V	
E-nose	V	V	V	V	V	V	V+	V+
Vibrometry	V	X	X	X	X	X		X
LIF	X	X	X	X	X	$V_{220°C}$		X
Bond Insp	V+	V+	V	V	X	V	V	V+
FTIR	V+	X	X	V+	X	V+	X	$N^{more\ data\ needed}$
Mech. test	V+	V+	V+	V+	V+	V+		
US	X	X	X	X	V+	V+		
μCT	V	V	V	V	V	V		
EMI	V	X	X	X	V+	V	N	X
MGSS	X	X	V	X	V	V	X	V^{FP}
NLUS	V	V+	V+	V+	V+	V+	$N^{more\ data\ needed}$	$N^{more\ data\ needed}$
LASAT	V	V	V	V	V	V+	V	V
CAPTION	V+: Detection & discrimination – V: detection – X: no detection/ not conclusive – N: Partial/ doubts remain							

Table 4-25 Summary of ComBoNDT technology performances [ComBoNDT deliverable 05/18]

Table 4-26 summarises the data gathered for each technology concerning all ten parameters. When possible, a comparison between the current and foreseen state of a technique was realised. Three grades could be associated to a parameter:

- A: the parameter is a strong advantage of the technology and will not represent any challenge.
- N: this parameter does not come with the technology right out of the box. A little bit of work is required
- C: this parameter is a constraint. It is money and/or time consuming

LASAT has currently three main constraints. The first one is the price of the technology. More specifically the price of the laser. However, this technology is quickly evolving. For example, over the course of 4 years, the size of the GAIA-HP laser produced by Thales and used in Hephaistos was divided by two (GAIA-I). This high price is also linked to all the security requirements for such equipment, referred to as "integration" in the chart: closed environment, specific optics, … However, with the reduction of the laser size as well as optic fibre beam transportation, future installation may not need such sophisticated facilities in order to perform LASAT, hence the foreseen "N" grade.

ENDT	TECHNOLOGY					PROCESS					OPERATIONS		
	Cost	Integration		automation		Contact less	Calibration time	Insp. Time (20*20)	Processing		Operator training	Warm up	Consumable costs
		current	foreseen	current	foreseen				Pre	Post			
OSEE	N	N	A	N	A	Yes	N	60s	A	A	A	A	A
LIBS	N	A	A	A	A	Yes	A	30s	A	A	A	N	A
E-nose (it)	A	N	A	N	A	No	N	5 min	A	A	N	N	A
E-nose (D)	A	A	A	A	A	No	N	5 min	A	A	A	N	A
Vibrometry	C	A	A	A	A	Y/N	N	60 min	A	A	A	A	A
LIF	N	N	A	A	A	Yes	A	10 min	A	A	A	A	A
Bond Insp	N	A		A		Yes	10 min	<10m/m²	A	A	A	A	A
FTIR	N	A	A	A	A	No	A	15 min	A	A	N	A	A
µCT	C	A	A	A	A	Y/N	N	20 – 60 min	A	C/A	C	A	A
EMI	A	A	A	A	A	No	N	60 min	A	A	A	A	A
MGSS	A	N	N	N	A	No	A	5 min	N	N	A	A	N
NLUS	N	C	N	C	N	No	N	5 min	A	A	N	A	A
LASAT	C	C	N	N	A	Yes	N	2 min	A	N	C	A	N
CAPTION	A: Advantage/ easy/ low cost – N: neutral/ easy to overcome – C: Constraint/ costly												

Table 4-26 Summary of the technologies current and foreseen capabilities [ComBoNDT deliverable 05/18]

The other significant limitation at the time of writing this manuscript, is the operator training. Because of the security requirements, the operator needs a specific laser training in order to use the technology. Moreover, a certain level of US expertise is required in order to analyse post-shots scans.

The main strengths of the technology are the inspection time, and its contactless use. The latter point ensures nothing needs to be fixed to the testing panels, facilitating the automation of the whole process.

The specified inspection time (2 minutes) for the 20x20 cm panel is an estimation based on the full scan of the sample. However, this may not be required and only part of the sample could be analysed in order to validate the whole part. This is still under discussion, and further studies would be required to confirm it.

3.12 Conclusion

The addition of the DOE allowed a better control of the loading provided under a symmetrical laser shock. It led to an increase of the overall precision of S-LASAT technique.

On coupon samples, the threshold obtained for the reference samples were higher than the one on the contaminated one, regardless of the contamination. On two of the five validated contaminations different thresholds were also found depending on the level of contamination.

The same study was performed using a standard single shot setup. Apart from 4 of the highest contaminated sample all of the remaining thirteen samples have seen their CFRP laminate destroyed, rendering this single shot setup not fit for this type of test. These observations were similar as the one found by Ecault [107].

In his study, Ehrhart [39] also underlined that performing the single shot LASAT could have a negative influence on the bond mechanical properties. Along with LTSM-UPAT, GIIC test were performed on samples shot at various percentages of the reference coupon threshold using S-LASAT. Initial conclusions did not show any loss of mechanical properties of these samples.

Studies realised on pilot samples had mixed results. The curved samples had to be removed from the test scenario due to poor manufacturing, and the multi-contamination on coupon type samples did not show convincing results. However, S-LASAT showed much better results with similar combination of contaminants on the scarfed samples. Moreover, symmetrical laser shock showed its modularity potential by opening the bond regardless of its relative depth.

The final prove was realised on two real panels, one typical of the production line, the other one from the repair line. The whole setup had to be rearranged and new features such as the solid confinement or the automated robot arm were used in order to process these parts.

Because of its geometry and the presence of stiffeners on one side of the repair panel, S-LASAT could only be partially used, the remaining area of the panel was tested using the non-optimised LASAT. The latter only managed to generate an opening on 20% of the contaminated area, failing the test. However, the same shots using S-LASAT showed a success rate of 100%.

The production panel was easier to test since, regardless of the area, both sides of the panel were reachable. The laser intensity was set at 80% of the bond threshold, and after testing the whole stiffener, the healthy areas returned negative to damage after inspection while all of tests realised on the contaminated areas generated an opening on the bond. This last test showed a 100% success rate when using S-LASAT, confirming the results previously obtained on the coupon samples.

The evaluation of the technology at the end of the project also showed promising results. If it falls a little short from TRL6 in its current state, most of the prerequisites are currently being implemented, most of them being linked to documentation for S-LASAT. The main constraints of the technology have also been identified, and solutions such as full automation or fibred laser are currently investigated to limit their impact on S-LASAT implementation.

CONCLUSION

There is nowadays a need for NDT solution to assess the integrity of bonds for bonded CFRP assemblies in the aeronautic industry. Used on production lines, bonded structures could help optimising composite parts which are currently over-sized due to the historical use of mechanical assemblies such as rivets or bolts. On repair lines, it could enable the use of patches to repair CFRP structures instead of replacing complete panels. In his study, Ecault showed the good potential of LASAT for the detection of weak bonds within composite structures. However, due its lack of modularity in the localization of the maximum tensile stress area, this technique tended to damage the CFRP assembly as well as the bond in presence of weak bonds. Hence, the technique could not be considered non-destructive.

Realised within the framework of the European project ComBoNDT, this work had for main purpose the study of one optimisation suggested by Ecault: S-LASAT. Series of contaminated samples were produced using know contaminants specified by Airbus. Each series was scanned using US to show no default were inherently spotted by standard NDT, and some of them were also mechanically tested using both GIC and GIIC tests to assess the mechanical loss generated by the contamination of one of the bonded surfaces.

Initial S-LASAT experiments performed within Hephaïstos facility showed that by using symmetrical laser shocks, it is possible to open a bond without damaging the CFRP assembly, regardless of the presence or not of contaminant. However, the energy levels required to open the bond or the CFRP laminate itself was too erratic from a sample to another, making it impossible to assert whether or not a bond was contaminated. This study also revealed that the technique requires a high level of mastery of both the intensity level and the energy repartition of each beam.

The wide range of intensity used has shown that passed a certain intensity level, the CFRP structure would get damaged, but not the bond. This phenomenon was associated with the intrinsic mechanisms of S-LASAT. Indeed, time-wise, secondary tensile stress locations are generated by the reflection of the two shockwaves generated by each beam. However, if part of their energy is used to open the CFRP laminate, no enough energy remains when later both release waves criss-cross, living the bond intact.

Moreover, initial results showed small and off-centered debonding. These cracks were associated with the heterogeneity of the laser beams. To confirm this hypothesis and better

understand the physics behind these local damages, a finite element model was implemented. An Abaqus VUMAT was created based on Ecault's LS-DYNA simulations. However, due to a high computational time required to perform these simulations, a simplified isotropic model was eventually used to apprehend the overall behaviour of shockwaves during S-LASAT. Combined with a DOX, this model showed that it was not possible to overcome the effect of the inherent irregularities of Hephaïstos. To overcome the problem, DOE were installed on the experimental setup, and the new spatial distribution of the intensity was validated using the same FE model.

The implementation of DOEs on the experimental setup drastically improved the results obtained on the coupon samples: regardless of the contamination, it is now possible to distinguish a contaminated sample from a healthy one, solely on the intensity level required to open the bond. Similar observations were made on the scarfed samples. However, mixed results were obtained for samples including several contaminants at once.

During his study, Ehrhardt noticed that the LASAT could lower the mechanical strength of a bond even when intensities were below the bond threshold. A similar study was realised with the LTSM lab from Patras University using S-LASAT over GIIC samples. No mechanical loss was recorded on samples tested using S-LASAT, even when shot at intensities as high as 90% of the bond threshold were applied.

Final tests executed onto a repair panel showed that S-LASAT can be applied on more complex structures with off-centered bonds and yet be able to assess the integrity of a bond given a reference level obtained on a healthy area. It also showed that one of the main limitations of the process in its current state, is the need to have access to both sides of the bonded area. When this is not possible, the non-optimised LASAT does not suffice to assess the bond quality. However, for more accessible parts, such as the production panel where the whole piece was tested using S-LASAT, a 100% detection rate was achieved.

All implementations made on the facility such as the DOEs, solid confinement or the installation of a robot allowed the technology to validate TRL5.

PERSPECTIVES

NUMERICAL

The implementation of specific user defined constitutive law required important development efforts and resulted in numerical simulations with high computational time. However, Ecault's model using LS-Dyna software proved to be at least as effective for LASAT simulations than the model realised on Abaqus and yet required less computational time.

Coupled with a shadowgraphy study of the symmetrical shot, his model could be validated for S-LASAT and used to generate more precise data, especially on the conversion between the laser intensity and the generated pressure within the sample. Important information such as the size of the tensile stress area could also be studied with this model.

An alternative for these simulations is the use of response surface-based simulations. The idea is similar to the numerical study realised in this manuscript using DOX. Instead of launching calculations for each specific case, a value range is assigned to all input parameters. The output of these simulations is map of all outputs obtainable with the initial range of inputs, using both simulated and interpolated values.

Currently the Proper Generalised Decomposition (PGD) [162] works in a similar fashion. After defining each parameter value range as well as the desired outputs (for example stresses along a specific direction), the simulation is run over and over until a complete mapping of the output is realised. The main strength of this method is its computational time. Through a decomposition of each dimension during the calculation process, this method reduces the number of degrees of freedom, thus decreasing the required computational. Once a database with the wanted response surface is generated, the output for any input values within the defined range becomes instantaneous. This database is comparable to an abacus.

EXPERIMENTAL

Despite the good results given by S-LASAT, more advanced physicochemistry studies are now required. Indeed, it has been noticed that the type of contaminant can have a direct impact on the way the bond reacts under a shock load: RA contaminations showed a clear crack propagation while DI samples tend to produce lots of microcracks.

Initial observations have been made on the effect of S-LASAT onto the mechanical properties of a healthy bond. Results were promising, but more thorough study is required to fully confirm these observations.

The use of a solid confinement was required in this study and will be as well for industrial usage. The thick transparent adhesive tape gave good results. However, a more polymer-based approach could enhance the current capabilities of solid confinements. A specific constraining medium could be formulated for LASAT applications and produced with an integrated sacrificial layer to further improve the robustness of the technique.

Last, the way a part is scanned using S-LASAT method needs to be discussed. Should the panel be completely scanned? Would a partial scan be enough to ensure the bond quality of the whole part? This parameter is user dependant and may vary from one industrial partner to another.

DETECTION DE JOINTS FAIBLE AU SEIN DE STRUCTURES PRFC A L'AIDE DE CHOCS LASER SYMETRIQUES

INTRODUCTION

De par leurs très bonnes performances mécaniques et leur faible poids, les matériaux composites sont de plus en plus utilisés, notamment dans le domaine de l'aérospatial. Par exemple, en 2005, l'A380 était constitué à 23% de matériaux composites et huit ans plus tard, pour l'A350 XWB, ce ratio dépasse les 50%.

Cependant, bien que les matériaux utilisés aient évolués, les techniques d'assemblages sont restées les mêmes. Les techniques traditionnelles basées sur l'utilisation de boulons ou de rivets ne sont plus adaptés à ces nouveaux matériaux. En effet, parce qu'elles nécessitent un perçage, ces méthodes d'assemblages créent des contraintes locales et favorisent la corrosion, notamment pour les structures en PRFC (Polymère Renforcé en Fibre de Carbone).

L'utilisation d'adhésifs serait une solution beaucoup plus adaptée. Mais, bien que des colles capables de jouer ce rôle existent déjà sur le marché, il n'existe pour l'heure aucun Test Non-Destructif (TND), capable d'évaluer les propriétés mécaniques de ces assemblages collés. Il n'est donc pas possible de repérer des défauts d'assemblage comme les « joints faibles », i.e. des joints dont les propriétés mécaniques ont été dégradées.

Le Test d'Adhérence par Choc Laser (LASAT) a d'ores et déjà montré sa capacité à détecter ce genre de défauts dans des structures PFRC. Le travail présenté dans ce document s'intéresse à l'une des optimisations de la technique, le LASAT Symétrique (S-LASAT). Cette étude a été réalisée dans le cadre du projet européen ComBoNDT.

Le **Chapitre 1** s'intéresse aux principaux défis liés au collage de structures composites PFRC. Il y sera également introduit la technologie LASAT avant de conclure sur les principaux objectifs de la thèse.

Les outils expérimentaux sont présentés dans le **Chapitre 2**. Y sont décrites les principales caractéristiques ainsi que les améliorations apportées à la plateforme Héphaïstos, utilisée pour générer l'intégralité des données de cette étude. Le processus de créations des échantillons contaminés y est également décrit.

Le **chapitre 3** s'intéresse aux premières expériences réalisées sur la plateforme Héphaïstos, et analyse à l'aide de simulations numériques, les résultats obtenus. Il souligne notamment l'importance d'une bonne distribution spatiale de l'intensité laser au niveau du point focal et la nécéssité d'utiliser des lames de phases (Diffractive Optical Element – DOE).

Basé sur ces observations, un nouveau banc expérimental est mis en place. Les résultats obtenus avec cette nouvelle configuration sont analysés dans les **Chapitre 4**. De plus, une première dans la validation du caractère non destructif du S-LASAT est proposée grâce à une étude faite conjointement avec le laboratoire LTSM de l'université de Patras. Les capacités de la technique sont également testées sur de vraies pièces d'avion, permettant de conclure sur le taux de maturité de la technologie (Technology Readiness Level – TRL), ainsi que ses performances comparées aux autres solutions proposées par les partenaires du projet européen.

Une **Conclusion Globale** ainsi que des **Perspectives** pour cette technologie complètent ce document.

Chapitre 1.   CONTEXTE ET ETAT DE L'ART

1.1 Contexte

La réduction de l'empreinte carbone est un défi auquel beaucoup d'entreprise doivent faire face. Cela est notamment vrai pour les entreprises dans le domaine du transport où beaucoup de réglementations ont été définies ces dernières années [1]–[4].

En ce qui concerne les entreprises dans le domaine de l'aérospatial, l'Association Internationale du Transport Aérien (AITA), a défini un certain nombre d'objectifs à atteindre d'ici 2050, dont notamment la réduction de l'émission de CO2 par les transports aériens [6]. Des avancées notables ont déjà été réalisées dans le domaine, avec par exemple le développement du moteur LEAP qui a permis une réduction de 15% la consommation en carburant des A320 et C919.

Cependant, les objectifs définis par l'AITA ne sont pas encore remplis et de nouvelles pistes de recherches sont à l'étude [7]–[10]. L'une d'elles est l'allègement des structures. Cela passerait par l'optimisation des designs actuels ou l'utilisation de nouveaux matériaux comme les matériaux composites. Ces matériaux ont déjà été utilisés avec succès dans la conception du A380 et plus récemment de l'A350 XWB et du 787 Dreamliner.

Cependant, l'utilisation de composites pose actuellement un problème majeur : les techniques d'assemblage telles que le rivetage ou le boulonnage ne sont pas adaptées aux matériaux, créant des contraintes locales et favorisant la corrosion [12].

L'utilisation de colles en lieu et place des rivets permettrait de palier au problème, et d'avoir une meilleure optimisation des structures. Il est estimé qu'à terme, l'utilisation d'adhésifs permettrait de réduire jusqu'à 15% la masse totale de l'avion [107].

Il reste cependant certains verrous à cette technique, l'un d'eux étant la détection de joints faibles. Un joint est qualifié de faible quand sa tenue mécanique est inférieure à sa tenue nominale. Cette situation peut arriver quand l'une des surfaces collées a été contaminée (humidité, empreinte de doigts, …)

 Il est actuellement impossible pour les Tests Non Destructifs (TND) standards comme les ultrasons (US) de détecter ce genre de défaut. En effet, il est nécessaire de stimuler le joint mécaniquement pour repérer un joint faible et pour le moment seul des tests destructifs comme le GIC en sont capables.

1.2 Le Projet Européen ComBoNDT

De 2010 à 2014 le projet européen ENCOMB (Extended Non-destructive testing from COMposites Bond) s'est intéressé au problème des joints faibles. En 4 ans, 31 différentes solutions pour repérer ou prévenir ce genre de défaut ont été évaluées. A terme, seul 8 techniques ont été retenues pour figurer dans le projet ComBoNDT.

Ces techniques se divisent en deux groupes : celles destinées à repérer une contamination de surface lors du collage et celles proposant une détection des joints faibles après l'assemblage de la pièce.

Le projet européen ComBoNDT commencé en 2015 et faisant parti du framework H2020 a eu quant à lui pour but l'augmentation du taux de maturité (TRL) de chacune des technologies sélectionnées. Tout comme pour ENCOMB, un certain nombre de contaminants sont sélectionnés et « ajoutés » à des assemblages PRFC collés. La principale différence réside dans les niveaux de contaminations beaucoup plus bas pour ComBoNDT, plus proche de ce qu'un industriel comme Airbus voudrait détecter (Figure 1-1).
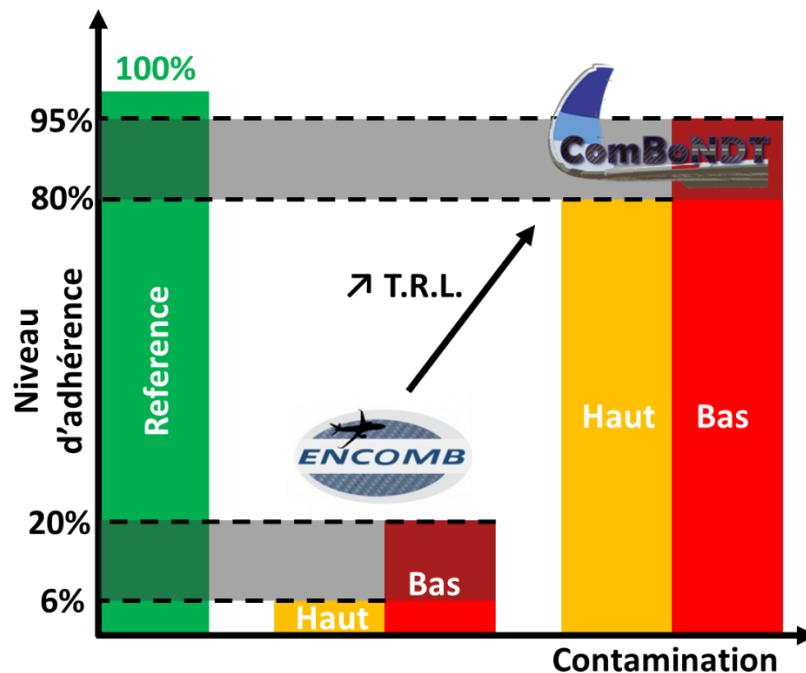
Figure 1-1 Comparaison entre les niveaux d'adhésion étudiés durant ENCOMB et ceux prévus par le projet ComBoNDT

En plus de permettre aux technologies d'affiner leur détection, le projet veut leur faire atteindre le TRL 6 correspondant à un taux de maturité permettant l'industrialisation du procédé.

1.3 Le Test d'Adhérence par Choc Laser (LASAT)

La méthode étudiée dans ce document est le test d'adhérence par choc laser, ou LAser Choc Adhesion Test (LASAT). Cette méthode repose sur la recombinaison d'ondes de chocs générées par choc laser. Cette technique permet la création d'une zone de traction localisée dans le matériau.

1.3.1 Choc Laser et Zone de Traction

Un faisceau laser est focalisé sur l'une des surfaces de l'échantillon, créant au contact du matériau un plasma chaud et dense. Ce plasma se dilate rapidement, et par effet d'action / réaction (3ème loi de Newton), exerce une pression sur l'échantillon (Figure 1-21 a) [83].
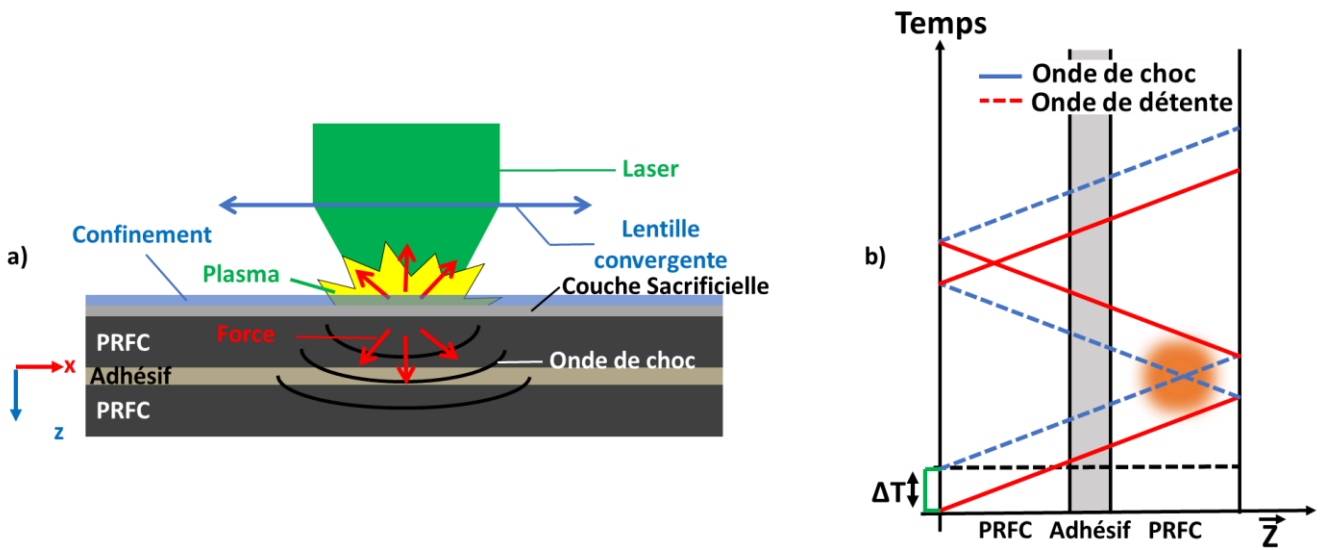
Figure 1-21 a) Principe du choc laser b) Diagramme espace/temps d'un choc simple

Le confinement (en bleu sur la Figure 1-21) permet, pour une même intensité, de démultiplier la pression générée [84], [85]. La couche sacrificielle quant à elle a un double rôle : elle permet à la fois de protéger l'échantillon (notamment des effets thermiques du choc) et un meilleur contrôle de la pression appliquée en assurant une interaction laser/matière constante d'un tir l'autre.

La Figure 1-21 b) est un diagramme XT ou espace/temps, schématisant le comportement de l'onde de choc dans le matériau. L'onde de choc est représentée en rouge, et l'onde de détente permettant le retour du matériau à son état de pression initial en bleu. A l'intersection de l'onde de choc réfléchie en onde de détente, et de l'onde de détente incidente, une zone de traction est créée.

1.3.2 LASAT et Verrous

Correctement positionnée, cette zone de traction permet de tester le niveau d'adhérence de joints d'adhésifs. Initialement utilisée pour l'adhérence de revêtements fins [91]–[94], plusieurs études montrent les capacités de la technique sur des empilements plus épais [95], [96] et furent étendues aux assemblages composites [98], [99]. Gilath a été le premier à se servir de la technique pour tester le niveau d'adhérence de joints collés [97].

Lors du projet ENCOMB, Ecault arrive, à l'aide du LASAT, à différencier des joints aux propriétés mécaniques dégradées de joints sains [100], [107]. Cependant, il montre également les limites de la technique. En effet, la zone de traction générée est toujours située à l'intersection des deux ondes de détentes, qui sont elles-mêmes directement liées à la durée d'impulsion du laser, propriété intrinsèque du laser. Ce manque de souplesse sur le positionnement de la zone de traction se traduit par des endommagements parasites dans le composite lui-même et non le joint de colle. Au point que le LASAT ne peut plus être considéré comme non destructif.

1.3.3 Optimisations

Au terme de son étude, Ecault propose deux optimisations du procédé pour permettre de contourner ce verrou.

La première est le double choc frontal. Deux chocs sont réalisés en face avant de l'échantillon. Une première zone de traction est créée en face arrière comme pour le choc simple. Une seconde zone est générée à l'intersection de l'onde de choc réfléchie du premier impact, et de l'onde de détente du second impact. Le positionnement de la seconde zone ne dépend plus des paramètres du laser, mais du délai entre chacun des tirs.
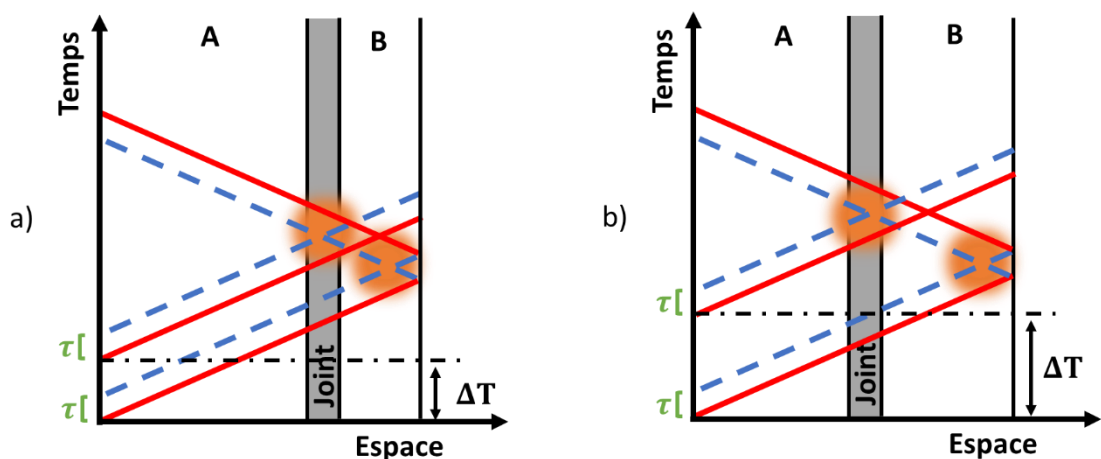
Figure 1-3 Digramme du double choc frontal avec deux décalages temporels a) dans le cas d'un joint décentré b) dans le cas d'un joint centré

Comme le montrent les Figure 1-3 a) et b), cette technique permet de localiser la traction sur le joint quel que soit sa position [108]–[110].

Cependant, le niveau de contrainte au sein de la seconde zone de traction est, dans un cas idéal, aussi important que dans la première. Donc, si la différence de propriétés mécaniques entre le substrat (partie collée) et le joint de colle est trop proche il est pour le moment impossible d'effectuer un test d'adhérence laser sans être destructif [108]–[110].

La seconde optimisation proposée par Ecault est le choc symétrique, ou S-LASAT. Un impact laser est réalisé de part et d'autre de l'échantillon. Comme pour le choc simple, chaque choc va entrainer la création d'une zone de contraire, qualifiée de secondaire ici, proche de la face opposée de l'impact (zones vertes sur les Figure 1-). En se recombinant, une zone de traction plus intense est créée (zones oranges sur les Figure 1-). On la qualifie de zone de contrainte principale.
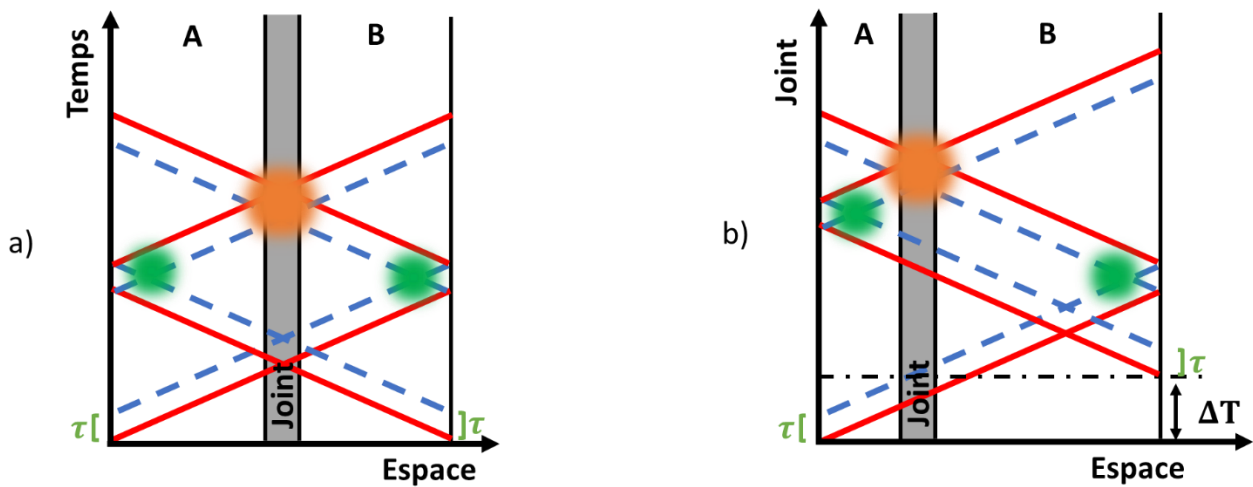
Figure 1-4 Digramme du choc symétrique avec deux décalages temporels a) dans le cas d'un joint centré b) dans le cas d'un joint décentré

Le positionnement de la zone de traction dépend uniquement du décalage temporel entre les deux chocs comme illustré par les Figure 1-4 a) et b). Le décalage temporel nécessaire s'obtient directement grâce à la formule suivante :

$$\Delta T = \sum_i t_{l_i} \times \frac{\rho_{l_i}}{Z_{l_i}} - \sum_j t_{r_j} \times \frac{\rho_{r_j}}{Z_{r_j}} \tag{1.29}$$

avec t_{l_i} l'épaisseur de la couche i située à gauche de la zone à tester, ρ_{l_i} sa densité et Z_{l_i} son impédance. Même chose pour les variables avec la lettre "r" qui correspondent aux couches à droite de la zone.

La différence entre les niveaux des zones de contraintes secondaires et principale permet de tester des empilements où le substrat et le joint de colle ont des propriétés mécaniques similaires [112]. Une étude basée sur le principe de l'approximation acoustique réalisée à

l'aide du logiciel python PyHugo permet d'estimer à 1,5 le rapport entre la contrainte principale et les contraintes secondaires dans le cas d'empilements PRFC/epoxy/PRFC utilisés lors de l'étude présentée dans ce document.

La zone de traction est également beaucoup plus localisée temporellement et spatialement dans le cas du choc symétrique, permettant un meilleur contrôle lors du test.

Le principal défaut du choc symétrique est la nécessité d'accès aux deux côtés de l'échantillon ou de la pièce testée.

1.3.4 Détection Ultrason (US)

Le choc laser ne permet pas en soit de révéler la présence d'un joint faible. Il doit être combiné à un TND post-tir qui permettra de déterminer si le joint a pu ou non résister à la traction exercée. Les ultrasons ont largement été adoptés pour la détection de défauts dans les structures composites et métalliques. Ils sont simples d'utilisation et offrent une bonne résolution des défauts. Ils seront utilisés tout au long des études proposées pour vérifier si un joint a passé le test ou non.

Le Gekko™ de M2M est utilisé pour l'application LASAT. Il est utilisé avec une sonde de 32 éléments de 5MHz. La résolution de l'appareil est entre 100µm et 150µm.

1.4 Objectifs de la Thèse

1.4.1 Projet Européen

Le projet européen est divisé en trois grandes phases : tests sur des échantillons écoles en composite, tests d'échantillons à géométries plus complexes et tests sur pièces réelles. Tout au long de l'étude, une attention particulière sera portée sur l'augmentation du TRL de la technologie du S-LASAT tout en essayant d'identifier les capacités de la technologie en termes de détection de joints faibles.

1.4.2 Etude du Procédé

L'environnement d'étude offert par le proket ComBoNDT est une excellente occasion de mieux comprendre certains aspects de la technologie. Ainsi, les principaux axes d'études seront :

- L'influence des paramètres laser sur les résultats (énergie, durée d'impulsion, durée du pulse, …)
- L'influence des paramètres liés au S-LASAT : confinement, précision de la symétrie, …

- Compréhension du comportement d'assemblages collés sous d'importantes contraintes mécaniques.

Chapitre 2.   MOYENS EXPERIMENTAUX

2.1 La Plateforme Héphaïstos

L'intégralité des expériences de cette étude a été réalisée sur la plateforme Héphaïstos au sein du laboratoire PIMM à Paris. La plateforme est utilisée à la fois pour les tests LASAT, mais aussi pour des applications de shock peening.

2.1.1 Le Laser

Un laser Nd:YAG, le GAÏA HP de Thales, est utilisé sur la plateforme. Il émet dans le vert à une longueur d'onde de 532nm. Comparé à un laser Nd:YAG standard à 1064nm, cette longueur d'onde doublée permet une meilleur adsorption de l'énergie laser par des matériaux comme l'aluminium, largement utilisé dans les applications de choc laser.

Le GAÏA se compose de deux lasers polarisés à 90° l'un par rapport à l'autre. Il est donc possible de séparer le faisceau sortant du laser en 2 « sous-faisceaux » simplement à l'aide d'un polariseur. Les termes « voie A » et « voie B » seront utilisés en référence aux deux faisceaux après séparation. Le délai entre les tirs, ainsi que l'intensité de chacun des lasers peuvent être définis via un programme utilisateur, .

Le laser est capable de fournir 2x7J à une durée d'impulsion fixe de 7ns. Cela permet de générer des intensités de l'ordre du GW/cm² pour des tâches focales allant jusqu'à 10mm de diamètre.

2.1.2 Répétabilité des Tirs Laser

L'énergie du laser se règle via un paramètre appelé « transmission ». Il définit la quantité d'énergie du laser passant par une optique en sortie du laser. Sa valeur sur le GAÏA HP va de 5% de l'énergie max, jusqu'à 100%.

Afin de s'assurer que l'énergie fournie par le laser est constante à une valeur de transmission donnée, une série de 15 tirs est réalisée pour 11 valeurs de transmission allant de 5% à 100%. Le test est réalisé pour chaque voie (A et B). Les mesures d'énergie sont réalisées sur le banc expérimental, après la dernière optique. L'intégralité des valeurs d'énergie sont données dans ce document.

Les résultats montrent une variation d'énergie inférieur à 0.1% d'un tir à l'autre, que ce soit pour la voie A (Figure 2-1 a) et la voie B (Figure 2-1 b). Les tirs sont considérés comme reproductibles.
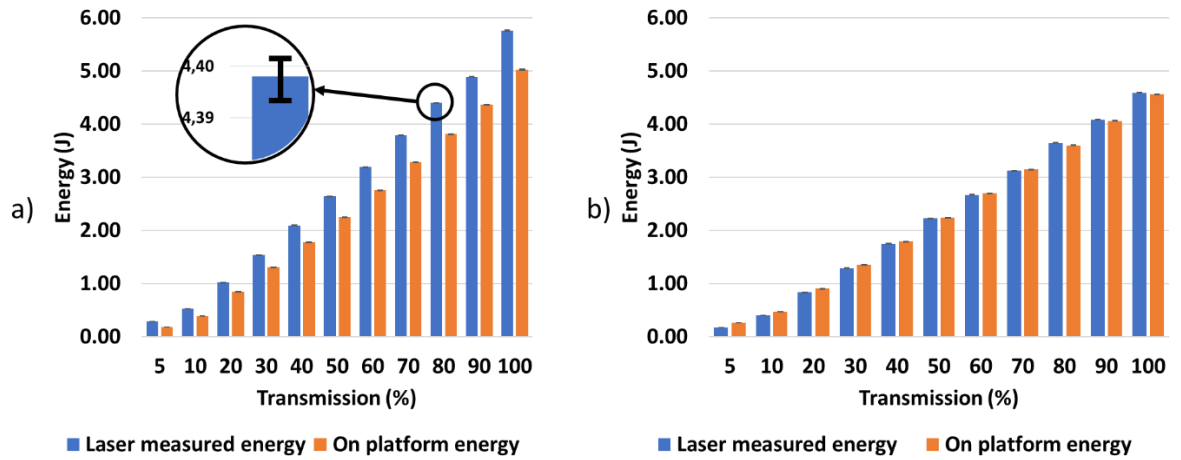
Figure 2-1 Variation d'énergie obtenue pour différent niveau de transmission laser a) pour la voie A b) pour la voie B

2.1.3 Tâche Focale

Deux différentes configurations ont été utilisées lors des expériences. La première n'avait pas de lame de phase inclue dans le chemin optique. L'empreinte de la répartition spatiale a été capturé à l'aide d'une caméra placé en lieu et place de l'échantillon.
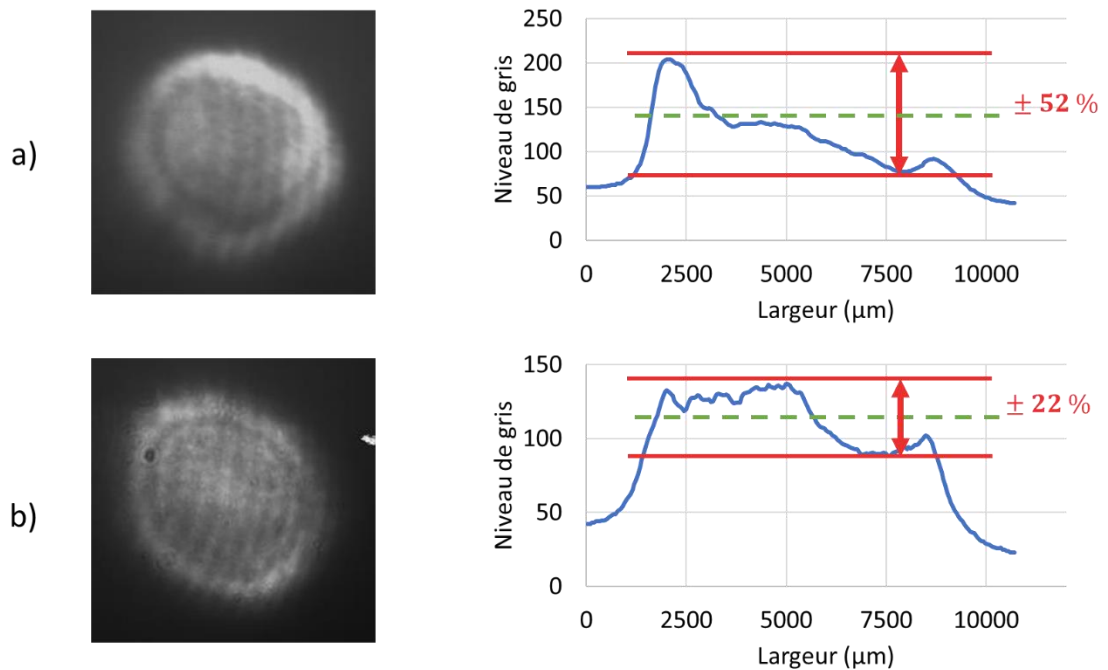
Figure 2-2 Répartition spatiale du laser pour une tâche focale de 8mm pour a) la voie A b) la voie B

La Figure 2-2 montre une importante variation d'énergie sur la tâche avec des différences d'intensité allant du simple au double du point le moins éclairé au point le plus éclairé. Aucune symétrie n'est également observée.

La seconde configuration avait une lame de phase placée juste avant la dernière lentille convergente du chemin optique. Le but des lames de phase ou DOE est, dans ce cas, d'améliorer la répartition spatiale de l'énergie au niveau de la tâche focale.
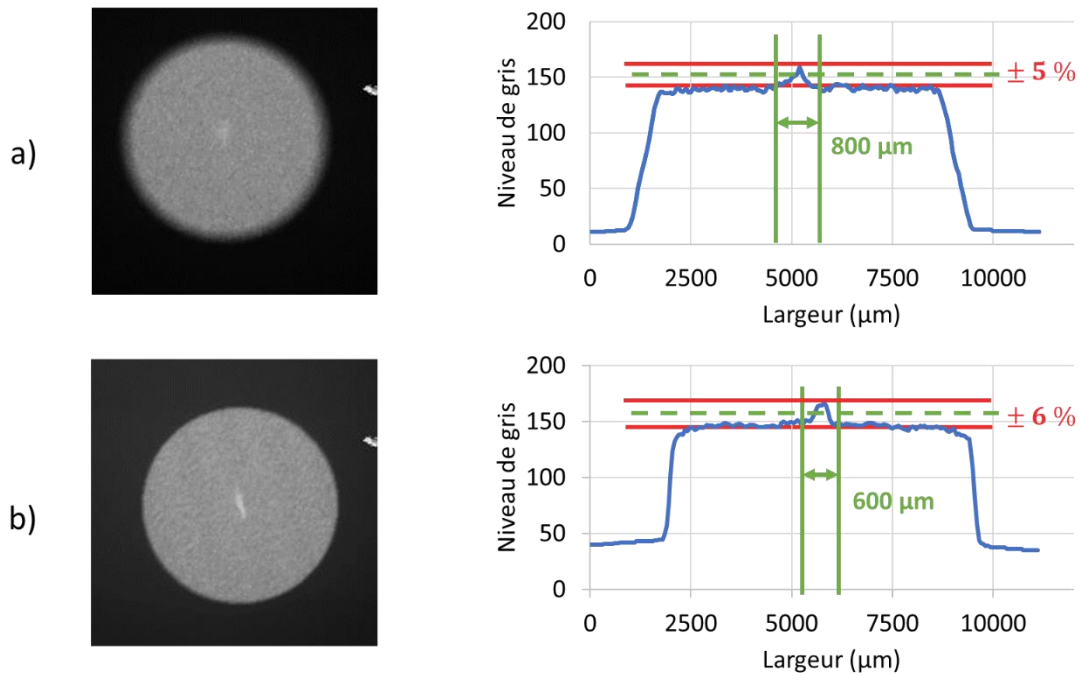
Figure 2-3 Répartition spatiale du laser, avec DOE, pour une tâche focale de 8mm pour a) la voie A b) la voie B

Prise de la même façon que dans la Figure 2-2, les empreintes de la voie A (Figure 2-3 a) et de la voie B (Figure 2-3 b) avec DOE sont beaucoup plus homogènes. Peu de variation d'énergie est enregistrée, et une bonne symétrie est observée.

2.1.4 Confinement et Couche Sacrificielle

Par sa simplicité d'accès et de mise en place, l'eau est le confinement le plus souvent utilisé. Il permet de travailler avec des niveaux d'intensité allant jusqu'à 6GW/cm² avant d'atteindre le seuil de claquage [109], [120]. Courapied a également étudié les performances d'autres matériaux pouvant servir au confinement comme le verre ou des vernis, le critère principal étant la bonne transparence du milieu à la longueur d'onde du laser. Son étude permet d'isoler un adhésif double face de Coroplast™ substitut efficace à l'eau. Ce confinement solide présente notamment l'avantage d'être plus facile d'utilisation que l'eau : simple à mettre en place, aucun système de récupération n'est nécessaire lors des expériences.

Dans une seconde étude, Courapied et El-Karnighi-Tanguy ont également défini les propriété optimales que devrait avoir une couche sacrificielle pour permettre de non seulement

protéger l'échantillon, mais également d'augmenter la pression générée lors du choc [109]. Un adhésif avec en moyenne 40µm de colle et 30µm d'aluminium est, dans la configuration laser actuelle, le plus efficace.

2.2 Echantillons

Un échantillon est formé de deux substrats de 8 couches de pré-imprégné (prepreg), collées entre elles par un joint d'adhésif. L'une des deux surfaces collées est également contaminée à l'aide d'un des agents définis plus loin (Figure 2-4 a). Tout au long du projet, deux grands scénarios sont étudiés : les contaminations pouvant apparaitre sur les lignes de productions et celles pouvant apparaitre sur les lignes de réparation.

Plusieurs types d'échantillons sont également produits. Les échantillons écoles (Figure 2-4 b), carrés et plat, des échantillons courbes, et des échantillons écoles avec le joint d'adhésif à 45°.
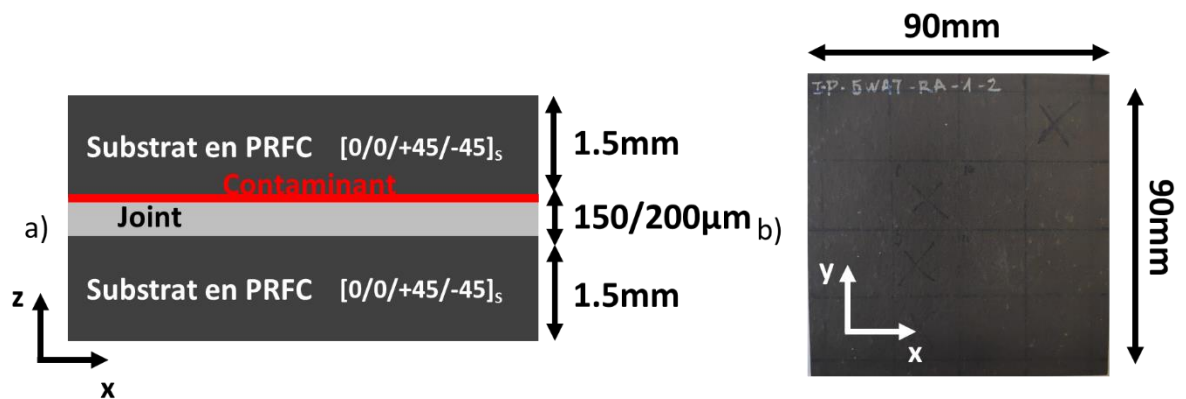
Figure 2-4 a) Schéma d'un échantillon type du projet b) Photo d'un échantillon

2.2.1 Le composite

Les échantillons sont tous composés de PRFC fabriqué par Hexel. Afin de se rapprocher au plus des application Airbus, le HexPly M21E/IMA est utilisé ici. L'orientation des plis de chacun des substrats est toujours la même : [0/0/+45/-45]$_S$.

2.2.2 L'adhésif

La différence entre un échantillon type « production » et un autre type « réparation » réside dans l'adhésif choisit et la méthode d'assemblage des deux substrats.

Dans le cas d'un échantillon de production, l'adhésif est constitué d'une trame en fil. Cette trame permet de faciliter la manipulation de la colle sur les lignes de production. L'adhésif utilisé est le FM300-K, et il est cuit à 444°K. On peut voir sur la Figure 2-5 a) les résidus de l'époxy utilisé pour le prépreg.
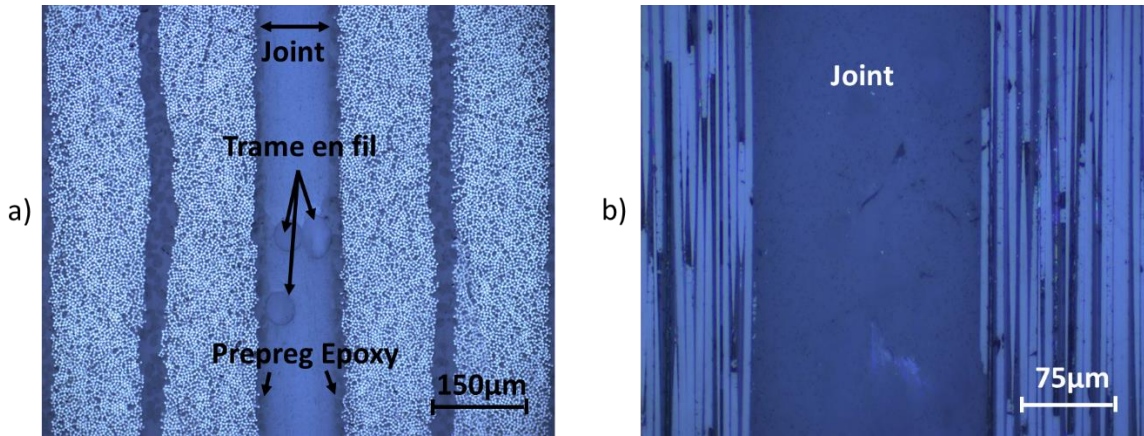
Figure 2-5 Micrographie d'un joint d'un échantillon type a) production b) réparation

La méthode d'assemblage pour les échantillons réparation est différente. Les substrats doivent être poncés jusqu'à la fibre avant collage. Ainsi sur la Figure 2-5 b), il n'y a plus la colle du prepreg entre l'adhésif et le substrat. L'adhésif est également différent. Il s'agit du FM300-2M qui ne comporte pas de trame en son centre. L'échantillon est cuit à 394°K.

2.3 Contamination

2.3.1 Les Contaminations

Airbus a défini trois différentes contaminations par scénario (Figure 2-6), et pour chacun des contaminants, 3 niveaux de contamination.
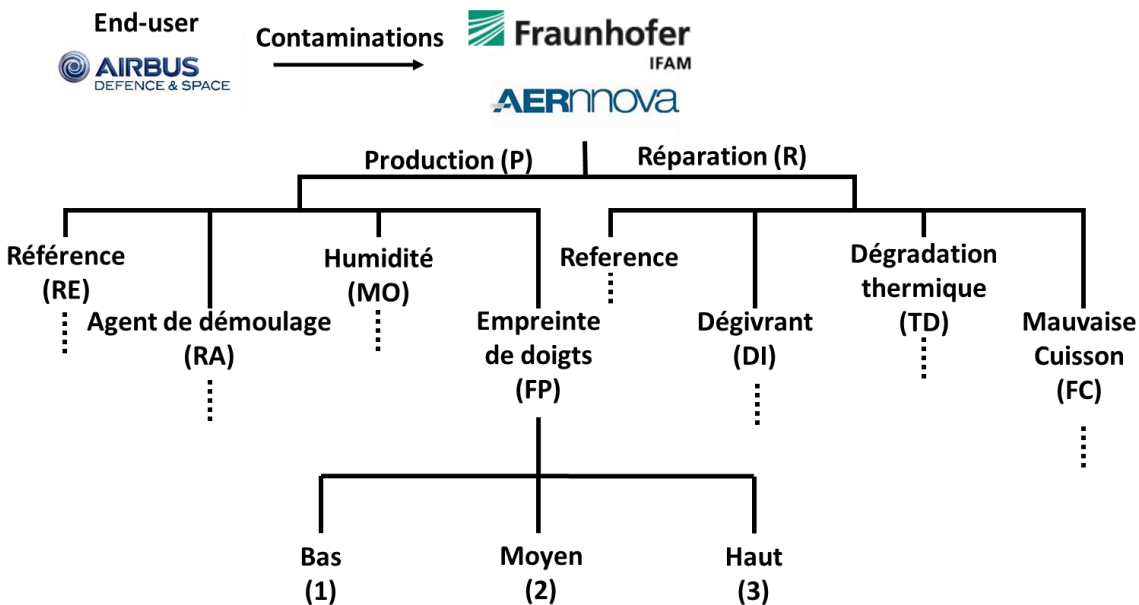
Figure 2-6 Scénarios de contamination de ComBoNDT

La notation utilisée pour faire référence à un échantillon donne en premier le scénario, puis la contamination et enfin le niveau de contamination. Ainsi le P-RA-3 et un échantillon type

production contaminé à l'agent de démoulage, avec le niveau de contamination le plus élevé (comparé aux deux autres).

2.3.2 Contamination et Validation

La contamination et l'assemblage des échantillons ont été réalisés par le Fraunhofer de Brême. La quantité de contaminant présent à la surface de chaque échantillon est suivit grâce à la spectrométrie photo-électronique X (XPS).

Un fois l'échantillon contaminé assemblé suivant les standards d'Airbus, deux étapes sont nécessaires pour valider la présence d'un joint faible.

 D'abord un panel d'échantillon est testé mécaniquement à l'aide de tests GIC et GIIC. Si les propriétés mécaniques d'un échantillon contaminé sont inférieures à celles d'un échantillon sain, les échantillons peuvent être scannés à l'aide d'ultrasons. En effet, pour valider la présence d'un joint faible, aucun défaut ne doit être repéré par US. Si les échantillons passent également ce test, ils pourront être utilisés par les différentes technologies post-collage du projet.

Sur l'intégralité des échantillons fournis pour les tests LASAT, seuls les échantillons courbés et ceux avec un défaut de cuisson ne pourront pas être utilisés.

2.4 Pièces réelles

2.4.1 Production
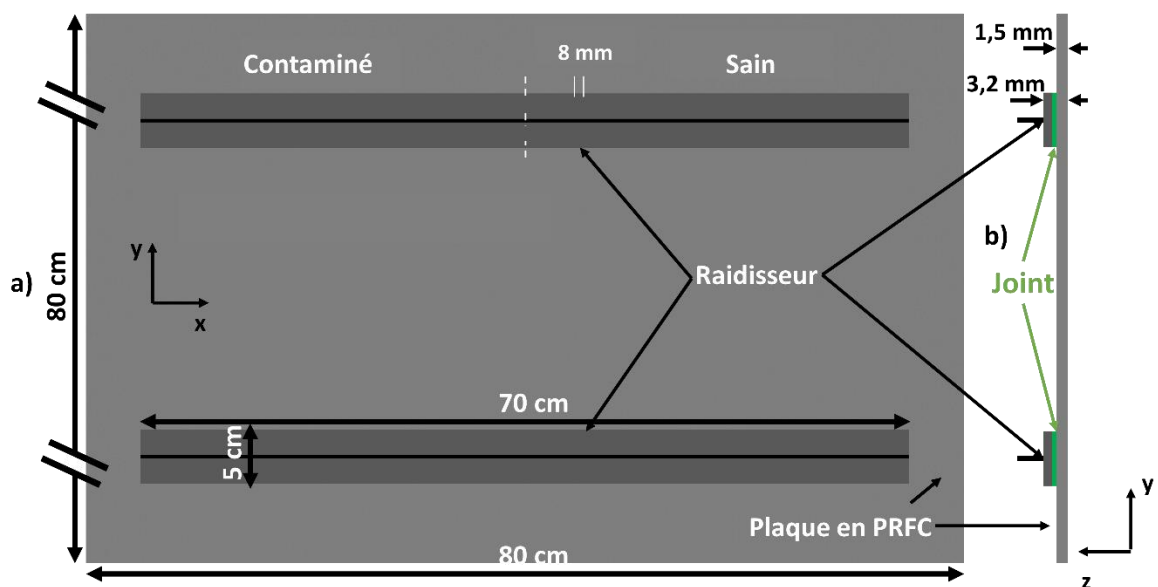
Figure 2-7 Schéma de la plaque de production vue a) du haut b) de la tranche

Le panneau production se rapproche des assemblages que l'on peut trouver dans des avions comme le A350. Il s'agit d'une plaque de PRFC de 800x800x1,5 sur laquelle deux raidisseurs de 700x50x1,7 ont été collés. Une moitié de la surface du raidisseur a été contaminée avec de l'agent de démoulage et des empreintes de doigts (Figure 2-7).

2.4.2 Réparation

Un bout d'A350 a pu être récupéré pour la simulation de réparation. Une zone a été poncée et les plis complémentaires ont été collés sur cette zone afin de combler le trou (Figure 2-8 b). La moitié du patch a été contaminée à l'aide de dégivrant et d'empreintes de doigts, l'autre a été laissée saine (Figure 2-8 a).
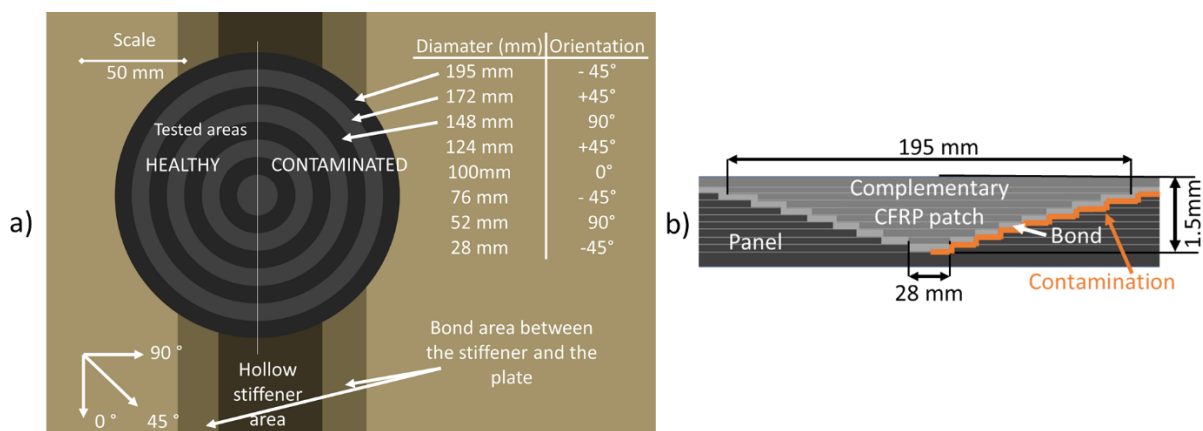
Figure 2-8 Schéma du panneau de réparation

Chapitre 3.   OPTIMISATION DU LASAT SYMETRIQUE

3.1 Premiers Résultats

3.1.1 Procédure Expérimentale

Des zones de 2cm x 2cm sont définies sur les échantillons école décrits dans la section précédente. Un choc laser symétrique est réalisé au centre de chacune des zones, avec un diamètre de tâche de 8mm (Figure 3-1 a).

L'énergie laser utilisée pour générer le choc augmente d'une zone à l'autre (Figure 3-1 b). L'objectif est de comprendre le comportement de l'échantillon et du joint de colle pour plusieurs niveaux de contrainte.
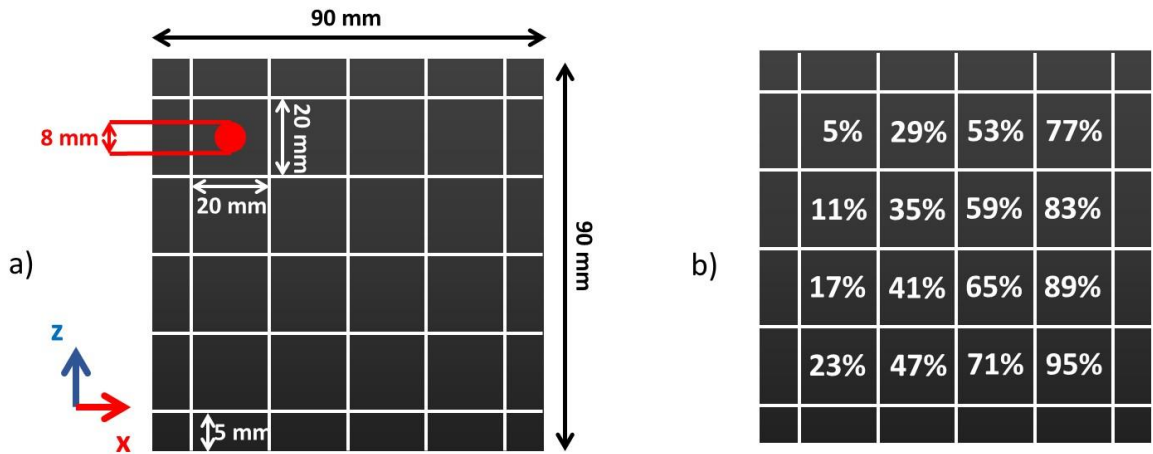
Figure 3-1 a) Division d'un échantillon école en 16 zones égales. b) Niveau d'énergie par zone

La Figure 3-2 a) est une photo du dispositif expérimental. En entrée un polariseur sépare le faisceau principal en deux sous-faisceaux, qui sont ensuite conduits jusqu'à l'échantillon par un jeux de miroirs. Les échantillons sont protégés à l'aide d'un adhésif en aluminium, et le confinement se fait par le biais de buse d'eau (Figure 3-2 b).
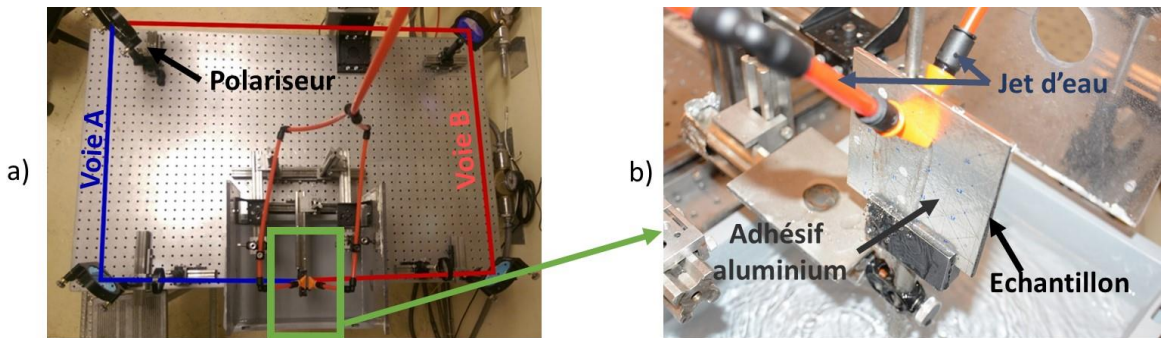
Figure 3-2 a) Dispositif expérimental b) Gros plan sur l'échantillon et sa préparation

L'analyse de l'échantillon en post-mortem se fera à l'aide du Gekko™.

3.1.2 Résultats

La Figure 3-3 résume les résultats ultrasons obtenus après avec avoir scanné la face A de l'échantillon. La face A est la surface de l'échantillon éclairée par la voie A.

La figure résume les résultats US obtenus pour les échantillons de type production. Pour presque tous les échantillons, 4 zones sont définies. La zone verte représente la plage d'énergie n'ayant pas du tout endommagé l'échantillon. La plage d'énergie ayant seulement endommagé le joint est représentée en orange, et celle ayant endommagé les peaux, et donc à éviter, est en rouge. Entre chaque intervalle, une zone blanche est présente. Parce que le test a été réalisé via des incréments d'énergie, il n'est pas possible de statuer sur l'état de l'échantillon pour des niveaux d'énergie non testés entre deux intervalles.
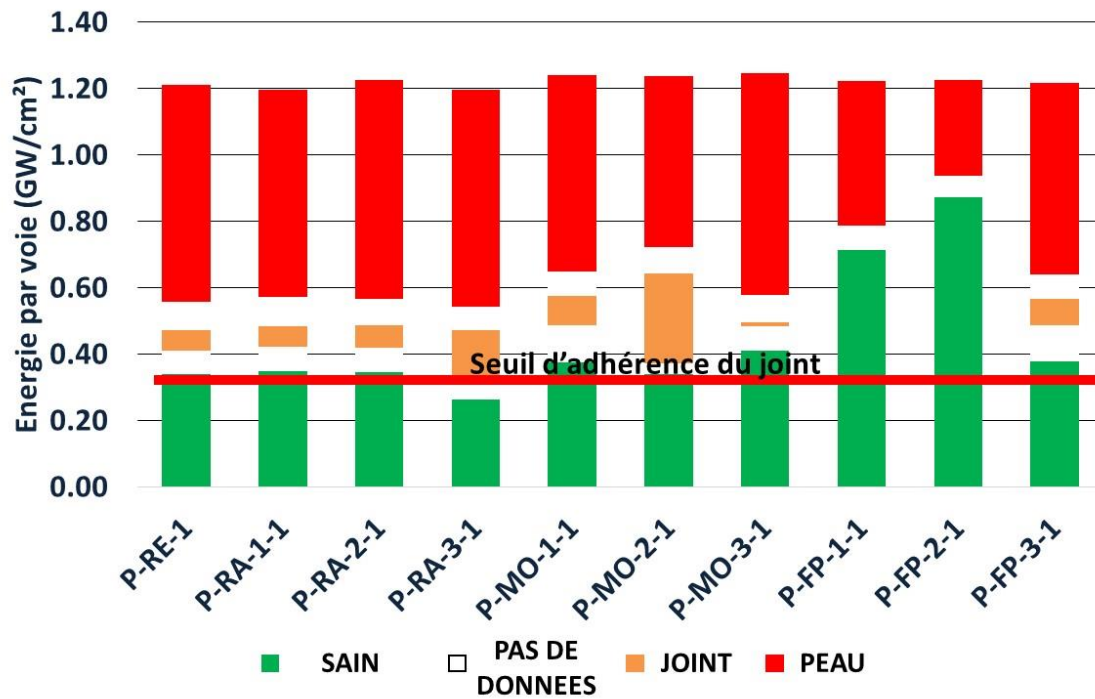
Figure 3-3 Résultat obtenu pour les échantillons production après scan ultrason de la face A

La capacité du S-LASAT à détecter des joints faibles repose sur deux principes :

1) Le seuil d'adhérence du joint doit être inférieur à celui des peaux. Dans le cas contraire il n'est pas possible d'ouvrir le joint sans endommager le composite, le test ne serait plus ND

2) Le seuil d'adhérence d'un échantillon contaminé doit être inférieur à celui d'un sain. Dans le cas contraire il est impossible de discriminer un joint sain d'un joint altéré.

La présence d'une zone orange sur la Figure 3-3 permet de valider le critère 1) pour presque tous les échantillons, exception faite des échantillons contaminés par des empreintes de doigts.

Cependant, ces résultats soulèvent plusieurs problèmes. Le premier concerne les niveaux de seuil d'adhérence des joints contaminés. Ils sont équivalents, voire plus haut que celui de référence. Il semblerait que le S-LASAT ne permette pas de repérer des joints faibles dans la configuration donnée.

De plus, l'énergie laser nécessaire pour ouvrir les peaux n'est pas constante. Or, par construction, tous les laminés de CFRP sont fabriqués de la même manière. L'énergie nécessaire pour ouvrir les peaux devrait donc être constante.

Pour plus de détails, ainsi que les résultats obtenus sur les échantillons de type réparation, le lecteur est invité à la section 3.2.2 du document en anglais.

3.1.3 Micrographies

A la suite de l'étude US, une série de micrographies a été réalisée sur les échantillons. Les observations réalisées ont notamment permis de valider le test US comme moyen de diagnostique post-tir laser. En effet, dans tous les cas, si un défaut est observé via une coupe micrographique, il est également repéré par US. Pour les défauts de très petite taille, il est même fréquent de ne rien voir en micrographie.

Les micrographies ont également révélé des ouvertures dans le joint, beaucoup plus petites que le diamètre du spot utilisé, et souvent décentrées. Idem pour les défauts observés dans les peaux.

Les irrégularités au niveau de la tâche focale sont mises en cause, et permettraient d'expliquer ces observations.

3.2 Modélisation Numérique

Certains paramètres tels que la répartition spatiale de l'énergie, semblent avoir une grande influence sur les résultats obtenus. Cette étude numérique a pour but de quantifier cette influence pour un jeu de paramètres donné

3.2.1 Model Isotrope

Une plaque de 10mm x 3,2mm x $5 \cdot 10^{-3}$mm est modélisée sous Abaqus. Dans sa thèse, Ecault [107] qualifie cette simulation de « fausse 2D » car il s'agit d'un modèle 3D de seulement 1 élément d'épaisseur. Cela permet de grandement réduire le temps de calcul tout en permettant une bonne représentation des phénomènes mis en jeu.

Une loi de comportement isotrope hydrodynamique est utilisée pour ce modèle [107], [151]. Bien que moins fidèle qu'une loi orthotropique, elle a l'avantage d'être rapide à calculer, et dans cette étude, ce sont majoritairement les déplacements transverses qui seront étudiés.

La répartition temporelle de l'énergie est définie d'après des mesures faites directement sur l'installation Hephaïstos, et la distribution spatiale par défaut suivra une loi gaussienne. Pour plus de détails concernant le modèle ainsi que sa validation, veuillez vous référez à la partie anglaise de ce manuscrit.

3.2.2 Plan d'Expérience et Paramètres

Le plan d'expérience est un outil statistique permettant d'analyse l'influence de paramètres sur la réponse d'un système. Un Central Composite Circumcised Design (CCC) est utilisé dans cette étude.

Quatre paramètres ont été sélectionnés et 5 niveaux sont nécessaires par valeur pour pouvoir appliquer le design CCC. Les paramètres ainsi que leurs valeurs sont précisés dans le tableau 3-1

	Epaisseur	Tâche focale	Hauteur de l'irrégularité	Largeur de l'irrégularité
-α	2	4	0.2	0.2
-1	2.5	5.5	0.65	0.9
0	3	7	1.1	1.6
1	3.5	8.5	1.55	2.3
α	4	10	2	3

Tableau 1 Résumé des paramètres du modèle

Afin de pouvoir mieux comprendre l'influence des irrégularités, une formule paramétrique a été définie afin de pouvoir inclure une irrégularité d'une hauteur et d'une largeur définie avec un profil gaussien idéal (cf rapport anglais 3.3.3.3).

L'influence de chacun de ces paramètres sera étudiée via une sortie commune à toutes les simulations : la largeur de la zone correspond au top 20% de tractions générées lors du choc. Par exemple, dans le cas d'un choc symétrique au profil idéal, avec tâche focale de 8mm et avec une pression en entrée de 1GPa, la simulation isotrope donne un maximum de traction de 363MPa à t=2148ns. A ce moment, la largeur de la zone pour laquelle les éléments subissent une contrainte en traction supérieur à 291MPa (80% de 363MPa) est de 6.675mm (cf Figure 3-4)
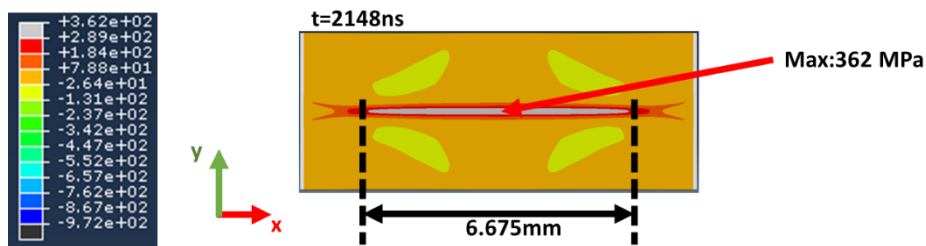
Figure 3-4 Contrainte suivant l'axe y lors de la propagation d'une onde de choc dans 3,2mm d'epoxy

3.2.3 Résultat

Cette étude numérique à permis de mettre en avant l'influence relative de chacun de 4 facteurs sur la largeur de la zone de traction générée. Les résultats sont résumés par le diagramme de Pareto (Figure 3-5). Ce diagramme donne l'influence de chacun des paramètres et de leurs combinaisons. Leurs combinaisons, ayant une valeur purement mathématique et non physique, ne seront pas étudiées ici.

Pour être considéré comme influent, un paramètre doit dépasser la valeur seuil de 2.14, limite à partir de laquelle un paramètre peut être considéré comme significatif d'un point de vu statistique.
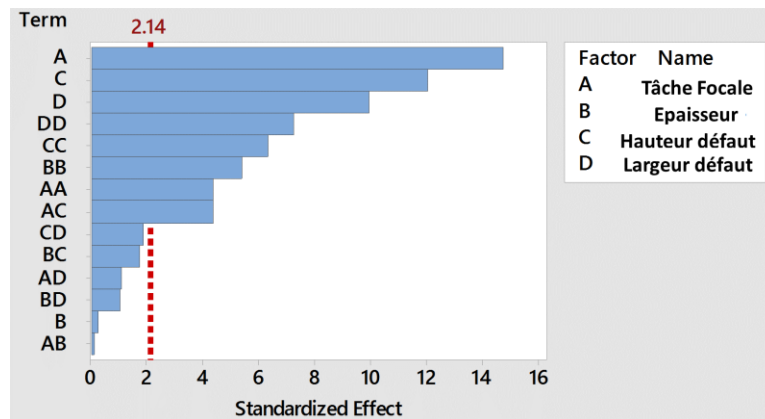
Figure 3-5 Diagramme de Pareto

Ainsi, ce diagramme montre que l'épaisseur de l'échantillon dans la gamme testée n'a pas d'influence. Seuls la tâche focale et les paramètres liés à l'irrégularité de répartition spatiale sont importants.

Cette étude a également permis de générer des surfaces de réponse. Ces surfaces permettent de d'anticiper les valeurs que prendrait la sortie (ici la taille de la zone de traction), pour 2 paramètres fixés, et deux paramètres variables. La Figure 3-6 représente les valeurs que la sortie prend en fonction du couple « hauteur de défaut » et « largeur de défaut » pour une épaisseur et une tâche focale donnée. L'épaisseur des échantilons est : 3.2 mm. Quatre graphiques sont générés pour 4 tâches focales différentes.
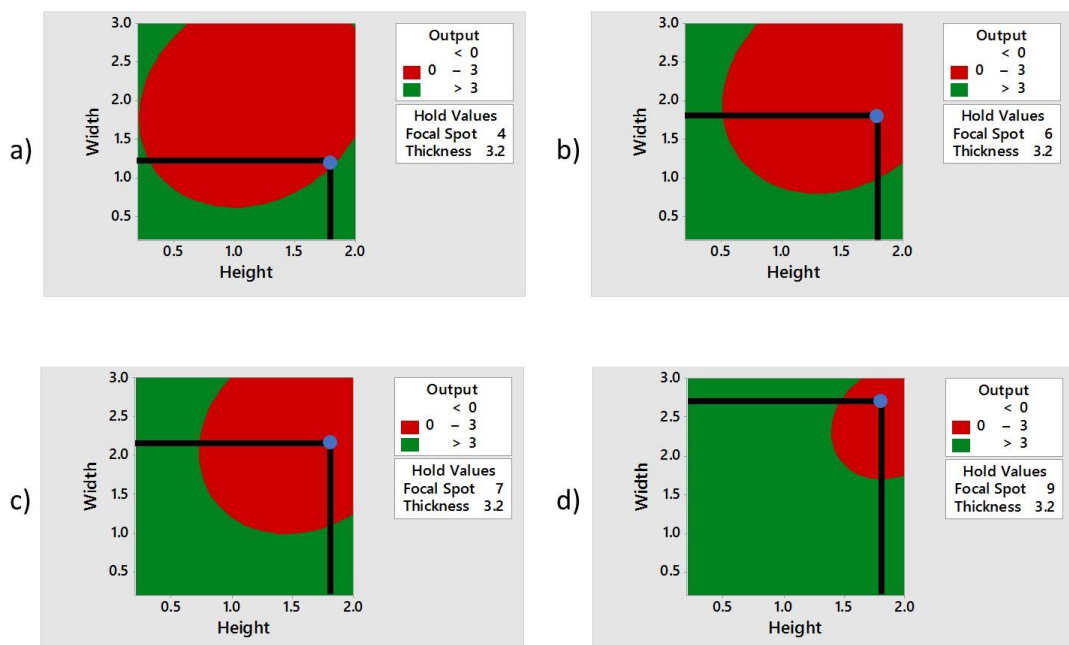
Figure 3-6 Surface de réponse pour 4 tâches focales différents : a) 4mm b) 6mm c) 7mm d) 9mm

La zone verte représente les combinaisons donnant une zone de traction supérieur à 3 mm, taille de défaut minimum considérée pour s'assurer d'une bonne détection. Dans le cas contraire la zone est rouge.

On observe, comme attendu, que plus la tâche est large, plus l'application est permissive vis-à-vis des dimensions du défaut (augmentation de la taille de la zone verte).

Le point bleu sur chacun des graphiques, est le couple (hauteur, largeur) mesuré sur la plateforme Héphaïstos. On remarque que dans ce cas, et ce, quel que soit la taille de la tâche focale, la zone de traction générée est systématique en dessous de 3mm.

Cette analyse révèle que la répartition spatiale est un point clé de la technologie, et qu'en l'état, le faisceau laser de la plateforme Héphaïstos n'est pas suffisamment bien maîtrisé pour permettre au S-LASAT de fonctionner

3.2.4 Lame de Phase

Les lames de phases sont des optiques permettant de remodeler un faisceau laser. Comme l'ont montrées les figures 2-2 et 2-3, ces optiques améliorent grandement la répartition spatiale de l'énergie laser.

La figure 3-7 montre la largeur de la zone de traction lorsque les profils de répartitions spatiales des lames de phase sont utilisés dans le modèle numérique.
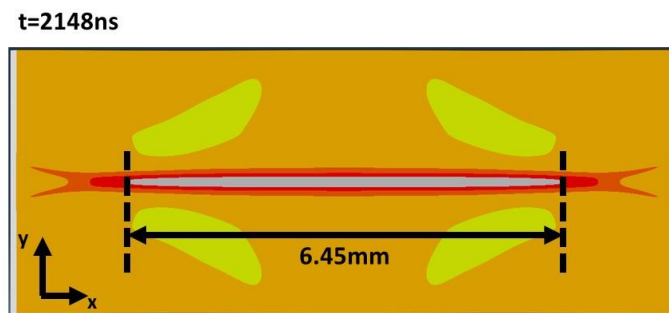
Figure 1-22 Largeur de la zone de traction avec les profils spatiaux obtenus suite à l'ajout de DOE sur le banc expérimental

Dans ce cas, pour une tâche focale de 8mm, une zone de traction presque aussi large que dans le cas idéal est obtenu.

Chapitre 4.   RESULTATS APRES OPTIMISATION DU S-LASAT

4.1 Nouveau Procédé Expérimental

Afin de limiter les problèmes potentiels d'homogénéité, les recherches de seuils se font par chocs consécutifs sur la même zone de l'échantillon. Entre chaque tir, la zone est vérifiée, et si aucun défaut n'est constaté aux US, l'énergie laser est augmentée. La procédure boucle jusqu'à ce qu'une ouverture soit détectée (Figure 4-1).
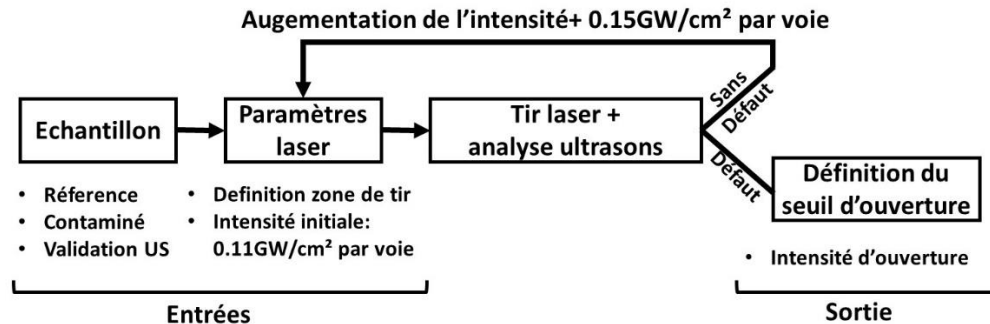
Figure 4-1 Procédure expérimentale

Deux lames de phases on était rajoutée sur chaque voie, juste après la dernière lentille faisant converger le faisceau sur l'échantillon (Figure 4-2). La tâche focale, le confinement et la couche sacrificielle sont les mêmes qu'avant.
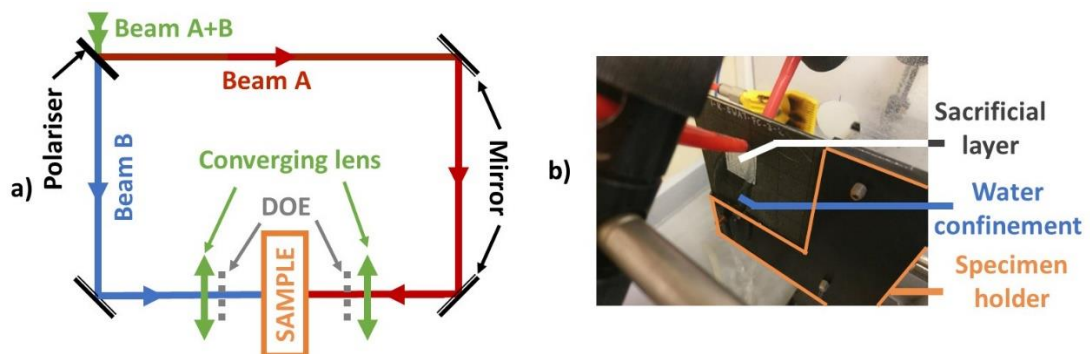
Figure 4-2 a) Schéma du banc d'essais b) Préparation de l'échantillon

4.2 Résultats sur Echantillons Ecoles

La Figure 4-3 résume les résultats obtenus sur les échantillons écoles type production et la Figure 4-4 pour les types réparation.

Ces résultats montrent que la technologie est capable, dans la presque totalité des cas, de faire la différence entre un échantillon sain et un échantillon contaminé. Les deux exceptions sont :

- Le plus haut niveau de contamination à l'humidité. Cependant cette amélioration des propriétés du collage pour une quantité d'absorption d'eau donnée est un comportement connu [161].

- Le second niveau de mauvaise cuisson. Cependant, comme cette série d'échantillon n'a pas passé la validation préliminaire US, les résultats ne seront pas pris en compte.
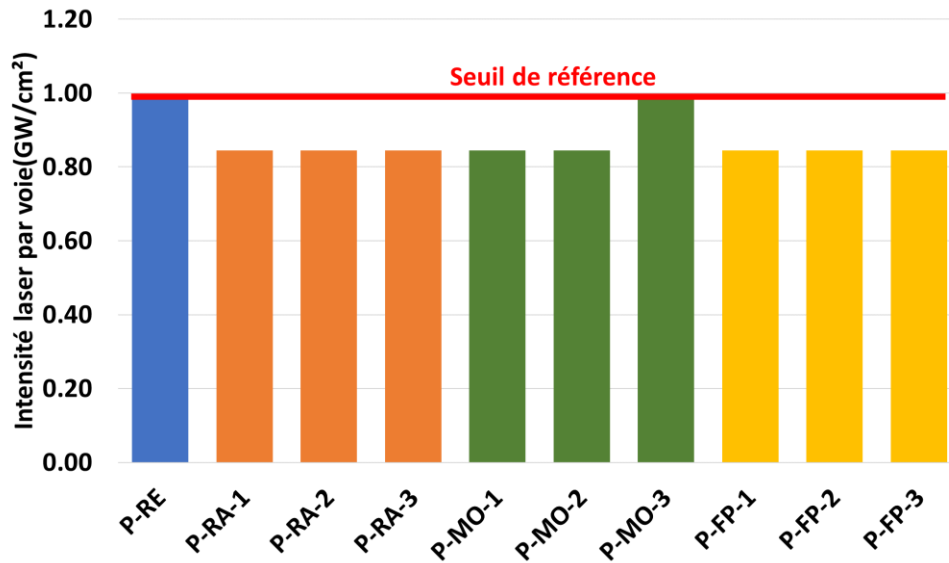
Figure 4-3 Résultats obtenus pour les échantillons écoles de type production
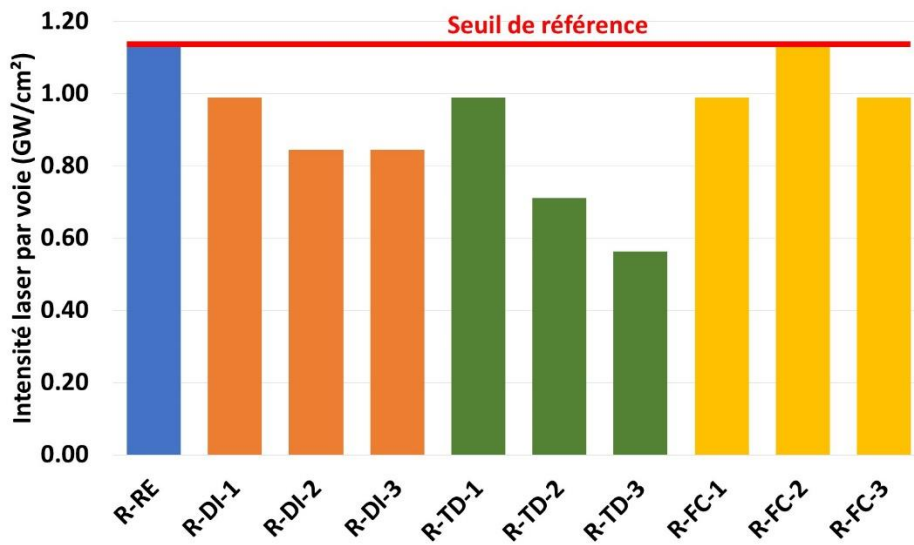
Figure 4-4 Résultats obtenus pour les échantillons écoles de type production

On remarque également que dans certain cas, comme pour la contamination à l'agent de dégivrage, ou de façon encore plus marquée, pour la dégradation thermique, il est possible de différencier chaque niveau de contamination.

Les résultats obtenus lors de cette campagne expérimentale sont plus concluants que précédemment, et montrent notamment que le S-LASAT est capable de discriminer un échantillon sain d'un échantillon contaminé.

4.3 Etude US Post-Mortem

Une étude micrographique est réalisée sur les échantillons afin de comprendre les processus de rupture mis en œuvre dans le cas d'une ouverture lors d'un choc laser symétrique.

L'analyse des échantillons post-mortem a permis de souligner les différences modes de rupture et de propagation dans les échantillons en fonction de deux paramètres principaux : la méthode de fabrication (production ou réparation) et les types de contamination.
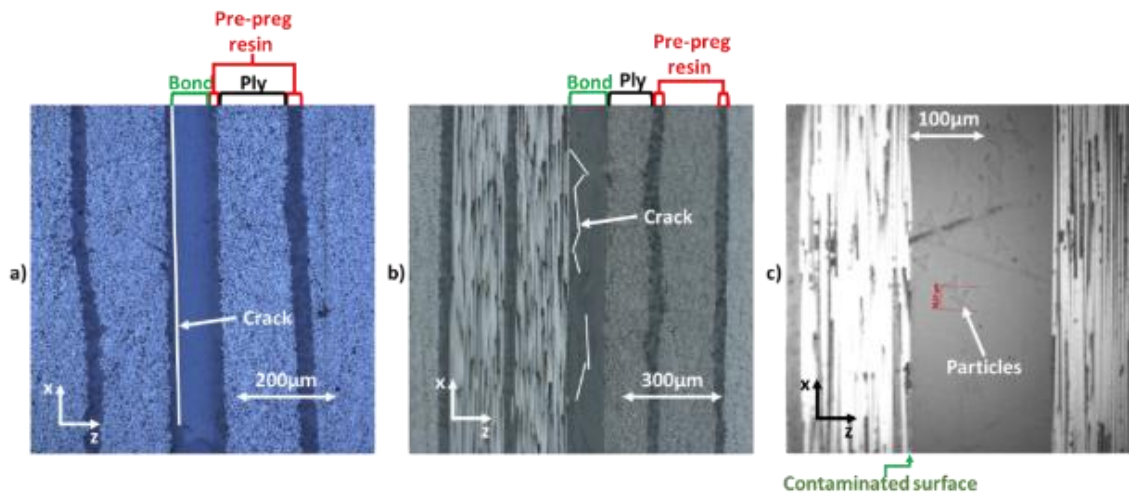
Figure 4-5 Fissuration obtenue pour différents échantillons : a) référence production b) référence réparation c) plus haut niveau de contamination au liquide de dégivrage

Dans le cas d'un échantillon production (Figure 4-5 a), la fissure se propage entre la colle du prepreg et l'epoxy du joint. L'échantillon réparation (Figure 4-5 b) ne possédant pas cette interface prepreg/epoxy, la fissure semble se propager préférentiellement dans le joint lui-même.

La Figure 4-5 c) quant à elle montre une migration de la contamination, sous forme de particule, vers l'intérieur du joint. Il en résulte non plus une fissuration nette, mais la création d'un réseau de microfissures. Une étude physico-chimique est ici nécessaire pour mieux comprendre l'influence de la contamination sur le schéma de rupture.

4.4 Validation de l'Aspect Non-Destructif

Ehrhart [39] a vérifié les propriétés d'un joint de colle (GIC) après que l'échantillon ait été testé en choc simple pour une intensité inférieure à celle définie comme intensité seuil. Son étude a révélé une diminution des propriétés mécaniques du joint.

Si le S-LASAT, veut être considéré comme Non-Destructif, une étude similaire doit être réalisée afin d'attester des propriétés mécaniques du joint après un choc symétrique. Cette étude a été réalisée avec l'aide de l'université de Patras (LTSM-UPAT). Pour plus d'information le lecteur est invité à se référer à la partie 4.3.6 de la version anglaise de la thèse.

Cette étude conclue notamment que le S-LASAT n'a pas modifié les propriétés mécaniques du joint de colle du moment que l'énergie utilisée est inférieure à l'énergie seuil définie lors de la campagne.

4.5 Etude sur pièce réelle

Afin de pouvoir étudier les pièces réelles fournies par Airbus, d'importantes modifications sont apportées à la plateforme de tir symétrique. L'utilisation d'un bras robotisé et d'un confinement solide font partie des ajouts majeurs comparés aux campagnes précédentes.

Le procédé de recherche de seuil est similaire à celui présenté en Figure 4-1. Une fois le seuil trouvé, l'intégralité de la pièce est ensuite testée avec une intensité égale à 80% de cette valeur.

Le S-LASAT est utilisé chaque fois que cela est possible. Les seules exceptions sont lors du test de la pièce « réparation » qui ne permettait pas tout le temps l'accès aux deux faces du collage (raidisseurs creux d'un côté). Le LASAT standard est utilisé dans ce cas.

La Figure 4-6 résume les résultats obtenus après vérification ultrason. Dans le cas du panneau type production, tous les tirs sont réalisés à l'aide du S-LASAT. Il en résulte que 100% des tirs sur la zone contaminée ont générés une ouverture, alors qu'aucun tir n'a apparemment endommagé la partie saine.

Panneau	Zone	CONFIGURATION SYMETRIQUE			CONFIGURATION TIR SIMPLE		
		Seuil S-LASAT (intensité par voie)	Nombre de tirs à 80%	Nombre de tir générant une ouverture	Seuil LASAT (intensité totale)	Nombre de tirs à 80%	Nombre de tir générant une ouverture
Production	Sain	0.85GW/cm²	32	0			
Production	Contaminé		21	21			
Réparation	Sain	0.72GW/cm²	8	0	0.84GW/cm²	7	0
Réparation	Contaminé		8	8		10	2
		Réussite : 100%			Réussite : 20%		

Figure 4-6 Résumé des résultats sur pièce réelle

Le constat est le même pour le panneau réparation dans le cas d'un test S-LASAT, cependant le taux de réussite devient très faible (20%) lorsque seul l'utilisation du LASAT en tir simple est possible.

Ce résultat souligne bien le degré de maitrise supérieur qu'offre le S-LASAT en terme de localisation de l'effort dans le joint ainsi que sa modularité.

4.6 Conclusion

L'utilisation de lames de phases dans le montage expérimental a permis d'améliorer le niveau de contrôle de la technologie S-LASAT. Cela s'est notamment démontré sur les résultats obtenus lors de la campagne sur les échantillons écoles.

Une étude micrographique a également souligné l'impact que pouvait avoir les processus de fabrication ainsi que le type de contamination sur le type de dommage obtenu lors d'une ouverture de joint. Elle a également montré le besoin d'une étude physico-chimique afin de mieux comprendre le comportement d'une surface contaminée vis-à-vis du joint de colle.

Une première étude réalisée avec l'université de Patras a permis de montrer le côté non-destructif du S-LASAT, mais une étude plus poussée est également nécessaire pour complètement le valider.

Enfin, les tests sur les échantillons réels ont eux aussi confirmé la capacité du S-LASAT à discriminer une zone saine d'une zone contaminée. Elle a souligné l'avantage du S-LASAT comparé au LASAT standard.

Plus d'information sont disponibles dans la partie anglaise du rapport, notamment sur le TRL de la technologie ainsi que de ses performances vis-à-vis des autres technologies développées lors du programme ComBoNDT.

CONCLUSION GLOBALE

Un TND capable d'évaluer l'intégrité de joints collés permettrait l'utilisation d'adhésifs pour l'assemblages de pièces structurelles en PRFC. Remplacer les rivets sur les lignes de production permettrait d'optimiser le design de pièces jusqu'alors surdimensionnées. De plus, l'utilisation d'adhésifs permettrait des économies de temps et de coûts pour la réparation de pièces composites en offrant la possibilité de simplement traiter localement les dommages les plus petits. Ecault a démontré les capacités de la technologie LASAT. Cependant, son étude a également révélé une limite majeure du procédé : la position de la zone de traction dépendait uniquement de la géométrie de l'échantillon, limitant le test d'adhérence a certains empilements spécifiques.

Les travaux présentés dans ce document s'intéressent à l'une des optimisations proposées par Ecault : le S-LASAT. Afin de tester les capacités de la technologie à détecter les joints faibles, des échantillons contaminés ont été produits dans le cadre du projet européen Com-BoNDT. Pour chacune des séries d'échantillons, la présence d'un joint faible a été validée par une non-détection de défaut par ultrasons combinée à une perte des propriétés mécaniques du joint confirmée à l'aide de tests GIC et GIIC.

Une première étude réalisée sur ces échantillons met en avant la capacité du test S-LASAT à n'endommager uniquement le joint d'adhésif. L'optimisation apportée au procédé lui permet donc de positionner la zone de traction, indépendamment de la géométrie de l'échantillon. Cependant, telle quelle, la technique ne permet pas de différencier un échantillon sain d'un échantillon contaminé.

Une étude numérique est réalisée pour essayer d'interpréter les profils de ruptures obtenus au niveau du joint de colle. Basé sur le model LS-Dyna proposé par Ecault, un modèle Abaqus isotrope du choc est proposé. Utilisé en parallèle d'un plan d'expérience, l'étude numérique permet de mettre en avant l'influence relative de certains paramètres. On en déduit notamment l'importance de la bonne répartition spatiale de l'intensité laser au niveau du point focal du laser. Cette conclusion amène à l'ajout de lames de phases sur le banc expérimental.

Une nouvelle campagne de tirs est réalisée à l'aide du nouveau banc d'essais. Le processus expérimental est également modifié afin de pallier aux hétérogénéités des contaminations telles que l'empreinte de doigt. L'étude des niveaux d'énergie nécessaire à l'ouverture de

chacun des échantillons montre que le S-LASAT est cette fois capable de distinguer un échantillon sain d'un échantillon contaminé, et ce quelle que soit la contamination ou le niveau de contamination. Selon le contaminant il est même possible de différencier les différents niveaux de contamination entre eux.

L'étude réalisée par Ehrhart avait montré que le LASAT pouvait avoir un effet négatif sur les propriétés mécaniques du joint. Les tests GIC réalisés après un choc non optimisé montraient qu'à partir d'un certain seuil, inférieur au seuil d'ouverture du joint, une diminution des propriétés mécaniques de l'adhésif était enregistrée. A l'aide du laboratoire LTSM de l'université de Patras, une étude similaire a été réalisée à l'aide d'éprouvettes GIIC, en se servant du S-LASAT à des intensités laser proches de la limite d'ouverture du joint. Aucune perte de propriété mécanique n'est observée. Cette étude est un premier pas vers la validation de l'aspect non destructif de la méthode.

Une dernière campagne de tir a été réalisée sur des pièces aéronautiques réelles. Un panneau type « production » a été réalisé en suivant la méthode d'assemblage décrite par Airbus. Un second panneau a été récupéré directement chez Airbus et une réparation par patch a été simulée. Dans chacun des cas, une moitié du panneau est laissée saine et l'autre est artificiellement contaminée. L'intégralité des tirs réalisés à l'aide du S-LASAT sont discriminant, une différence peut être faite entre la partie saine et celle altérée. Du fait de la présence de raidisseurs sur la pièce réparée, une grande partie du patch a dû être testé à l'aide de la technique LASAT non-optimisée. Il en résulte un faible taux de détection de joints faible.

Au terme de l'étude, et grâce aux améliorations apportée à la technique (confinement solide, lames de phase, robotisation du test), le TRL 5 est atteint.

PERSPECTIVES NUMERIQUES

Une VUMAT Abaqus a été développée lors de cette étude. L'objectif principal était de mieux comprendre les processus d'endommagement liés à la technique LASAT. Cependant le modèle numérique proposé par Ecault à l'aide de LS-Dyna s'avérait être au moins aussi précis et ne nécessitait pas autant de puissance de calcul.

En l'associant à une campagne d'ombroscopie, le modèle d'Ecault pourrait être validé également pour le S-LASAT, permettant ainsi de trouver une relation entre l'intensité laser et la quantité de traction générée au niveau d'un joint collé. Des données, telles que la taille de cette dernière, pourraient être également étudiées plus précisément qu'avec le modèle d'approximation acoustique.

De nouvelles techniques telle que la Proper Generalised Decomposition (PGD), sont aussi disponibles. Tout comme dans l'étude réalisée à l'aide de plans d'expériences, des surfaces de réponses sont générées permettant la modélisation de comportements complexes. Un

certain nombre de paramètres sont définis en entrée, puis une série de simulations est lancée en faisant varier ces paramètres au sein d'un intervalle prédéfini. L'idée derrière ce procédé est la création d'abaques contenant les différents cas de figure.

PERSPECTIVE EXPERIMENTALES

L'étude de la technique de S-LASAT a permis de mettre en avant sa capacité à détecter de manière non-destructive des joints faibles dans des structures en PRFC. Cependant, il a été remarqué que la contamination pouvait avoir une influence sur le profil de rupture à l'interface. Par exemple, les échantillons contaminés à l'agent de démoulage présentaient un profil de rupture très net, alors que celui obtenu avec une contamination à l'agent de dégivrage s'apparentait à un réseau de microfissures. Une étude physico chimique est maintenant nécessaire pour mieux comprendre l'influence du contaminant sur les propriétés mécaniques du joint.

L'étude réalisée avec l'aide de l'université de Patras n'est qu'un premier pas vers la validation de l'aspect non destructif du S-LASAT. Une étude plus approfondie est nécessaire pour valider ces observations.

Le passage au confinement solide a été crucial pour le bon déroulement des tests, notamment sur les pièces aéronautiques réélles. Le confinement actuel n'a pas été optimisé. De plus amples recherches permettraient de définir un matériau plus efficace et plus adapté au LASAT.

Les scans ultrason réalisés après chaque tir pourraient également être optimisés. Il est actuellement encore très dépendant de l'utilisateur, et deux utilisateurs différents pourraient obtenir deux conclusions différentes. L'automatisation de cette phase améliorerait grandement la robustesse du procédé.

Enfin, la façon dont les pièces vont être scannées doit encore être discutée. Doit-on scanner l'intégralité de panneau ou seulement certains points choisis aléatoirement ? Une étude sur la Probabilité de Détection (PoD) plus poussée doit être réalisée.

APPENDIX A

This appendix regroups all the numerical data used to perform the Central Composite Circumcised Design (CCC) described in chapter 3.

Four factors were selected, and 5 different levels assigned to each one (cf Table 1-27).

	Thickness (mm)	Focal Spot (mm)	Irregularity Height	Irregularity width
-α	2	4	0.2	0.2
-1	2.5	5.5	0.65	0.9
0	3	7	1.1	1.6
1	3.5	8.5	1.55	2.3
α	4	10	2	3

Table 1-27 Summary of the parameters' level

Table 1-28 lists all required simulations to perform such study using Minitab 18. A total of 30 simulations are needed, however only 26 unique ones are actually performed. Indeed, design of experiments were initially developed for experimental purposes, so duplicating several times the same experiment and considering the spread of values obtained given the same initial condition helps defining the uncertainty range for a given DOX. However, when doing numerical simulation, this spread does not exist.

To optimise the output measurement time (in this case the maximum tensile stress area width), python scripts were used to generate each input file, launch the simulations, and measure the width of the surface.

Combined with data given in chapter 3, Table 1-28 can be used either to compare similar simulation and the results obtained during this study, or results can be directly implemented within a CCC to compare the results with the study presented in the same chapter.

Sim #	Focal Spot (mm)	Thickness (mm)	Height	Width	Max Tensile Stress Area Width (mm)
1	5.5	2.5	0.65	0.9	3.6
2	8.5	2.5	0.65	0.9	6.6
3	5.5	3.5	0.65	0.9	3.7
4	8.5	3.5	0.65	0.9	6.4
5	5.5	2.5	1.55	0.9	3.0
6	8.5	2.5	1.55	0.9	3.9
7	5.5	3.5	1.55	0.9	3.3
8	8.5	3.5	1.55	0.9	5.3
9	5.5	2.5	0.65	2.3	2.8
10	8.5	2.5	0.65	2.3	5.6
11	5.5	3.5	0.65	2.3	2.9
12	8.5	3.5	0.65	2.3	5.3
13	5.5	2.5	1.55	2.3	1.6
14	8.5	2.5	1.55	2.3	2.9
15	5.5	3.5	1.55	2.3	2.0
16	8.5	3.5	1.55	2.3	2.9
17	7	3	1.1	1.6	2.3
18	7	3	1.1	1.6	2.3
19	7	3	1.1	1.6	2.3
20	7	3	1.1	1.6	2.3
21	4	3	1.1	1.6	1.2
22	10	3	1.1	1.6	5.1
23	7	2	1.1	1.6	3.7
24	7	4	1.1	1.6	3.0
25	7	3	0.2	1.6	5.5
26	7	3	2	1.6	1.8
27	7	3	1.1	0.2	5.4
28	7	3	1.1	3	2.3
29	7	3	1.1	1.6	2.3
30	7	3	1.1	1.6	2.3

Table 1-28 List of simulations and their parameters used to generate results from chap. 3

APPENDIX B

REQUIREMENTS

PyHugo is composed of 4 different files:

- GUIV3.py = user interface
- Berthimus3000.py = contains all acoustic approximation algorithms
- Tools.py = contains the tools (plotting, intersection finding,….) called in Berthimus3000.py
- Material.db = sql library containing materials and their properties.

To launch the app, simply execute /.Berthimus3000.py. Python 2.7 is required for the script

to run, as well as the latest version of Matplotlib. No other libraries should be required.

USING THE PROGRAMME

Upon executing the script, the following window appears:

If the launch simulation is selected:
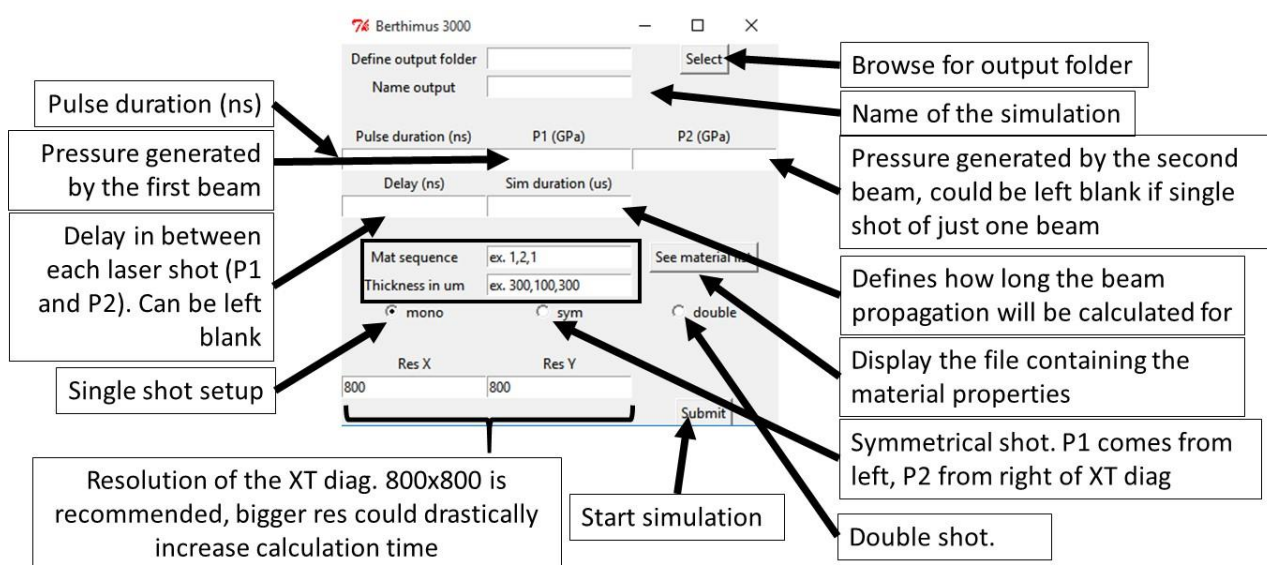
with:

This is the piling sequence. Currently, from left to right, there is 300μm of the material with ID 1 (cf "See material list"), 100μm of the material with ID 2, and again 300μm of the material with ID 1

and:

ID to use in the main window for the Mat sequence

Fill in the material properties you want to create. ID is automatic

Delete the material with the ID specified in the red area

Create a material with infos specified in the green areas

Otherwise, if the user wants to reopen an already <u>calculated</u> solution with "open simulation":

Browse the simulation

Re-use the resolution used for the initial simulation

Plot XT diag

PROGRAMME ALGORITHM

Parameter initialisation and propagation

One or two curves are created depending on the initial user's input. For each new beam and object Curve() is created (see Figure B-1) :

Curve(Xini, Yini, Xend, Yend,previousCurve,cType,direction,pressure,velocity)

Where:

- (Xini,Yini) = coordinated of the origine of the curve
- (Xini,Yini) = coordinated of the origine of the curve)
- previousCurve = ID of the curve that generated this one
- cType = 0 if shock wave 1 if release wave
- direction = 0 if shock wave going from right to left 1 if from left to right
- Pressure = pressure
- Velocity = velocity

Each new curve is added to the dictionary curve{} where it is given an ID.

For each curve, the acoustic approximation is used to calculated the slope (Z), and the velocity and the pressure associated to it (see 1.4.3).
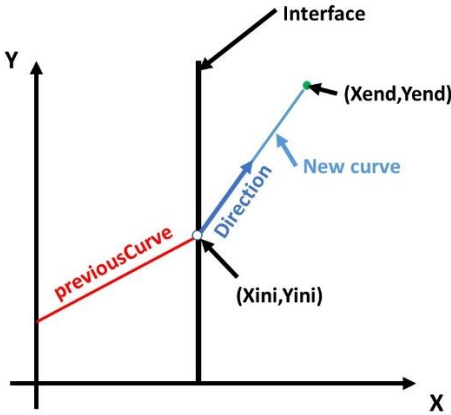
Figure B-1 Representation of the data stored in a Curve() obj

 This part of the code runs until Xend is greater or equal to the simulation time specified by the user. It is possible to obtain a visual of all the curves calculated by uncommenting lines 819 to 831. However, due to the huge number of curves created, it may become difficult to read after the initial wave has passed a few interfaces (Figure B-2).
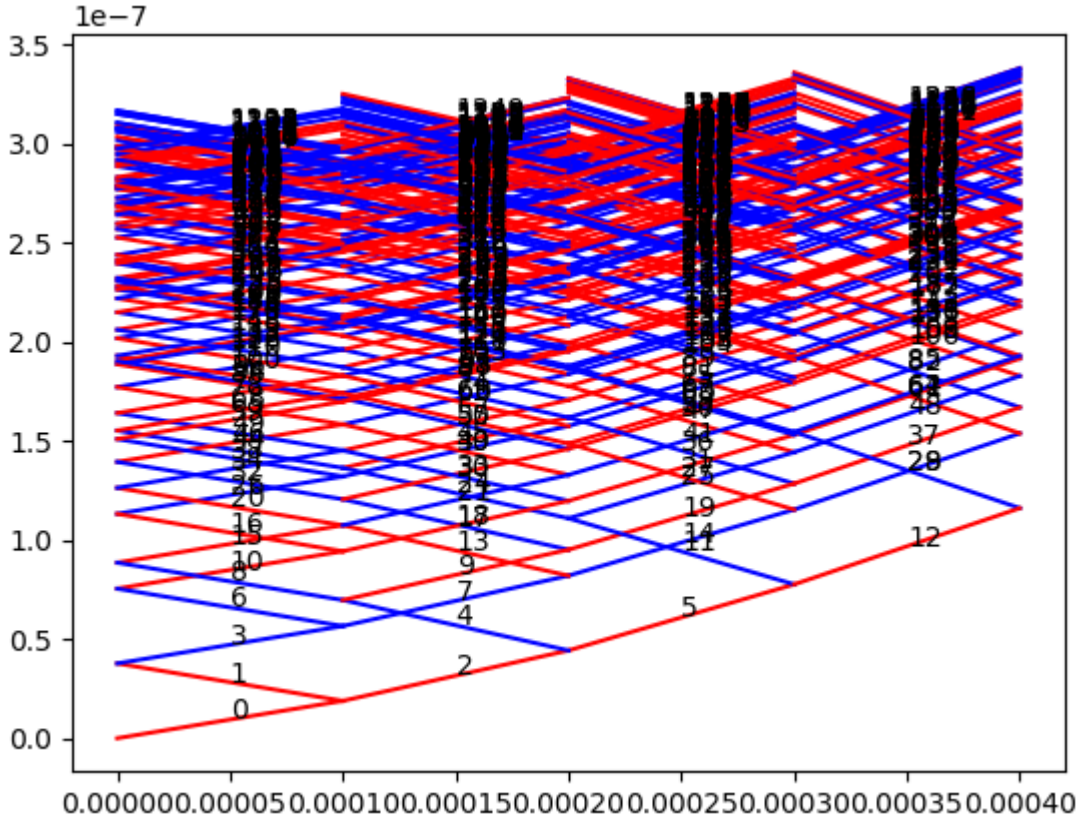
Figure B-2 Representation of the curve creation for 4 different materials (aluminium, copper, isotropic equivalent of CFRP and epoxy) during 0.3µs. Time (s) in ordinate, position (m) on the abscise.

LAYING DOWN THE CURVES ON A GRID.

A dictionary containing all the point of a grid of "Res X" by "Res Y" is generated. Each time a curve "passes over" one of the grid's square coordinate (Figure B-3 a), it's ID is added to the dictionary of coordinate. If several curves passe over the same square, each ID is added to that square (Figure B-3 b).
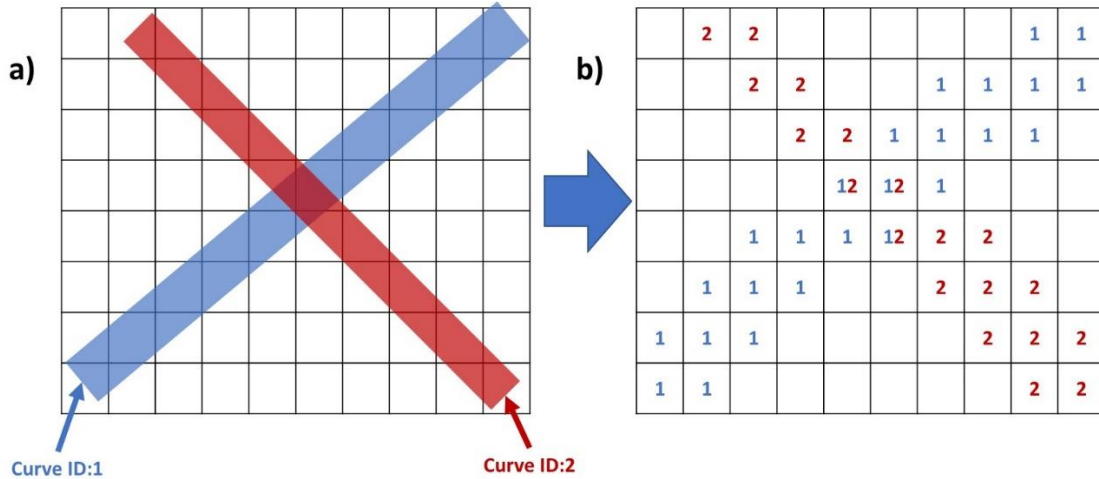
Figure B-3 a) Two random curve over a grid of ResX x ResY b) the visualisation of the stored data

CREATION OF THE XT DIAGRAM

Once all the squares have been processed, the state (velocity and pressure) of each grid is calculated. To avoid any missing data, the grid calculated in a chronological manner (from the bottom to the top). Each new curve combination is added to the "*calculated{}*" dictionary to avoid recalculating it. Hence, the previous would have given:

calculated{(1):[pressure1,velocity1], (2):[pressure2,velocity2], (1,2):[pressure12,velocity12]}

Once everything has been calculated, each square has been assigned a value, the XT diagram is plotted, but this time with the pressure and the velocity values (Figure B-4)
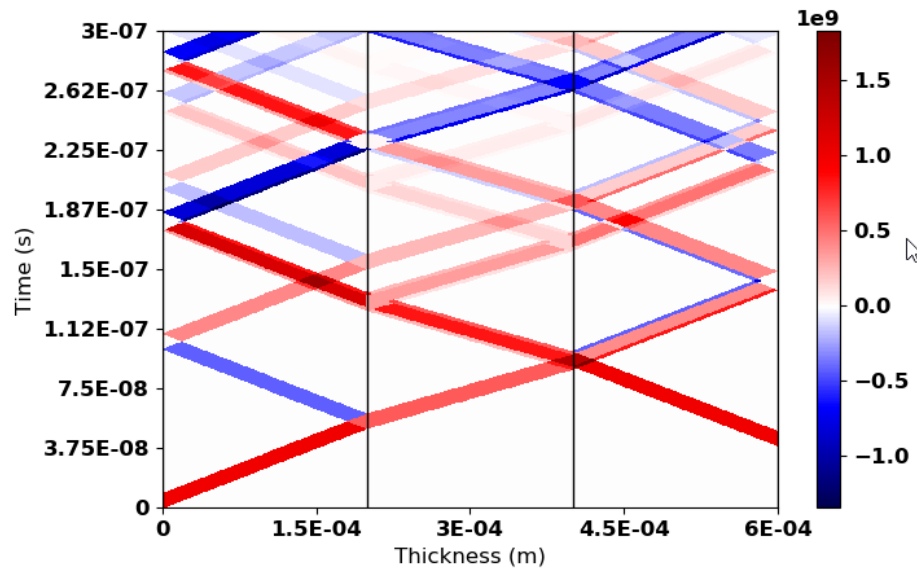
Figure B-4 Aluminium / copper / aluminium sample

Left clicking on the graph display the pressure and velocity value **in the console**. Right clicking displays, on the position where the mouse is, the velocity over the time (Figure B-5). Click with the wheel displays, on the position where the mouse is, the pressure over the time (Figure B-6).
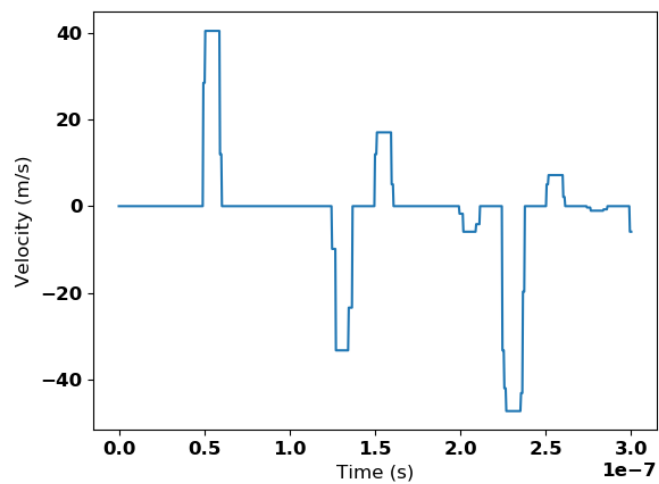
Figure B-5 Velocity plotted at the first interface of the simulation plotted in Figure B-4
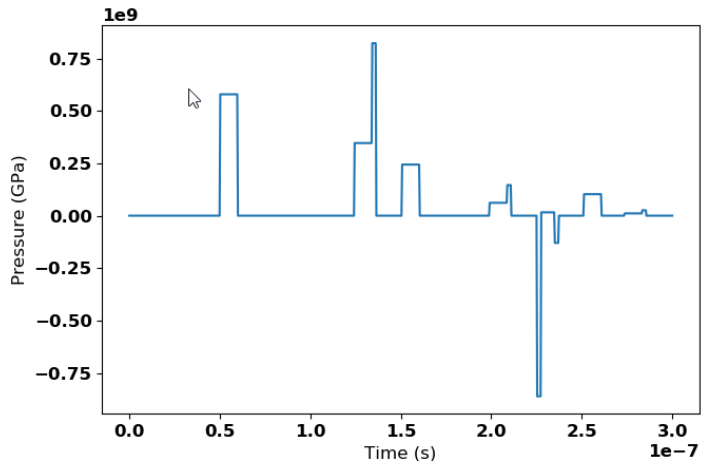
Figure B-6 Pressure plotted at the first interface of the simulation plotted in Figure B-4

One on the main improvement that can be added to the current script would be to rewrite it in C++ ou C. This should improve by almost 100 times the calculation time. That number could even go higher with a good management of the threads.

REFERENCES

[1]   Carbon Market Watch, "The CORSIA : ICAO ' s market based measure and implications for Europe," no. October, 2016.

[2]   G. Santos, "Road transport and CO 2 emissions : What are the challenges ?," *Transp. Policy*, vol. 59, no. June, pp. 71–74, 2017.

[3]   S. A. Shaheen, D. Ph, T. E. Lipman, and D. Ph, "REDUCING GREENHOUSE EMISSIONS AND FUEL CONSUMPTION – Sustainable Approaches for Surface Transportation –," *Int. Assoc. Traffic Saf. Sci.*, vol. 31, no. 1, pp. 6–20, 2007.

[4]   U.S. Department of Energy, "Combining Strategies for Deep Reductions in Energy Consumption and GHG Emissions." 2013.

[5]   A. Anger, "Including aviation in the European emissions trading scheme: Impacts on the industry, CO 2 emissions and macroeconomic activity in the EU," *J. Air Transp. Manag.*, vol. 16, pp. 100–105, 2010.

[6]   "IATA Technology Roadmap," 2013.

[7]   M. J. Benzakein, "What does the future bring? A look at technologies for commercial aircraft in the years 2035–2050," *Propuls. Power Res.*, vol. 3, pp. 165–174, 2015.

[8]   P. Schimming, "Counter Rotating Fans An Aircraft Propulsion for the Future?," in *J. of Thermal Science*, 2003, vol. 12, no. 2.

[9]   A. Abbas, J. De Vicente, and E. Valero, "Aerodynamic technologies to improve aircraft performance," *Aerosp. Sci. Technol.*, vol. 28, pp. 100–132, 2013.

[10]   R. H. Liebeck, "Design of the Blended Wing Body Subsonic Transport," *J. Aircr.*, vol. 41, no. 1, pp. 10–25, 2004.

[11]   J. Cinquin, "Airbus Composite - workshop," 2017.

[12]   G. Di Franco, L. Fratini, and A. Pasta, "Influence of the distance between rivets in self-piercing riveting bonded joints made of carbon fiber panels and AA2024 blanks," *J. Mater.*, vol. 35, pp. 342–349, 2012.

[13]   H. S. Wolko and J. D. Anderson, *The Wright Flyer : an engineering perspective*, Smithsonia. Washington, D.C. : National Air and Space Museum, 1987.

[14]   F. Anderson, *Northrop: An Aeronautical History*. Northrop Corporation, 1976.

[15]   P. Cognard, *Handbook of Adhesives and Sealants: Volume 1*, vol. 1. 2005.

[16]   C. J. Moss, "'Redux' Bonding a French Fighter Aircraft," *Aircr. Eng. Aerosp. Technol.*, vol. 21, no. 7, pp. 218–219, 1949.

[17]   NMAB ad hoc Committee on Structural Adheslves For Aerospace Use, "Aerospace structural adhesive," 1974.

[18]   A. J. Kinloch, *Adhesion and Adhesives*. Science and Technology, 1987.

[19]   S. Ebnesajjad, "Introduction and adhesion theories," *Handb. Adhes. Surf. Prep.*, pp. 3–13, 2011.

[20]   J.-J. Villenave, *Assenblage Par Collage*, Dunod-L'. 2005.

[21]   K. B. Katnam, L. F. M. Da Silva, and T. M. Young, "Bonded repair of composite aircraft structures: A review of scientific challenges and opportunities," *Prog. Aerosp. Sci.*, vol. 61, pp. 26–42, 2013.

[22]   D. E. Packham, "The Mechanical Theory of Adhesion—Changing Perceptions 1925-1991," *J. Adhes.*, vol. 39, no. 2–3, pp. 137–144, 1992.

[23]   A. Pizzi and K. Mitta, *Handbook of Adhesive Technology, third edition*. Boca Raton: CRC press, 2018.

[24]   J. W. McBain and D. G. Hopkins, "On Adhesives and Adhesive Action," *J. Phys. Chem.*, vol. 29, no. 2, pp. 188–204, 1924.

[25]   A. K. Vijh, "The influence of metal-metal bond energies on the adhesion, hardness, friction and wear of metals," *J. Mater. Sci.*, vol. 10, no. 6, pp. 998–1004, 1975.

[26]   M. Rabe, D. Verdes, and S. Seeger, "Understanding protein adsorption phenomena at solid surfaces," *Adv. Colloid Interface Sci.*, vol. 162, no. 1–2, pp. 87–106, 2011.

[27]   J. J. Bikerman, "Causes of Poor Adhesion: Weak Boundary Layers," *Ind. Eng. Chem.*, vol. 59, no. 9, pp. 40–44, 1967.

[28]   R. J. Good, "Theory of 'Cohesive' vs 'Adhesive' Separation in an Adhering System," *J. Adhes.*, vol. 4, no. 2, pp. 133–154, 1972.

[29]   R. D. Adams, *Adhesive bonding*, vol. 44, no. 6. Reinforced Plastics, 2000.

[30]   K. Mohamed Bak, K. Prasanna Venkatesn, and K. Kalai Chelvan, "Parametric Study of Bonded, Riveted and Hybrid Composite Joints Using FEA," *J. Appl. Sci.*, vol. 10, no. 12, pp. 1058–1062, 2012.

[31]   J. Y. Mann, R. A. Pell, R. Jones, and M. Heller, "REDUCING THE EFFECTS OF RIVET HOLES ON FATIGUE LIFE BY ADHESIVE BONDING," *Theor. Appl. Fract. Mech.*, vol. 3, pp. 113–124, 1985.

[32]   A. Ghorbani, "Stress analysis of composite adhesive bonded joints under incipient failure conditions," *Procedia Struct. Integr.*, vol. 8, pp. 552–560, 2018.

[33]   J. Careless, "The MRO composite challenge – Aerospace Manufacturing Magazine," p. 1, 15-May-2016.

[34]   K. Richter and J. Walther, *Supply Chain Integration Challenges in Commercial Aerospace*. Springer, 2017.

[35]   C. Spafford, T. Hoyland, and A. Medland, "TURNING THE TIDE A WAVE OF NEW AVIATION TECHNOLOGY WILL SOON HIT THE MRO INDUSTRY," *Oliver Wyman*, 2015.

[36]   K. Senthil, A. Arockiarajan, R. Palaninathan, B. Santhosh, and K. M. Usha, "Defects in composite structures: Its effects and prediction methods - A comprehensive review," *Compos. Struct.*, vol. 106, pp. 139–149, 2013.

[37]   R. D. Adams and P. Cawley, "A riveiw of defect types and non-destructive testing techniques for composites and bonded joints," *Constr. Build. Mater.*, vol. 3, no. 4, pp. 170–183, 1989.

[38]   R. D. Adams and B. W. Drinkwater, "Nondestructive testing of adhesively-bonded joints," *NDT E Int.*, vol. 30, no. 2, pp. 93–98, 1997.

[39]   B. Ehrhart, "Quality Assessment of Bonded Primary Cfrp Structures By Means of Laser Proof Testing," PhD Thesis, Bremen, 2016.

[40]   "Quality assurance in adhesive bonding technology - New DIN2304 standard and its use in practice," *Adhes. Adhes. SEALANTS*, vol. 4, 2015.

[41]   M. Hoffmann, "ENCOMB Final Report," *FP7 Eur. Framew.*, pp. 1–61, 2014.

[42]   C. J. Allen, C. Kerr, and P. Walker, "The Use of Optically Stimulated Electron Emission for the Detection of Surface Contamination," *Ahdesion 15*, pp. 131–147, 1990.

[43]   M. K. Chawla, *Optically Stimulated Electron Emission*, vol. 7. Elsevier Inc., 2015.

[44]   ENCOMB, "ENCOMB Project - Optically stimulated electron emission," YouTube, 2016.

[45]   K. Brune *et al.*, "Pre-bond quality assurance of CFRP surfaces using optically stimulated electron emission," *Eng. Against Fail. - Proc. 3rd Int. Conf. Eng. Against Fail. ICEAF 2013*, no. June, pp. 26–28, 2013.

[46]   K. Brune *et al.*, "Surface analytical approaches contributing to quality assurance during manufacture of functional interfaces," *Appl. Adhes. Sci.*, vol. 3, no. 1, 2015.

[47]   S. N. Thakur and J. P. Singh, *Fundamentals of Laser Induced Breakdown Spectroscopy*, no. 1. 2007.

[48]   R. Noll *et al.*, "Laser-induced breakdown spectrometry - Applications for production control and quality assurance in the steel industry," *Spectrochim. Acta - Part B At. Spectrosc.*, vol. 56, no. 6, pp. 637–649, 2001.

[49]   S. Millar, C. Gottlieb, G. Wilsch, T. Eichler, C. Bohling, and A. Molkenthin, "Laser Induced Breakdown Spectroscopy (LIBS) – On-site investigations on a bridge with a mobile LIBS-system," pp. 15–19, 2015.

[50]   "Overview of Laser Induced Breakdown Spectroscopy," http://www.easternapplied.com/LIBS-Technology-Overview. .

[51]   "Laser classification table - Laser Safety Facts," http://www.lasersafetyfacts.com/laserclasses.html. .

[52]   S. De Vito *et al.*, "Electronic noses for composites surface contamination detection in aerospace industry," *Sensors (Switzerland)*, vol. 17, no. 4, 2017.

[53]   S. De Vito *et al.*, "Detection and quantification of composite surface contaminants with an e-nose for fast and reliable pre-bond quality assessment of aircraft components," *Sensors Actuators B. Chem.*, vol. 222, pp. 1264–1273, 2016.

[54]   A. Helwig, K. Maier, G. Müller, T. Bley, J. Steffensky, and H. Mannebach, "An optoelectronic monitoring system for aviation hydraulic fluids," *Procedia Eng.*, vol. 120, no. December, pp. 233–236, 2015.

[55]   J. Burlachenko, I. Kruglenko, B. Snopok, and K. Persaud, "Sample handling for electronic nose technology: State of the art and future trends," *TrAC - Trends Anal. Chem.*, vol. 82, pp. 222–236, 2016.

[56]   R. C. Young, W. J. Buttner, B. R. Linnell, and R. Ramesham, "Electronic nose for space program applications," *Sensors Actuators, B Chem.*, vol. 93, no. 1–3, pp. 7–16, 2003.

[57]   ENEA, "E-NOSE Encomb," 2016, https://www.youtube.com/watch?v=7EaVQHXEbCo. .

[58]   S. Heckner, M. Geistbeck, C. U. Grosse, S. Eibl, and A. Helwig, "FTIR Spectroscopy as a Nondestructive Testing Method for CFRP Surfaces in Aerospace," *7th Int. Symp. NDT Aerosp.*, pp. 1–9, 2015.

[59]   A. Kraft, K. Brune, C. Tornow, G. Mühlhofer, B. Mayer, and B. Valeske, "Nondestructive testing of contaminated CFRP surfaces with the - BonNDTinspect ® system," *Appl. Adhes. Sci.*, pp. 1–21, 2017.

[60]   Ifam   -   Fraunhofer,   "AWT-Encomb,"   2016, https://www.youtube.com/watch?v=KCjAIk5o2iE. .

[61]   G. Wachinger and C. Thum, "New Trends in CFRP Treatment and Surface Monitoring for Automated Structural Adhesive Bonding," *Proc. Int. Conf. Compos. Mater.*, 2009.

[62]   M. Amkreutz *et al.*, "Method and device for testing a surface quality," 2006.

[63]   "bonNDTinspect®   Bondability   Test," https://www.youtube.com/watch?time_continue=47&v=zBZEdjJjVYY. .

[64]   P. Kudela, T. Wandowski, P. Malinowski, and W. Ostachowicz, "Application of scanning laser Doppler vibrometry for delamination detection in composite structures," *Opt. Lasers Eng.*, vol. 99, no. October, pp. 46–57, 2017.

[65]   P. Malinowski and T. Wandowski, "Characterization of CFRP Using Laser Vibrometry," *Key Eng. Mater.*, vol. 569–570, pp. 710–717, 2013.

[66]   P. Castellini, M. Martarelli, and E. P. Tomasini, "Laser Doppler Vibrometry: Development of advanced solutions answering to technology's needs," *Mech. Syst. Signal Process.*, vol. 20, no. 6, pp. 1265–1285, 2006.

[67]   P. H. Malinowski, M. Sawczak, T. Wandowski, W. M. Ostachowicz, and A. Cenian, "Characterisation of CFRP surface contamination by laser induced fluorescence," vol. 9064, p. 90640E, 2014.

[68]   "NIST: X-Ray   Mass   Attenuation   Coefficients," https://physics.nist.gov/PhysRefData/XrayMassCoef/tab1.html. .

[69]   R. Stoessel, "Computed Tomography for weak bond detection - ComBoNDT deliverable," 2016.

[70]   S. Jevšnik *et al.*, "Seam properties of ultrasonic welded multilayered textile materials," *J. Ind. Text.*, vol. 46, no. 5, pp. 1193–1211, 2017.

[71]   G. Scarselli, F. Ciampa, F. Nicassio, and M. Meo, "Non-linear methods based on ultrasonic waves to analyse disbonds in single lap joints," *Proc. Inst. Mech. Eng. Part C J. Mech. Eng. Sci.*, vol. 231, no. 16, pp. 3066–3076, 2017.

[72]   B. Ehrhart, B. Valeske, C.-E. Muller, and C. Bockenheimer, "Methods for the Quality Assessment of Adhesive Bonded CFRP Structures - A Resumé," *Proc. Int.*, pp. 1–9, 2010.

[73]   S. Hirsekorn, A. Koka, A. Wegner, and W. Arnold, "Quality assessment of bond interfaces by nonlinear ultrasonic transmission," vol. 1367, no. 2000, 2016.

[74]   P. Zabbal, G. Ribay, J. Jumel, and B. Chapuis, "Nondestructive evaluation of adhesive joints by using nonlinear ultrasonic and guided waves," in *ECNDT*, 2018.

[75]   F. T. Calkins, A. B. Flatau, and M. J. Dapino, "Overview of magnetostrictive sensor technology," *J. Intell. Mater. Syst. Struct.*, vol. 18, no. 10, pp. 1057–1066, 2007.

[76]   D. K. Kleinke and H. Mehmet Uras, "A noncontacting magnetostrictive strain sensor," *Rev. Sci. Instrum.*, vol. 64, no. 8, pp. 2361–2367, 1993.

[77]   A. Christopoulos, E. Hristoforou, I. Koulalis, and G. Tsamasphyros, "Inductive strain sensing using magnetostrictive wires embedded in carbon fibre laminates," *Smart Mater. Struct.*, vol. 23, no. 8, 2014.

[78]   G. Kanderakis, "Strain monitoring and damage detection of bonded composite structures, using magnetostrictive sensors – Latest developments and applications," in *EASN*, 2016.

[79]   T. Wandowski, "8 th International Symposium on NDT in Aerospace , November 3-5 , 2016 Electromechanical impedance method for assessment of adhesive bonds of CFRP at the production and repair stage," pp. 1–5, 2016.

[80]   P. H. Malinowski, W. M. Ostachowicz, K. Brune, and M. Schlag, "Study of electromechanical impedance changes caused by modifications of CFRP adhesive bonds," *Fatigue Fract. Eng. Mater. Struct.*, vol. 40, no. 10, pp. 1592–1600, Oct. 2017.

[81]   P. Malinowski, T. Wandowski, and W. Ostachowicz, "The use of electromechanical impedance conductance signatures for detection of weak adhesive bonds of carbon fibre–reinforced polymer," *Struct. Heal. Monit.*, vol. 14, no. 4, pp. 332–344, 2015.

[82]   M. Rosiek, A. Martowicz, and T. Uhl, "An Overview of Electromechanical Impedance Method for Damage Detection in Mechanical Structures," *6th Eur. Work. Struct. Heal. Monit. - Fr.1.B.4*, pp. 1–8, 2012.

[83]   R. Fabbro, J. Fournier, P. Ballard, D. Devaux, and J. Virmont, "Physical study of laser-produced plasma in confined geometry," *J. Appl. Phys.*, vol. 68, no. 2, pp. 775–784, 1990.

[84]   L. Berthe, R. Fabbro, P. Peyre, L. Tollier, and E. Bartnicki, "Shock waves from a water-confined laser-generated plasma," *J. Appl. Phys.*, vol. 82, no. 1997, pp. 2826–2832, 1997.

[85]   L. Berthe *et al.*, "State-of-the-art laser adhesion test (LASAT)," *Nondestruct. Test. Eval.*, vol. 26, no. 3–4, pp. 303–317, Sep. 2011.

[86]   C. R. Phipps *et al.*, "Impulse coupling to targets in vacuum by KrF, HF, and CO2single-pulse lasers," *J. Appl. Phys.*, vol. 64, no. 3, pp. 1083–1096, 1988.

[87]   S. P. Marsh, "LASL Shock Hugoniot Data," *Los Alamos Ser. Dyn. Mater. Prop.*, p. 150, 1980.

[88]   Z. Rosenberg, "On the relation between the Hugoniot elastic limit and the yield strength of brittle materials," *J. Appl. Phys.*, vol. 74, no. 1, pp. 752–753, 1993.

[89]   P. Ballard, "Contraintes résiduelles induites par impact rapide . Application au choc-laser . To cite this version : HAL Id : pastel-00001897," PhD Thesis, Ecole Polytechnique, 1991.

[90]   C. Bolis, "Ecole Doctorale Sciences pour l ' Ingénieur SEPARATION PAR CHOCS BREFS D ' INTERFACE DE," *Test*, 2004.

[91]   J. Vossen, "Measurements of Film-Substrate Bond Strength by Laser Spallation," in *Adhesion Measurement of Thin Films, Thick Films, and Bulk Coatings*, ASTM International, 1978, pp. 122-122–12.

[92]   J. Yuan and V. Gupta, "Measurement of interface strength by the modified laser spallation technique. I. Experiment and simulation of the spallation process," *J. Appl. Phys.*, vol. 74, no. 4, p. 2388, 1993.

[93]   V. Gupta and J. Yuan, "Measurement of interface strength by the modified laser spallation technique. II. Applications to metal/ceramic interfaces," *J. Appl. Phys.*, vol. 74, no. 4, p. 2397, 1993.

[94]   J. Yuan, V. Gupta, and A. Pronin, "Measurement of interface strength by the modified laser spallation technique. III. Experimental optimization of the stress pulse," *J. Appl. Phys.*, vol. 74, no. 4, pp. 2405–2410, Aug. 1993.

[95]   M. Boustie, E. Auroux, J.-P. Romain, A. Bertoli, and D. Manesse, "Determination of the bond strength of some microns coatings using the laser shock technique," *Eur. Phys. J. AP*, vol. 5, pp. 149–153, 1999.

[96]   C. Bolis, L. Berthe, M. Boustie, M. Arrigoni, S. Barradas, and M. Jeandin, "Physical approach to adhesion testing using laser-driven shock waves," *J. Phys. D. Appl. Phys.*, vol. 40, no. 10, pp. 3155–3163, 2007.

[97]   I. Gilath, S. Eliezer, T. Bar-Noy, R. Englman, and Z. Jaeger, "Material response at hypervelocity impact conditions using laser induced shock waves," *Int. Z Impact Engng*, vol. 14, pp. 279–289, 1993.

[98]   R. Bossi, K. Housen, and C. Walters, "Laser Bond Inspection Device for Composites : Has The Holy Grail Been Found ?," *NTIAC (Nondestructive Test. Inf. Anal. Center)*, vol. 30, no. June, 2005.

[99]   E. Gay, L. Berthe, M. Boustie, M. Arrigoni, and M. Trombini, "Effects of the shock duration on the response of CFRP composite laminates," *Compos. Part B Eng.*, vol. 64, pp. 108–115, 2014.

[100]   R. Ecault *et al.*, "Experimental and numerical investigations of shock and shear wave propagation induced by femtosecond laser irradiation in epoxy resins," *J. Phys. D. Appl. Phys.*, vol. 48, no. 9, p. 095501, 2015.

[101]   R. Bossi, K. Housen, W. Sheperd, and M. Voss, "Bond strength measurement system using shock loads," 18-Oct-2001.

[102]   R. Bossi and V. Brustad, "Using laser shock loads to debond structures," patent number: US 7,507,312 B2, 23-Aug-2005.

[103]   R. Bossi, "NDE for Adhesive Bond Strength," in *Spring Conference*, 2011.

[104]   R. Bossi, K. Housen, C. T. Walters, and D. Sokol, "Laser Bond Inspection," *Mater. Eval.*, vol. 67, no. 7, 2009.

[105]   J. Little, "Apparatus and method for nondestructive testing of dielectric materials," patent number: US 6,359,446 B1, 22-Sep-1998.

[106]   "Laser   Bond   Inspection   (LBI)   System   Overview," https://www.youtube.com/watch?v=oJ6QeocQY_E&t=22s. .

[107]   R. Ecault, "Experimental and numerical investigations on the dynamic behaviour of aeronautic composites under laser shock - Optimization of a shock wave adhesion test for bonded composites," PhD Thesis, Poitiers, ENSMA, 2013.

[108]   D. Courapied, L. Berthe, P. Peyre, F. Coste, J.-P. Zou, and A.-M. Sautivet, "Laser-delayed double shock-wave generation in water-confinement regime," *J. Laser Appl.*, vol. 27, no. S2, p. S29101, 2015.

[109]   D. Courapied, "Etude de l'interaction laser matière en régime de confinement par eau avec deux impulsions laser . Application au test d'adhérence par choc laser . To cite this version : HAL Id : tel-01495241 l'École Nationale Supérieure d'Arts et Métiers par eau," PhD Thesis, ENSAM, 2017.

[110]   S. Bardy, "Contrôle et optimisation du test d'adhérence par choc laser sur assemblages collés," PhD Thesis, ENSAM, 2018.

[111]	T. De Rességuier and M. Hallouin, "Interaction of two laser shocks inside iron samples," *J. Appl. Phys.*, vol. 90, no. 9, pp. 4377–4384, 2001.

[112]	M. Ghrib *et al.*, "Generation of controlled delaminations in composites using symmetrical laser shock configuration," *Compos. Struct.*, vol. 171, pp. 286–297, Jul. 2017.

[113]	M. Boustie *et al.*, "Study of damage phenomena induced by edge effects into materials under laser driven shocks," *J. Phys. D. Appl. Phys.*, vol. 40, no. 22, pp. 7103–7108, 2007.

[114]	J. P. Cuq-Lelandais, "Etude du comportement dynamique de matériaux sous choc laser subpicoseconde," PhD Thesis, ENSMA, Poitiers, 2010.

[115]	M. Perton, A. Blouin, and J.-P. Monchalin, "Adhesive bond testing of carbon-epoxy composites by laser shockwave," *J. Phys. D. Appl. Phys.*, vol. 44, no. 44, pp. 1–12, 2010.

[116]	S. Gholizadeh, "A review of non-destructive testing methods of composite materials," *Procedia Struct. Integr.*, vol. 1, pp. 50–57, 2016.

[117]	C. Garnier, M. L. Pastor, F. Eyma, and B. Lorrain, "The detection of aeronautical defects in situ on composite structures using non destructive testing," *Compos. Struct.*, vol. 93, no. 5, pp. 1328–1336, 2011.

[118]	"Water absorption spectrum," http://www1.lsbu.ac.uk/water/water_vibrational_spectrum.html. .

[119]	"LASER MARKING: How to choose the best laser for your marking application_Technology Information_News_Wuhan HGLaser Engineering Co,.Ltd.," 2011, http://en.hglaser.com/news/13506_for_TechnologyInformation_text.htm. .

[120]	L. Berthe, "Processus de claquage de milieux transparents sous irradiation laser. Application au choc laser en régime de confinement par eau," PhD Thesis, Paris XI Orsay, 1998.

[121]	A. Sollier, "Etude des plasmas générés par interaction laser-matière en régime confiné. Application au traitement des matériaux par choc laser," PhD Thesis, Université de Versailles St-Quentin, 2002.

[122]	S. Bardy, "Recherche du seuil d'endommagement d'un composite époxy en régime confiné par eau." 2016.

[123]	E. Moutsompegka *et al.*, "Experimental study of the effect of pre-bond contamination with de-icing fluid and ageing on the fracture toughness of composite bonded joints," *Fatigue Fract. Eng. Mater. Struct.*, vol. 40, no. 10, pp. 1581–1591, 2017.

[124]   E. Moutsompegka *et al.*, "The effects of pre-bond contamination with de-icing fluid on the mode-I and mode-II fracture toughness of composite bonded joints," in *6th EASN International*, 2016.

[125]   E. Moutsompegka, K. Tserpes, K. Brune, M. Schlag, and S. Pantelakis, "The effect of pre-bond contamination with fingerprint and ageing on the fracture toughness of composite bonded joints," in *6th EASN International*, 2016.

[126]   C. Schuecker and B. D. Davidson, "Evaluation of the accuracy of the four-point bend end-notched flexure test for mode II delamination toughness determination," *Compos. Sci. Technol.*, vol. 60, no. 11, pp. 2137–2146, 2000.

[127]   F. Pierron and A. Vautrin, "Accurate comparative determination of the in-plane shear modulus of T300/914 by the iosipescu and 45° off-axis tests," *Compos. Sci. Technol.*, vol. 52, no. 1, pp. 61–72, 1994.

[128]   J. Jumel, M. K. Budzik, N. Ben Salem, and M. E. R. Shanahan, "Instrumented end notched flexure - Crack propagation and process zone monitoring. Part I: Modelling and analysis," *Int. J. Solids Struct.*, vol. 50, no. 2, pp. 297–309, 2013.

[129]   Hexcel, "Hexcel ready to fl y on the A350 XWB," *REINFORCEDplastics*, no. June 2013, pp. 25–26, 2013.

[130]   C. Paris, G. Bernhart, P. A. Olivier, and O. De Almeida, "Influence de cycles de cuisson rapides sur le préimprégné aéronautique M21/T700 : suivi de polymérisation et propriétés mécaniques," in *JNC 17*, 2011, p. 10.

[131]   D. Tilbrook, D. Blair, M. Boyle, and P. MacKenzie, "Composite materials with blend of thermoplastic particles," patent number: US 7,754.322 B2, 17-Apr-2006.

[132]   "Aernnova," http://www.aernnova.com/en/. .

[133]   H. I. Kim, B. A. Morgan, J. P. Nokes, and R. J. Zaldivar, "Quantitative Evaluation of Silicone Contamination Effect on Composite Bonding," *J. Adhes.*, vol. 91, no. 4, pp. 320–329, 2015.

[134]   A. Mubashar, I. A. Ashcroft, G. W. Critchlow, and A. D. Crocombe, "Moisture absorption-desorption effects in adhesive joints," *J. Adhes. Adhes.*, vol. 29, no. 8, pp. 751–760, 2009.

[135]   K. J. Wong, "Moisture absorption characteristics and effects on mechanical behaviour of carbon/epoxy composite : application to bonded patch repairs of composite structures," PhD Thesis, Université de Bourgogne, 2013.

[136] "Grinding and Polishing - Knowledge. Struers.com," https://www.struers.com/en/Knowledge/Grinding-and-polishing#grinding-polishing-troubleshooting. .

[137] A. Johnson, "Simulation Methodology for High Velocity Impact in Composite Aircraft Structures," *Air Sp. Eur.*, 2001.

[138] M. Wicklein, S. Ryan, D. M. White, and R. A. Clegg, "Hypervelocity impact on CFRP: Testing, material modelling, and numerical simulation," *Int. J. Impact Eng.*, vol. 35, no. 12, pp. 1861–1869, 2008.

[139] S. Ryan, M. Wicklein, A. Mouritz, W. Riedel, F. Schäfer, and K. Thoma, "Theoretical prediction of dynamic composite material properties for hypervelocity impact simulations," *Int. J. Impact Eng.*, vol. 36, no. 7, pp. 899–912, 2009.

[140] O. I. Okoli, "The effects of strain rate and failure modes on the failure energy of fibre reinforced composites," *Compos. Struct.*, vol. 54, pp. 1–5, 2001.

[141] H. M. Hsiao, I. M. Daniel, and R. D. Cordes, "Strain rate effect on the transverse compressive and shear behavior of unidirectional composites," *J. Compos. Mater.*, vol. 33, no. 17/1999, 1998.

[142] J. Tsai and C. T. Sun, "Strain rate effect on in-plane shear strength of unidirectional polymeric composites," *Compos. Sci. Technol.*, vol. 65, pp. 1941–1947, 2005.

[143] G. C. Jacob, J. M. Starbuck, J. F. Fellers, S. Simunovic, and R. G. Boeman, "Strain rate effects on the mechanical properties of polymer composite materials," *J. Appl. Polym. Sci.*, vol. 94, no. 1, pp. 296–301, Sep. 2004.

[144] A. De Luca, F. Di Caprio, F. Caputo, G. Lamanna, and M. Ignarra, "On the Tensile Behaviour of CF and CFRP Materials under High Strain Rates," *Key Eng. Mater.*, pp. 111–114, 2017.

[145] P. M. Rozycki, "Contribution au développement de lois de comportement pour matériaux composites soumis à l'impact," PhD Thesis, Université de Valienciennes et du Hainaut-Cambresis, 2000.

[146] P. Feraboli, "Simulating Laminated Composite Materials Using LS-DYNA Material Model MAT54 : Single-Element Investigation - Report from U.S. Department of Transportation Federal Aviation Administration," 2017.

[147] F.-K. Chang and K.-Y. Chang, "Post-Failure Analysis of Bolted Composite Joints in Tension or Shear-Out Mode Failure," *J. Compos. Mater.*, 1987.

[148]   F.-K. Chang and K.-Y. Chang, "A Progressive Damage Model for Laminated Composites Containing Stress Concentrations," *J. Compos. Mater.*, 1987.

[149]   P. Wriggers, *Computational Contact Mechanics*. John Wiley & Sons Ltd., 2002.

[150]   R. Ecault, F. Touchard, M. Boustie, L. Berthe, and N. Dominguez, "Numerical modeling of laser-induced shock experiments for the development of the adhesion test for bonded composite materials," *Compos. Struct.*, vol. 152, pp. 382–394, 2016.

[151]   D. Laporte, "Analyse de la reponse d'assemblages colles sous des sollicitations en dynamique rapide. Essais et modelisations," PhD Thesis, ISAE-ENSAM Ecole Nationale Supérieur de Mécanique et d'Aéronautique - Poitiers, 2011.

[152]   S. S. Karna and R. Sahai, "An Overview on Taguchi Method," *Int. J. Eng. Math. Sci.*, vol. 1, no. 1, pp. 2319–4537, 2012.

[153]   G. E. . Box, "On the Experimental Attainment of Optimum Conditions," *J. R. Stat. Soc.*, vol. Series B, no. 13, pp. 1–45, 1951.

[154]   Z. Zhang and Baixiaofeng, "Comparison about the three central composite designs with simulation," *Proc. - Int. Conf. Adv. Comput. Control. ICACC 2009*, no. 3, pp. 163–167, 2009.

[155]   B. A. Oyejola and J. C. Nwanya, "Selecting the Right Central Composite Design," *Int. J. Stat. Appl.*, vol. 5, no. 1, pp. 21–30, 2015.

[156]   "Interpret the key results for Normality Test," https://support.minitab.com/en-us/minitab-express/1/help-and-how-to/basic-statistics/summary-statistics/normality-test/interpret-the-results/key-results/. .

[157]   A. Fenech, T. Fearn, and M. Strlic, "Use of Design-of-Experiment principles to develop a dose-response function for colour photographs," *Polym. Degrad. Stab.*, vol. 97, no. 4, pp. 621–625, 2012.

[158]   R. M. Pabari and Z. Ramtoola, "Application of face centred central composite design to optimise compression force and tablet diameter for the formulation of mechanically strong and fast disintegrating orodispersible tablets," *Int. J. Pharm.*, vol. 430, no. 1–2, pp. 18–25, 2012.

[159]   "Support - Minitab," http://www.minitab.com/en-us/support/. .

[160]   "How to Predict with Minitab: Using BMI to Predict the Body Fat Percentage, Part 2," https://blog.minitab.com/blog/adventures-in-statistics-2/how-to-predict-with-minitab-using-bmi-to-predict-the-body-fat-percentage-part-2. .

[161]   C. Schoberleitner, V.-M. Archodoulaki, T. Koch, S. Lüftl, M. Werderitsch, and G. Kuschnig, "Developing a Sealing Material: Effect of Epoxy Modification on Specific Physical and Mechanical Properties," *Materials (Basel).*, vol. 6, no. 12, pp. 5490–5501, Nov. 2013.

[162]   F. Chinesta and E. Cueto, *PGD-Based Modeling of Materials , Structures and Processes*. Springer, 2014.

DETECTION DES JOINTS FAIBLES PAR DES TECHNIQUES DE CHOC PRODUIT PAR LASER.

Résumé : l'une des grandes problématiques actuelles des secteurs aéronautique et spatial est la réduction du taux d'émission de CO2. Une des solutions est l'allègement et l'optimisation des structures. Dans cette optique, certains avions comme l'a380 ou l'a350 XWB ont été fabriqués en grande partie à l'aide de matériaux composites. Plus résistants et plus légers, ils permettent un gain de poids important comparés aux matériaux métalliques. Cependant, ces pièces composites sont encore assemblées à l'aide de rivets ou de boulons. Ces procédés non adaptés aux matériaux composites limitent le gain de poids que pourrait engendrer leur utilisation. L'emploi de colles en revanche permettrait ce palier à ce problème, permettant ainsi de réduire de manière plus efficace le poids des structures. Cependant, ce procédé peut aussi être à l'origine de la création de joints faibles. Un joint est qualifié de faible quand sa tenue mécanique est inférieure à sa tenue nominale prévue. Actuellement, l'absence de Control Non Destructif (CND) permettant d'évaluer les propriétés mécaniques de ces pièces collées est l'un des principaux verrous à l'utilisation de ce procédé d'assemblage.

Le Test d'Adhérence par Choc Laser (LASAT) a déjà prouvé sa capacité à évaluer la tenue mécanique de joints de colle dans des structure en Polymère Renforcé de Fibres de Carbone (PRFC). Cependant il ne peut s'appliquer qu'à quelques géométries d'assemblage spécifiques et a aussi démontré des limites en termes de détection de joint faible. Ce travail propose une étude expérimentale et numérique d'une des optimisations du LASAT : le Test d'Adhérence par Choc Laser Symétrique (S-LASAT). Le but est d'approfondir la compréhension de la physique mise en jeu afin de mieux appréhender les prérequis nécessaires à la technologie pour détecter les joints faibles. Cette étude conclura sur une étude unique de test d'adhérence réalisée sur de vraies pièce aéronautiques collées.

Mots clés : composite, choc laser, joint faible, collage

DETECTION OF WEAK BONDS IN COMPOSITE MATERIALS USING SYMMETRICAL LASER IMPACTS.

ABSTRACT: The limitation of carbon dioxide emissions is one of today's greatest challenges for the aerospace industry. Weight reduction is seen as one of the most promising lead for that matter and a first step has already been made toward this goal through the use of composite materials. Lighter and more mechanically efficient than their metallic counterparts, their use helped optimising the weight of several aircrafts such as the A350 XWB or A380. Nevertheless, if the material has changed, the assembly process did not evolve along with it. Hence, techniques such as riveting or bolting previously used for metallic structure are still used for composite parts assembly, but they are not suitable anymore for this type of material (creation of local constraints, corrosion, …). Instead, bonding composite parts using adhesives would be a better solution and could help further reducing the overall weight of the aircraft. However, with this new assembly method also come new problems, such as weak bonding. A weak bond is characterised by a loss of mechanical adherence that cannot be spotted using conventional Non-Destructive Tests (NDTs) such as ultrasound scanning. Since the industry currently lacks these NDTs to assess the mechanical integrity of bonded structures, the use of adhesives for composite assembly is limited.

The LAser Shock Adhesion Test (LASAT), has already demonstrated its capacity to evaluate bonded composite assembly but also proved to be limited in terms of assembly configuration and weak bond detection capability. This work focuses on one of its optimisations, the Symmetrical LASAT (S-LASAT). Both experimental and numerical studies are realised to better understand the prerequisites of the technique as well as the level of mastery required for the technology to best detect weak bonds within Carbon Fibre Reinforce Polymer (CFRP) structures. This manuscript concludes with a one of a kind experimental campaign realised on real bonded CFRP aircraft parts.

Keywords : composite, laser shock, weak bond, NDT